Displacement Flow of Complex Fluids in an Inclined Duct

by

Kamran Alba

B.Sc., Iran University of Science and Technology, 2006
M.Sc., The University of Western Ontario, 2008

A THESIS SUBMITTED IN PARTIAL FULFILLMENT OF
THE REQUIREMENTS FOR THE DEGREE OF

DOCTOR OF PHILOSOPHY

in

The Faculty of Graduate Studies

(Mechanical Engineering)

THE UNIVERSITY OF BRITISH COLUMBIA

(Vancouver)

July 2013

© Kamran Alba 2013

Abstract

This thesis studies buoyant displacement flows with two miscible fluids in pipes and 2D channels that are inclined at an angle β measured from vertical changing from 0° to 90°. The focus is on inclination angles away from nearly horizontal since these flows are previously studied in full details in the literature. Detailed experimental, analytical and computational approaches are employed in an integrated fashion.

Both density stable (light fluid displacing heavy one) and density unstable (heavy fluid displacing light fluid) displacements are studied. For density stable flows the study is purely experimental in the limit of iso-viscous Newtonian fluids. The density stable configuration has been found to produce highly efficient displacements, with the bulk of the interface moving steadily at the mean velocity. The streamwise length of the stretched interface increases with the mean flow velocity, viscosity and inclination β from vertical, and decreases with density difference.

The rest of the thesis deals with density unstable configuration. From experimental point of view, the pipe displacement flows are studied for iso-viscous Newtonian and also viscoplastic fluids. In the Newtonian limit, completely different regimes than nearly-horizontal case are observed. As a first order approximation, different regimes are classified in a two-dimensional (Fr; $Re\cos\beta/Fr$ plane) providing leading order correlations to transitions to different regimes. Similar regimes are found for channel geometry through numerical simulations of PELICANS code. For non-Newtonian fluids we have focused on industrially interesting cases of large yield stress fluids in the pipe. The two distinct flow regimes namely central-type and slump-type first observed in nearly horizontal angles were found to also persist over other inclinations. Completely new and exotic behaviors were also observed due to the effect of inclination angle and instabilities.

From mathematical and modeling point of view a two-layer weighted residual model for generalized Newtonian fluids has been developed. The model works for channel geometry and can be used to predict the displacement interface height, the front velocity and more importantly, the flow stability.

Preface

In this preface, we briefly explain the contents of the papers that are published or submitted for publications from this thesis. We also mention the relative contributions of collaborators and co-authors in the papers.

- **K. Alba**, S.M. Taghavi, and I.A. Frigaard. *Miscible density stable displacement flows in inclined tube.* ***Phys. Fluids*** **24**, 123102-11 (2012).
  This work deals with the displacement of two miscible iso-viscous fluids of different densities in a tilted pipe with the two fluids initially in a gravitationally stable configuration i.e. light fluid displacing a heavier one downwards. In this experimental work we first observe that the displacement efficiency is highest in density stable configuration and that the length of the stretched interface between the two fluids remains constant over time. This stretch length was found to depend on imposed velocity, inclination, density difference and the common viscosity of the two fluids. After quantifying this dependency we are able to represent the scaled stretch length as a function of a simple parameter which represents the ratio of the buoyancy and viscous stresses. I wrote the paper with I.A. Frigaard. S.M. Taghavi provided useful comments. The experiments were conducted by me. I also supervised co-op students, Messrs E. Stuart, H. Abou Jaoude and G. Hatzikiriakos in running the experiments who are also acknowledged in the paper. S.M. Taghavi assisted in the experiments too by consulting about the range of experimental parameters to be used in the study. This research was supervised by I.A. Frigaard.

- **K. Alba**, S.M. Taghavi, and I.A. Frigaard. *Miscible density unstable displacement flows in inclined tube.* **Accepted for publication in Phys. Fluids.**
  This work deals with the displacement of two miscible iso-viscous fluids of different densities in a tilted pipe with the two fluids initially in a gravitationally unstable configuration i.e. heavy fluid displacing a lighter one downwards. In this experimental work we first observe

that the displacement efficiency is less than density stable configuration and that different flow regimes may appear at different inclination angles e.g. viscous, inertial, diffusive etc. In a phenomenological study approximation, these regimes are classified in a two-dimensional dimensionless planes providing leading order correlations to transitions to different regimes. The effect of the imposed flow on front velocity and macroscopic diffusion is also investigated for different flows. The stabilizing and/or de-stabilizng effects of the mean flow on buoyant exchange flows are finally given for broad range of dimensionless parameters. I wrote the paper with I.A. Frigaard. S.M. Taghavi provided very useful comments. The experiments were conducted by me. I also supervised co-op students, Messrs E. Stuart, H. Abou Jaoude and G. Hatzikiriakos in running the experiments who are also acknowledged in the paper. S.M. Taghavi assisted in the experiments by lengthy discussions about the results and making the connection with the nearly-horizontal studies of his carried out before. This research was supervised by I.A. Frigaard.

- **K. Alba**, S.M. Taghavi, and I.A. Frigaard. *Weighted residual method for two-layer non-Newtonian channel flows*. **Submitted for publication.**
  In this work we have developed a two-layer model based on weighted residual approach for generalized Newtonian fluids. The improvement over the previous lubrication model is that it takes into account the presence of weakly inertial terms as well as viscous stresses. The model developed can be used for simulating the co-extrusion and displacement flows although the latter is of our interest. We give predictions of interface shape and front velocity over a broad range of geometrical and rheological parameters. Through a linear stability analysis carried in this work we have shown the stability diagrams of the two layer flows in different planes of governing parameters. The paper was written by I.A. Frigaard and I. S.M. Taghavi read the paper and provided useful comments. In a close collaboration with I.A. Frigaard, I developed the mathematical model and carried out the numerical solutions for the model. S.M. Taghavi assisted in writing the intense code developed for solving the weighted-residual model numerically. I developed the stability analysis section codes/results assisted by I.A. Frigaard. This research was supervised by I.A. Frigaard.

- **K. Alba**, S.M. Taghavi, J.R. de Bruyn and I.A. Frigaard. *Incomplete*

fluid-fluid displacement of yield stress fluids in inclined pipes. **Submitted for publication.**
The experimental paper studies the displacement of a yield stress fluid from an inclined pipe in the situation that the yield stress is strong relative to typical viscous forces. In fact this work is the extension of our previous work on nearly-horizontal displacement flows to other inclination angles. We interestingly observed that the center-type and slump-type displacements found in nearly horizontal regime also exist at higher angles with the same value of Archimedes number for transition between the regimes. As we move away from horizontal angles to vertical we observe completely new and exhotic flows within the category of the slump-type displacements which are studied in detail. The flows were also studied from instantaneous and non-instantaneous point of view. I wrote the paper with I.A. Frigaard. The other authors read the draft and provided comments. The experiments and rheologies were conducted by me. I also supervised co-op students, Messrs H. Abou Jaoude and G. Hatzikiriakos in running the experiments who are also acknowledged in the paper. S.M. Taghavi also assisted in the experiments by discussing about the range of experimental parameters to choose for the study since the work was tightly related with nearly horizontal regime we had explored before. J.R. de Bruyn gave detailed comments on how to present the results and assisted in better studying the highly-unstable flows discussed earlier. This research was supervised by I.A. Frigaard.

Although the focus of the thesis is on displacement flows away from nearly-horizontal angles, a good amount of time was spent with Mr. S.M. Taghavi, former Ph.D. student in our group studying the displacement flows in nearly-horizontal angles to gain the sufficient modeling/experimental skills before moving to the main project. Therefore the publications related to these studies are also outlined here since they are inevitably closely related to the findings in this thesis. The contribution that set the ground for developing the *weighted-residual model* for two-layer flow system in this thesis (chapter 6) is also mentioned first.

- **K. Alba**, P. Laure and R.E. Khayat. *Transient two-layer thin-film flow inside a channel.* ***Phys. Rev. E*** **84**, 026320-14 (2011).
  This work set the basis of deriving the two-layer weighted-residual model for channel flows in this thesis. In this paper the two-layer flow of two Newtonian fluids in a channel (co-extrusion flow) is studied

analytically. The developed model is then solved numerically for a range of governing parameters e.g. viscosity ratio, flow rate ratio etc. I used a finite difference scheme to solve the equations numerically with two types of boundary conditions at the inflow: a Dirac-type pulse and periodic forcing. The perturbation takes the form of a wave packet which may or may not be amplified as it moves downstream, depending on the values of the parameters involved in problem. Both the model presented and the results can be used to avoid non-uniform extruded products by choosing processing parameters appropriately. The calculations for developing the model and the computations were carried out by me with insightful discussions with the rest of the authors. The manuscript were first written by me and then corrected by P. Laure and R.E. Khayat for final submission. The work was supervised by Professor R. E. Khayat in University of Western Ontario and co-supervised by Professor P. Laure in Universit de Nice.

- S.M. Taghavi, **K. Alba** and I.A. Frigaard. *Buoyant miscible displacement flows at moderate viscosity ratios and low Atwood numbers in near-horizontal ducts.* ***Chem. Eng. Sci.*** **69**, 404-418 (2012).
  In this work, results from a study of buoyant miscible displacements flows at moderate viscosity ratios in near-horizontal pipes and plane channels were presented. We show that small viscosity ratios lead to more efficient displacements, as is intuitive. In each geometry we find a mix of viscous and inertial flows, in broadly the same pattern as for the iso-viscous displacements studied before. Predictive models are proposed for the viscous regime, in the case of the plane channel, and for the inertial exchange flow regime, in both geometries. The displacement flows with shear-thinning fluids were also studied, over a more restrictive range of parameters. We show that with an appropriate definition of the effective viscosity the scaled front velocities fit well with the results from the Newtonian displacements, in both pipe and plane channel geometries. S.M. Taghavi and I.A. Frigaard wrote this paper together and I read the draft and provided comments. S.M. Taghavi conducted the experiments and simulations and developed the analyses. I assisted with the rheology of shear-thinning fluids, running the experiments and designing them in a few cases. I also co-supervised S. Gharib (undergraduate co-op student in the lab) with S.M. Taghavi in running the experiments. I.A. Frigaard supervised the research.

- S.M. Taghavi, **K. Alba**, M. Moyers-Gonzalez and I.A. Frigaard. *In-*

complete fluid-fluid displacement of yield stress fluids in near-horizontal pipes: experiments and theory. ***J. non-Newton. Fluid Mech.*** **167-168**, 59-74 (2012).
The paper is a primarily experimental study of displacement of a yield stress fluid from an inclined pipe in the situation that the yield stress is strong relative to typical viscous forces. This results in an interesting balance between inertia and buoyancy in yielding the fluid. The main finding is that the type of displacement front observed can be one of two types (central or slump) and that this division depends primarily on the ratio of Reynolds number to densimetric Froude number (also known as the Archimedes number). It is notable that this particular group does not depend on the mean displacement velocity. S.M. Taghavi and I.A. Frigaard wrote this paper together; M. Moyers-Gonzalez and I read the draft and provided comments. M. Moyers-Gonzalez collaborated through code development of the finite element method used in this paper; S.M. Taghavi ran the code and produced the results. S.M. Taghavi conducted the experiments and was assisted by me in developing fluid preparation criterion, rheology and running the actual experiments. I also co-supervised S. Gharib (undergraduate co-op student in the lab) with S.M. Taghavi in running the experiments. I.A. Frigaard developed the simple analytical model, which S.M. Taghavi solved numerically; he also supervised the entire research.

- S.M. Taghavi, **K. Alba**, T. Seon, K. Wielage-Burchard, D.M. Martinez and I.A. Frigaard. *Miscible displacements flows in near-horizontal ducts at low Atwood number.* ***J. Fluid Mech.*** **696**, 175-214 (2012).
In this extensive study buoyant displacement flows were considered with two miscible fluids of equal viscosity in the regime of low Atwood number and in ducts that are inclined close to horizontal. It was shown that three dimensionless groups largely describe these flows: Fr (densimetric Froude number), Re (Reynolds number) and β (duct inclination). The flow regimes were shown to in fact collapse into regions in a two-dimensional (Fr; $Re\cos\beta/Fr$)-plane. S.M. Taghavi and I.A. Frigaard wrote this paper together; the other authors read the draft and provided comments and corrections. S.M. Taghavi conducted the experiments and simulations and developed the analytical lubrication model in collaboration with I.A. Frigaard. T. Seon supervised the experiments and K. Wielage-Burchard helped with code development. I assisted S.M. Taghavi in developing the weighted residual model ap-

proach presented in this paper as an improvement to the lubrication model. The model was used to capture the displacement interface shape and predict the flow stability. I.A. Frigaard and D.M. Martinez supervised the research.

- M. Moyers-Gonzalez, **K. Alba**, S.M. Taghavi and I.A. Frigaard. *A semi-analytical closure approximation for pipe flows of two Herschel-Bulkley fluids with a stratified interface.* ***J. Non-Newton. Fluid Mech.*** **193**, 49-67 (2012).
  We propose a semi-analytical closure approximation to the stratified flow of two Herschel-Bulkley fluids flowing along a circular pipe. The closure model proposed appears to approximate the volumetric fluxes within 10-15% over a broad range of interface heights and rheological parameters. We demonstrate that the closure is able to give a good prediction of viscous regime displacement front velocities, comparing well with experimental values, and can be used for approximating other design features of a displacement process, for example the maximal static wall layer when yield stress fluid are concerned. The other design feature can be estimating the minimal flow rate to prevent back flow. M. Moyers-Gonzalez and I.A. Frigaard wrote this paper together; S.M. Taghavi and I read the draft and provided comments. M. Moyers-Gonzalez developed the closure model in collaboration with I.A. Frigaard. The model results were compared against experimental data obtained by S.M. Taghavi and me. Using the closure model, I also assisted in predicting the onset of back flow over a wide range of rheological parameters. I.A. Frigaard supervised the entire research.

Conference presentations and proceedings

- **K. Alba**, S.M. Taghavi, S. Gharib, T. Seon, D.M. Martinez and I.A. Frigaard. *Displacement flows in conduits: front velocity regimes and shear-thinning effects.* ***Annual European Rheology Conference (AERC)***, Gothenburg, Sweden (2010).

- **K. Alba**, S.M. Taghavi, S. Gharib, T. Seon, D.M. Martinez and I.A. Frigaard. *Miscible two-fluid displacement flows in a near-horizontal pipe.* ***Canadian Society for Mechanical Engineers (CSME) Forum***, Victoria, Canada (2010).

- **K. Alba**, S.M. Taghavi, S. Gharib, T. Seon, D.M. Martinez and I.A. Frigaard. *Displacement flow of shear thinning fluids in tube: The effect of density and viscosity ratio.* ***ASME International Mechanical Engineering Congress and Exposition***, Vancouver, Canada (2010).

- **K. Alba**, S.M. Taghavi and I.A. Frigaard. *A weighted residual method for two-layer non-Newtonian fluids.* ***International Congress on Industrial and Applied Mathematics (ICIAM)***, Vancouver, Canada (2011).

- **K. Alba**, P. Laure and R.E. Khayat. *Transient Two-Layer Channel Flow.* ***Canadian Congress of Applied Mechanics (CANCAM)***, Vancouver, Canada (2011).

- S.M. Taghavi, **K. Alba** and I.A. Frigaard. *Weakly inertial buoyant displacement flows in nearly horizontal channels.* ***Canadian Congress of Applied Mechanics (CANCAM)***, Vancouver, Canada (2011).

- S.M. Taghavi, **K. Alba** and I.A. Frigaard. *A Weighted Residual Method for 2-Layer Flows with Yield Stress Fluids.* ***4th Workshop on Viscoplastic Fluids: From Theory to Application***, Rio de Janeiro, Brazil (2011).

- **K. Alba**, S.M. Taghavi and I.A. Frigaard. *Displacement of yield stress fluids in inclined pipes.* ***6th European Congress on Computational Methods in Applied Sciences and Engineering (ECCOMAS)***, Vienna, Austria (2012).

Table of Contents

Abstract ii

Preface iii

Table of Contents x

List of Tables xiv

List of Figures xv

Acknowledgements xxiii

Dedication xxv

1 Synopsis 1
1.1 Problem of study 1
1.2 Outline of the thesis 5

2 Background 6
2.1 Primary cementing background 6
2.2 Associated fundamental problems 9
2.2.1 Flow stability 9
2.2.2 Exchange flows 15
2.2.3 Boycott effect 20
2.2.4 Displacement flows in nearly horizontal ducts 21
2.2.5 Structured displacement flows 24
2.2.6 Averaged inertial models 26
2.2.7 Axial dispersion 29
2.2.8 Conclusions and research objectives 33

3 Miscible density stable displacement flows in an inclined pipe 38
3.1 Experiments and parameters range 39

3.2 Results . . . 40
3.2.1 The transition from density unstable to density stable 41
3.2.2 Characteristics of density stable displacements 43
3.2.3 Parametric variation in the fully developed stretch length . . . 49
3.3 Discussion points . . . 54

4 Miscible density unstable displacement flows in an inclined pipe . . . 56
4.1 Experiments and parameters range . . . 57
4.2 Results . . . 59
4.2.1 Exchange flows . . . 59
4.2.2 Displacement flows: main qualitative features 60
4.2.3 Front velocity measurement and characteristics 64
4.2.4 Macroscopic diffusion . . . 72
4.3 Regime classification and leading order approximations . . . 80
4.4 Discussion points . . . 88

5 Miscible density unstable displacement flows in inclined channels: Numerical simulations . . . 90
5.0.1 Parameter range . . . 91
5.0.2 Simulation overview . . . 92
5.1 Results . . . 94
5.1.1 Displacement flows: main qualitative features 95
5.1.2 Front velocity measurement and characteristics 101
5.1.3 Instantaneous and non-instantaneous displacements . 106
5.1.4 Displacing front phenomena . . . 112
5.1.5 Macroscopic diffusion . . . 121
5.1.6 Overall regime classification . . . 128
5.2 Discussion points . . . 130

6 Weighted residual method for two-layer non-Newtonian channel flows . . . 132
6.1 Displacement flow in channel . . . 135
6.1.1 Constitutive equations considered . . . 136
6.1.2 Parallel flow solution . . . 137
6.1.3 Long-thin flows . . . 140
6.1.4 Standard thin-film approach . . . 142
6.2 Weighted residual approximation . . . 143
6.2.1 Velocity closure . . . 145

6.2.2 Weighted residual equation . . . 146
6.2.3 Calculating the weight functions and terms in the residual equation (6.55) . . . 148
6.3 Results: displacement flows . . . 153
6.4 Stability of 2-layer flows . . . 158
6.4.1 Weighted residual method stability of a parallel flow . 159
6.4.2 Orr-Sommerfeld analysis . . . 161
6.4.3 Comparisons with the Orr-Sommerfeld analysis . . . 164
6.4.4 Stability results . . . 164
6.5 Discussion points . . . 175

7 Incomplete fluid-fluid displacement of yield stress fluids in inclined pipes . . . 177
7.1 Experiments and parameters range . . . 178
7.2 Results . . . 181
7.2.1 Slump regime . . . 183
7.2.2 Central regime . . . 192
7.2.3 Turbulent-mixed displacements . . . 196
7.2.4 Exchange flows . . . 199
7.2.5 Dimensionless flow classification . . . 203
7.3 Discussion points . . . 207

8 Conclusions . . . 208
8.1 Contributions to fluid dynamics understanding . . . 208
8.1.1 Newtonian iso-viscous displacement flows . . . 208
8.1.2 Yield stress fluids displacement . . . 211
8.1.3 Modeling and stability of the displacement flows . . . 212
8.2 Industrial implications and recommendations . . . 213
8.3 Limitations of the present study and future work . . . 217
8.3.1 Main limitations of the current study . . . 217
8.3.2 Experimental perspectives . . . 220
8.3.3 Numerical simulation perspectives . . . 222
8.3.4 Mathematical modeling perspectives . . . 222

Bibliography . . . 225

Appendices

A Research methodology . . . 238

A.1 Experimental technique . . . 238
A.1.1 Fluid preparation and delivery . . . 241
A.1.2 Valves . . . 247
A.1.3 Velocity measurements . . . 249
A.1.4 Image Processing and Visualization Technique . . . 250
A.1.5 Fluid rheology . . . 256
A.1.6 Experimental results validation . . . 258
A.2 Numerical technique . . . 259
A.2.1 Code benchmarking . . . 263

B Weight functions and residual equation . . . 265
B.1 Newtonian fluids . . . 265
B.2 General specification of the weight functions . . . 266
B.3 Calculating the terms in the residual equation (6.55) . . . 267
B.4 Terms in the residual equation: acceleration terms . . . 269
B.5 Terms in the residual equation: convective terms . . . 269
B.5.1 Buoyancy term and flux function . . . 271

C The functions $I_{k,p}$ and $J_{k,p}$ . . . 272
C.1 Heavy fluid layer . . . 272
C.1.1 $I_{H,p}$ and $J_{H,p}$ . . . 272
C.1.2 Integrals of $I_{H,p}$ and $J_{H,p}$ . . . 272
C.1.3 Integrals of quadratic products of $I_{H,p}$ and $J_{H,p}$ . . . 273
C.1.4 Integrals of selected cubic products of $I_{H,p}$ and $J_{H,p}$. 273
C.2 Light fluid layer . . . 275
C.2.1 $I_{L,p}$ and $J_{L,p}$ . . . 275
C.2.2 Integrals of $I_{L,p}$ and $J_{L,p}$ . . . 275
C.2.3 Integrals of quadratic products of $I_{L,p}$ and $J_{L,p}$ . . . 275
C.2.4 Integrals of selected cubic products of $I_{L,p}$ and $J_{L,p}$. 276

D Long-wave limit of the Orr-Sommerfeld problem . . . 278
D.1 Solution of the leading order problem . . . 278
D.2 Solution of the first order problem . . . 279

List of Tables

3.1 Parameter range of density stable experiments 40

4.1 Parameter range of Newtonian density unstable experiments . 58

5.1 Parameter range of our numerical study 92

7.1 Parameter ranges of viscoplastic experiments 181

List of Figures

1.1 Schematic of the problem of study 2

2.1 Deepwater Horizon accident in the Gulf of Mexico 7
2.2 Simplified schematic of primary cementing process 8
2.3 Development of Kelvin-Helmholtz instability 11
2.4 Development of Rayleigh-Taylor instability 12
2.5 Two-dimensional concentration field at dimensionless time $t = 2$ for Rayleigh-Taylor flow numerical simulations given in [31] 13
2.6 Snapshots of the exchange flow concentration field obtained at different tilt angles using laser-induced-florescence (LIF) . 17
2.7 Boycott effect in the sedimentation of a suspension of particles in a tube 20
2.8 A sequence of snapshots from nearly horizontal displacement flow experiments for $\beta = 83\,^\circ$, $At = 0.01$ and $\hat{\nu} = 1$ (mm^2/s) . 23
2.9 Different flow types observed in displacing layer in downward miscible displacement of two fluids in a vertical pipe 24
2.10 Experimental results of a full depth lock-exchange with Benjamin's potential flow solution (dashed line) [15] 27
2.11 Pulses recorded at $\hat{x} = 15$ (cm) and $\hat{x} = 468$ (cm) showing the dispersion of brine in turbulent pipe flow 31
2.12 Concentration $c(x, z)$ at dimensionless time $t = 0.3$ for displacement flow of two Newtonian fluids in a vertical channel . 34

3.1 Density unstable and density stable displacements at $\beta = 70\,^\circ$ and $\hat{\nu} = 1$ (mm^2/s) 42
3.2 Spatiotemporal diagrams obtained for the same experiments as Figs. 3.1a and 3.1b 44
3.3 Experimental profiles of normalized $h(\hat{x}, \hat{t})$ and the evolution of stretch length value for the same experiments as Figs. 3.1b and 3.2b 45

3.4 The dependency of the dimensionless time taken to reach fully developed flow, t_{FD}, on χ and Fr 47
3.5 Front velocity values, $\hat{V}_f$, plotted against the mean flow velocity, $\hat{V}_0$, for different density stable experiments 48
3.6 Experimental profiles of $\hat{h}(\hat{x},\hat{t})/\hat{D}$ at different times for $\beta = 60\,^\circ$ and $\hat{\nu} = 1$ (mm^2/s) 49
3.7 Variations in dimensional stretch length $\hat{L}$, for different β, $\hat{V}_0$ and $\hat{\nu}$ values 50
3.8 Snapshots of density stable displacement flow experiments in a vertical pipe for $\hat{\nu} = 1$ (mm^2/s) and $At = -0.0035$ 52
3.9 Experimental dimensionless stretch length values L, plotted against χ 53

4.1 Comparison of the experimental front velocity values for the exchange flow versus the data reported by Seon *et al.* [112] . 60
4.2 Change in iso-viscous displacement mixing with β for $At = 0.0035$ and kinematic viscosity $\hat{\nu} = 1$ (mm^2/s) 61
4.3 Spatiotemporal diagrams of depth-averaged concentration field for the same experiments as shown in Fig. 4.2 63
4.4 Ultrasound Doppler Velocimetry (UDV) measurements obtained for $At = 0.004$ and $\hat{\nu} = 1$ (mm^2/s) for different inclination angles 64
4.5 Evolution of the depth-averaged concentration field, C, and the front velocity value, $\hat{V}_f$, with time for $\beta = 30°$ 65
4.6 Dependency of the displacing front velocity, $\hat{V}_f$, versus the imposed flow velocity, $\hat{V}_0$, showing the experiment repeatability 67
4.7 Change in displacing front velocity, $\hat{V}_f$ with tilt angle, β, and imposed velocity, $\hat{V}_0$ 68
4.8 Change in $\hat{V}_f - \hat{V}_{Exchange} - \hat{V}_0$ with tilt angle, β, and imposed velocity, $\hat{V}_0$ 69
4.9 Presentation of our results in Fr and $Re\cos\beta/Fr$ plane for the full range of experiments showing $\hat{V}_f/\hat{V}_0$ and instantaneous displacements 70
4.10 Collapse of depth-averaged concentration profiles with $(\hat{x} - \hat{V}_0\hat{t})/\sqrt{\hat{t}}$ for $\beta = 45°$, $At = 0.08$ and $\hat{\nu} = 1$ (mm^2/s) 73
4.11 Variation of the dimensionless diffusion coefficient versus tilt angle; comparison with Seon *et al.* [114] experiments 74
4.12 Collapse of depth-averaged concentration profiles with $(\hat{x} - \hat{V}_0\hat{t})/\sqrt{\hat{t}}$ for for $At = 0.0035$ and $\hat{\nu} = 1$ (mm^2/s) 76

4.13 Variation of the diffusion coefficient, $\hat{D}_M$ versus mean imposed flow velocity, $\hat{V}_0$ for different Atwood numbers 77
4.14 Contours of the normalized diffusion coefficients versus Fr and $Re\cos\beta/Fr$ 77
4.15 Reynolds number, Re, plotted against Fr and $Re\cos\beta/Fr$ for different experiments 78
4.16 Comparison of the experimental macroscopic diffusion coefficient, $\hat{D}_M$, versus Taylor dispersion coefficient, $\hat{D}_T$ 79
4.17 Classification of our results in $(Fr, Re\cos\beta/Fr)$-plane for the full range of experiments showing viscous, intermittent and fully diffusive flows 81
4.18 Comparison of the viscous flows front velocity values obtained with the predictions of the lubrication model 82
4.19 Scaled front velocity values, $\hat{V}_f/\hat{V}_t$, for intermittent flows and comparison with the predicted values 85
4.20 Variation of the diffusion coefficient $\hat{D}_M - \hat{D}_{M,Exchange}$ with $\hat{D}\hat{V}_0$ and c_1 with β 86
4.21 Comparison of the experimental macroscopic diffusion diffusion coefficient, $\hat{D}_{M,exp}$, against the prediction of (4.7) 87
4.22 Front velocity values, $\hat{V}_f - \hat{V}_{f,D}$, plotted against the mean flow velocity for diffusive flows 88

5.1 Schematic view of the numerical domain used 91
5.2 Evolution of $(1-\bar{C}(\hat{t}))/(1-\bar{C}(0))$ and the displacing front position with time for $\beta = 40°$, $At = 0.0035$, $\hat{V}_0 = 2.6$ (mm/s) and $\hat{\nu} = 1$ (mm^2/s) 94
5.3 Change in iso-viscous displacement flows with β for $At = 0.0035$ and $\hat{\nu} = 1$ (mm^2/s 96
5.4 spatiotemporal diagrams of the depth-averaged concentration field for the same simulations as shown in Fig. 5.3 98
5.5 The variation of the streamwise scaled velocity component with time $\hat{t}$ and depthwise location $\hat{y}$ 99
5.6 The averaged concentration, $\bar{C}_{\hat{x}}$, along the length of the computational domain plotted at different times 100
5.7 Evolution of $(1-\bar{C}(\hat{t}))/(1-\bar{C}(0))$ with time for the same simulation as in Fig. 5.3 ($\beta = 90°$) 101
5.8 Evolution of the depth-averaged concentration field, $\bar{C}_{\hat{y}}$, and the front velocity value, $\hat{V}_f$, with time for $\beta = 60°$, $At = 0.0035$ and $\hat{V}_0 = 15.7$ (mm/s) 103

5.9 The evolution of the front velocity value, $\hat{V}_f$, with time showing increase and decrease in $\hat{V}_f$ 103
5.10 Change in displacing front velocity, $\hat{V}_f$ with β, $\hat{V}_0$ and At for $\hat{\nu} = 1$ (mm^2/s) 104
5.11 Change in $\hat{V}_f - 1.5\hat{V}_0$ with β, $\hat{V}_0$ and At for $\hat{\nu} = 1$ (mm^2/s) . 106
5.12 Presentation of our results for the full range of simulations in Fr and $Re\cos\beta/Fr$ plane showing normalized front velocity $\hat{V}_f/\hat{V}_0$ 107
5.13 Snapshots of the numerical simulations, Spatiotemporal diagram of the depth-averaged concentration and vectors of velocity field for $\beta = 60°$, $At = 0.0035$, $\hat{\nu} = 1$ (mm^2/s) and $\hat{V}_0 = 15.7$ (mm/s) 109
5.14 Classification of the results for the full range of simulations in the plane of Fr and $Re\cos\beta/Fr$ showing instantaneous/non-instantaneous displacement flows 110
5.15 Snapshots of the numerical simulation at different times run for $\beta = 10°$, $At = 0.01$, $\hat{\nu} = 1$ (mm^2/s) and $\hat{V}_0 = 15.7$ (mm/s) 111
5.16 Snapshots of the numerical simulation, vectors of velocity field and evolution of the depth-averaged concentration field with time run for $\beta = 20°$, $At = 0.001$, $\hat{\nu} = 1$ (mm^2/s) and $\hat{V}_0 = 26.2$ (mm/s) showing the detachment of the front from the displacing fluid layer 113
5.17 Snapshot of the numerical simulation, contours of the speed, vorticity and vectors of the velocity field for the same parameters as in Fig. 5.16 115
5.18 Snapshots of the numerical simulation and evolution of the depth-averaged concentration field for $\beta = 80°$, $At = 0.0035$, $\hat{\nu} = 1$ (mm^2/s) and $\hat{V}_0 = 15.7$ (mm/s) showing the acceleration of the tip of the displacement front 116
5.19 Snapshots of the numerical simulation and evolution of the depth-averaged concentration field, $\bar{C}_{\hat{y}}$ for $\beta = 90°$, $At = 0.001$, $\hat{\nu} = 1$ (mm^2/s) and $\hat{V}_0 = 10.5$ (mm/s) showing the appearance of spike at the displacement tip 117
5.20 Classification of our results for the full range of simulations in the plane of Fr and $Re\cos\beta/Fr$ showing detachment, leaking front and spike-like flows 118
5.21 Snapshots of the numerical simulation and velocity vectorfield for $\beta = 0°$, $At = 0.001$, $\hat{\nu} = 1$ (mm^2/s) and $\hat{V}_0 = 2.6$ (mm/s) showing the formation of Rayleigh-Taylor instability 120

5.22 Snapshots of the numerical simulation, spatiotemporal diagram of the averaged concentration and the evolution of the leading and trailing front velocity values for $\beta = 20°$, $At = 0.01$, $\hat{\nu} = 1$ (mm^2/s) and $\hat{V}_0 = 2.6$ (mm/s) showing oscillation in $\hat{V}_f$ with time 122
5.23 Classification of our results for the full range of simulations in the plane of Fr and $Re\cos\beta/Fr$ showing the flows with oscillatory behavior in the front velocity 123
5.24 Collapse of depth-averaged concentration profiles with $(\hat{x} - \hat{V}_0\hat{t})/\sqrt{\hat{t}}$ for $\beta = 20°$, $At = 0.01$ and $\hat{\nu} = 1$ (mm^2/s) 124
5.25 Collapse of depth-averaged concentration profiles with $(\hat{x} - \hat{V}_0\hat{t})/\sqrt{\hat{t}}$ for the same simulations as shown in Figs. 5.3 126
5.26 Change in macroscopic diffusion coefficient with mean imposed velocity $\hat{V}_0$ and tilt angle, β, for $\hat{\nu} = 1$ (mm^2/s) and different Atwood numbers 127
5.27 Contours of the normalized diffusion coefficients versus Fr and $Re\cos\beta/Fr$ 127
5.28 Classification of our results for the full range of simulations in the plane of Fr and $Re\cos\beta/Fr$ showing viscous, intermittent and fully diffusive flows 129

6.1 Schematic of displacement geometry considered in the flow modeling 135
6.2 Change in the base flow velocity profile with upper layer Bingham number and power-law index 139
6.3 Examples of heavy and light fluid weight functions varying with B_L and n_L 150
6.4 Contours of the inertial coefficients A^h, A^b, C^h, C^b, S and q, in (b,h)-plane 152
6.5 Dependency of the interface evolution on mesh size and the evolution of the interface height with time for $B_H = 0$, $B_L = 0$, $m = 1$, $n_H = 1$, $n_L = 1$, $\chi = 0$ and $\delta Re = 0$ 153
6.6 Collapse of the interface heights for $B_H = 0$, $B_L = 0$, $m = 1$, $n_H = 1$, $n_L = 1$, $\chi = 0$ and different δRe values 154
6.7 Self-similarity of $q(h, b)$, plotted against ξ/T for the parameters as in Fig. 6.6 154
6.8 Effects of various parameters on similarity shape of interface as a function of ξ/T 156
6.9 Effects of varying inertia (δRe) on similarity shape of the interface 157

6.10 Comparison of the leading order growth rate c_0 and the imaginary part of the first order growth rate, c_1/i in the long-wave limit: weighted residual and Orr-Sommerfeld analysis 165
6.11 Evolution of the perturbation interface height, $h-h_0$, at times $T = 0, 2, 4, ..., 10$, and location, ξ for $h_0 = 0.8$, $B_H = B_L = 0$, $n_H = n_L = 1$, $m = 1$ and $\delta Re = 10$ 167
6.12 Marginal stability curves for the long-wave limit and stability diagram indicating stable and unstable flows 168
6.13 Spatiotemporal diagram of the interface height values for the parameters used in Fig. 6.12 169
6.14 Marginal stability curves for the long-wave limit for $h_0 = 0.5$ and different viscosity ratio values 170
6.15 Contours of critical value of χ in $(\delta Re, m)$-plane for $B_H = 0$, $B_L = 0$, $n_H = 1$, $n_L = 1$ and $h_0 = 0.5$ 171
6.16 Marginal stability curves for the long-wave limit for $h_0 = 0.5$ and different n_H and n_L values 171
6.17 Spatiotemporal diagram of the displacement interface height for $n_H = 0.85$, $B_H = B_L = 0$ 173
6.18 Marginal stability curves for the long-wave limit for $h_0 = 0.5$ and different B_H and B_L values 174
6.19 Base flow velocity profiles corresponding to Fig. 6.18b for $B_L = 0.5$ and $\chi = 40, 55$ and 70 174
6.20 Spatiotemporal diagram of the interface height values, h, for $B_L = 0.5$, $\delta Re = 3$ and different χ values 175

7.1 Primary classification of the observed flows showing slump and central displacements 183
7.2 Slump-type displacement for $\beta = 45°$, $At = 0.01$, $\hat{\tau}_Y = 7.9$ (Pa) and $\hat{V}_0 = 81.5$ (mm/s) 185
7.3 Ripped-type displacement for $\beta = 45°$, $At = 0.016$, $\hat{\tau}_Y = 16.4$ (Pa) and $\hat{V}_0 = 61.3$ (mm/s) 187
7.4 Formation of a ripped-type displacement for $\beta = 75°$, $At = 0.016$, $\hat{\tau}_Y = 4.3$ (Pa) and $\hat{V}_0 = 48.1$ (mm/s) 188
7.5 Ripped-type displacement for $\beta = 60°$, $At = 0.016$, $\hat{\tau}_Y = 14.9$ (Pa) and $\hat{V}_0 = 26.8$ (mm/s) 189
7.6 Corkscrew-type displacement for $\beta = 15°$, $At = 0.016$, $\hat{\tau}_Y = 19.7$ (Pa) and $\hat{V}_0 = 61.3$ (mm/s) 190
7.7 Front and top view images of the helical structure formed in the experiment shown in Fig. 7.6 191

7.8 Blockage-type displacement for $\beta = 30°$, $At = 0.0143$, $\hat{\tau}_Y =$ 6.9 (Pa) and $\hat{V}_0 = 113.2$ (mm/s) 193
7.9 Slump-type displacement showing the formation of a blockage for the same parameters as used in Fig. 7.3 194
7.10 Central displacement for side and top views for $\beta = 30°$, $At = 0.0035$, $\hat{\tau}_Y = 26.3$ and $\hat{V}_0 = 73.3$ (mm/s) 195
7.11 Displacement flow for $\beta = 0°$, $At = 0.016$, $\hat{\tau}_Y = 11.7$ (Pa) and $\hat{V}_0 = 97.6$ (mm/s) showing efficient mixing 197
7.12 Collapse of the depth-averaged concentration profiles for the same parameters as in Fig. 7.11b 198
7.13 Snapshots of the exchange flow experiments carried out for $At = 0.016$ and different inclination angles 200
7.14 Presentation of our experimental results in the Fr–$Re\cos\beta/Fr$ plane showing instantaneous displacements 204
7.15 Experimental results plotted in the Fr–Re/Fr and Fr–$Re\cos\beta/Fr$ planes marking highly unstable flows 206

A.1 Simplified schematic of the experimental apparatus used . . . 239
A.2 The experimental setup used in the current project 240
A.3 The scales used in the experimental study 242
A.4 The mixer-blade system used in the experimental study . . . 242
A.5 The density meter, thermometer and pH meter used in the experiments 243
A.6 The centrifugal pumps used in the experiments 245
A.7 Schematic and actual pictures of the acrylic pressurized tanks used for driving the fluids into the system 247
A.8 The solenoid valves used in upper section of the flow loop . . 248
A.9 The schematic of the pneumatic air slide used as gate valve and the picture taken from the actual gate valve in place . . . 249
A.10 The fish tank pipe system used in the experimental apparatus 251
A.11 The light-emitting-diode (LED) system used for illuminating the pipe from behind 252
A.12 The first-surface mirror used in the experimental apparatus . 253
A.13 Average light intensity within the second fish tank varying as a function of ink added 255
A.14 Sample snapshots of a density unstable displacement 255
A.15 Evolution profiles of the averaged concentration across the pipe and the spatiotemporal diagram 256
A.16 The rheometer used for measuring the viscosity of the fluids and the thermal unit attached to it 257

A.17 Example flow curve for a viscoplastic solution 259
A.18 Schematic view of the numerical domain used 260
A.19 Snapshots of the numerical simulation, vectors of velocity field, evolution of the depth-averaged concentration field and the spatiotemporal diagram 264

Acknowledgements

First of all, I would like to thank my supervisor, Professor Ian Frigaard for giving me this spectacular opportunity of working with him during my Ph.D. program. It was undoubtedly the most enjoyable professional experience that I have ever had in my life. I will never forget the valuable lessons you taught me during these years. I understood what a high quality research means. You were always supportive, responsible, patient, disciplined and helpful more than the limit one can even imagine. You were more than just a supervisor for me, a true friend or a part of my family who was always there when I needed. The experience of working with such a knowledgable and meanwhile humble professor has just been an amazing experience for me that I will never forget. Thank you Ian for everything again.

I would also like to thank Professor Mark Martinez for helping me with the experimental side of the project and giving useful hints and comments whenever I became stuck. Also your management skills has always been a great example for me to follow during my Ph.D. I thank Dr. Thomas Seon too for sharing his valuable experimental skills with me during the first few years of my Ph.D. I am sure your robust attitude about how to approach a research problem has affected mine too and made me improve my skills even more. I also do not forget the good times we spent together outside the research world as friends.

I want to take this opportunity and thank Dr. Seyyed Mohammad Taghavi, my dear colleague in the lab, research collaborator, beloved friend and trustworthy buddy. Undoubtedly you are the closest co-worker I have ever had. The time we spent together, discussing the project, running the experiments, working on the results and attending the conferences just made me improve my research skills a lot and meanwhile strengthened our friendship. I also learnt how to be hardworking, meticulous and have always positive attitude in the research and in a larger scale in life. Thank you for everything Mohammad!

During my Ph.D. program I had the honor of working with five highly skilled and qualified interns/co-ops in our lab for the experimental side of the project that took about two years. I would like to thank Messrs Saman

Gharib, Ethan Stuart, Hadi Abou Jaoude and George Hatzikiriakos and Ms. Kwang Pithayachariyakul who helped me with the modifying the apparatus and running the experiments. During their 4-to-8 months of internship in our lab, they always kept me motivated and gave positive energy to me by their dedication, discipline and useful helps and comments. I wish you success in your career and happiness in your lives.

Related to the experiments, I would like to thank UBC mech. stores keeper, Mr. Perry Yabuno who helped me with ordering an immense number of items required for the experiments while always keeping his wonderful smile on his face. The technical support of Marcus Fengler, Erik Wilson from mech. machine shop and Glenn Jolly and Sean Buxton from mech electronics is also greatly acknowledged.

This research was supported financially by Schlumberger and NSERC. This support is gratefully acknowledged.

The support and kindness of my family throughout my life and specially during my Ph.D. program is something that I want to acknowledge here from the bottom of my heart. Without you this whole research was impossible for me to do. Thank you for all the love you gave me and the sacrifices you made for me!

I extend my gratitude and special thanks to my friends who from outside of the project helped me by their warm support and soothing company. In particular I want to thank Mr. Mohammad Vazifeh who spent the most time with me during my Ph.D. and always kept me happy, motivated and energetic. Mohammad your friendship means a lot to me. Thank you for everything! I would also thank Mr. Amir Abbas Aliabadi for his great support during my Ph.D. I wish you success Amir in your ahead life. Also I want to express my gratitude to the members of Atomic Racing club in Vancouver that helped me stay fit and healthy by accompanying me in bike group rides in the shine or rain. I am sure there has been a lot more people that have helped me during my Ph.D. but I have forgotten to thank here. Thank you all...

Dedication

I dedicate this thesis to my precious mother, Nasrin, for all her love, support, encouragement and kindness throughout my life and during my Ph.D. I want you to know how much I appreciate all you have done for me and how much I love you deep in my heart...

Chapter 1

Synopsis

1.1 Problem of study

This thesis studies the miscible displacement flow of two fluids of differing densities in an inclined duct, in the downward direction. Both density-stable (light fluid displacing heavy fluid) and density-unstable (heavy fluid displacing light fluid) configurations are studied. The focus is more on density-unstable configuration. Buoyancy is a significant driving force for all flows we study. However there is also a net imposed flow in the downward direction, along the duct. We study the effects of constant imposed flow rates (with mean velocity[1] $\hat{V}_0$), small density differences (quantified by the Atwood number, At), inclination angles (β), viscosity ratios between the two fluids (m), and the rheology of the fluids.

The diameter or width of the duct, denoted by $\hat{D}$, is small compared to its length ($\hat{L}$). The inclination angle β can change from horizontal ($\beta = 90°$) to vertical ($\beta = 0°$) where we expect to find more mixing. The focus however is on inclination angles away from horizontal since these fluids have been studied in detail for both Newtonian and non-Newtonian fluids in [123]. The fluids used in this study are generalized Newtonian fluids which include Newtonian fluids, shear thinning fluids with a power-law index n and shear thinning fluids with a yield stress $\hat{\tau}_Y$. Figure 1.1 shows a schematic view of our problem geometry.

There are many industrial processes in which it is necessary to remove a gelled material or soft-solid from a duct. Examples include bio-medical applications (mucus [73], biofilms [145]), cleaning of equipment, food processing [28], oil well cementing [89] and waxy crude oil pipeline restarts [144]. Although such displacement problems have applications in oceanography, hydrology, petroleum or chemical engineering, our main motivation comes from complex displacement flows that exist in many processes related to the oil and gas industry. These processes are either concerned with well con-

[1] In this thesis, we adopt the convention of denoting dimensional quantities with $\hat{}$ symbol (e.g. the pipe diameter is $\hat{D}$) and dimensionless quantities without.

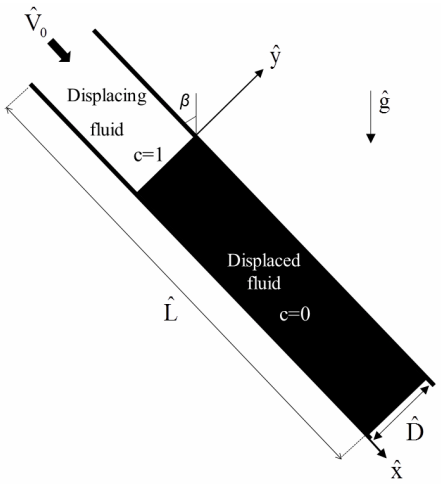

Figure 1.1: Schematic of the problem of study. The displacing and displaced fluids are initially separated. The duct has the transverse dimension $\hat{D}$. The mean imposed velocity is $\hat{V}_0$ depicted by the arrow.

struction (drilling, cementing, fracturing) or production (pipelining). The well cementing process can also be used in CO_2 sequestration, where the excess Carbon dioxide has to be pumped into the ground through a well for storage. After drilling an oil well, the metal casing with circular cross section is placed into the well. The drilling mud inside the pipe has to be displaced by pumping cement slurry. The mud then leaves the system from the very bottom of the pipe through the gap between the casing and rock wall. The question might be why not pump an immense amount of cement slurry to finally displace the whole mud inside the pipe. This is not feasible due to either disposal issues or cost of the fluids. In fact it is desirable to fully displace the *in-situ* drilling mud with more or less a single "duct volume" of cement slurry. Also it was found that in some ranges of viscosity ratios, density differences and inclination angles, the displaced fluid can not be displaced properly no matter how much displacing fluid is pumped [130]. These are called stationary residual layers. Also we have other issues related to displacement that are as important. In our study we aim to understand the underlying mechanisms of displacement flows in depth to finally be able to design the displacement process as efficient as possible. From a fluid mechanics perspective, the final goal of a displacement flow

process is to remove (displace) as much drilling mud as possible by pumping as little cement slurry as needed.

Usually the pipe aspect ratio, defined as the ratio of the pipe diameter to its length, is small and the pipe can be inclined at different angles depending on the depthwise location. Nearly horizontal wells can be more productive due to the increased contact area with the reservoir. However these wells are also first drilled in a strictly vertical condition and then adopt the desired curvature as depth increases. Laminar flows often occur in these processes, due to either high viscosities or other process constraints. Fluids with non-Newtonian characteristics are always used in the well cementing process depending on the related stage.

This thesis is related to a previous Ph.D. thesis in Complex Fluids Laboratory of The University of British Columbia titled "From Displacement to Mixing in a Slightly Inclined Duct" [123], but is also significantly different in scope. Whereas [123] focuses on understanding the displacement flows in nearly horizontal ducts, here we study the full range of inclinations ranging from vertical to near-horizontal. The main novelty in doing this is that the flow phenomena observed at these inclinations are markedly different to those in [123]. The overlap between the two theses is in using a similar experimental apparatus and some computational tools, although both are modified and new analyses are introduced. The main questions to be addressed in this thesis are the same as those in [123] for nearly-horizontal displacement flows, as the underlying objectives are the same. These questions are:

(i) to what degree do the displacing and displaced fluids mix across the duct;

(ii) what is the longitudinal extent of the *mixed region* in the duct? By mixed region we mean the region in which the average concentration across the duct is different than the concentration of either displacing or displaced fluids.

In the limit of nearly horizontal ducts the displacement flows are more structured [123], typically stratifying into 2 streams with minimal mixing at the interface. For these structured flows the velocity of the displacing front is the most important quantity to be measured since it reveals how successful the displacement has been [128]. As the duct inclination angle increases the flows naturally become more inertial and unstable due to the larger buoyancy forces along the streamwise direction. In the case of fully mixed flows the

longitudinal extent of the mixed region can be defined by finding the speed at which the mixed region spreads, typically via diffusion/dispersion.

Turbulent displacing regimes are typically more effective, but the problem is they are not always possible due to process constraints on the maximum flow rates. Once removed, the displaced fluid leaves the pipe through the very bottom of the drilled section. It then comes back up to the ground by passing through the annulus-like region between the casing and rock wall. It is most important that in the annulus region the displaced fluid be lighter than the displacing one to ensure a stable displacement flow. The displacing fluid (the cement slurry) finally is left to rest in the annulus region and solidify over time. This density configuration (heavy displacing and light displaced fluids) will create a buoyant flow inside the pipe section. Most of the analyses and results presented in this thesis focus on unstable density configuration. However in some stages of the process it is possible that the displacing fluid inside the casing is less dense. Therefore, flows with a stable density configuration are also studied as a chapter in this thesis. The density differences used in the current project are fairly small and are defined through a single dimensionless parameter called Atwood number ($At = \frac{\hat{\rho}_1 - \hat{\rho}_2}{\hat{\rho}_1 + \hat{\rho}_2}$) where $\hat{\rho}_1$ and $\hat{\rho}_2$ are displacing and displaced fluids densities respectively. Although the Atwood numbers used are small the resulting buoyancy forces are significant. In the case of density-stable flows the Atwood number is negative and for density-unstable cases it is positive. It is found that there is a striking difference between the flows in these two density configurations. In the density stable configuration the efficiency of the displacement is increased a lot. The extent of the mixed-region along the pipe for these flows is much reduced compared to the case of density-unstable displacement.

The closest research works in literature to displacement flows in inclined ducts are those in [87, 124–130] for nearly horizontal angles and in [111–115] for the lock exchange flow of buoyant flows in titled geometries. By the lock exchange flow we mean that the two ends of the duct are closed and the fluids interpenetrate one another due to the buoyancy. So in summary our aim is to see how the imposed flow changes the lock exchange flow and how the steeper inclination angles affect the displacement flows.

The approaches taken to understand the displacement flows in this thesis are experimental, numerical and analytical. The major part of the results are obtained by experiments carried out in lab scale apparatus explained in detail in the appendix A. Computational fluid dynamics (CFD) is also used to numerically solve the governing equations and further understand these flows. Due to the complexity of the pipe flows, the geometry used

in numerical simulations is a plane channel, as opposed to the pipe used in the experiments. Based on the experimental observations and numerical simulations appropriate mathematical models are developed to predict the quality of the displacement and estimate their stability. The final aim through these integrated studies is to better understand the physics behind the displacement flows, give quantitative measures of the design parameters where feasible and to improve the whole process. This can be done by looking for regimes where the fluids contamination is minimized and the efficiency of the displacement is maximized. The eventual aim is that our new knowledge will be used to improve real displacement flow process designs, thus helping to reduce environmental impact and increase productivity.

1.2 Outline of the thesis

The outline of this thesis is as follows. The next chapter looks into the industrial background of the problem and the associated fundamental studies of displacement flows. The research methodology adopted including experimental procedures, devices and computational technique is explained in appendix A. The experimental approach taken will be discussed in detail explaining the modifications applied to the previous apparatus in [123] along with the improvements in imaging and postprocessing the data. The numerical methodology followed will also be discussed in the same appendix. In chapter 3 we present experimental results on density-stable displacement of Newtonian iso-viscous fluids. Chapter 4 experimentally looks into the Newtonian iso-viscous displacement flows but when the configuration is density-unstable i.e. heavy fluid displacing the light fluid. Chapter 5 is closely related to chapter 4 with solely a numerical approach and in channel geometry. The mathematical study in this thesis which can be used for modeling displacement flows and predicting their stability is laid out in chapter 6. The method follows the weighted residual approach for thin-film flows. In chapter 7 the displacement flow of a viscoplastic fluid by a Newtonian one is investigated experimentally. The thesis is wrapped up in chapter 8 by highlighting the novel contributions of the thesis, some concluding remarks, industrial recommendations and future perspectives.

Chapter 2

Background

This chapter reviews both the engineering background of the problem considered in this thesis (the primary cementing process, which has been our main motivation) and associated fundamental problems that are closely related (in §2.2). The chapter wraps up with a summary of the most relevant existing literature and outlines the research objectives.

2.1 Primary cementing background

Much of the motivation for our study comes from common operations present in the construction and completion of oil wells, (e.g. primary cementing [89], drilling, gravel-packing, hydraulic fracturing). Over the past many years oil prices have increased significantly as a result of a diminishing supply of oil and gas from easily accessible reservoirs coupled with an increased demand due to population and consumption growth. This has led to a growth in the number of techniques used in oil extraction. On the one hand, one of the possible alternatives (for Canada) comes from oil sand exploitation, which has various environmental issues associated with it. For more conventional extraction, we have seen a tendency towards deeper wells offshore and towards more challenging wells onshore, e.g. moving into the foothills in Alberta. Many oil and gas wells are long ($5 - 10$ (km)) and are inclined anywhere from vertical to fully horizontal. This range of wells brings new challenges, a wider range of fluids used in the processes and additional higher risks as operational failures can become highly expensive and catastrophic (as seen recently in the gulf of Mexico; see Fig. 2.1).

These processes often involve displacing one fluid with another or with a sequence of different fluids. The geometries are typically pipe, annular or duct-like, all with long-thin aspect ratios. Depending on the depth-wise location in an oil well, the pipe's inclination angle at which the displacement occurs can range from vertical to horizontal. Usually large volumes are pumped so that the fluids may be considered separated, i.e. we have a two-fluid non-Newtonian displacement. A very wide range of fluids are used. Density differences of up to 500 (kg/m^3) can occur, shear-thinning

Figure 2.1: Deepwater Horizon accident in the Gulf of Mexico happened on April 20, 2010. Eleven people were killed and nearly 5 million barrels of oil were released into the ocean [30]. Photo courtesy of US Environmental Protection Agency (EPA).

and yield stress rheological behaviors are widely found and are often the dominant non-Newtonian effects, (more exotic non-Newtonian effects may also be present). In this thesis we focus on primary cementing, although the results may be more widely useful.

In primary cementing we aim to provide a continuous hydraulic seal of the annular space between a steel casing and the reservoir. This is done by placing a cement slurry into this space, which is accessed from the bottom of the well. The fluids therefore travel downwards inside the steel casing to the bottom of the well. Depending on the precise process, different sequences of cement slurry, wash, or spacer can be pumped into the casing, which is initially filled with drilling mud. Several potential problems of this operation have been classified by Sabins [105]. Many questions of a more fundamental physical nature remain without proper scientific understanding and may strongly affect the process. A schematic geometry of the described industrial problem can be seen in Fig. 2.2, which shows an inclined pipe filled with series of fluids of different densities. Figure 2.2a shows that the *in-situ* drilling mud is being displaced by pumping a series of fluids (wash, spacer and cement slurry). The fluids exit from the very bottom section of the pipe and come back up to the ground. Figure 2.2b shows the well once the cementing job is complete. Ideally there should be pure cement slurry in the annulus area, to be left at rest to solidify and seal the well. Note that

the fluid inside the pipe at the end of the operation is drilling mud, placed to balance the hydrostatic pressure along the pipe during the solidification process.

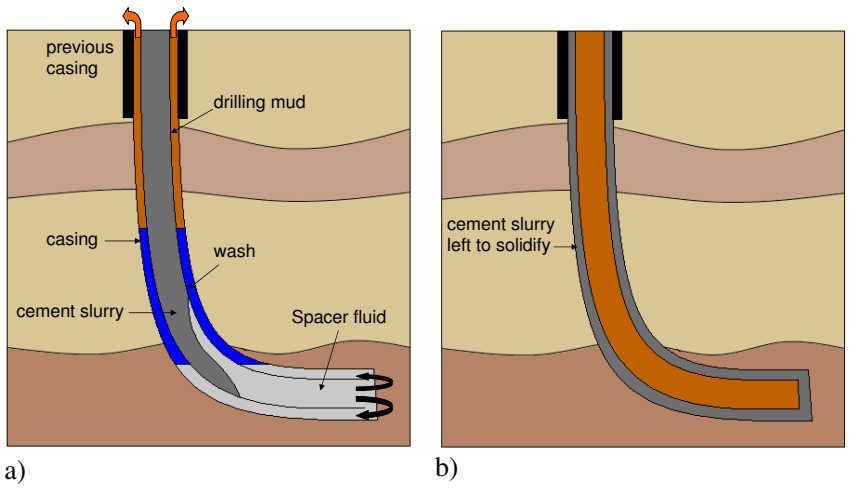

Figure 2.2: Simplified schematic of primary cementing process showing different stages of mud removal a) the drilling mud inside the system is being displaced by pumping wash, spacer and cement slurry fluids b) the pumped cement is left at rest to solidify over time and support the casing. Note that the fluid inside the pipe at this stage is the extracted drilling mud to ensure the pressure balance in pipe during the cement solidification process.

In general, primary cementing and other similar operations deal with buoyancy-driven miscible displacement and/or mixing of non-Newtonian fluid flows with or without an imposed flow, in confined configurations. The problem complexities are the effects of a large number of flow parameters, as well as different configurations and non-Newtonian behaviors. Depending on contributions of these parameters, different types of displacement and/or mixing flow can occur, and depending on balances between competing effects, different flow regimes (e.g. inertial, viscous) are possible. Thus, it is hard to predict the degree of mixing between two fluids traveling in a pipe. Consequently, it is difficult to accurately design fluid volumes needed, rheological properties and flow rates. Our aim is to understand the underlying mechanisms of displacement flows inside the pipe section in order to finally optimize design of the primary cementing process.

2.2 Associated fundamental problems

The phenomena of gravity driven flow of a heavy fluid displacing a lighter fluid widely occurs both in nature and in industry, particularly in chemical and petroleum engineering applications [15]. Although gravity (buoyancy) is a main driving force, these flows are affected by many other physical parameters, including viscosity, density, geometric configuration, mean flow and the types of fluids used. In addition, the inclination angle of the pipe seems to also play an important role in the flow movement [114]. In this section, a number of different fundamental flow problems related to this thesis are discussed, to help later to understand the underlying phenomena observed.

2.2.1 Flow stability

Throughout the experiments run in this study and the numerical simulations carried out, we found many unstable flows. These instabilities usually appear in the form of waves at the interface of the two fluids which can cause rapid and efficient mixing. Possibly some of the instabilities observed originate from the high speed of the mean flow, from the viscosity ratio, the density difference etc. [13, 41]. Studying the stability of these displacement flows is one of the goals of the thesis since it can affect many design factors. Below we list some of the underlying instability mechanisms that could possibly affect the flow.

Transition to turbulence

Given the fact that the displacing flow in our case has a mean imposed speed, makes us question up to how large a flow rate does the imposed flow itself stay stable. In fact, one of the most relevant instabilities to the current study is transition from laminar flow to turbulent flow. This instability was first studied by O. Reynolds [100]. He carried a series of experiments on Poiseuille flow in a pipe and found that the flow transitions from laminar to turbulent at $Re \gtrsim 2000$ where $Re = \hat{\rho}\hat{V}_0\hat{D}/\hat{\mu}$ is called the Reynolds number, which describes the relative importance of inertial to viscous forces. Above this value, the flow is unstable to perturbations of sufficiently large amplitude. These perturbations can be practically introduced into the flow at the inlet or by pipe wall irregularity. The perturbations rapidly grow to an extent that nonlinearity becomes strong and large eddies and/or turbulent structures start to form. At higher Reynolds numbers, the threshold amplitude of perturbations needed to trigger the instability decreases. In this

case, turbulence occurs due to the unavoidable presence of perturbations of very small amplitude. Above transition the flow becomes strongly three-dimensional, chaotic, non-axisymmetric and strongly nonlinear everywhere in domain [41]. The precise range of values of Re for transition has been widely studied. It depends to a great extent on how well the flow perturbation level is controlled in any given setup. Therefore, a nominal transition value $Re \approx 2300$ is often used for engineering purposes.

Kelvin-Helmholtz instability

In the displacement flow experiments reported in this thesis we have observed instabilities caused close to the interface that appear to be caused by the relative motion of the fluid layers with respect to one another. Similar instabilities were observed in nearly horizontal pipes displacement flows, [126], and in exchange flows [111–115]. Some of these instabilities are shown in Figs. 2.6 and 2.8. It is believed that these instabilities are mostly related to the well-known Kelvin-Helmholtz instability [41] due to their very similar nature, although there are also other closely related instabilities.

Through a linear stability analysis, the stability of stratified layers of fluids with different densities which are in relative motion can be predicted. Let us consider the basic flow of two incompressible inviscid fluids in horizontal parallel infinite streams in two-dimensional plane of $\hat{x}$, $\hat{y}$; see Fig. 2.3. The fluids have different velocities, $\hat{V}_H$ and $\hat{V}_L$, and densities, $\hat{\rho}_H$ and $\hat{\rho}_L$. The subscripts H and L correspond to heavy and light respectively. The light stream is above the other heavy one. By studying the linear stability of two incompressible inviscid fluid layers, it is not too difficult to obtain necessary and sufficient conditions for linear instability of the given flow; see e.g. [41]:

$$\sqrt{\hat{k}^2 + \hat{l}^2}\ \hat{g}(\hat{\rho}_H^2 - \hat{\rho}_L^2) < \hat{k}^2 \hat{\rho}_H \hat{\rho}_L (\hat{V}_H - \hat{V}_L)^2, \tag{2.1}$$

where $\hat{k}$, $\hat{l}$ are the wavenumbers in $\hat{x}$ and $\hat{z}$ (axis perpendicular to the paper) directions respectively. Given $\hat{V}_H \neq \hat{V}_L$ the flow is always unstable to short wave modes which have sufficiently large $\hat{k}$. Also note that for non-zero density difference (light fluid on top of heavy fluid), condition 2.1 for Kelvin-Helmholtz instability reveals a competition between the destabilizing effect of inertia and the stabilizing effect of buoyancy. Note that the simple model of analysing Kelvin-Helmholtz instability explained here is only a first attempt at understanding the basics behind this instability.

Note that the relative motion of the fluids in the case of exchange or displacement flows is largely driven by the buoyancy force due to the density

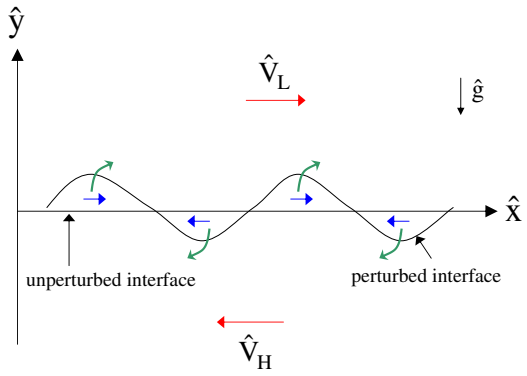

Figure 2.3: Development of Kelvin-Helmholtz instability for fluid layers of different densities moving with different velocities. A small perturbation at the interface is amplified once condition 2.1 is satisfied.

difference. In fact once the heavy layer slumps underneath the light layer, streamwise buoyancy force acts to push the light layer upstream causing a backward velocity component. This will eventually cause a reverse velocity gradient within the flow which makes the flow potentially unstable.

Experiments on the Kelvin-Helmholtz instability were mentioned by O. Reynolds [100]. Those experiments were later advanced by A. Thorpe [136–139] in detail. He showed that in an angled stratified flow setting, the two fluids begin to accelerate in different directions. In this stage the fluids are perfectly separated giving the highest density gradient at the interface. The velocity gradient increases more and more until it destabilizes the interface and the characteristic waves of the Kelvin-Helmholtz instability appear. The induced waves cause transverse mixing between the two fluids which in turn decreases transverse concentration gradients. The decreased density and velocity gradients may finally take the system to a stable state avoiding the appearance of further Kelvin-Helmholtz instabilities.

Note that although increasing the density contrast can increase the longitudinal pressure and velocity gradients consequently triggering the Kelvin-Helmholtz instabilities, it can also promote transverse pressure gradients which in turn help to stabilize the stratified flow. This is a dual effect of buoyancy [126]. This mechanism was very often observed throughout our experimental study, at least in density unstable Newtonian displacement

flows.

Rayleigh-Taylor instability

Due to the industrial motivation, most of the flows studied in this thesis are in a density unstable configuration, i.e. heavy fluid displacing light fluid. Since the duct is tilted at an angle, initially the heavy displacing fluid is above the light displaced layer. This configuration is inherently unstable [13, 41]. The instability associated with this configuration is called Rayleigh-Taylor instability. A review of studies of Rayleigh-Taylor instability is given by D. Sharp in [116]. Understanding this type of instability is of importance as it can be the underlying mechanism in many of the unstable displacement flow cases observed. Figure 2.4 shows schematically how a perturbation of the interface can cause a non-homogeneous hydrostatic pressure distribution that destabilizes the flow. As shown in the figure, the interface shape means the static pressure is lower below the high points and higher above the lower points, and this pressure imbalance drives the flow in the directions indicated by the arrows.

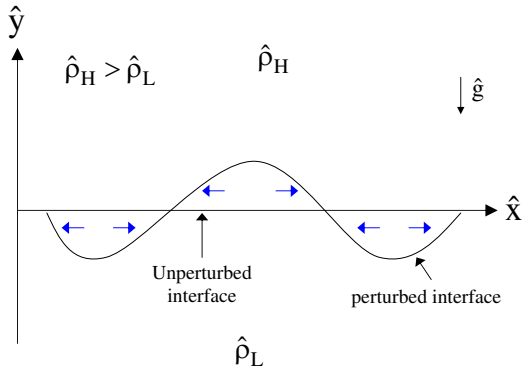

Figure 2.4: Development of Rayleigh-Taylor instability for fluid layers of different densities (heavy fluid on top of the light fluid). A small perturbation at the interface is amplified unboundedly with time in the inviscid limit [41].

A linear stability analysis can be carried out for inviscid incompressible flow of two fluids with differing density showing that the heavy-light configuration is unconditionally unstable. The small disturbances grow ex-

ponentially in time as $\exp \hat{\gamma}\hat{t}$ where $\hat{\gamma} = \sqrt{At\hat{g}\hat{k}}$ is the temporal growth rate with At being the Atwood number and $\hat{k}$ being the spatial wavenumber in the $\hat{x}$ direction [41]. If the viscosity of the fluids is also taken into account there is a threshold beyond which small perturbation can grow in time. As the instability develops, outward-moving irregularities known as *dimples* are quickly magnified. They then turn into sets of inter-penetrating RayleighTaylor fingers. The less dense fluid that moves upward is shaped into mushroom-like caps and makes the downward figures take similar shape; see Fig. 2.5. Several studies have been performed to explore the underlying mechanisms of the Rayleigh-Taylor instability through either experiments [31, 35] and/or numerical simulations [29, 36].

Figure 2.5: Two-dimensional concentration field at dimensionless time $t = 2$ for Rayleigh-Taylor flow numerical simulations taken from [31]. The figure shows the formation of the fingers and mushrooms over time due to the flow instability.

Regarding the two-fluid system that we study, it is worth noting that, as the duct is tilted more towards the horizontal, the Rayleigh-Taylor instability effect is expected to decrease. In fact this instability is most important when the duct is tilted close to the vertical. Considering the experimental observations for exchange flows in titled pipes (see [111–115]), after opening the gate valve the heavy fluid will tend to slump underneath the light

layer, thus weakening the chance for Rayleigh-Taylor instabilities to grow. In other words if the fluids are separated towards upper and lower walls of the duct then the base flow needed for Rayleigh-Taylor instabilities to develop is further from the configuration that we have. Further discussions are given in chapters 4 and 5 for iso-viscous Newtonian displacement flows in pipe and channel respectively.

Multi-layer flow instability

Based on previous experimental findings in nearly-horizontal displacement flows [123] and in lock exchange flows [110], it is expected that when the flows are buoyant the density difference will act to segregate the displacing and displaced layers towards lower and upper walls. In other words the fluids initially adopt a slumping pattern. When the pipe is inclined close to horizontal, there is higher chance that this two-layer slumping pattern remains stable as it develops. As we move away from nearly horizontal to higher inclinations the fluids are observed to mix more, and thus the observed flows are further from a structured two-layer system; see e.g. Fig. 2.6 for an illustration. However, we should not forget that the mixed complex-looking flows observed at higher inclination angles evolve from a more structured two-layer slumping flow that does not remain stable. Therefore, a natural direction to take in modeling the displacement flows is to assume an established two-layer or multi-layer flow and then assess if that flow is stable or not. Once the flow stability is known we can find out the transition between the stable viscous and unstable mixed fluids. There are many works in the literature on modeling and stability of two-layer flows. These works usually consider the combined effects of density gradient, velocity gradient and viscosity difference, some of which are explained earlier.

From the theoretical point of view, the occurrence of such interfacial instabilities has been analyzed by looking at the temporal linear stability of the two-layer plane Poiseuille flow. Earlier studies focused on Newtonian fluids both theoretically [25, 66, 99, 142, 143, 152, 153] and experimentally [24, 77]. Joseph *et al.* [76] carried out a linear stability analysis for the flow of two immiscible fluids of different viscosities and equal density in a pipe. They showed that the volume ratio, related to the fluid thicknesses, is a crucial factor determining the interface stability. The Couette flow of two superposed viscous fluids in an infinite region was studied by Hooper and Boyd [69]. They showed that the flow is always unstable to short wavelength instabilities. Hooper [68] also showed that introducing a thin layer of viscous fluid next to the channel walls would have a destabilizing effect. Thereafter,

the instability of two co-current superposed viscous fluids in a channel was examined by Hooper and Grimshaw [70]. They found that the interface may or may not be stable.

A number of authors have considered the linear stability of a two-layer power law fluid channel flow, using the Orr-Sommerfeld equation, e.g. [78, 94, 122]. The results of our long wavelength Orr-Sommerfeld analysis compare qualitatively well with these studies. If one or more of the fluids has a yield stress, the linear stability problem can only be posed in layers for which the fluid is yielded; see e.g. [52, 53]. If such a layer is bounded by an unyielded plug layer within the fluid layer then the unyielded plug layer is not accelerated by the flow. Sahu *et al.* [107], look at the linear stability analysis of a similar two-layer system (with upper layer being a Newtonian fluid and the lower layer being a Herschel-Bulkley fluid). The main assumption in their work is that the yield-stress layer is always yielded (i.e. low Bingham number). Whereas these authors find regimes of linear instability, if the interface is occupied by a yield stress fluid that is unyielded, linear stabilities are suppressed; see e.g. [50]. This same effects extends to nonlinear analysis [88] and is observable experimentally [74]

A simplified approach to modelling thin-film flows is the *weighted residual* methodology first proposed by [103, 104]. Extensions of the approach to two layer thin film flow models in channels and pipes are fairly recent, by [8, 85]. These have been developed with the idea that the simplified models will have similar stability characteristics to the analogous two-layer flows. The results do show good agreement with Orr-Sommerfeld predictions ([152] for channel flow and [67] for a pipe geometry), in the long wavelength limit.

2.2.2 Exchange flows

In the absence of an imposed flow, e.g. if the end of the pipe is closed, the flow is called an exchange flow. This type of flow is less directly relevant to primary cementing, except perhaps at the end of the operation, but does occur in plug cementing. In this process, when cement plugs are positioned above the bottom of the well, we have a heavy fluid (cement or viscous pill) lying above a lighter fluid (viscous pill or drilling mud). Therefore, these studies have direct industrial relevance. They are also relevant as the limit of a low imposed flow rate for the more general displacement flow that we study.

Experimental studies

In an exchange flow the only driving force is buoyancy. Debacq *et al.* [33, 34] and later on Seon *et al.* [111–115] experimentally investigated the exchange flow of two miscible Newtonian fluids in vertical and inclined pipes respectively. Depending on the flow parameters, diffusive, transitionary and viscous flows can appear. The transition between diffusive/non-diffusive regimes in vertical pipe was found to be a function of density difference in a vertical pipe [33]. Debacq *et al.* [33] showed that when the flows are diffusive a macroscopic diffusion coefficient, $\hat{D}_M$, can be defined, as a global flow characteristic, and this can be up to 10^5 times bigger than the molecular diffusion. They characterized the macroscopic diffusion coefficient and the velocity of the penetrating exchange flow fronts (front velocity, $\hat{V}_f$) as a function of density contrast, fluid viscosities and pipe diameter; see [34].

Following the same approach to [34], but adding the pipe inclination angle to the parameters, Seon *et al.* [111] found the boundary between diffusive/non-diffusive flows and investigated the dependency of the macroscopic diffusion coefficient on other parameters. They showed that the transition between diffusive/non-diffusive flows is a function of the tilt angle measured from vertical, β, that increases with density contrast and decreases with fluid viscosities. Increasing the fluid viscosities coarsens the mixing zones within the flow. This in turn, increases local density contrast and buoyancy forces, which finally leads to a higher front velocity, $\hat{V}_f$ and less mixing; see e.g. [34]. Later on, Seon *et al.* [112] focused on the front dynamics of the exchange flows in tilted geometries by analyzing the front velocity measurements. They observed three different regimes: starting from vertical, front velocity was found to first increase with tilt angle, β, then reach a plateau at intermediate β, and then decrease again as $\beta \to 90°$. In the first regime, the interplay between fluid layers segregation and mixing dictates the value of $\hat{V}_f$. Segregation and mixing effects increase and decrease respectively, with β. For the plateau regime, $\hat{V}_f$ is not dependent on the fluid viscosity and is instead proportional to $\hat{V}_t$, an inertial velocity scale obtained by the balance between inertia and buoyancy ($\hat{V}_t = \sqrt{At\hat{g}\hat{D}}$ where At is the Atwood number and $\hat{g}$ and $\hat{D}$ are gravitational acceleration and pipe diameter respectively). In the third regime, the inclination angle is close to horizontal, the fluid layers separate into two counter currents which are almost parallel to one another. This regime is controlled by viscosity and is called the viscous regime. The relevant velocity scale in this case is $\hat{V}_\nu = At\hat{g}\hat{D}^2/\hat{\nu}$ obtained from the balance between buoyant and viscous

forces (note that $\hat{\nu}$ is the kinematic viscosity obtained from the common viscosity and average density of the fluids).

Due to the interesting nature of the plateau regime described earlier, Seon *et al.* [113] decided to run experiments using a high resolution imaging technique called laser-induced-florescence (LIF). By applying a laser sheet, this technique allowed these researchers to look more precisely at the point-wise concentration of the penetrating fronts inside the pipe instead of a depth-averaged value. Figure 2.6 shows the exchange flow of two buoyant flows at different inclination angles taken from [113]. The figure clearly shows the segregation effect at nearly horizontal angles and increased mixing at higher inclinations.

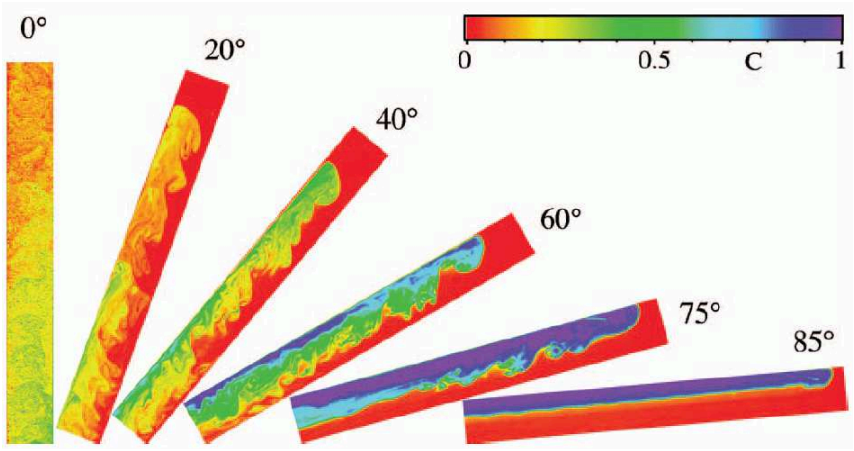

Figure 2.6: Snapshots of the concentration field obtained at different tilt angles using laser-induced-florescence (LIF). The configuration is exchange flow of two buoyant flows in a pipe. Field of view is 20×300 (mm^2). The color bar for the normalized concentration is shown at the top right of the figure. The picture is taken from [113].

Interestingly, it was found that the front velocity in the plateau regime is a function of the front concentration in the form of $\hat{V}_f \propto C^{0.5}$ where C is the concentration varying between 0 and 1, of the upper fluid at the front (also measured via the LIF technique). Focusing only on diffusive exchange flows, Seon *et al.* [114] studied the macroscopic diffusion coefficients, $\hat{D}_M$ and front velocity, $\hat{V}_f$, using scaling arguments to interpret their results They found that mixing can have two different mechanisms depending on the value of Re_t, (a Reynolds number defined based on the inertial velocity,

$\hat{V}_t$: $Re_t = \hat{V}_t\hat{D}/\hat{\nu}$). For $Re_t < 1000$, the parameter $\hat{D}_M/\hat{V}_t\hat{D}$ decreased as $Re_t^{-3/2}$ whereas for $Re_t > 1000$ it decreased as $Re_t^{-1/2}$. In fact this difference was found to be related to the quality of the transverse mixing in different ranges of Re_t. Seon *et al.* [114] recommended a detailed local-scale analysis of the dynamics of the mixing process to understand and model the mixing behavior in different regimes. The exchange flow experiments and analyses carried out by Seon *et al.* [111–114] were mostly concerned with long-time behavior after the initial transients. They studied the transient behavior of the exchange flows in [115] for nearly-horizontal pipes. It was found that the front is initially controlled by inertia but later limited by viscous effects. This yields to a high front velocity value that decays to a steady state with time proportional with $\sin\alpha$ where α is the angle of inclination measured from horizontal ($\alpha = \pi/2 - \beta$). The transition from viscous flows to inertial flows, occurring at $\hat{V}_f \approx 0.7\hat{V}_t$, was also studied. They found that the transition is a function of inclination angle α. This critical angle, α_c, measured from horizontal decreases when the density contrast increases. In the case of viscous flows a conceptual model was developed which could capture the interface evolution and predict the front velocity. It was shown that the velocity of the front follows a shock-wave type dynamics, a fact that later on was also confirmed by Taghavi *et al.* [128] for displacement flows based on lubrication model.

When the pipe is strictly vertical, the buoyant exchange flow essentially resembles the famous Rayleigh-Taylor configuration (explained in §2.2.1) in a long-thin aspect-ratio geometry. Dalziel *et al.* [32] studied this flow confirming the fact that the turbulence generated by RayleighTaylor instability and the resulting mixing are much stronger than those driven by other mechanisms. Although the flow is initially dominated by inertia and then by viscous effects, the efficiency of the mixing seems to stay constant during the experiment. Throughout the initial growth the vertical transport happens through turbulent diffusion with the diffusivity decreasing with time. As the density difference becomes smaller and the strength of the driving buoyancy force decreases, inertia begins to play a less important role and the molecular viscosity takes the control of the flow dynamics. More recently Znaien *et al.* [156] studied qualitative flow structure and momentum transport mechanism for buoyancy driven exchange flows at different tilt angles. Three different regimes were observed namely laminar, intermittent and turbulent, depending on the tilt angle and density difference. For laminar regime, three parallel stable layers with different densities were observed. In the turbulent regime, the density was found to vary slowly across the pipe in the core of

the flow because of the dominance of the transverse turbulent momentum transfer. As density difference decreases and tilt angle β measured from vertical increases, the core flow density gradient and the resulting buoyancy forces become larger, which result in higher velocity maximum and a less efficient mixing. Although the mean concentration in the turbulent regime varies with time, the mean velocity stays constant. Finally the experimental results of velocities and density profiles were compared against a conceptual model developed in their paper [156].

Numerical studies

Apart from the experimental exchange flow studies, Hallez *et al.* looked into exchange flows in channels [63] and pipes [62, 64] using direct numerical simulations. They discovered that there are essential differences in 2D and 3D flows which arise from different dynamic vorticity fields. From this perspective the strong coherent vortices found in channel flows enable them to cut through the layers of pure fluid that feed the advancing fronts, in a periodic manner. In contrast, vortical motions in 3D are such that they promote segregation effect and thus avoid cutting the pure fluid layers [62]. Another interesting finding from the pipe exchange flow simulations in [64] was that for turbulent flows, non-zero radial and azimuthal components of velocity were found that govern the mixing mechanism. These secondary motions are induced by a combined effect of the lateral wall and turbulent velocity fluctuations. Although the current study has mean flow component added to the exchange flow problem, the underlying mechanism for the diffusive regimes to be shown later should be very similar to the finding of Hallez *et al.* [64]. They found that the lateral wall plays a key role in the anisotropic nature of the secondary flows, even though no geometrical anisotropy exists in the pipe geometry in contrast to the plane channel. The other important element which is also relevant to the buoyant displacement problem in hand is the existence of the non-axisymmetric mean shear in the flow which originates from the heavy-light configuration. In other words the density difference in each layer modifies the mean pressure gradient driving the flow. The turbulent fluctuation produced along the streamwise direction can then be unevenly distributed along the other two directions; see also [65, 131, 132] for similar mechanisms in homogeneous shear flows.

2.2.3 Boycott effect

As discussed earlier, Seon *et al.* [112] found three different regimes for pipe exchange flows, namely where front velocity first increases with tilt angle, β, reaches a plateau and then decreases again. This trend can also be looked at in a different way. In fact the underlying mechanism of the exchange flows is very similar to the *Boycott effect* [61]. When a suspension of particles is agitated in a geometry and left to sediment, it is not difficult to check that the sedimentation happens faster if the geometry is tilted; see Fig. 2.7. The reason behind this is that particles move in a random way in suspension. If the suspension is left in a vertical pipe due to the interaction of particles and fluid, it takes longer for particles to reach down the pipe. Whereas if the pipe is tilted, the heavier elements that are particles accumulate close to the lower walls and the lighter ones are pushed towards the upper walls. This finally results to a faster sedimentation.

Figure 2.7: Boycott effect in the sedimentation of a suspension of particles in a tube. The left tube is vertical and the right one is inclined at 30° with respect to the vertical. The photos are taken after the same period of time after agitation the suspension homogeneously. Photos are taken from [61].

In the case of exchange flows, when the pipe is titled close to the horizontal, the fluids are well separated but on the other hand the buoyant driving force for moving the layers is very weak (small front velocity). As the pipe is more inclined, the driving component of buoyancy force in streamwise

direction increases so the front velocity increases as well. Theoretically the driving buoyancy force is maximum when the pipe is tilted at vertical. However due to the growing instability as the inclination is becomes ore vertical, the fluid layers mix together and the chaotic behavior induced from their mixing slows down the front, essentially a Boycott effect. This is why the front velocity experiences three different phases with inclination angle. It is worth noting that the same mechanism exists for the displacement flow of two buoyant flows in a duct. In fact similar qualitative trends are observed for these flows that will be discussed in more details in the following chapters.

2.2.4 Displacement flows in nearly horizontal ducts

As explained before, exchange flows are well studied for a broad range of inclination angles, viscosities and density differences at least in the Newtonian limit. The effect of imposing a mean flow on the exchange flow of two miscible fluids is studied by Taghavi *et al.* [124–130] in full detail for nearly-horizontal ducts; see also [87]. The first study was based on an analytical model in the lubrication limit [128]. Basically a closure model was developed for interface height and lower layer flow rate flux to predict the shape of the interface, front velocity and finally the displacement efficiency (the volume of the displaced to displacing fluid in a given control volume). Later on, they carried out experiments for iso-viscous Newtonian fluids in a nearly-horizontal pipe [129]. The main finding was that three flow regimes may appear depending on the strength of the mean flow speed, $\hat{V}_0$. When the mean flow is low, the flow resembles the exchange flow [112] (regime 1). As mean flow is increased the front velocity $\hat{V}_f$ was found to vary linearly with $\hat{V}_0$ (regime 2). When the mean speed is further increased we enter turbulent regime where $\hat{V}_f = \hat{V}_0$ (regime 3). They also found that the mean flow can counter-intuitively stabilize the flow (in regime 1) through increasing the local gradient Richardson number, Ri, [129]. In this case the back flow is reduced and the flow becomes stabilized. Figure 2.8 shows the three regimes, discussed using experimental snapshots taken from [126]. It can be seen that in the exchange-dominated regime 1 there are inherent waves at the interface due to the strong back flow. The flow is stabilized by the mean flow in regime 2. further increasing the mean velocity will make the flow turbulent which finally causes mixing across the pipe.

In this thesis we will investigate whether the stabilizing effect of the mean flow is valid for other inclination angles or not. Taghavi *et al.* [130] later on studied the trailing front behavior and clarified the boundary be-

tween instantaneous and non-instantaneous displacements using the control parameters, $\chi = 2Re\cos\beta/Fr^2$. By instantaneous displacement we mean that the displaced fluid does not go upstream of the gate valve once the simulation/experiment starts. If the displacement is non-instantaneous we have inevitably had some back flow of the displaced fluid layer up above the gate valve. The dimensionless parameter χ governs the dynamics of the viscous flows at long time and represents the competition between buoyancy stresses in the axial direction and viscous stresses due to the mean flow. More recently Taghavi *et al.* [126] looked at iso-viscous Newtonian displacement flows in nearly horizontal ducts from three perspectives: experiments, numerical simulations and analytical modeling. For the experiments the dimensionless maps were given classifying different viscous/inertial and instantaneous/non-instantaneous regimes. The numerical simulation were carried out for a channel geometry using the code PELICANS developed at IRSN (French Nuclear Safety Research Institute). The lubrication model first presented in [128] was further improved in [126] to take into account the effect of weak inertia through the weighted residual approach.

Through a semi-analytical approach, the lubrication model can also be applied to pipe geometry when the fluids are generalized non-Newtonian [87]. The effect of viscosity ratio and shear-thinning was then studied in [124] giving predictions of the front velocity as a function of χ and viscosity ratio, m. For shear-thinning fluids, it was shown that with an appropriate definition of the effective viscosity the scaled front velocities fit well with the results from the Newtonian displacements, in both pipe and plane channel geometries. The effect of yield stress on the displacement flow at nearly horizontal angles was investigated in [125]. The slumping pattern observed in all previous Newtonian experiments was found to be not the only existing pattern. In fact depending on the density difference the displacing fluid can either slump or advance along the middle of the displaced fluid. It is worth noting that the slumping effect is also reduced when the geometry is a channel, compared to the pipe; see [126]. Based on the experiments and numerical simulations carried in [124–126, 128–130], Taghavi and Frigaard gave estimates of the longitudinal extent of the interface and the degree of mixing for nearly horizontal angles [127]. This last study was motivated from the industrial point of view: to estimate the volume of displacing fluid required to pump the displaced fluid out of the confined geometry in hand. Note that both Newtonian and non-Newtonian fluids were considered.

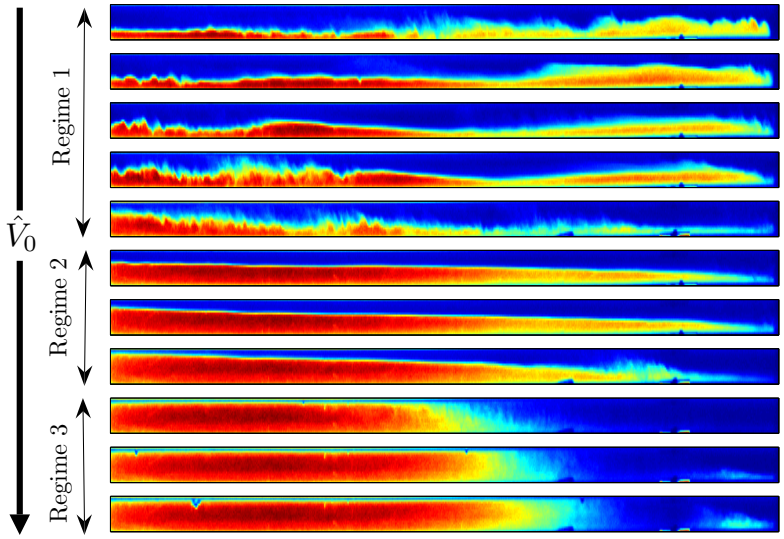

Figure 2.8: A sequence of snapshots from experiments with increased imposed flow rate for $\beta = 83\,^{\circ}$, $At = 0.01$ and $\hat{\nu} = 1$ (mm^2/s). From top to bottom images are shown for for $\hat{V}_0 = 9,\ 19,\ 31,\ 44,\ 56,\ 57,\ 72,\ 108,\ 257,\ 474,\ 841$ (mm/s). The figure shows a 1325 (mm) long section of the pipe a few centimeters below the gate valve. The picture is extracted from [126].

2.2.5 Structured displacement flows

There are also quite a few studies on displacement flows similar to the current study but concerning regimes where the flow is more structured. These are mostly in viscous regimes, in the low Reynolds number range or include symmetric pipe or channel flow features, e.g. [96]. One example is the study of interface instabilities in a vertical pipe during displacements of two miscible fluids, by Scoffioni *et al.* [109]. The focus of their study lies in studying the effect of viscosity ratio and flow rate on flow stability as observed in downward, strictly vertical displacement of miscible and Newtonian fluids. Three flow types were found depending on the flow rate and viscosity ratio value namely a stable finger, axisymmetric and Corkscrew modes. Figure 2.9 shows these three regimes observed in a vertical pipe.

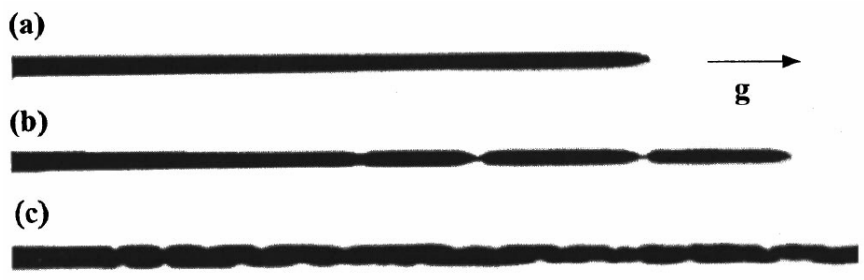

Figure 2.9: Different flow types observed in displacing layer in downward miscible displacement of two fluids in a vertical pipe: a) stable finger b) axisymmetric mode c) corkscrew mode. The lighter displacing layer is water and the heavier displaced fluid (not shown) is mixture of water and glycerin solution. Photos are taken from [109].

The degree of molecular diffusive transport compared to advective transport is governed by the Péclet number. The high Péclet regime inevitably approaches the zero surface tension immiscible limit, provided the displacement flow remains stable, as has been shown computationally by Chen and Meiburg [27], and experimentally by Petitjeans and Maxworthy [93]. Miscible displacements have been studied experimentally by a number of authors, considering both density differences and viscosity differences between the fluids, in Hele-Shaw cells [45, 75] in regimes where the Péclet number is significantly larger than the ratio of length to diameter. In general for upwards displacements, a more effective displacement is achieved by a displacing fluid

that is both heavier and more viscous. Where density differences are present there is a large body of work targeted at viscosity effects in vertical geometries, and much of the published work is focused at onset of fingering/spike type instabilities.

The upward displacement of miscible non-Newtonian fluids inside a vertical pipe was studied experimentally and numerically by Gabard and Hulin [56]. Both shear-thinning and viscoplastic fluids were considered for the displaced layer. The fluids were iso-density. The influence of rheology on the displacement of a viscous fluid by a less viscous, Newtonian one was studied as a function of the mean flow rate. For shear-thinning fluids (mostly xanthan-water solutions), the residual film thickness was found to be $28 - 30$ % of the pipe radius. For viscoplastic fluids, (Carbopol-water solutions), the thickness further decreases down to $24 - 25$ % of the radius. Importantly however, the shear-thinning fluids experienced instabilities over longer timescales. Another study on the instability of the interface between two fluids in vertical displacement flow in pipe is that carried out by Balasubramaniam *et al.* [11]. This paper focused on the experimental study of both upward and downward displacement of Newtonian fluids, with the displaced fluid being less viscous. Kuang *et al.* [80] investigated the displacement problem in vertical pipes experimentally. Both upward and downward configurations were considered when displaced fluid is denser and more viscous than displacing fluid. Taking miscible Newtonian fluids, Particle Image Velocimetry (PIV) measurements were used to get the velocity distribution and finger tip shape.

The downward displacement flow in a vertical Hele-Shaw cell was studied experimentally and theoretically by Lajeunesse and co-workers [81]. Fluids were chosen to be miscible and Newtonian. Neglecting diffusive effects, the dependence of the flow stability on viscosity ratio and flow rate value was investigated. In the limit of Stokes flow, Goyal *et al.* [58] carried out a computational study for downward displacement for the same geometry (vertical Hele-Shaw cell). Fluids were taken to be miscible and Newtonian to compare the results with those in [81]. It was found that both the growth rate and the dominant wave-number depend only weakly on Péclet number and also moderately stable density stratification can stabilize a viscously unstable displacement. More recently Kuang *et al.* [79] studied miscible displacement of silicone oils in capillary tubes experimentally focusing on the viscous fingering effect observed and measuring the fractional volume of more viscous fluid left on tube wall after passing the finger front.

2.2.6 Averaged inertial models

In an attempt to mathematically model the buoyant flows of two fluids, there have been different approaches. Among these approaches, the control-volume based methods have obtained increased popularity due to their simplicity and while having reasonable accuracy in predicting the large scale features of the flow. The computational cost of this prediction is also not high at all, compared to full CFD simulations. Benjamin [15] studied gravity currents following an energy-conservation approach. He looked at three geometries, namely 2D plane channel, liquid emptying from a horizontal pipe and very-deep layer geometry. Whether there were energy losses in the system or not, he gave predictions of the interface height. For instance he found that in the absence of energy losses the interface between the heavy and light fluid layers stays in the middle of the channel. He assumed that the flow far upstream and downstream of the front is hydrostatic and inside the gravity current no relative flow exists i.e. no internal flow. This is a fair assumption where viscous effects are minimal, e.g. velocity measurements in an intrusion revealed that the internal velocities are typically around 10% of the current speed [83]. More complicated interface heights can arise if energy loss is to be taken into account. Following a force balance approach, he obtained the shape of the interface and the angle of the trailing front for the case when heavy liquid leaves the pipe and lighter fluid occupies its space. For the case when the depth of the liquid upstream is considered to be very much greater than the mean depth of the cavity (caused by gravity current), Benjamin [15] pointed out that a net hydrostatic force acting horizontally has to be balanced by momentum loss in the receding flow. This requirement apparently cannot be met when there is no dissipation and with a flat free surface (the hydrodynamic drag force on a smooth "half-body" is zero [95]). When the interface is wavy he investigated whether the momentum loss can cause wave breakage or not.

Thorpe [136] considered a horizontal channel with closed ends containing two stratified fluids at rest in a stable way. The whole system was then tilted, resulting in a continuously accelerated stratified shear flow in the central part of the channel, that remained until it was affected by the end walls. Assuming an inviscid flow, he developed a unidirectional model for the stratified shear flow which was in good agreement with experimental observations up to the onset of shear-driven Kelvin-Helmholtz instabilities (see §2.2.1). Later, he studied these instabilities further experimentally and theoretically in [138]. Several other authors followed similar modeling approaches to Benjamin's [15] and tackled gravity current problems in different

regimes and/or geometries. For instance Allen [4] looked at mixing at turbidity current fronts by expressing the inflow rate of the ambient medium into the front region. Fluid motions behind the head of a gravity current advancing over horizontal and inclined surfaces were studied in [21, 119] and [14, 20] respectively, through experiments and averaged-type models.

As mentioned earlier, Benjamin's study [15] suggested that the dynamics of gravity currents are strongly influenced by dissipation coming from turbulence and mixing between the current and the surrounding environment. Later on, Shin *et al.* [117] looked into improving the lock-exchange flow control volume style of model and showed that dissipation is not important when the Reynolds number is sufficiently high. Although mixing is present, the amount of energy dissipated is relatively small, which reduces the current speed by only a few percent from its energy-conserving value. Their theoretical model was compared against new experiments and showed good agreement. Shin *et al.* [117] experimentally verified that Benjamin's potential flow theory [15] can approximate the lock-exchange interface shape fairly accurately despite the mixing and dissipation between the two fluids; see Fig. 2.10. This shows that the front propagation speed in this case can be determined by finding the equilibrium of pressure at the front, taking advantage of inviscid flow theory and assuming negligible dissipation of energy downstream.

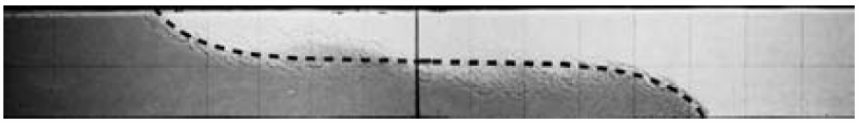

Figure 2.10: Experimental results of a full depth lock-exchange with Benjamin's potential flow solution (dashed line) [15]. This image is taken from [117].

Lowe *et al.* [84] developed a two-layer hydraulic theory to model their experiments on non-Boussinesq lock-exchange problem. The experiments were run in a rectangular channel using water-based solutions that would give density ratios of 0.61 to 1. Upon comparison of their model against experiment and numerical simulations they found out that a model in which the two gravity currents are connected by a simple expansion wave (without an internal bore) represents the high density difference lock exchange flows appropriately. Birman *et al.* [16] compared their simulations on lock-exchange flows in sloping channels with the more conceptual model of Thorpe [136]

and found good agreement. The simulations showed that a two-layer stratification model is suitable for the early stages of the flow but for the later stages a three-layer stratification model is required. This is due to the intense mixing at the interface in the central part of the cross-section of the channel. The two and three-layer stratification models were then employed to estimate the time after which the velocities of the current fronts were affected by the accelerating stratified layers.

In the category of modeling gravity flows on inclined surfaces, Webber *et al.* [147] and Tickle [141] derived similarity solutions to the shallow-water equations and proposed wedge models for three-dimensional gravity currents on slopes due to the release of heavy fluid into light ambient. Ross *et al.* [101] then performed the corresponding experiments and extended the wedge models to include entrainment effects. They however emphasized that these simplified models do not capture all the significant features of the flow although they predict front densities fairly well. More recently Neophytou *et al.* [90] looked at buoyant displacement of fire smoke in a confined and semi-confined tunnel at different inclination angles. The experimental and theoretical results were compared along with CFD simulations to determine the smoke concentration profiles. The integral model presented in their work solves for fire smoke concentration and net pollutant volume flux. The qualitative flow structure and momentum transport mechanism for buoyancy driven exchange flows at different tilt angles was studied by Znaien *et al.* [156]. They observed three regimes namely laminar, intermittent and turbulent, depending on the tilt angle and density difference. A conceptual model was developed in integral form to predict the layer velocities and density profiles which showed good agreement with the experimental results.

In summary, the control-volume approaches present in the literature are mostly targeted on exchange flows and not on displacement flows, and also largely neglect viscous effects. A good addition to these studies would be to include the effect of imposed flow on the buoyant gravity currents. The above mentioned conceptual models then could be a very effortless (and useful) tool for predicting global characteristics of the buoyant displacement flows such as the velocity of the propagating front, average interface height in the case of slumping displacements, etc.

In chapter 6 we consider a two-layer channel flow model for our displacement problem. The usual approach is to apply scaling arguments to eliminate extensional stress terms and simplify the transverse momentum balance. If inertial terms are also small this leads to a conventional thin-film/lubrication model. Retaining the inertial terms produces the boundary layer equations which are still simpler than the full Navier-Stokes system and

faster to solve numerically, but have the same dimensionality. On assuming a particular form for the streamwise velocity profile, integrating the momentum equations across the fluid layer(s) leads to a system of one-dimensional (1D) equations, e.g. [118].

More recently, [103, 104] have proposed a methodology that is intermediate between the boundary layer approach and the integral approach of [118]. In place of an assumed form of velocity profile, a more general series approximation is postulated. Instead of satisfying the axial/streamwise momentum equation pointwise they multiply by a weight function and integrate across the fluid layer, setting the residual to zero. On assuming different degrees for terminating the series (reducing the degrees of freedom) different orders of approximation ensue. This *weighted residual* methodology has been extended to two layer thin film flows in channels and pipes by [8, 85] and used to study channel co-extrusion flows by [1]. In [126] we have used the derivation of [8] in working with iso-viscous Newtonian fluid displacements.

Some authors have worked on non-Newtonian flow problems of this genre. N. Balmforth [12] develop an integral approach for thin film flows of Herschel-Bulkley fluids, focusing on evolution of the interface and the yielded layer thickness. Amaouche *et al.* [7] derive a Shkadov-type model for a power law fluid thin film flow. Very recently the weighted residual approach has been extended to thin film flows of shear-thinning fluids [6, 102]. In both cases the authors propose special treatment of the low shear rate limit close to the interface in order to avoid the singularity in the viscosity at a free surface.

2.2.7 Axial dispersion

In the displacement problem, we have two fluids in contact with each other. Since our fluids are miscible they inevitably mix over time. However the mechanism of mixing can be different depending on the regime we are at (laminar or turbulent). The diffusion that causes transverse mixing is also responsible for spreading the mixed fluids axially along the pipe. The presence of a velocity field however facilitates this process by advecting the mixed volumes in the axial direction. This mechanism through which the fluids spread axially while diffusing transversely is called dispersion. Dispersion is important when the ratio of the timescale for diffusion across the pipe to advection along the pipe is very small, in other words $\hat{V}_0\hat{R}^2/\hat{L}\hat{D}_l \ll 1$. Here $\hat{V}_0$ is mean flow speed, $\hat{L}$ is the length of the pipe, $\hat{R} = \hat{D}/2$ is the pipe's radius and $\hat{D}_l$ is a representative local diffusivity. For laminar flow the local diffusivity is nothing but the molecular diffusion coefficient, which

is typically very small $\hat{D}_l = \hat{D}_m$. Thus the requirement for dispersion reduces to $Pe_m/L \ll 1$ where Pe_m is the molecular Péclet number (typically very large in our experiments and industrial situations) and $L = \hat{L}/\hat{D}$. In general this condition is not feasible to be satisfied in primary cementing with laminar flows, nor in our experiments.

In contrast, when the flow is turbulent, the local diffusion is nothing but the eddy diffusivity which scales with $\hat{V}_0\hat{R}\sqrt{f_f}$ where f_f is the friction factor. In this case the dispersion requirement reduces to $L\sqrt{f_f} \gg 1$ which only needs a moderately long pipe. When the flow is turbulent, the principal phenomenon which spreads the transversely mixed fluids axially along the pipe, is dispersion. Turbulence might be induced through different mechanisms, e.g. buoyancy, mean flow, etc.

The basic study that investigated the axial spreading of the mixed fluids was first developed by G.I. Taylor in [133, 135] for laminar flows and in [134] for turbulent flows. Figure 2.11 shows Taylor's experiment for dispersion of a soluble matter (brine in this case) in turbulent pipe flow. He recorded signals using conduction. This signals were related to the brine concentration in the mixed solution. It was shown that the soluble matter in turbulent flow disperses axially in the following form:

$$C = 1/2 - 1/2\mathrm{erf}(\frac{(\hat{x} - \hat{V}_0\hat{t})\sqrt{\hat{K}}}{2\sqrt{\hat{t}}}), \tag{2.2}$$

where C is the concentration of the matter in mixed solution varying between 0 (pure soluble matter) and 1 (pure solvent), erf the error function, $\hat{K}$ the virtual diffusion coefficient, $\hat{V}_0$ the mean flow speed and $\hat{x}$, $\hat{t}$ are streamwise location and time, respectively. The relation (2.2) shows that as time goes by the concentration of the soluble matter in the flow decreases downstream of the pipe which results in an increase to the longitudinal extent of the mixed zone (Fig. 2.11). Note that relation (2.2) is nothing but the solution of the diffusion equation:

$$\partial C/\partial\hat{t} = \hat{K}\partial^2 C/\partial\hat{x}_1^2,$$

in an infinite domain, setting $\hat{x}_1 = \hat{x} - \hat{V}_0\hat{t}$.

The total dispersion in the system is the combination of the Taylor dispersion (caused by the convective nature of the flow) and the eddy diffusion for turbulent flow. Aris [9] extended Taylor's study on laminar flows [135] for a broader range of parameters and geometries other than pipe. The geometry of the duct can have significant influence on dispersion coefficient.

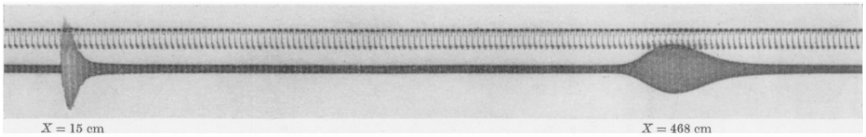

Figure 2.11: Pulses recorded at $\hat{x} = 15$ (cm) and $\hat{x} = 468$ (cm) showing the dispersion of brine in turbulent pipe flow. The brine concentration in the flow decreases downstream of the pipe resulting in an increase to the extent of the mixed zone. The picture is taken from [134].

For instance Aris [9] showed that the dispersion in a pipe is less than an elliptical pipe of the same area. Tichacek *et al.* [140] looked into the problem of axial mixing in a straight pipe and modified Taylor's analysis to include the effect of both Schmidt and Reynolds numbers in turbulent-flow range. They showed that the axial spreading increases rapidly as the flow approaches the laminar limit. The pipe roughness was found to increase axial mixing by a small amount and the effect of the turbulent eddy diffusion axially was shown to be negligible. The simplification made in their study was that the kinematic viscosity of the mixture solution was assumed not to change greatly with concentration. Later, Elder [43] extended Taylor's study to turbulent open channel flow geometry and compared the model predictions against experiments showing agreement. A broad overview of techniques for experimentally measuring fluid dispersion was given in [17] by Bischoff and Levenspiel. They also reviewed and generalized existing mathematical models for finding dispersion coefficients in [18]. Taylor's studies were limited to the where there is no density difference. The effect of buoyancy on axial dispersion of fluids was investigated by several authors [44, 92, 97, 98]. Reejhsinghani *et al.* [98] experimentally showed that in a horizontal pipe, natural convection can both enhance and weaken the laminar flow dispersion, even when the density differences are extremely small. Erdogan and Chatwin [44] in a similar study found that buoyancy should not have a noticeable effect on the longitudinal dispersion for Péclet numbers near a certain value at which the horizontal spreading due to gravity balances the effect of lateral mixing caused by secondary flow. They also showed that for all common liquids and most gases the curvature in the pipe decreases the diffusivity. However, the limit, based on which, they derived their equation was sufficiently large curvatures. Later on, Nunge and Gill [92] investigated miscible displacement and dispersion in porous media consisting of different

microstructure models. They also explained the mechanism through which a favorable density difference can smooth out the displacement front in such media. The dispersion in porous media was studied in more details later by Brenner [19] based on the concepts of Brownian motion theory.

When the pipe is vertical Reejhsinghani *et al.* [97] developed an approximate theory for transient dispersion when free and forced convection are both present. They also tested their predictions experimentally finding a reasonably good agreement. Dispersion was found to be enhanced significantly when lighter fluid on the bottom displaces a heavier one. In the vertical tank situation and when the fluid densities are different (heavy on top of light in particular), mixing and dispersion is inevitably complcated by Rayleigh-Taylor instabilities. Youngs studied such flows through 2D direct numerical simulations and experiments [154]. The viscous dissipation within the flow field was treated as a source of turbulence kinetic energy which was then used to define a turbulent diffusion coefficient (see also [32] for Rayleigh-Taylor experiments in a long-thin aspect ratio pipe). The axial mixing in turbulent flows was studied in concentric annuli by Smith and Perona [120] both theoretically and experimentally. When the hydraulic diameter is used as the length parameter the axial dispersion coefficient of annuli and pipes are the same. The predicted dispersion numbers turned to be about 60 to 70% of the measured experimental values. Dispersion in rectangular conduits was also studied by several authors later on [26, 40]. Focusing on the transitional regime ($300 < Re < 10000$) for gas systems, Flint and Eisenklam [47] studied longitudinal dispersion in a straight pipe experimentally. Results in the laminar regime diverged from Taylor's theory at a Reynolds numbers lower than the onset of turbulence.

The study of dispersion for non-Newtonian fluids was initiated by Wasan and Dayan [146] for turbulent pipe flows. This theoretical study focused on power law fluids and revealed that the dispersion increases with power law index, at constant Schmidt and Reynolds numbers. Atesmen *et al.* solved the mass conservation equation for dispersion numerically in [10] with practical interest in pipe and natural streams flow metering and in pollution control; see also [121] for simplified models of contaminant dispersion prediction and [46] for a complete review of turbulent mixing studies on stratified flows. Freitas *et al.* [48] presented a model for predicting the contaminated mixing volume in pipelines, that takes into account time-dependent flow rate and concentration-dependent axial dispersion coefficients. The governing equations of the model were solved via a finite element method. Field test data showed reasonable agreement with those of the proposed method over a wide range of concentrations. A similar numerical study for turbulent and

transitional regions in axial mixing of pipe flows was carried out by Ekambara and Joshi [42]. The flow based on low Reynolds number $k-\epsilon$ CFD model was solved using a control-volume type approach for the range of $2500 < Re < 10000$. Zhang and Frigaard [155] calculated the Taylor dispersion coefficient for laminar generalized Newtonian fluids of Herschel-Bulkley type. They also looked into miscible displacement flows of two fluids with different viscosities in channel following a perturbation-based model called Total Flow Equilibrium (TFE). The study was limited to the dispersive regime of small ϵPe, where ϵ, the duct aspect ratio is very small ($\epsilon \ll 1$). Figure 2.12 shows different dispersive displacement flow regimes found by numerical study of Zhang and Frigaard [155] for Newtonian displacement flow of two Newtonian fluids in a vertical channel. As shown in the figure for very low values of ϵPe, the flow is very well mixed across the channel, giving a uniform concentration profile in depthwise direction. As ϵPe increases (molecular diffusion coefficient decreases) the variation in the concentration profile across the channel also increases due to less dispersion in the axial direction.

Most recently Taghavi and Frigaard [127] presented a methodological framework for estimating the degree of mixing between miscible fluids pumped in a near-horizontal pipe. The fluids can be non-Newtonian, of Herschel-Bulkley type. Due to the industrial motivation the idea was to minimize mixing. In laminar regimes the mixing length estimates are based on front velocity of the leading displacement front. In turbulent regime however, the spreading mechanism is dispersion. In this case the basis for the mixing length prediction is an extension of the Taylor dispersion methodology. They used a method for deriving the dispersion coefficients, similar to that in [155]. Dispersion can have complicated effects on the flow stability too. Mishra *et al.* [86] studied the pressure-driven miscible displacement flow in a channel computationally based on finite-volume approach. The displacing fluid is more viscous than the displaced which is a classically stable system. However, double diffusive effects cause instability at the interface. Double diffusive effects can appear when the fluid is made of a solvent containing two solutes and both influence the viscosity of the mixed solution and diffuse at different rates.

2.2.8 Conclusions and research objectives

Due to the nature of the flow that we study, the displacement flow problem is interesting from both fundamental and engineering aspects. In fact, two-fluid systems with buoyancy forces have attract scientists from many

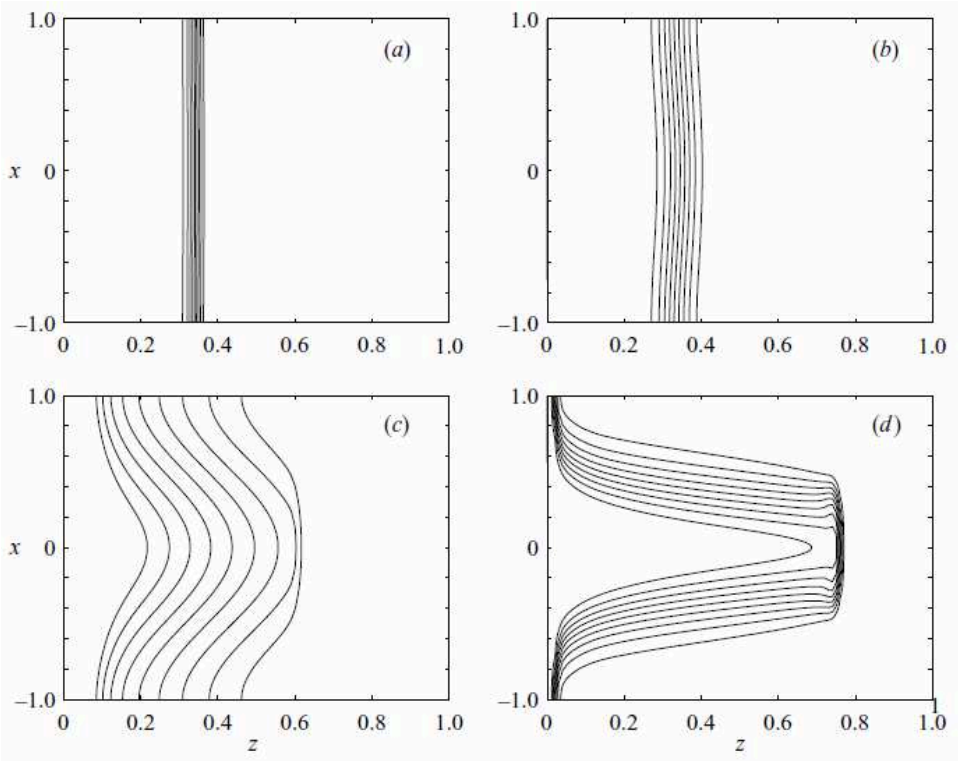

Figure 2.12: Concentration $c(x, z)$ at dimensionless time $t = 0.3$ for displacement flow of two Newtonian fluids in a vertical channel. The flow is from left to right and the displacing fluid is 100 times more viscous than the displaced one. a) $\epsilon Pe = 0.01$ b) $\epsilon Pe = 0.1$ c) $\epsilon Pe = 1$ d) $\epsilon Pe = 10$. The pictures are taken from the numerical study in [155].

different areas. From the fundamental point of view, the interest comes from many areas of study.

One of these areas is gravity currents. Gravity currents have been studied in detail experimentally, numerically and analytically. The exchange flow of two buoyant flows is the another very fundamental study close to our work. These flows have been studied extensively, at least in the Newtonian limit. Adding a mean flow component to the exchange flow and studying its effects is one of the main objectives of this work.

Displacement flows have also been studied in the literature, from experimental, numerical and analytical aspects. However, these studies are limited to specific ranges of parameters. In fact the flows looked into are mostly structured in a way that an understandable model or physical trend is able to be extracted. These studies of structured flows are far from the range of phenomena that are likely to be observed when it comes to the industrial application we are interested in, at least in highly inclined geometries. In this thesis we have tried to include a sufficiently broad range of parameters to cover the range of flow patterns that are likely to appear. Note that displacement flows in similar range of parameters are studied in [123], but for nearly horizontal ducts assuming both Newtonian and non-Newtonian fluids. Another contribution of this thesis is studying the effect of higher inclination angles on these flows. It is expected *a priori* that we will find fluid segregation to be the usual case in near horizontal configuration and mixing to occur usually as the pipe or channel is inclined closer to vertical.

A limit of our work is when turbulent flows occur. When the imposed flow is turbulent, the mixing is inevitably very efficient across the duct. In fact the fluids mix and disperse along the duct. This dispersive regime is well explained by Taylor dispersion theory for turbulent flows [134]. There is less motivation in our work to study the turbulent flows in this regime. Firstly, this regime is known to be the most efficient displacement regime and therefore there is not much potential for improving efficiency in these flows. Secondly the mixing zone spreading times and lengths can be estimated reasonably well from Taylor dispersion [134]. Lastly, due to laboratory and computational limitations detailed study of turbulent flows is not feasible. Therefore, we mostly study the flows with laminar imposed flow. Note that once the fluids are mixed, the flow can become turbulent but this is also induced by other mechanisms e.g. buoyancy, rather than, only by the imposed flow. Where we do find fully mixed/diffusive flows, our aim is to quantify the virtual (macroscopic) diffusion coefficient for predicting the mixing zone spread, rather than on detailed study of the flow structure.

From the modeling perspective, there is large body of work on averaged-type models, as discussed earlier. However the models introduced fail to give the quantities we are after, e.g. front velocity, interface height etc., with acceptable accuracy. In some limits, certain dynamic forces are neglected in the existing models, e.g. inertia, viscosity etc. Due to the complex nature of the flow, a unique model capable of capturing different regimes is not feasible to develop. There has to be assumptions made in order to be able to come up with a working model. This is also the case in the modeling approach we have taken in this thesis. We have tried to develop a *weighted residual* model that can simulate the displacement flow of two stratified flows with weak inertia in the presence of buoyancy force. The model mostly applies to the viscous flows where mixing at the interface in negligible, i.e. we aim to predict that onset. However a big advantage of the model is in predicting the instability of these viscous flows in an economical way.

Throughout the course of experiments run for this thesis, many types of instability were observed. Fortunately the literature is so rich in the area of stability analysis of similar flows that we have many examples to help us understand more complex flows better. These instabilities are either caused by the high imposed flow velocity, velocity gradients within the flow, by viscosity and/or density differences. Since the fluids we consider are miscible we do not need to deal with the instabilities affected by surface tension between the fluids. Another objective of this thesis is to better understand the combined effect of the different physical effects and pave the way for broader predictions. One of the main motivations of developing the *weighted residual* model in chapter 6 is to predict the onset of instability given an interface shape (height) in the displacement zone. It is believed that even when the flows exhibit mixing and instabilities at higher inclination angles, there is initially a clean interface between the fluids that has gone unstable due to perturbation. A natural attempt to understand the mixed flows then is to predict the onset of the mixing/instability.

In summary, through an extensive literature survey we have found that relatively few studies have been carried out in the following areas:

- Displacement flows in inclined geometry.
- Imposed-flow dominated displacement flows.
- Non-Newtonian displacement flows.
- Useful mathematical models for displacement flows.

The thesis aims to contribute selectively to improving this situation.

The technical/scientific aim of the current project is to provide reliable knowledge to be used for oil and gas well construction processes, by studying mixing/displacement flows using analytical, experimental, and computational methods. In particular we focus on primary cementing. The plan is to understand displacement/mixing flows in a pipe of two miscible generalized Newtonian fluids. Dimensional analysis reveals that there are at least 11 non-dimensional parameters governing and formulating the displacement/mixing flows. A key objective is to quantify the effect of each parameter on displacement/mixing flows and possibly on displacement efficiency. This starts from examining the effects of pumping speed, tilt angle, density difference, viscosity ratio, and rheological parameters. It seems impossible to cover a wide range for each of these parameters. However, it is aimed to have as wide coverage as possible based on time and resources. We have tried to advance our knowledge of displacement/mixing flows through 3 main activities:

- We have conducted scaled laboratory displacement flow experiments in a circular pipe with orientations away from horizontal. We consider a range of fluid properties and flow parameters. We have determined the effects of each parameter on displacement efficiency as well as displacement/mixing flow regimes, and provide flow regime diagrams to identify the principal flow types.

- We have computed high quality flow simulations, in a 2D channel. We compare these results with the experimental results and study the key displacement flow mechanisms in a more controlled way. In fact, through the numerical simulations, we can gain very useful information from the velocity field at each instant of time and location, something that is not possible to be studied in our experiments.

- In a simplified mathematical study, we have focused on a limiting parameter regime that appears to be tractable (semi)analytically and which also has practical relevance. Through this, we have investigated the onset of instability/mixing.

This thesis study was intended to deliver a significant amount of high quality experimental and computational data, which is largely lacking in literature. This then allows the development and calibration of simpler 1D models that are suitable for engineering design of oilfield displacement flow processes.

Chapter 3

Miscible density stable displacement flows in an inclined pipe

In this chapter[2] we study density stable laminar miscible displacement flow of two iso-viscous Newtonian fluids in an inclined pipe (of diameter $\hat{D}$). By density stable we mean that the less dense fluid displaces the heavier fluid in the downwards direction. Although the real well cementing industrial configuration is density unstable, at some stages of the process the displacing fluid can be lighter than the displaced. This is usually the case with wash or spacer fluids before pumping the cement slurry to directly remove the drilling mud.

We present a wide range of experimental results from displacement flow experiments performed in the setup explained in appendix A. Although the pipe is long we are in regimes where the Péclet number is significantly larger than the ratio of length to diameter, meaning we are far from the laminar dispersive regimes.

The significant novelty of the results presented in this chapter is as follows. Firstly, we know of no other experimental or numerical study of miscible displacement flow that covers a broad range of pipe inclinations in the density stable configuration. Secondly, we illustrate the very interesting transition that occurs as the density difference (dimensionlessly represented by the Atwood number At) passes through zero. For identical fluids ($At = 0$) the velocity adopts a Poiseuille profile, the centre of which moves at twice the mean speed. For density unstable displacements ($At > 0$) a buoyancy driven slumping interface was found in [126, 129, 130], with front speed around $26 \pm 5\%$ higher than the mean speed. Intuition suggests that the density stable displacement flow ($At < 0$) should displace at approximately

[2] A version of this chapter has been published as: **K. Alba**, S.M. Taghavi and I.A. Frigaard. *Miscible density stable displacement flows in inclined tube.* ***Phys. Fluids*** **24** 123102 (2012).

the mean speed, as we indeed find. In a long pipe, the displacement efficiency is given by the ratio of mean speed to front velocity and it is curious to observe non-monotone variation of the displacement efficiency with At.

The third novel contribution of this chapter is in finding a simple dimensionless relation that captures the spreading of the *interface* in the density stable configuration. By interface we mean a point or points at a streamwise location where the concentration gradient transversely is high and the two fluids meet and interact. Since our fluids are miscible we always have a diffusive interface with concentration varying between that of the displaced and displacing fluids. However due to the large Péclet number limit we consider throughout this thesis, we can assume that the interface between the two fluids stay sharp at least when there is not a strong mixing present. In the case of viscous flows detecting the interface between the fluids is much easier than the case where mixing and instabilities are strong. The density stable configuration has been found to produce highly efficient displacements, with the bulk of the interface moving steadily at the mean velocity. The streamwise length of the stretched interface, we have called the *stretch length* $\hat{L}$, and have measured over a wide range of parameters. The stretch length increases with the mean flow velocity, increases with inclination β from vertical, decreases with density difference and increases with viscosity. We find that our data can be represented by a dimensionless expression relating $\hat{L}/\hat{D}$ to a function of the inclination β and the parameter χ which is the ratio of buoyancy and viscous stresses.

3.1 Experiments and parameters range

Our experiments are conducted in the flow loop explained in appendix A. Basically we have an inclined acrylic pipe (4 (m) long, $\hat{D} = 19$ (mm)) capable of being tilted to any angle β measured from vertical. A gate valve separates the upper 80 cm of the pipe from the lower 320 (cm). Two fish tanks surround the pipes to reduce refraction effects and obtain high quality images. The gate valve is initially closed, separating displacing and displaced fluid. The fluids are pumped from two transparent tanks that are pressurized (to ~ 70 (kPa) gauge) by compressed air. By adjusting a needle valve located before the drain we can control the flow rate accurately, for low-to-moderate Reynolds numbers.

The dimensional parameter ranges we have considered for our experiments are given in Table 3.1. We also carried a series of experiment for $\beta = 85\,^\circ$, over similar ranges of parameters. The data for this set are not

Parameter	Range
At	$-0.0035,\ -0.01$
$\hat{V}_0$	$0-130$ (mm/s)
$\hat{\nu}$	$1,\ 5.6,\ 18.6$ (mm^2/s)
β	$0,\ 20,\ 45,\ 60,\ 70$ (deg)
Re	$0-2500$
Fr	$0-4.8$

Table 3.1: Parameter range of density stable experiments.

included here as the stretch length (to be defined later in §3.2.2) was mostly not fully developed during the time of the experiment and within the length of the apparatus. As $\beta \to 90^\circ$ we approach a singular case in which the interface between the two fluids in the pipe extends to infinity, given a sufficiently long pipe/experiment.

A dimensional analysis of this type of flow is given in [126]. We denote the density of the displacing fluid by $\hat{\rho}_L$ and that of the displaced fluid by $\hat{\rho}_H$. The Atwood number is defined as $At = (\hat{\rho}_L - \hat{\rho}_H)/(\hat{\rho}_L + \hat{\rho}_H)$, representing a dimensionless density difference. Note that for this study $At < 0$ since $\hat{\rho}_L < \hat{\rho}_H$. Our experiments are all performed at small $|At|$, the significance of which is that a Boussinesq approximation is valid. This means that density differences affect the buoyancy force significantly through the densimetric Froude number, $Fr = \hat{V}_0/\sqrt{|At|\hat{g}\hat{D}}$, but not the acceleration of individual fluids. Here $\hat{V}_0$ is the mean flow velocity and $\hat{g}$ the gravitational acceleration. Since we also study a high Péclet number range (as is most relevant industrially), the flow is governed only by 3 dimensionless groups: β, Fr and the Reynolds number $Re = \hat{V}_0\hat{D}/\hat{\nu}$, where $\hat{\nu}$ is defined using the mean density $\hat{\rho} = (\hat{\rho}_L + \hat{\rho}_H)/2$ and the common viscosity of the two fluids, $\hat{\mu}$. The range of dimensionless parameters is also shown in Table 3.1, from which we can see that significant buoyancy forces and inertial effects are present in our experimental range, as well as a broad set of pipe inclinations.

3.2 Results

We present our results in 3 main sections below. First we examine the interesting transition from density unstable to density stable flows as At decreases through zero (§3.2.1). The remainder of the results concern only density stable flows. In §3.2.2 we characterise the main features of the

density stable displacements, describing the evolution to a steady *stretch length*. Parametric variations in stretch length are described in §3.2.3.

3.2.1 The transition from density unstable to density stable

In density unstable displacement the heavier displacing layer slumps beneath the lighter displaced layer. In the absence of significant inertial mixing, we are able to identify two displacement fronts: the *leading front* advances more rapidly along the bottom of the pipe, whereas the *trailing front* lags behind so that the interface is progressively extended between the two fronts. If buoyancy forces are strong, the trailing front may propagate backwards against the mean imposed flow. After an initial transient the speed of the leading front settles to a steady value, $\hat{V}_f$, which may be calculated from image analysis; see [126, 129, 130]. In a very long pipe at time $\hat{t}$ the leading front has advanced an approximate distance $\hat{V}_f\hat{t}$. At the same instant in time, only a volume $\hat{V}_0\hat{t}$ of the pipe (behind the leading front) is occupied by displaced fluid. The *displacement efficiency* is therefore approximately equal to $\hat{V}_0/\hat{V}_f < 1$. This ratio is very important in the design of fluid displacements. Our previous studies of density unstable displacement flows in near-horizontal pipes yielded front speeds typically in the range $26 \pm 5\%$ faster than $\hat{V}_0$.

Figure 3.1 compares a sequence of images for density unstable and density stable displacement flows at the same $|At|$, for $\beta = 70\,^\circ$, $\hat{\nu} = 1$ (mm^2/s) and with very similar $\hat{V}_0$. The slumping interface in the density unstable case (Fig. 3.1a) is qualitatively similar to our previous work (at larger β). This particular displacement appears to be in in inertial regime. The density stable displacement (Fig. 3.1b) also shows two fronts advancing. Two key differences are that: (i) after an initial phase in which the interface is extended, the trailing front moves steadily at approximately the same speed as the leading front; (ii) the lighter displacing fluid layer now advances on top of the heavier displaced fluid. These two differences are common to all our density stable experiments.

Figures 3.2a & b show the spatiotemporal diagram of the same experiments as in Fig. 3.1. From these plots we are able to compute the velocity of the leading displacement front, $\hat{V}_f$. For the density unstable displacement, $\hat{V}_f = 38.9$ (mm/s) $> \hat{V}_0 = 20.3$ (mm/s), so that the interface elongates as the displacement evolves, whereas for Fig. 3.1b we have $\hat{V}_f \approx \hat{V}_0$, meaning a significantly more efficient displacement. This transition in displacement efficiency ($\hat{V}_0/\hat{V}_f$ apparently increases) as we change At from positive to negative appears intuitive. However, it is also remarkable what happens at

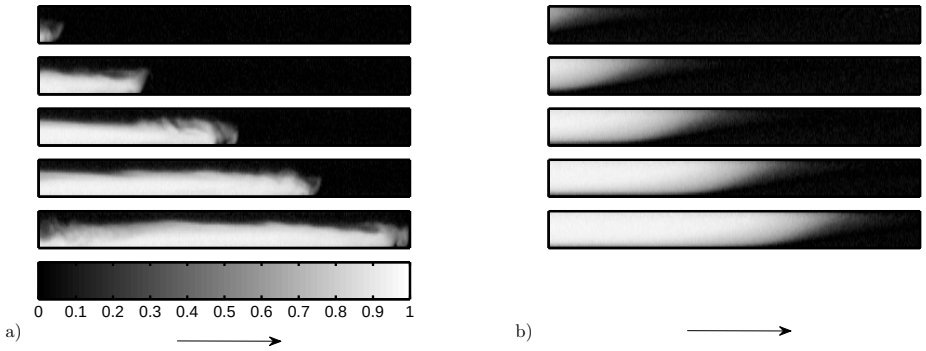

Figure 3.1: Density unstable and density stable displacements at $\beta = 70\,^\circ$ and $\hat{\nu} = 1$ (mm^2/s). a) $At = 0.0035$ (dark fluid is less dense than the lighter coloured fluid) and mean velocity $\hat{V}_0 = 20.3$ (mm/s); the sequence starts 16.25 (s) after opening the gate valve and the time interval between images is 2.5 (s). b) $At = -0.0035$ (dark fluid is more dense than the lighter coloured fluid) and $\hat{V}_0 = 20.9$ (mm/s); the sequence starts 21.5 (s) after opening the gate valve and the time interval between images is 3.25 (s). The field of view is 430×19 (mm^2), taken 800 (mm) below the gate valve. The last image at the bottom of figure a shows the grayscale for the concentration values, which can also be used for figure b. The arrows indicate the flow direction and the left end of the pipe is higher than the right (the fluid flows downhill).

the transition.

First of all, we comment that the density differences involved in our experiments are relatively small ($At = \pm 0.0035$ corresponds to a density difference of $\approx 0.7\%$), which suggests that the transition occurs very close to $At = 0$. Secondly, the change in $\hat{V}_0/\hat{V}_f$ is not monotone! For $At = 0$ the iso-viscous *displacement* flow is simply that of a passive tracer advected by a Poiseuille flow. The centerline advects at twice the mean flow and the entire front elongates progressively as the displacement continues. The spatiotemporal plot for an experiment at $At = 0$ is illustrated in Fig. 3.2c. We have marked on this plot the line $\hat{V}_f = 2\hat{V}_0$ (as a guide to the eye). This leading front is much less sharp than either of those with a density difference. We observe significant dispersion, but note that we are still far from the diffusive Taylor regime.

The leading front speed at $At = 0$ is significantly faster than those for small positive or negative At. There is no monotone increase in efficiency as At decreases through zero. Indeed, it seems that as $At \to 0$ from above, $\hat{V}_0/\hat{V}_f$ decreases towards a value of 0.5, but then increases rapidly to 1 for $At < 0$. Experimentally, we can not determine if the transition in efficiency is discontinuous or simply rapid at $At = 0$. This feature is at least noteworthy. As we will later see in chapter 4 for density unstable Newtonian displacements ($At > 0$), the instability and mixing increases at higher inclination angles compared to the stratified stable flows in nearly horizonal pipes. The higher degree of instability and mixing results in a value of $\hat{V}_f$ which is much closer to $\hat{V}_0$. In other words the displacement efficiency becomes closer to 100 %. The non-monotone behavior discussed above is only valid for nearly-horizontal cases. The displacement efficiency behavior with At differs at different inclination angles. In any case, $At = 0$ (iso-density displacement) seems to cause a non-monotonicity in displacement efficiency change with density difference.

3.2.2 Characteristics of density stable displacements

We turn now to exploring density stable displacements in more detail. The experiment of Figs. 3.1b and 3.2b is quite typical in that, after an initial transient the leading and trailing fronts move together. In order to capture this development we plot the averaged concentration profiles at successive times, as an equivalent interface height, $\hat{h}(\hat{x}, \hat{t})$. Figure 3.3a shows the experimental $\hat{h}(\hat{x}, \hat{t})/\hat{D}$ at $\hat{t} = 62,\ 68, .., 128,\ 134$ (s) for the same experiment as in Figs. 3.1b and 3.2b. At these times the flow has become fully developed and we can see that the distance between successive interfaces remains

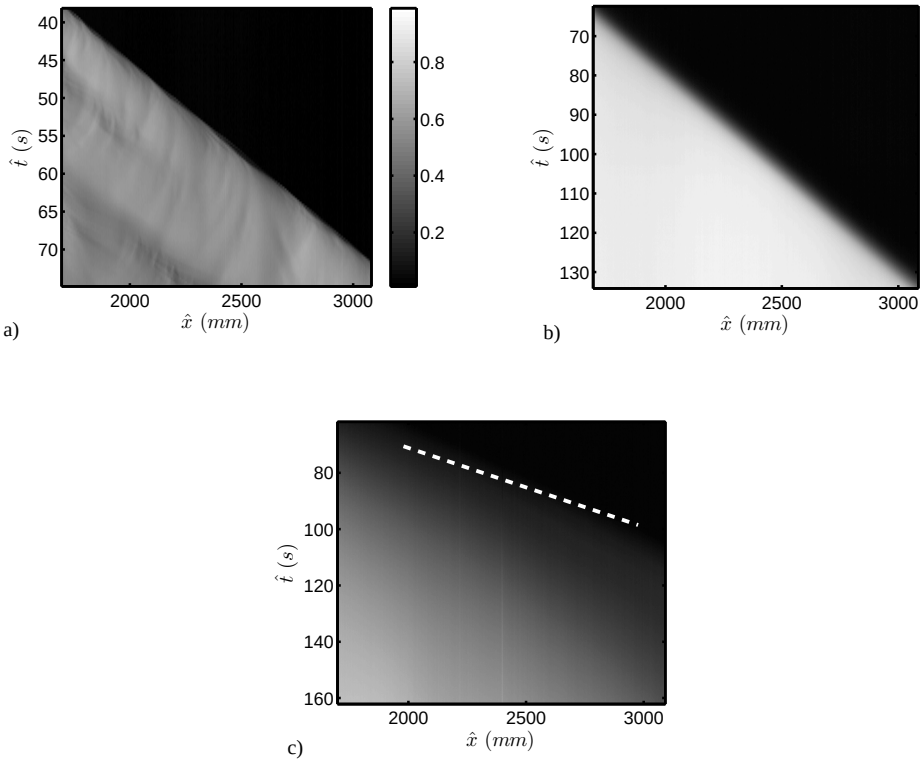

Figure 3.2: a,b) Spatiotemporal diagrams obtained for the same experiments as Figs. 3.1a and 3.1b. Figure 3.2c shows the spatiotemporal diagram of an iso-density experiment ($At = 0$) for $\hat{V}_0 = 16.2$ (mm/s). The dashed-line is an eye guide representing $\hat{V}_f = 2\hat{V}_0$. Note that $\hat{x}$ is the streamwise distance measured from the gate valve and $\hat{t}$ is the time spent after the start of the experiment. The colour bar in Fig. 3.2a refers to all figures and indicates depth-averaged concentration values with 0 indicating pure displaced fluid and 1 indicating pure displacing liquid.

constant in the central part of the pipe (marked by the two broken lines).

Where either $\hat{h}/\hat{D} < 0.15$ or $\hat{h}/\hat{D} > 0.85$ (approximately) the layers of displacing or displaced fluid become thin and visualisation from the side is through the top or bottom of the pipe where curvature is maximal. These wall regions are consequently those most affected by noise in measurement of the averaged concentrations. Even though the behaviour in these wall regions is hard to visualize, it is clear that the bulk of the interface is unaffected

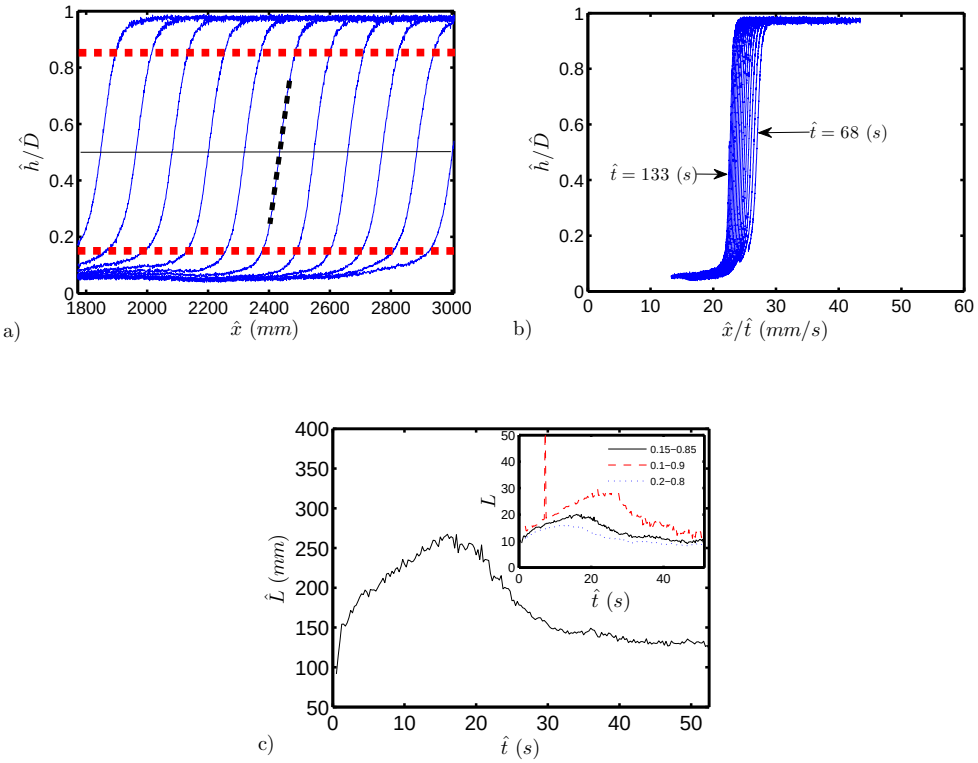

Figure 3.3: a) Experimental profiles of normalized $h(\hat{x}, \hat{t})$ for $\hat{t} = 68,\ 74.5, .., 126.5,\ 133$ (s) for the same experiments as Figs. 3.1b and 3.2b. The dotted lines show $\hat{h}/\hat{D} = 0.85$ and 0.15. The horizontal solid line indicates $\hat{h}/\hat{D} = 0.5$ and the inclined bold dashed line (eye guide) shows the slope of the collapsed curves which stays the same for different profiles. b) collapse of the normalized profiles $\hat{h}/\hat{D}$ with $\hat{x}/\hat{t}$ for the same experiment as part a. c) The evolution of stretch length value, $\hat{L}$, with time for the same experiment as part a. The fully developed stretch length is attained for approximately $\hat{t} > 40$ (s). The inset in part c shows the dependency of the scaled stretch length for different choices of lower and upper bounds of $\hat{h}/\hat{D}$ $(0.15 - 0.85,\ 0.1 - 0.9$ and $0.2 - 0.8)$.

by the wall regions. Indeed the slope of the evolution profiles in the center of the pipe remains constant as they advance. Interestingly, the evolution profiles change curvature at an inflection point around $\hat{h}/\hat{D} = 0.5$, which is the pipe center. The self-similar evolution profiles shown in Fig. 3.3a suggest

that these profiles might collapse onto one curve with an appropriate scaling. Figure 3.3b shows the evolution profiles $\hat{h}/\hat{D}$ plotted against $\hat{x}/\hat{t}$. We can see that the profiles converge to a value $\hat{x}/\hat{t} \approx 22.8$ (mm/s) at large times, (the very left curves in Fig. 3.3b). This value is very close to the mean flow speed, $\hat{V}_0 = 20.9$ (mm/s), suggesting that the interface between displacing and displaced fluids moves at a speed very close to that of the mean flow. Later on we will discuss this and its effect on displacement efficiency in more detail.

We call the streamwise distance between the leading and trailing fronts the *stretch length*, $\hat{L}$. In order to obtain the stretch length in a robust and consistent way from our experiments, we neglect the part of the interface below 15% and above 85% of the pipe's diameter. Figure 3.3c shows the evolution of $\hat{L}$ with time for the same experiment. We can distinguish an initial elongation phase, when the gate valve is opened at the start of the experiment. During this period the mean flow itself accelerates from zero to the set flow rate and we can also expect strong buoyancy effects as the initial interface is perpendicular to the pipe. In the second phase we see a slower relaxation towards a constant length, in this case after about 40 (s). A dimensionless stretch length is defined by scaling $\hat{L}$ with $(0.85 - 0.15)\hat{D}$. The inset in Fig. 3.3c shows the dependency of the scaled stretch length for different choices of lower and upper bounds of $\hat{h}/\hat{D}$ ($0.15-0.85$, $0.1-0.9$ and $0.2 - 0.8$). Note that for scaling each stretch length, $\hat{L}$, the corresponding percentage of the diameter, $\hat{D}$, in each case is naturally used. We see that although the stretch length values are dependent on the choice of diameter filter percentage at short times, they converge into a constant value over longer times when the flow is developed. Basically this is due to the constant slope over the central part of the pipe (Fig. 3.3a). This in turn confirms that the scaled stretch length measurements are not greatly sensitive to the choice of diameter filter percentage, and we stay with 15% and 85% as filter values. From here onward when we use the expression *stretch length*, we mean the longitudinal distance $\hat{L}$ between displacing and displaced fluids measured at any time after opening the gate valve, and will refer to the constant value obtained at long times as the *fully developed stretch length*.

Figure 3.4a plots the range of development times, $\hat{t}_{FD}$, required for the stretch length to become fully developed. We have scaled $\hat{t}_{FD}$ with $\hat{D}/\hat{V}_0$ which is the mean travel time for one diameter. Thus, the vertical axis measures the number of pipe diameters from the gate valve until the flow is fully developed. The length of pipe below the gate valve is roughly 170

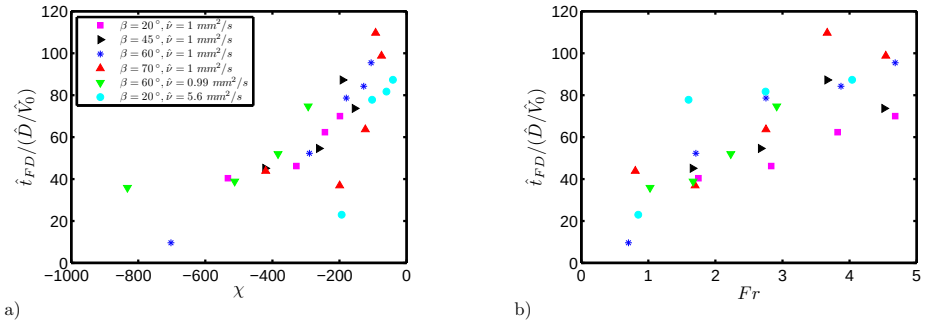

Figure 3.4: The dependency of the dimensionless time taken to reach fully developed flow, t_{FD}, on a) χ and b) Fr. The data in parts a and b correspond to: $\beta = 20\,°, \hat{\nu} = 1$ (mm^2/s) (■), $\beta = 45\,°, \hat{\nu} = 1$ (mm^2/s) (▶), $\beta = 60\,°, \hat{\nu} = 1$ (mm^2/s) (∗), $\beta = 70\,°, \hat{\nu} = 1$ (mm^2/s) (▲), $\beta = 60\,°, \hat{\nu} = 0.99$ (mm^2/s) (▼), $\beta = 20\,°, \hat{\nu} = 5.6$ (mm^2/s) (●).

diameters. The horizontal axis in Fig. 3.4a is the parameter:

$$\chi = \frac{2At\hat{g}\cos\beta\hat{D}^2}{\hat{\nu}\hat{V}_0}, \tag{3.1}$$

which captures the ratio of buoyant forces to viscous forces. We can see that as the magnitude of buoyancy force decreases with respect to the viscous forces ($|\chi| \to 0$), development times increase. Also note that when the ratio of inertial to buoyant forces increases (Fr increases), the dimensional time for a fully developed stretch length increases as well; see Fig. 3.4b. Note that the increasing trend of required time to reach fully developed flow with χ and Fr can be observed for approximately each experimental set shown in Figs. 3.4a and b using different symbols.

In all cases when the stretch length is fully developed we have a leading front velocity that is close to the imposed velocity. Figure 3.5 shows the range of $\hat{V}_f$ vs $\hat{V}_0$ from our experiments. The broken line is the linear fit $\hat{V}_f = 1.04\hat{V}_0$. In this case an average displacement efficiency for all our density stable experiments is $1/1.04 \approx 96\%$. The discrepancy from $\hat{V}_f = \hat{V}_0$ is quite small. Partly this may be attributed to measurement errors (e.g. $\hat{V}_f$ comes from flow visualisation and $\hat{V}_0$ from the flow meter). Partly there may be imperfect displacement in the upper and lower wall regions (thin film effects) and partly we must consider that there is some dispersion.

With regard to dispersion, it is worth reflecting on the consequences

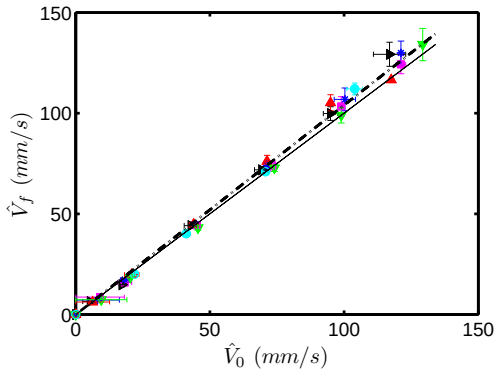

Figure 3.5: Front velocity values, $\hat{V}_f$, plotted against the mean flow velocity, $\hat{V}_0$ for different experiments as in Fig. 3.4. The dash-dotted line is the linear fit $\hat{V}_f = 1.04\hat{V}_0$. In this case an average displacement efficiency for all density stable experiments is $1/1.04 \sim 96\%$. The solid line represents the ideal displacement case with $\hat{V}_f = \hat{V}_0$.

of steadily advancing leading and trailing fronts with $\hat{V}_f \approx \hat{V}_0$ and steady stretch length. Both far upstream and downstream of the front, the flows adopts a Poiseuille profile but the frontal region advances uniformly. Globally speaking, this means that the centreline fluid behind the front must decelerate and move towards the walls. In advance of the front, the fluid close to the walls is pushed towards the centreline and accelerates forward. Thus, there is a net counter-current flow in the radial direction for any steadily moving front. For large Péclet number miscible displacements, significant diffusion only occurs close to sharp gradients in fluid concentration. However, now we have significant secondary flows on both sides of the front that can advect diffused mixture away from the frontal region. One consequence is that although the averaged concentration profiles can propagate apparently steadily (e.g. Fig. 3.3a) the fluid concentration in the frontal region can become diffuse (e.g. Fig. 3.1b).

A second consequence of the secondary flows described above is that there must exist recirculatory zones in the streamlines, as considered in a moving frame of reference. Thus, although the flow may become parallel far from the frontal region, close to the front it is multi-dimensional and the secondary flow velocity scale is evidently $\hat{V}_0$. This means that inertial effects

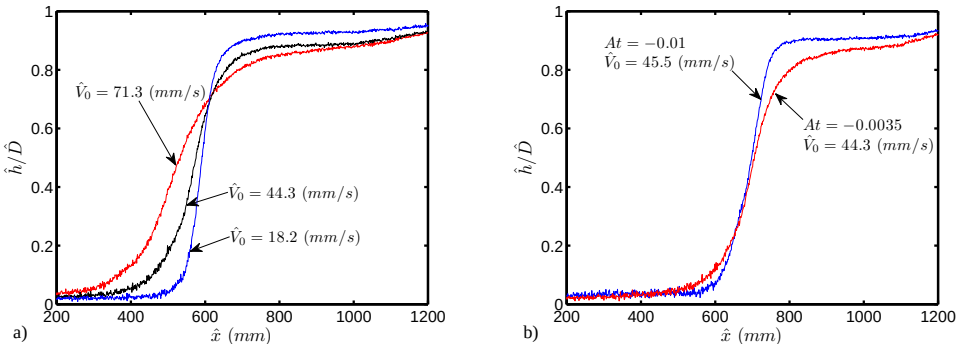

Figure 3.6: Experimental profiles of $\hat{h}(\hat{x},\hat{t})/\hat{D}$ at different times but at around the same position in the pipe for $\beta = 60\,^\circ$ and $\hat{\nu} = 1$ (mm^2/s); a) $At = -0.0035$ different $\hat{V}_0$; b) similar $\hat{V}_0$ and different $At < 0$. All experiments are density stable.

are always present in the frontal region, whenever $Re > 1$, which is for all our experiments.

3.2.3 Parametric variation in the fully developed stretch length

We now explore the sensitivity of the fully developed stretch length to our experimental variables: At, β, $\hat{V}_0$ and $\hat{\nu}$. Figure 3.6a shows the profiles of normalized $\hat{h}/\hat{D}$ for density stable displacements at different $\hat{V}_0$, with fixed $\beta = 60\,^\circ$, $\hat{\nu} = 1$ (mm^2/s) and $At = -0.0035$. An increase in density difference decreases the fully developed stretch length. Figure 3.6b shows the effect of the density difference (At) on the length of the interface for two otherwise similar cases ($\hat{V}_0$ values are also very close together). While the second of these is perhaps intuitive, the effect of increasing mean velocity is less obvious. One explanation, that we reinforce later below, is that the stretch length is controlled by the ratio of axial buoyancy forces to viscous stresses, $|\chi|$. As we increase the flow rate ($\hat{V}_0$) this ratio is reduced allowing the interface to spread more. Note too that we have seen that the development times $\hat{t}_{FD}$ also increase as $|\chi|$ decreases.

We note in Fig. 3.6 that the profiles $\hat{h}/\hat{D}$ are measured when the stretch length is fully developed. There is a degree of asymmetry that appears to increase with both $\hat{V}_0$ and $|At|$. Partly this may be due to asymmetry in the wall regions at top and bottom, i.e. the top is an advancing film and

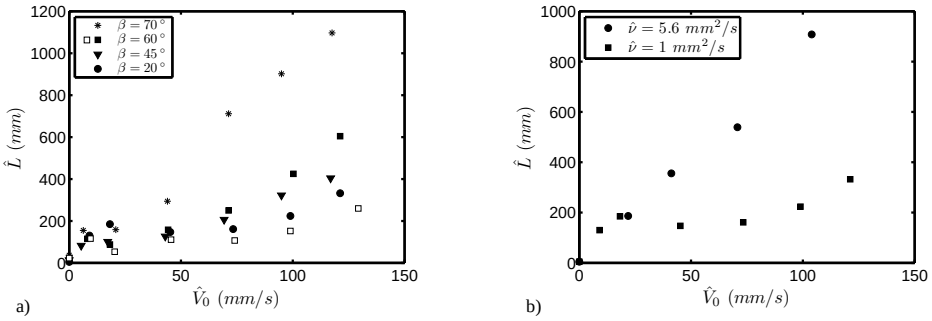

Figure 3.7: a) Variations in dimensional stretch length $\hat{L}$, for different β and $\hat{V}_0$. The solid symbols are for $At = -0.0035$ and the open symbols for $At = -0.01$. Note that $\hat{\nu} = 1$ (mm^2/s). b) Dimensional stretch length $\hat{L}$ versus V_0 for two different dynamic viscosities at fixed $At = -0.0035$ and $\beta = 20\,°$.

the bottom is a draining film. This may also be related to the pattern of secondary flows and dispersion being non-uniform across the pipe depth. It is hard to develop simplistic models that will give an interface shape prediction (e.g. by assuming a Poiseuille flow), since in the interfacial region the velocity field is far from a Poiseuille flow.

Figures 3.7a and b show the effects of inclination angle, mean flow speed, density difference and fluid viscosities on the fully developed stretch length. Figure 3.7a shows results for $At = -0.0035$ and $At = -0.01$. As we approach a horizontal configuration the stretch length increases. The trend shown in this figure suggests that as we move towards strictly vertical pipe the stretch length should become very small, which is also observed. Figure 3.8 shows snapshots of the flows for a series of strictly vertical experiments. The parameters used are $\beta = 0\,°$, $\hat{\nu} = 1$ (mm^2/s), $At = -0.0035$ and $\hat{V}_0 = 18.2,\ 48.1$ and 70.6 (mm/s). Due to the symmetric Poiseuille profile, advective velocity effects act to disperse the light displacing fluid ahead of the mean flow in the pipe centre. This dispersive effect is balanced by the stabilizing density difference between the fluids, preventing the interface from elongating noticeably: the stretch length remains very small (close to zero). We see that the interface between the fluids flattens out with a small *cap* region advancing in front of the pure displacing fluid. This *cap* region could either be due to fluid mixing or could be a visual effect due to a film of displaced fluid remaining on the wall. In any case the length

of cap region reduces as the mean flow is increased, suggesting that the residual film is more likely. Ahead of the cap and quite faint in these figures is dispersed spike-like region of mixed fluid (mostly displaced fluid), which we have outlined for clarity. These regions are formed during the initial phase of mixing after opening the gate valve, but they may also be "fed" by a small amount of diffusion/dispersion, from the tip of the front as the flow progresses. This diffuse mixed region disperses further ahead of the cap region with increasing mean flow, as is expected. These effects are interesting in their own right, but this has not been the focus of our study. The main practical conclusion is that the fully developed stretch length is small for vertical pipes. More details on vertical displacement flows in ducts can be found in [27, 81, 93, 109]. Where experiments have been performed they have typically been performed with more viscous fluids and at lower Reynolds numbers than here.

To investigate the effect of viscosity (note we are still interested in iso-viscous displacements) we have run comparison experiments at higher viscosity, obtained with a 54 weight-percent glycerine-water solution with $\hat{\nu} \sim 5.6$ (mm^2/s). Figure 3.7b shows that when the fluids become more viscous the stretch length also increases. A few experiments were run with an even higher glycerine concentration (72 percent (wt/wt)) with $\hat{\nu} \sim 18.6$ (mm^2/s). It was observed that the stretch length was much longer than the length of our apparatus (results are not presented here). In these experiments the trailing front did not appear to move at all from the gate valve over the duration of the experiment.

The increase in viscosity exposed a difference in qualitative behaviour of the displacement front near the top and bottom of the pipe. The leading front displaces immediately and keeps moving, stretching the interface. We postulate that the trailing front requires a critical stretching $\hat{L}$ before it begins to move. Presumably the angle of the interface contributes to a force balance in which buoyancy forces are opposed by viscous forces (hence the elongation with increased viscosity). Once the trailing front is moving it does so at approximately the same speed as the imposed flow, and we may measure $\hat{V}_f \approx \hat{V}_0$ from spatiotemporal plots such as Fig. 3.2b. In this case the displacement is very efficient (close to 100 percent); see Fig. 3.5. Note that although this suggests a viscous:buoyancy balance, if we were to develop a lubrication model such as in [128], this would predict that the interface is continually stretched: advancing at the upper wall while pinned at the lower wall.

Our results suggested that the fully developed stretch length is governed primarily by a balance between axial buoyancy forces and viscous stresses

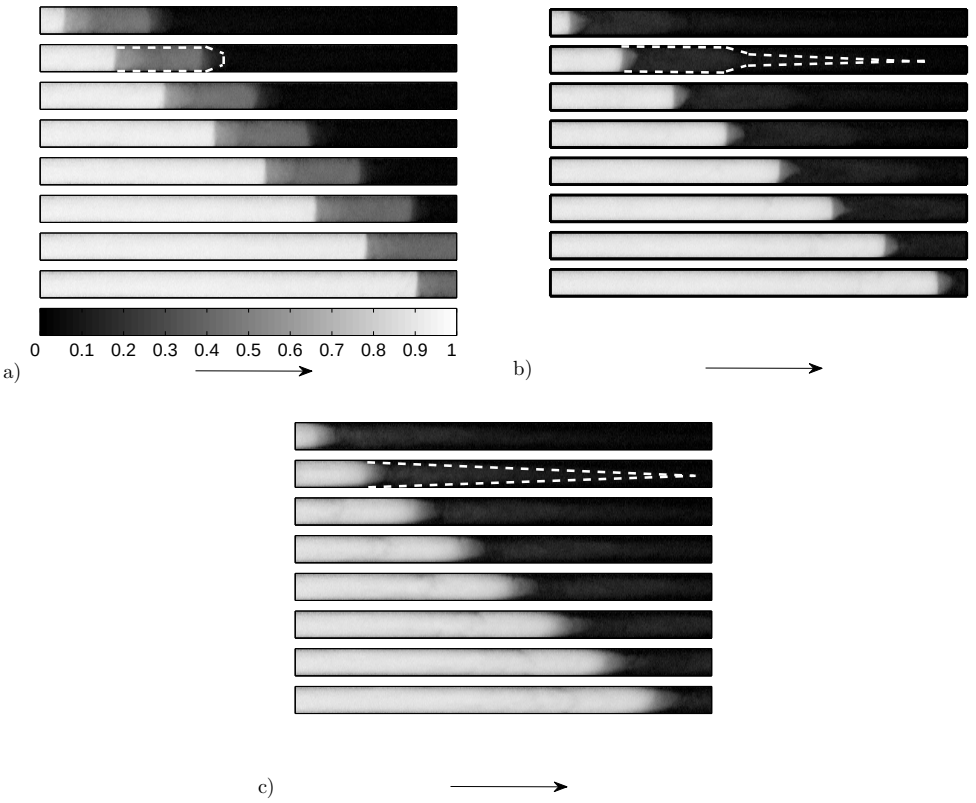

Figure 3.8: Snapshots of the vertical displacement flow experiment, $\beta = 0\,^{\circ}$, carried for $\hat{\nu} = 1$ (mm^2/s), $At = -0.0035$ and a) $\hat{V}_0 = 18.2$ (mm/s) b) $\hat{V}_0 = 48.1$ (mm/s) and c) $\hat{V}_0 = 70.6$ (mm/s). The sequence for part a starts 30.75 (s) after opening the gate valve and the time interval between images is 5 (s). For parts b and c the sequences start 80.75 (s) and 19.5 (s) after opening the gate valve and the time intervals between images are 2 (s) and 1.25 (s) respectively. The arrow indicates the flow direction and the left end of the pipe is higher than the right (the fluid flows vertically downhill). The field of view is 700×19 (mm^2), taken 1550 (mm) below the gate valve. The last image at the bottom of Fig. a is the colourbar of the concentration values and can be used for Figs. b and c too. The white dashed lines in Figs. a-c are eye-guide and indicate the boundaries of the mixed region moving upfront.

(originating from the mean flow). This balance is captured in the parameter $\chi = 2At\hat{g}\cos\beta\hat{D}^2/(\hat{\nu}\hat{V}_0)$. Since our stretch length values are calculated between $\hat{h}/\hat{D} = 0.15$ and $\hat{h}/\hat{D} = 0.85$ we subtract off the hydrostatic stretch

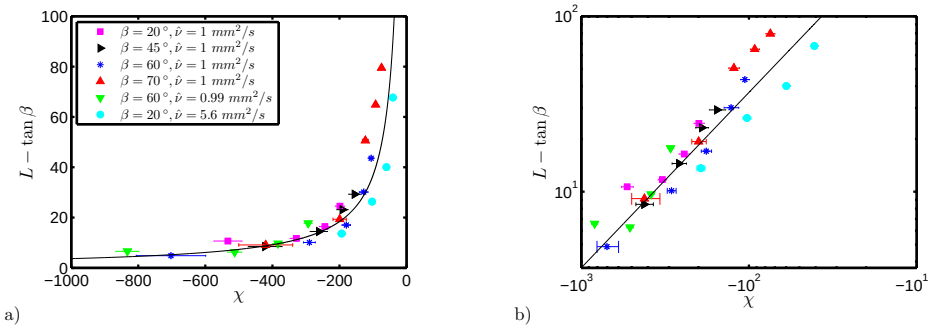

Figure 3.9: a) Experimental dimensionless stretch length values L, plotted against χ. The solid line is $L - \tan\beta = -3680/\chi$; b) the same data plotted in log-log scale. The data in parts a and b correspond to: $\beta = 20\,°, \hat{\nu} = 1$ (mm^2/s) (■), $\beta = 45\,°, \hat{\nu} = 1$ (mm^2/s) (▶), $\beta = 60\,°, \hat{\nu} = 1$ (mm^2/s) (∗), $\beta = 70\,°, \hat{\nu} = 1$ (mm^2/s) (▲), $\beta = 60\,°, \hat{\nu} = 0.99$ (mm^2/s) (▼), $\beta = 20\,°, \hat{\nu} = 5.6$ (mm^2/s) (●).

length ($0.7\hat{D}\tan\beta$) from $\hat{L}$ and normalize with $0.7\hat{D}$. Figure 3.9 plots the normalized fully developed stretch length against χ for our data, in linear and log scales. It appears that the data collapse well onto a single curve regardless of β, At and $\hat{\nu}$. Horizontal error bars for χ are shown. Vertical error bars are negligible. A model curve is fitted to the experimental data of the form

$$L - \tan\beta = -3680/\chi. \tag{3.2}$$

This in itself is interesting since our flows are performed at a range of non-trivial Re and the occurrence of secondary flows about a steadily advancing frontal region means that inertial effects are always present close to the advancing front. Note that only the data for $\beta \geq 20°$ has been used to fit (3.2). As discussed above, the stretch length in a vertical pipe is observed to be of the order of the diameter and consequently negligible. The expression (3.2) at $\beta = 0\,°$ is not singular, but indicates a stretch length larger than that observed and one that is strongly dependent on χ. This represents an extrapolation of (3.2) outside the range of the data used to make the curve fit. It is unclear how far below $\beta = 20°$ this expression will be valid.

By choosing $0.7\hat{D}$ as the scale for dimensional stretch length values, $\hat{L}$, one can now re-scale $L - \tan\beta = -3680/\chi$ with the full diameter value, $\hat{D}$, and calculate a predicted stretch length value over the whole pipe (not only over 70% of the pipe). In rescaling (3.2) in this way we effectively

assume that the interface evolution profiles (e.g. Fig. 3.3) extend *linearly* up to the point where they intersect with the pipe walls. This gives a closer prediction of the stretch length in the pipe. It is also worth noting that for the 72 percent (wt/wt) glycerine-water experiments in which the stretch length could not be measured within our apparatus, $\chi \approx -14$, for which the fitted model predicts a stretch length on the order of 5 (m), exceeding the length of our apparatus. This is precisely what we observed.

3.3 Discussion points

Laminar displacement flow of two miscible iso-viscous Newtonian fluids in an inclined pipe has been investigated experimentally in the case where the displacing fluid is less dense than the displaced fluid (i.e. density stable). Our experiments have covered a broad range of the governing dimensionless parameter space (β, Re, Fr).

The practical importance of our study is in predicting the displacement efficiency, which is quantified by the ratio $\hat{V}_0/\hat{V}_f$. We have demonstrated that there is an interesting transition in $\hat{V}_0/\hat{V}_f$ as the At changes from positive (density unstable) to negative (density stable). For $At > 0$ previous work shows that efficiencies are significantly < 1. As At decreases towards zero $\hat{V}_0/\hat{V}_f$ reduces further, bounded below by the theoretical $\hat{V}_0/\hat{V}_f = 0.5$ of passive scalar advection. However, for $At < 0$ the efficiency $\hat{V}_0/\hat{V}_f$ increases sharply to a value close to 1. Remarkably, this transition shows order 1 changes in $\hat{V}_0/\hat{V}_f$ over a very small range of At (corresponding to 0.7% density difference).

In the density stable range of our experiments ($At < 0$), our data is approximated well by the linear fit: $\hat{V}_f = 1.04\hat{V}_0$, suggesting an efficiency of around 96%. We expect that the displacement is never 100% efficient due to a very thin residual lower layer of the displaced fluid, and possible dispersion of diffused mixture in the frontal region.

At the start of a typical density stable experiment the trailing front remains stationary while the leading front advances, stretching the interface. On attaining a critical length the trailing front also moves, at approximately the same speed as the mean flow. The length of the interface along the pipe has been called the stretch length, $\hat{L}$. We have characterised the time taken for the stretch length to become constant in time, and portrayed this in terms of a development length. This development time increases with the mean imposed velocity and decreases with the axial buoyancy force.

The fully developed stretch length increases with the mean flow velocity,

decreases with the density difference, increases with inclination from vertical and increases with fluid viscosity. Our data is well represented by the scaled expression $L - \tan\beta = -3680/\chi$, where $\chi = 2At\hat{g}\hat{D}^2\cos\beta/(\hat{\nu}\hat{V}_0)$. This implies that stretch length is primarily due to a balance between axial buoyancy forces and viscous stresses from the mean flow. This in itself is interesting since our flows are performed at a range of non-trivial Re and the occurrence of secondary flows about a steadily advancing frontal region means that inertial effects are always present close to the advancing front.

Future experimental work on density stable displacement flows should focus on the effects of a viscosity ratio between two Newtonian fluids and on examining shear-thinning effects in these flows. It would also be of interest to derive a simple predictive model that produces the observed dominant dependence of the stretch length on χ, but apparent insensitivity to inertial effects.

Chapter 4

Miscible density unstable displacement flows in an inclined pipe

In the previous chapter the experimental results of density stable laminar miscible displacement flow of two iso-viscous Newtonian fluids in an inclined pipe were presented. In this chapter[3] everything stays the same except that we are now interested to see how the displacement flow is affected if the displacing fluid switched to the heavier fluid i.e. density unstable configuration. By density unstable we mean that the denser fluid displaces the lighter fluid as the fluids are pumped in the downwards direction.

Our experiments are performed in a long pipe (approximately 200 diameters), but at flow rates for which the Péclet number is significantly larger than the ratio of length to diameter. In this regime, although the fluids are miscible, they do not have time to mix over experimental timescales in the absence of hydrodynamic effects, (which are present here). Our study represents a continuation of our previous work on density unstable displacement flows; see [126, 128–130], which has been primarily focused at flows in ducts that are close to horizontal ($\beta \approx 90^\circ$). At large inclinations stratified viscous regimes are a dominant flow feature, but at lower inclinations inertial effects become increasingly significant, eventually resulting in instability and effective transverse mixing. Thus, inertial transitionary and fully diffusive regimes occur.

It was shown in chapter 3 that the density stable configuration produces highly efficient displacements, with the bulk of the *interface* moving steadily at the mean velocity. As mentioned earlier in chapter 3, by interface we mean a point or points at a streamwise location where the concentration gradient transversely is high and the two fluids meet and interact. Since we are in

[3] A version of this chapter has been accepted for publication in Phys. Fluids: **K. Alba**, S.M. Taghavi and I.A. Frigaard. *Miscible density unstable displacement flows in inclined tube.*

large Péclet number regime we can assume that the interface between the two fluids stays sharp at least when there is not a strong mixing present. The streamwise length of the stretched interface, $\hat{L}$, was measured over a wide range of parameters. As will be seen in the current chapter there is no such steadily moving interface in the case of density unstable flows. In fact the dominant flow pattern is *slumping* in this case which is completely different than the beaviour observed in density stable flows.

The significant novel contributions of this chapter are as follows. Firstly, we know of no other experimental or numerical study of miscible displacement flow in pipes (non-zero imposed mean flow velocity, $\hat{V}_0$) that covers a broad range of pipe inclinations in the density unstable configuration. Secondly, we classify the different flow regimes observed in terms of measurements of the advancing front velocity and the degree of diffusive mixing. Thirdly, we develop simple dimensionless relations that approximate two important flow characteristics: namely the front velocity and the macroscopic diffusion coefficient.

For a brief outline of this chapter, below in §4.1 we introduce the experimental setup. In presenting our results we first benchmark against existing exchange flow results for $\hat{V}_0 = 0$ (§4.2.1) and then (§4.2.2) discuss the main qualitative features of the displacement flows; i.e. $\hat{V}_0 > 0$. Front velocities and macroscopic diffusion are studied in §4.2.3 and §4.2.4, respectively. We give a quantitative characterisation of the different flow regimes in §4.3 and the chapter closes with a brief summary (§4.4).

4.1 Experiments and parameters range

Our experiments have been carried out in a 4-meter two-fluid flow loop capable of being tilted at any angle between horizontal and vertical via ball-screw jack; see appendix A for details. The flow loop consists of a a transparent acrylic pipe (diameter $\hat{D} = 19.05$ (mm)) mounted within two *fish tanks* to reduce the refraction errors and improve image quality. The pipe is divided into two parts, separated initially by an automated gate valve: 80 (cm) in the upper part and 320 (cm) in the lower part.

In an experiment the two fluids (both water) are initially filled above and below the gate valve. We add black dye (ink) to the displaced fluid in order to measure concentration via optical absorption. At the start of the experiment the gate valve is opened and the flow is driven by an over-pressure (≈ 70 (kPa) gauge pressure) applied by compressed air to a pressurized tank containing the displacing fluid. This ensures a smooth steady inflow. The

Parameter	Range
$\hat{V}_0$	$0 - 130$ (mm/s)
$\hat{\nu}$	1 (mm^2/s)
At	0.001, 0.0035, 0.004, 0.01, 0.08
β	0, 10, 20, 30, 45, 60, 70, 85 (deg)
Re	$0 - 2400$
Fr	$0 - 9$

Table 4.1: Parameter range of Newtonian density unstable experiments. Note that most of the experiments were run for $At = 0.001,\ 0.0035$ and 0.01.

flow rate, $\hat{Q} = \pi \hat{D}^2 \hat{V}_0/4$, is regulated by adjusting a needle valve located before the drain.

A dimensional analysis of the flow suggests that 5 dimensional parameters may govern the flow; see [126]. We denote the density of the displacing fluid by $\hat{\rho}_H$ and that of the displaced fluid by $\hat{\rho}_L$. The Atwood number is defined as $At = (\hat{\rho}_H - \hat{\rho}_L)/(\hat{\rho}_H + \hat{\rho}_L)$, representing a dimensionless density difference. For this study $At > 0$ since $\hat{\rho}_H > \hat{\rho}_L$. Our experiments are all performed for small At, the significance of which is that a Boussinesq approximation is valid. Briefly, this means that density differences can significantly affect buoyancy forces, captured by the densimetric Froude number, $Fr = \hat{V}_0/\sqrt{At\hat{g}\hat{D}}$, but not the acceleration of individual fluids. Here $\hat{g}$ is the gravitational acceleration and $\hat{V}_0$ is the mean imposed velocity. A third dimensionless parameter is the pipe inclination, β, measured from vertical. A fourth dimensionless parameter is the Reynolds number $Re = \hat{V}_0\hat{D}/\hat{\nu}$, where $\hat{\nu}$ is defined using the mean density $\hat{\rho} = (\hat{\rho}_L + \hat{\rho}_H)/2$ and the common viscosity of the two fluids, $\hat{\mu}$. Finally, since our fluids are miscible there is the potential for the Péclet number $Pe = \hat{V}_0\hat{D}/\hat{D}_m$ to influence the flow (here $\hat{D}_m$ is the molecular diffusivity). Typically, for the range of flow rates in our pipe we have $Pe \gg 1$. This suggests that on the timescale of interest, molecular diffusivity does not play a major role in the flows studied. In a typical experimental sequence we would fix the pipe inclination and Atwood number and then run a number of experiments at increasing fixed flow rates. The range of dimensionless and dimensional parameters is shown in Table 4.1. The 3 most relevant dimensionless parameters are β, Re and Fr, (providing $At \ll 1$ and $Pe \gg 1$). We see that we are able to cover a wide range of β, Re and Fr with our experiments.

4.2 Results

We now present our experimental results. First, in §4.2.1 we benchmark against existing exchange flow results ($\hat{V}_0 = 0$). We then give a broad phenomenological description of the main features we have observed in our displacement flow experiments ($\hat{V}_0 > 0$); see §4.2.2. We study variations in measured front velocity in §4.2.3. For those experiments dominated by strong transverse mixing we analyse the effective bulk axial diffusivity (or dispersivity), from measured concentration profiles (§4.2.4). In §4.3 we classify the flow regimes observed, approximating the boundaries in terms of (Re, Fr, β). We also give leading order approximations to the front velocity and bulk axial diffusivity.

4.2.1 Exchange flows

Seon *et al.* [113] used a LIF technique to visualize exchange flow patterns. They found the fluid layers well stratified with some slight mixing at the interface due to Kelvin-Helmholtz instabilities for near-horizontal angles. For near-vertical pipes the strong buoyancy component in the axial direction induces a back-flow which in turn yields to a mix of Rayleigh-Taylor and Kelvin-Helmholtz type instabilities, resulting in effective transverse mixing. These two regimes are separated at intermediate angles (and At) by flow patterns somewhere between strongly segregated and fully mixed, in which there is significant interfacial mixing, but also unbroken streams of pure fluid remain. In [112], Seon *et al.* characterized their results and analysis in terms of two dimensional velocities:

$$\hat{V}_\nu = \frac{At\hat{g}\hat{D}^2}{\hat{\nu}}, \qquad \hat{V}_t = \sqrt{At\hat{g}\hat{D}}, \tag{4.1}$$

representing velocity scales for which viscous and inertial stresses balance buoyancy, respectively. Seon *et al.* measured the front velocity $\hat{V}_f$ in the different regimes and found that for an intermediate range of inclination angles the dimensionless ratio $\hat{V}_f/\hat{V}_t$ attained a constant plateau, $\hat{V}_f/\hat{V}_t = 0.7$. The front velocity deviates from this line at high inclinations, where viscous effects dominate, and at small inclinations where the flow becomes fully diffusive.

Figure 4.1 shows the dimensionless experimental front velocity measured in our experiments (with $\hat{V}_0 = 0$) scaled with $\hat{V}_\nu \cos\beta$, plotted against $\hat{V}_\nu \cos\beta/\hat{V}_t$; *c.f.* Fig. 4 in [112]. The solid line in the figure is $\hat{V}_f/\hat{V}_t = 0.7$. We have also plotted data from [112] for the same At. The agreement between the two studies is clear. The data coincide both in terms of attaining

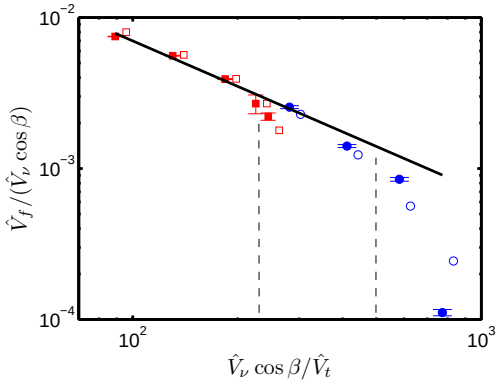

Figure 4.1: Comparison of the experimental front velocity values for the exchange flow (solid data) with the data reported by Seon *et al.* [112] (open data). The solid line shows $\hat{V}_f/\hat{V}_t = 0.7$ [112]. Squares correspond to $At = 0.001$ and circles to $At = 0.01$. Inclination angle, β varies between 20° and 70° in the experiments shown. The dashed lines show the limit of $\hat{V}_\nu \cos\beta/\hat{V}_t$ above which the exchange front velocity values deviate from $\hat{V}_f/\hat{V}_t = 0.7$, for corresponding At ($\hat{V}_\nu \cos\beta/\hat{V}_t \approx 230,\ 500$ for $At = 0.001$ and $At = 0.01$ respectively).

the plateau values and in terms of the point of deviation from the plateau (transition to fully mixed regime). This occurs at $\hat{V}_\nu \cos\beta/\hat{V}_t \approx 230$ for $At = 0.001$ and at $\hat{V}_\nu \cos\beta/\hat{V}_t \approx 500$ for $At = 0.01$.

4.2.2 Displacement flows: main qualitative features

We first address the most basic question: namely is the global qualitative behaviour observed for exchange flows ($\hat{V}_0 = 0$) significantly affected by introducing the mean flow ($\hat{V}_0 > 0$). Figure 4.2 shows typical results from our experiments, primarily illustrating the effect of inclination angle β on the flow pattern. The snapshots of the experiments shown in Fig. 4.2 are calibrated so that the color varies between 0 (displaced fluid) and 1 (displacing fluid), thus illustrating the concentration of displaced fluid. The data shown are obtained for $At = 0.0035$ and kinematic viscosity $\hat{\nu} = 1$ (mm^2/s), all with a mean imposed velocity in the range $\hat{V}_0 \in [29, 47]$ (mm/s). This figure suggests that the same overall behaviour is observed as for the exchange flows. For a given mean flow ($\hat{V}_0$) the degree of mixing and disorder in the

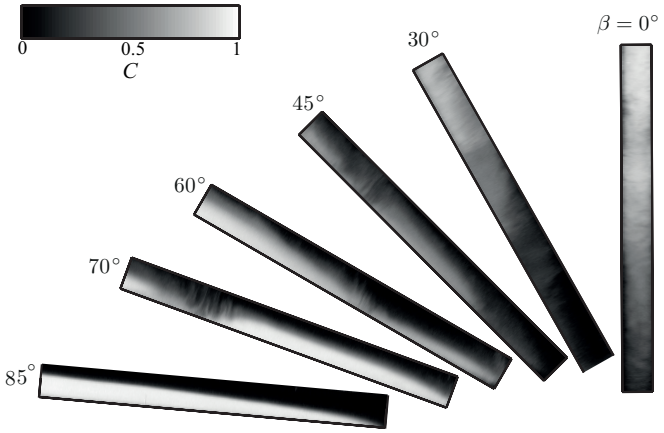

Figure 4.2: Change in iso-viscous displacement mixing with β for $At = 0.0035$ and kinematic viscosity $\hat{\nu} = 1$ (mm^2/s). Mean flow speed is $\hat{V}_0 \in [29, 47]$ (mm/s) (see Fig. 4.3). The field of view is 1330×19 (mm^2) located 1740 (mm) downstream of the gate valve. The color bar at the top left of the figure shows the corresponding concentration value, C, with 0 referring to the pure displaced fluid and 1 to the pure displacing fluid.

system increases as we move towards the vertical ($\beta \to 0°$). The flow pattern for more horizontal inclinations than shown remains qualitatively similar to that for $\beta = 85°$, i.e. viscous flow of two separated layers; see [126].

Figure 4.3 shows the spatiotemporal diagrams of the depth-averaged concentration fields for the same experiments as shown in Fig. 4.2. The depth-averaged concentration value $C(x, t)$ is simply the mean value of the fluid concentration averaged across the pipe at location $\hat{x}$ and time $\hat{t}$ and can be used to estimate the degree of mixing inside the pipe. As can be seen in Figs. 4.3a-f the flow stability increases as we move toward nearly horizontal inclinations. In principle we could extract statistical data on the wavelengths and growth rates of the instabilities from this data, but this is not the aim of the present study. When the degree of mixing is high it is difficult to distinguish the front between two fluids (Figs. 4.3a and b). However, when the fluids become more separated the location of advancing displacement front can be recognized clearly (Figs. 4.3c-f). The inverse slope of the line bounding the black region in the spatiotemporal diagram is minus the front velocity (see the dashed line in Fig. 4.3f). This boundary can be obtained through standard image processing methods when the boundary is clear (e.g. Fig. 4.3f), but when the boundary between displacing and

displaced fluid concentrations is unclear in the spatiotemporal diagram, the front velocity needs to be measured more carefully (as we discuss later in §4.2.3).

To gain additional insight into the flow dynamics we measured the velocity profile 150 (cm) downstream of the gate valve using an ultrasonic Doppler velocimeter DOP2000 (model 2125, Signal Processing SA). For the tracer, we used polyamid seeding particles with a mean particle diameter of 50 μm with volumetric concentration equal to 0.2 g/l in the both fluids. The UDV technique suits our experimental needs well since it does not require a transparent medium. The measuring volume has a cylindrical shape, with axial resolution in our fluids of about 0.375 (mm) and the lateral resolution is equal to the transducer diameter (5 (mm)), slightly varying with depth. The UDV probe was mounted at an angle $\approx 76^\circ$ relative to the axis of the pipe, selected to balance a good signal to noise ratio with a small ultrasonic signal reflections; see [22]. The method is non-intrusive as the probe is mounted outside the pipe, with the ultrasonic beam entering the fluid by passing through a 3.175 (mm)-thick plexiglass pipe wall. The method measures the flow velocity projection on the ultrasound beam: essentially giving the axial velocity. Reflection effects at the lower wall of the pipe make it hard to measure a zero velocity at the lower wall. Figure 4.4 shows characteristic velocities for the three different flow patterns we have observed. First, Fig. 4.4a shows the velocity profile across the channel at different times for a flow that mixes fully across the pipe. After mixing initially, the measured velocity profile appears to be close to a Poiseuille profile, which may be because the two fluids become a mixture with a density very close to the average density of the two fluids. The second regime is where there is significant mixing at the interface but it is not strong enough to completely break/mix the pure fluid layers. Some of the characteristic of such flows are puffs and waves appearing at the interface that get convected towards downstream/upstream depending on how strong the mean flow force is with respect to the buoyancy.

Figure 4.4b shows the UDV profile of such a flow obtained at $\beta = 60^\circ$. Positive high speed velocity regions adjacent to the lower wall are accompanied by strong negative velocity regions towards the upper layer (due to incompressibility). The third regime is where interfacial instabilities are weak in the system and the flow layers are basically separated at the interface by buoyancy forces. A typical velocity profile for this regime is given in Fig. 4.4c for $\beta = 85^\circ$. It is common to observe negative values of the velocity close to the top wall (back flow) where the lighter fluid exists and positive values close to the lower part of the pipe where the heavier fluid

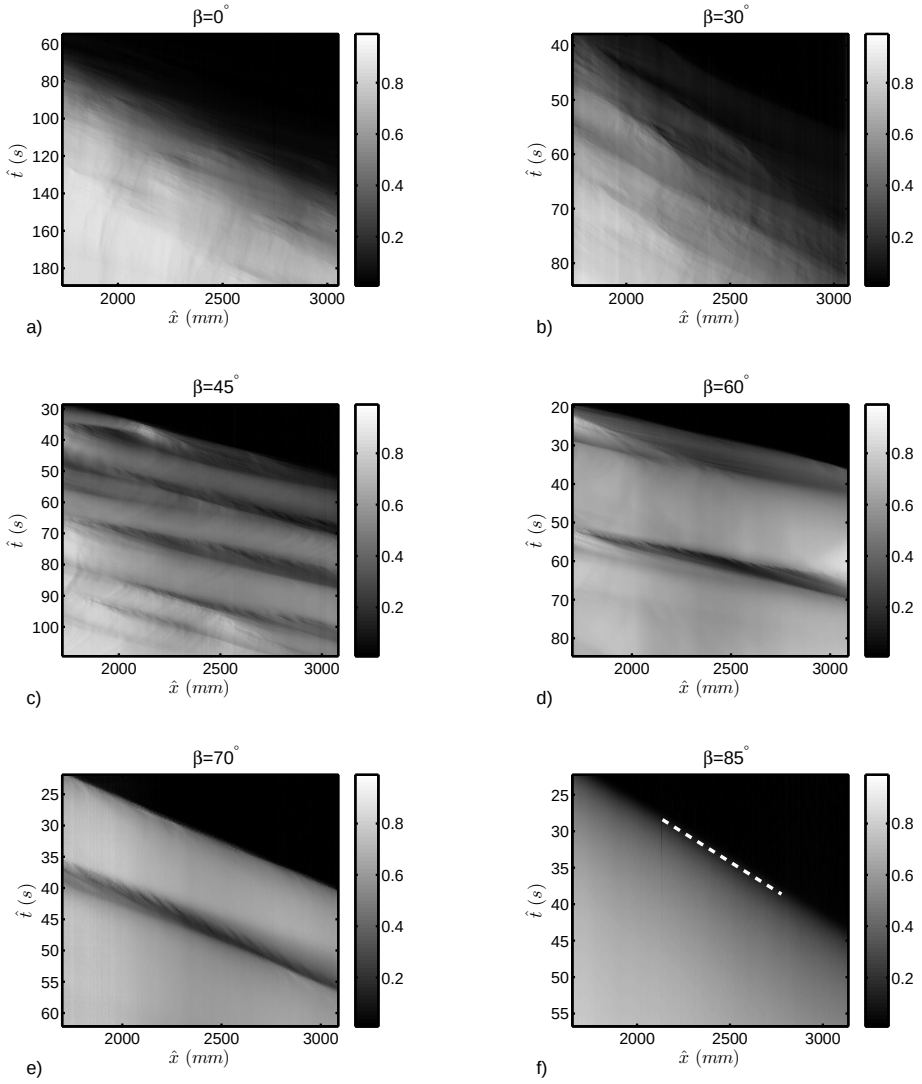

Figure 4.3: Spatiotemporal diagrams of depth-averaged concentration field, for the same experiments as shown in Fig. 4.2: a) $\beta = 0°$, $\hat{V}_0 = 32$ (mm/s); b) $\beta = 30°$, $\hat{V}_0 = 29$ (mm/s); c) $\beta = 45°$, $\hat{V}_0 = 32$ (mm/s); d) $\beta = 60°$, $\hat{V}_0 = 47$ (mm/s); e) $\beta = 70°$, $\hat{V}_0 = 43$ (mm/s); f) $\beta = 85°$, $\hat{V}_0 = 43$ (mm/s). The dashed line line in part f indicates the position of the displacing front and its slope is $-1/\hat{V}_f$. The spatiotemporal diagram gives a front speed $\hat{V}_f = 64$ (mm/s).

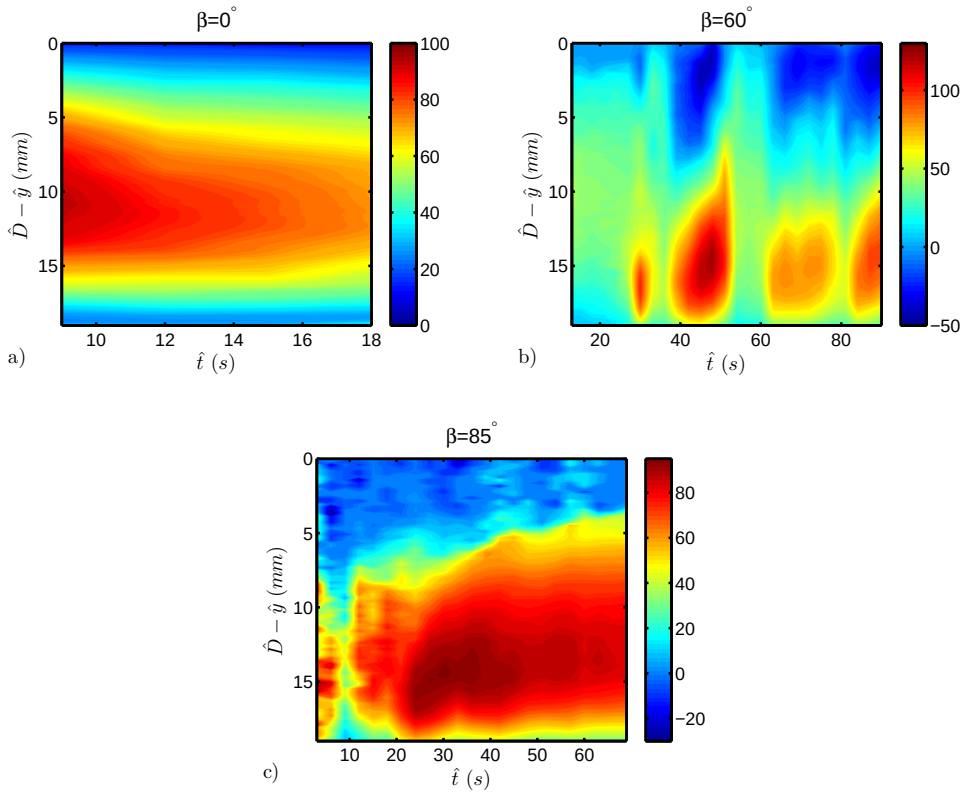

Figure 4.4: Ultrasound Doppler Velocimetry (UDV) measurements obtained for $At = 0.004$, $\hat{\nu} = 1$ (mm^2/s) and a) $\beta = 0°$, $\hat{V}_0 = 44$ (mm/s) b) $\beta = 60°$, $\hat{V}_0 = 20$ (mm/s) and c) $\beta = 85°$, $\hat{V}_0 = 46$ (mm/s).

flows. Note that the current UDV results only depict the streamwise velocity components.

4.2.3 Front velocity measurement and characteristics

In a long pipe, the ratio of the mean flow speed to the leading front velocity, $\hat{V}_0/\hat{V}_f$, indicates the proportion of the pipe displaced in an experiment, i.e. the displacement efficiency. Consequently, it becomes important to measure $\hat{V}_f$ in a consistent and repeatable way, regardless of the degree of mixing. Whereas edge detection and calculation of the slope from the spatiotemporal diagram has proven effective in our previous work, at pipe inclinations close to horizontal (see [126]), strong transverse mixing such as in Fig. 4.2 (Figs. 4.3a & b) makes this method less reliable. Figure 4.5a

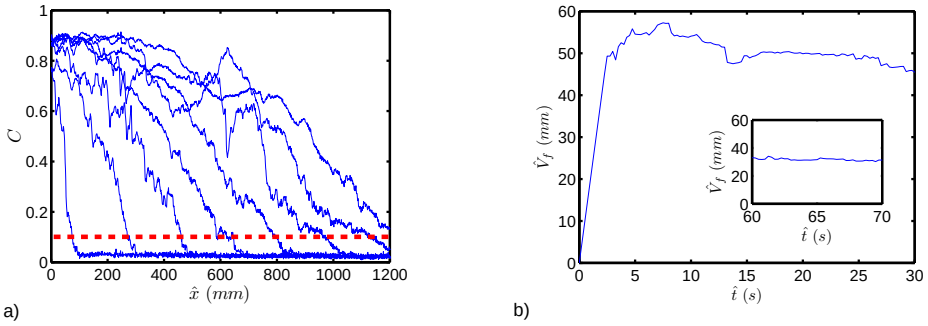

Figure 4.5: a) Evolution of the depth-averaged concentration field, C, with time, $\hat{t} = [2, 7, 12, ..., 32]$ (s), and streamwise location, $\hat{x}$, measured form the gate valve for the same experiment as in Figs. 4.2 ($\beta = 30°$) and 4.3b. The dashed line shows $C = 0.1$ which is used for measuring the displacing front velocity, $\hat{V}_f$, consistently. b) Evolution of the front velocity value, $\hat{V}_f$, with time for the same experiment. The inset shows the constant value of the front velocity when the flow is fully developed ($\hat{V}_f = 31.3$ (mm/s) in this case with 2% standard deviation).

shows the concentration profiles at instants of time along a section of the pipe for the same experiment as shown in Fig. 4.3b. Note that the profiles of concentration shown in Fig. 4.5a and the spatiotemporal diagram data in Fig. 4.3b are interchangeable. To avoid very diffuse concentrations and noise in the data close to the lower wall of the pipe, we estimate the speed of the displacement front by the velocity of the concentration level $C = 0.1$ (see the dashed line in Fig. 4.5a). Evidently, selection of a threshold value is a trade-off between robustness and proximity to $C = 0$. Figure 4.5b shows the variation of the front velocity, $\hat{V}_f$ with time, which is quite typical of most of our experiments. In those cases that instability and mixing causes slow oscillation and noise in the profile of front velocity with time, an average value is adopted over long times so that the flow is well developed.

Initially the front velocity accelerates as the gate valve is opened and the flow initiates. There is some development timescale during which instability and mixing initiates, slowing the front propagation. As the flow becomes fully-developed the front velocity reaches an almost constant value (Fig. 4.5b inset). We use this thresholded front velocity, taken at long times in the experiment, as our measured $\hat{V}_f$. The transient and short-time behavior of the front in the limit of exchange flows in nearly-horizontal pipes was well

studied by Seon *et al.* [115]. It was also found that the front is initially controlled by inertia but later limited by viscous effects. This yields to a high front velocity value that decays to a steady state with time. A similar effect is observed in almost all our displacement flow experiments. Due to the fluid separation by gate valve the buoyancy force at the very beginning of the experiment is dominant over all other forces. This results to a fast acceleration of the displacing fluid along the pipe. Similar results are reported for gravity currents forming from the release of a heavy fluid into a light fluid [23]. In the case of density stable displacements (light fluid displacing heavy fluid), we also found a similar accelerating behavior at the start of the experiment [2]. Although studying transient/short-time effects in displacement flows is not studied much in the literature, and can be interesting, it is beyond the scope of our study.

We can compare our measured $\hat{V}_f$ with that obtained directly from the spatiotemporal plot via edge detection. For near-horizontal displacement flows, where the latter method is effective, typical relative errors in front velocity measurement are less than 2 %. For example, for the experiment in Fig. 4.3f the threshold method gives $\hat{V}_f = 63$ (mm/s) and the edge detection method from the spatiotemporal diagram gives $\hat{V}_f = 64$ (mm/s). By its nature, the threshold method tends to under-predict front velocity. The threshold method proves quite repeatable. Figure 4.6 shows the results of measuring $\hat{V}_f$ in repeated experimental sequences (for increased $\hat{V}_0$) at two different Atwood numbers and at $\beta = 30°$. Although there are some differences, good general agreement is found over a wide range of mean flow speed, $\hat{V}_0$. Note that at $\beta = 30°$ most of these experiments exhibit significant mixing. Taghavi *et al.* [129] found that when the mean flow is high enough to be away from the exchange-dominated regime, the front velocity, $\hat{V}_f$ varies linearly with $\hat{V}_0$, in nearly horizontal angles. Upon comparison with Fig. 4.6 we can see that this might not be the case when the inclination angles is decreased towards vertical. The main reason is that inertial forces are becoming more and more important. The non-linear effect can be better seen for higher Atwood number experiments in Fig. 4.6b where the instabilities and mixing are higher.

We now explore the main characteristics of front velocity measurements across our experimental range, where we have varied inclination angles, β, density differences, At, and mean flow speeds $\hat{V}_0$. Figures 4.7a-c show $\hat{V}_f$ for experiments conducted with $At = 0.001$, $At = 0.0035$ and $At = 0.01$, respectively. In each experimental sequence, at fixed At and β, the experiment is repeated at successively higher $\hat{V}_0$, starting from exchange flows ($\hat{V}_0 = 0$).

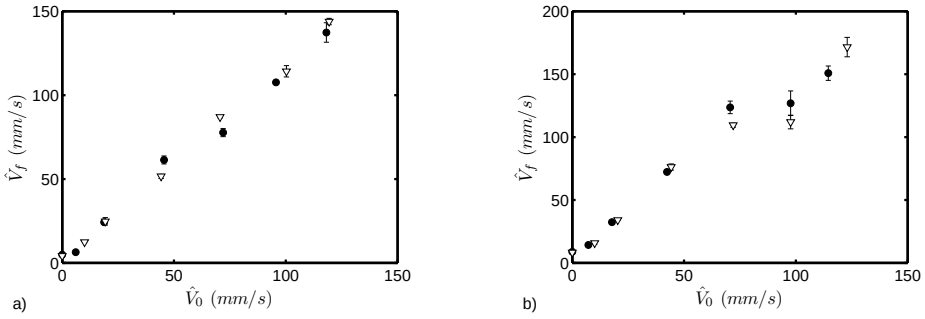

Figure 4.6: Dependency of the displacing front velocity, $\hat{V}_f$, versus the imposed flow velocity, $\hat{V}_0$, showing the experiment repeatability at a typical inclination angle, $\beta = 30°$, for $\hat{\nu} = 1$ (mm^2/s) and a) $At = 0.001$ and b) $At = 0.01$. The symbols show two sets of experiments for increasing imposed mean flows.

The data for nearly horizontal experiments from [126] are also added for completeness. The first thing to note is that the values of the front velocity naturally increase with mean flow speed $\hat{V}_0$. The second observation is that the front velocity seems to be highest for β between 60° and 70° roughly. This might be due to the fact that in this range the counter-current flow is strong enough to increase $\hat{V}_f$ but not strong enough to promote Kelvin-Helmholtz instabilities (which in turn tend to decrease $\hat{V}_f$). Qualitatively, at each $\hat{V}_0$, the front velocity variation with β is similar to that reported by Seon *et al.* [112, 113] for $\hat{V}_0 = 0$, although a constant plateau is not clearly distinguished in all our experiments.

In order to better see the effect of the mean flow relative to the underlying buoyancy driven exchange flow, we subtract the mean flow ($\hat{V}_0$) and exchange flow front velocity ($\hat{V}_{Exchange}$) from the measured front velocity values $\hat{V}_f$; see Fig. 4.8. For the smallest density difference, $At = 0.001$, Fig. 4.8a shows that most of values of $\hat{V}_f - \hat{V}_{Exchange} - \hat{V}_0$ are still positive. Imposing a displacement velocity to these (relatively weak) exchange flows does not change the structure in inclined pipes. In fact the flow remains mostly stratified and the front moves with a relatively high velocity, augmented by the imposed flow. As we move to higher Atwood numbers (Figs. 4.8a-c) we observe more negative values of $\hat{V}_f - \hat{V}_{Exchange} - \hat{V}_0$ indicating that simple superposition of physical effects becomes meaningless. For these flows significant instability and transverse mixing is induced by the combination

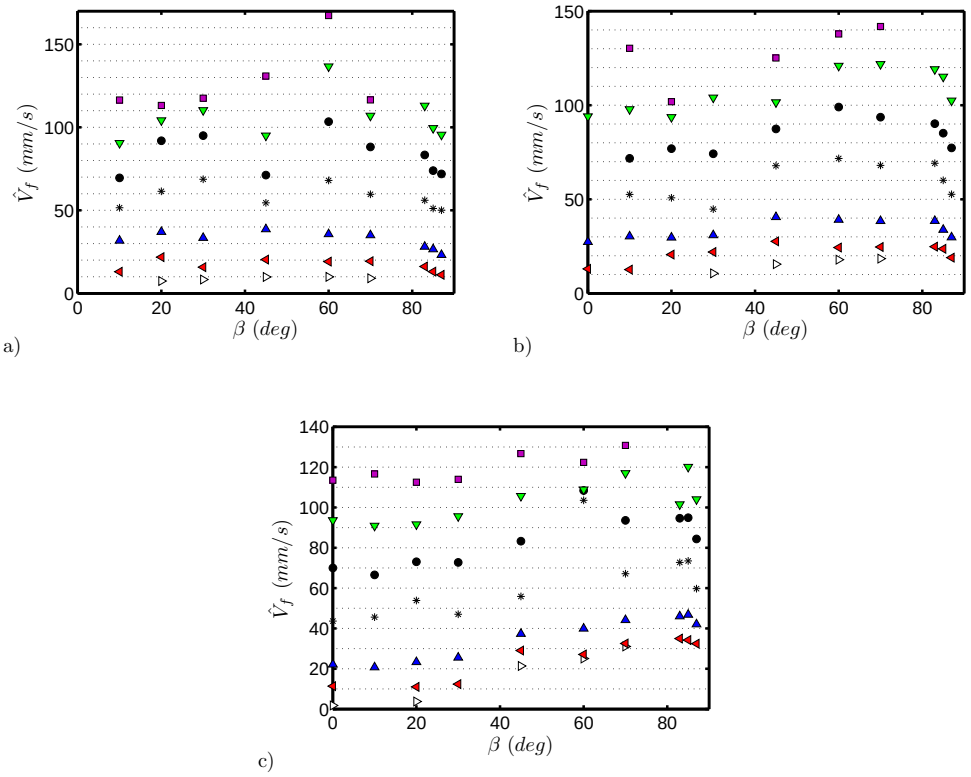

Figure 4.7: Change in displacing front velocity, $\hat{V}_f$ with tilt angle, β, and imposed velocity, $\hat{V}_0$ for $\hat{\nu} = 1$ (mm^2/s) and a) $At = 0.001$, b) $At = 0.0035$ and c) $At = 0.01$. Different markers represent $\hat{V}_0 = 0$ (mm/s) ($\triangleright$), 10 ($\blacktriangleleft$), 20 ($\blacktriangle$), 40 ($*$), 60 ($\bullet$), 80 ($\blacktriangledown$) and 100 (mm/s) ($\blacksquare$). The dashed lines are guide to the eye plotted at $\hat{V}_f = 10, 20, 30, ...$ (mm/s).

of mean imposed flow and strong buoyancy, modifying the flow structure. The front velocity is significantly lower than that which would be predicted by methods such as the lubrication/thin-film approach we have developed in [128], as the physical assumptions underlying these models are invalid. A new characterization is needed.

We now proceed with a dimensionless analysis of the results, focusing on the normalized front velocity $V_f = \hat{V}_f/\hat{V}_0$. In our previous study of near-horizontal displacements [126], we were able to classify all flows in the $(Fr, Re\cos\beta/Fr)$ plane, and therefore start with this description. Figure 4.9a shows the normalized front velocity $V_f = \hat{V}_f/\hat{V}_0$, plotted against Fr and

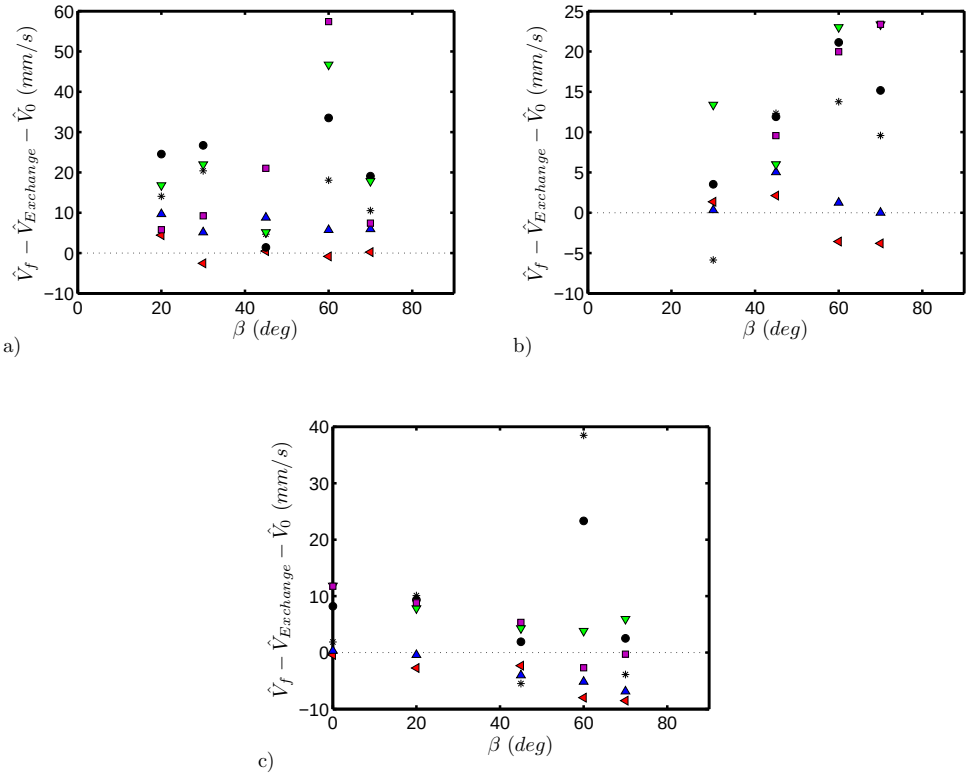

Figure 4.8: Change in $\hat{V}_f - \hat{V}_{Exchange} - \hat{V}_0$ with tilt angle, β, and imposed velocity, $\hat{V}_0$ for the same experiments as shown in Fig. 4.7 a) $At = 0.001$, b)$At = 0.0035$ and c)$At = 0.01$. Different markers represent $\hat{V}_0 = 10$ (mm/s) (◀), 20 (▲), 40 (∗), 60 (•), 80 (▼) and 100 (mm/s) (■). The dashed lines show $\hat{V}_f - \hat{V}_{Exchange} - \hat{V}_0 = 0$ (mm/s).

$Re\cos\beta/Fr$, for all experiments conducted in this study. The parameter regime studied by Taghavi *et al.* [126] is marked by the rectangle: $0 < Re\cos\beta/Fr < 120$ and $0 < Fr < 6$. It can be seen that the present study covers a much wider parameter range (primarily due to variations in β).

Our first observation is that over nearly the entire range of $Re\cos\beta/Fr$ studied V_f increases as Fr decreases. The parameter $Re\cos\beta/Fr$ is independent of $\hat{V}_0$, so that as $Fr \to 0$ we approach the exchange flow limit. For small Fr we observe a number of flows for which $V_f > 2$. We refer to these as *exchange flow dominated* and note that since we have scaled with the mean flow velocity, large $V_f > 2$ strongly suggests that some part of the velocity

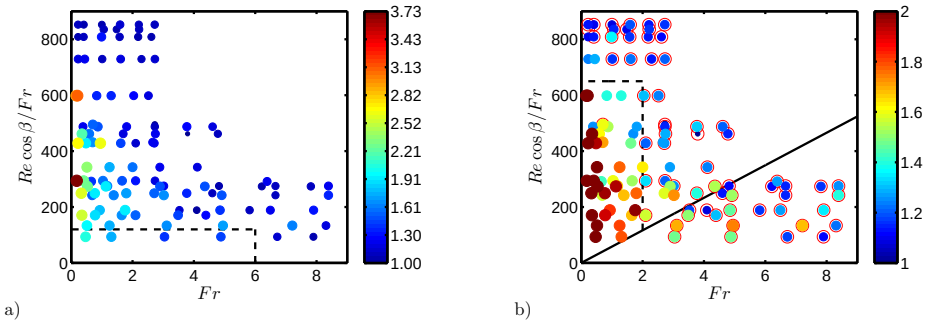

Figure 4.9: a) Presentation of our results for the full range of experiments: normalized front velocity $\hat{V}_f/\hat{V}_0$, plotted against Fr and $Re\cos\beta/Fr$. The rectangular area ($0 < Re\cos\beta/Fr < 120$, $0 < Fr < 6$) indicated by dashed lines, locates the range of nearly horizontal experiments and is studied in full details in [126] b) Instantaneous displacement flows marked by the superposed circles plotted against Fr and $Re\cos\beta/Fr$. The heavy line represents the prediction of the lubrication model for the stationary interface. The dashed lines $Re\cos\beta/Fr = 650$ and $Fr = 2$ roughly indicate the boundary between instantaneous and non-instantaneous displacement. Normalized front velocity scale is limited to 2 in part b to better show the variations of the front velocity in the plane of Fr and $Re\cos\beta/Fr$.

field is moving backwards against the mean flow, driven by buoyancy. The data is replotted in Fig. 4.9b with scale adjusted to emphasize those experiments for which $V_f > 2$. Back flows also can occur for lower values of $V_f > 2$. Figure 4.9b identifies those parameters for which back flows are observed and those that displace instantaneously. Exchange dominated flows generally lie within the limits $50 < Re\cos\beta/Fr < 650$ and $0 < Fr < 2$, although this is not precise. Similar flows were identified in Taghavi *et al.* [126] in the range $50 < Re\cos\beta/Fr < 120$ and $0 < Fr < 0.9$, but the upper limit on $Re\cos\beta/Fr$ was simply due to the extent of experiments performed. The lower limit is an extension of the exchange flow studies of Seon *et al.* [112] into the range of positive imposed flow: Seon *et al.* identified the transition from viscous to inertial exchange flows at $Re\cos\beta/Fr \approx 50$. Thus, the lower range of our results coincides with those of [112, 126]. The main finding is therefore that the upper limit for exchange dominated inertial flows extends up to approximately $Re\cos\beta/Fr = 650$.

In considering practical aspects of displacement, one important parame-

ter is the displacement efficiency $1/V_f$, based on the behaviour of the leading displacement front. A second important consideration is knowing whether the trailing front advances along the pipe in the direction of flow or upstream against the flow, driven by buoyancy (a back flow). In the former case, if it is possible to wait long enough the pipe will be fully displaced, but in the latter case residual fluid will remain. In [130], the criterion $Re\cos\beta/Fr \lessapprox 58Fr$ was developed to predict the onset of back flows. The methodology used involved a thin-film/lubrication model of viscous regime displacements. In such models a single parameter, $\chi = 2Re\cos\beta/Fr^2$ governs the dynamics at long times: χ represents the competition between buoyancy stresses in the axial direction and viscous stresses due to the mean flow. The critical value $\chi_c = 116.32$ was found to be the limit above which there is always a back flow. It is interesting to see how this value compares with our experiments, where mixing and instability are inevitably present. Figure 4.9b shows the experimental data in the $(Fr, Re\cos\beta/Fr)$ plane. We have marked those displacements that proceed instantaneously, i.e. with no evidence of a back flow, and have included the prediction of the lubrication model ($\chi_c = 116.32$) for comparison. Interestingly we observe that all the data points falling below $\chi = \chi_c$ line are found to be displacing instantaneously after opening the gate valve, i.e. $\chi < \chi_c$ appears to be a sufficient condition to avoid back flows, However, we see that many flows in the regime $\chi > \chi_c$ also displace instantaneously. Phenomenologically, these flows are inertial and well-mixed, and thus not well represented by the assumptions underlying the model behind $\chi = \chi_c$.

On examining Fig. 4.9 closely we observe that within the exchange dominated regime, there are interesting variations in V_f with $Re\cos\beta/Fr$. Let us consider a fixed Fr in the range $0 < Fr < 0.9$ and start with a low value of $Re\cos\beta/Fr$. Firstly, for $Re\cos\beta/Fr \lessapprox 58Fr$ ($\chi < \chi_c$) the flows are viscous dominated at long times and do not have a sufficiently strong buoyancy component to promote a back flow. For $58Fr \lessapprox Re\cos\beta/Fr \lessapprox 50$ the flows are exchange dominated but still viscous, i.e. with counter-current buoyancy driven well-defined stable laminar layers advancing downstream and upstream back against the flow. These regimes are studied at length in [126, 130]. Increasing $Re\cos\beta/Fr > 50$ we enter the inertial regime. Although counter-current streams persist we begin to observe instability and mixing close to the interface. On further increasing $Re\cos\beta/Fr$ buoyancy forces increase, driving both lighter fluid upwards and denser fluid downwards, hence increasing V_f. However, the degree of instability and mixing also increases progressively as $Re\cos\beta/Fr$ is increased. As transverse mixing comes to dominate, the streams of pure fluid are no longer able to remain

intact while flowing counter-currently and a fully diffusive regime is entered as V_f decreases towards unity.

The competition between buoyancy-driven advection and transverse mixing leads to a maximum in V_f at an intermediate value of $Re\cos\beta/Fr$. This competition is captured physically in the parameter $Re\cos\beta/Fr$, which is defined as:

$$\frac{Re\cos\beta}{Fr} = \frac{\hat{V}_0\hat{D}}{\hat{\nu}}\cos\beta\frac{\sqrt{At\hat{g}\hat{D}}}{\hat{V}_0} = \frac{\cos\beta}{\sqrt{2}}\left[\frac{(\hat{\rho}_H+\hat{\rho}_L)(\hat{\rho}_H-\hat{\rho}_L)\hat{g}\hat{D}^3}{2\hat{\mu}^2}\right]^{1/2}. \tag{4.2}$$

The parameter in the square brackets above is the Archimedes number. An interpretation of this expression is as the relative strengths of buoyancy stresses $(\hat{\rho}_H-\hat{\rho}_L)\hat{g}\hat{D}$, and viscous stresses, $\hat{\mu}\hat{V}_t/\hat{D}$. Note that here the velocity scale used for the viscous stresses is $\hat{V}_t$, which is itself driven by buoyancy. It is this feature of self-reinforcement that tends to promote the onset of (buoyancy driven) instability, i.e. if the viscous stresses induced by the buoyant motion are unable to balance the buoyant stresses.

4.2.4 Macroscopic diffusion

In this section we focus on those experiments where the degree of transverse mixing is high. In such cases we expect that advective transport due to the mean flow will be supplemented by diffusive spreading along the pipe. Debacq *et al.* [33, 34] used a similarity scaling for exchange flows in vertical pipes to collapse profiles of the cross-sectionally averaged concentration C, measured at each location $\hat{x}$ and time $\hat{t}$, onto a master curve defined with respect to $\hat{x}/\sqrt{\hat{t}}$. On fitting the master curve to an error function form, estimates were derived for the macroscopic diffusion of the mean concentration along the pipe. Seon *et al.* [114] followed the same approach for inclined pipes and we adopt an analogous approach here.

In the presence of a mean flow ($\hat{V}_0$), when the flows fully mix transversely it is logical to assume a core of the mixture traveling with the speed $\hat{V}_0$ and therefore use $(\hat{x}-\hat{V}_0\hat{t})/\sqrt{\hat{t}}$ as a similarity scaling. Figure 4.10 shows two examples of this for $\beta = 45°$, $At = 0.08$, $\hat{\nu} = 1$ (mm^2/s). We can see that all the concentration evolution profiles have collapsed onto one curve. The solid line shows a curve fit of the form $C = 0.5\mathrm{erfc}(\frac{\hat{x}-\hat{V}_0\hat{t}}{2\sqrt{\hat{D}_M\hat{t}}})$, motivated by the analytical solution to the linear diffusion equation. In Fig. 4.10a we find $\hat{D}_M = 0.0052$ (m^2/s) and in Fig. 4.10b we find $\hat{D}_M = 0.006$ (m^2/s). Here $\hat{D}_M$ is the macroscopic diffusion coefficient. Although

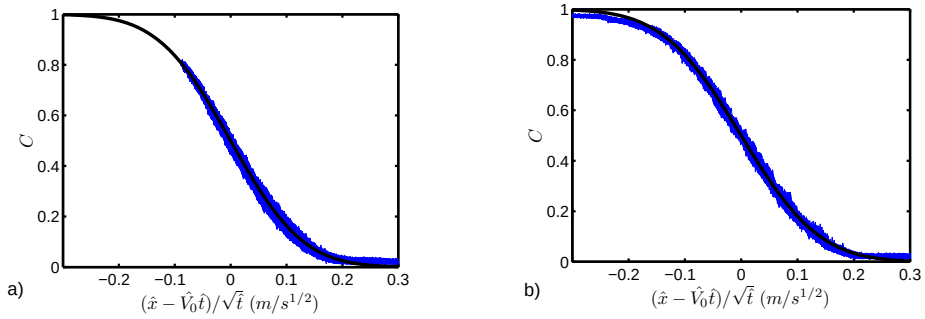

Figure 4.10: Collapse of depth-averaged concentration profiles with $(\hat{x} - \hat{V}_0\hat{t})/\sqrt{\hat{t}}$ for $\beta = 45°$, $At = 0.08$, $\hat{\nu} = 1$ (mm^2/s) and a) $\hat{V}_0 = 14$ (mm/s) b) $\hat{V}_0 = 113$ (mm/s). The solid lines show the complementary error-function fit obtained for $\hat{D}_M = 0.0052$ (m^2/s) and $\hat{D}_M = 0.006$ (m^2/s) for parts a and b respectively.

the quality of the data collapse appears similar in both Figs. 4.10a & b, it can be observed that the curves C in Fig. 4.10a do not extend up to $C = 1$. In this experiment the mean flow is relatively weak ($\hat{V}_0 = 14$ (mm/s)) and during the experimental time there is still displaced fluid present in the field of view, due to a strong back flow. In Fig. 4.10b the parameters are the same except for a higher mean flow ($\hat{V}_0 = 113$ (mm/s)) and over the timescales considered the concentration C reaches to the value 1.

Note that to determine $\hat{D}_M$ we only analyze the concentration in the lower section of the experimental apparatus and at later times in the experiment, so that the flow is as fully developed as our experiment allows. The initial stages of every experiment are complex, as there is an initial acceleration phase, followed by an inertia-buoyancy balance, then development of either instabilities and mixing, or advective transport (as considered earlier). While physically interesting, these initial phenomena are not the focus of our study.

Seon *et al.* [114] fitted their measured $\hat{D}_M$, for the case $\hat{V}_0 = 0$, to an expression of form:

$$\hat{D}_{M,Exchange} = 5 \times 10^3 (\hat{V}_t \hat{D})(1 + 3.6 \tan\beta)^2 \left(\frac{\hat{V}_t}{\hat{V}_\nu}\right)^{3/2} \tag{4.3}$$

Note that the range of applicability of 4.3 in [114] is for $Re/Fr \lesssim 1000$, which covers the range of our exchange flow experiments. In order to check

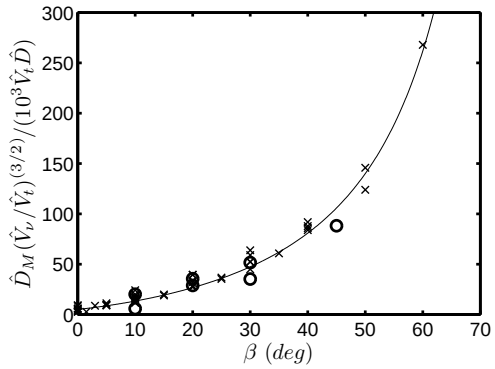

Figure 4.11: Variation of the dimensionless diffusion coefficient versus tilt angle. The circles are based on current measurements and the crosses are added from Seon *et al.* [114] experiments. The curve fit is also taken from Seon *et al.* [114]; see equation (4.3).

the consistency of our macroscopic diffusion coefficient measurements, the data are compared with (4.3) in Fig. 4.11, for those of our experiments run at $\hat{V}_0 = 0$ that were fully mixed. The agreement is good, with a similar deviation as for the data in [114].

Although for most experiments with a high degree of mixing the similarity scaling provides an excellent fit to the data (e.g. Fig. 4.10), as we examine a wider set of our experimental data this scaling fails in variety of different ways. Firstly, this error-function fit assumes that the area behind and ahead of the mixed core (moving with speed $\hat{V}_0$) should be symmetric. This is not always true since the mixing quality can be slightly different behind and ahead of the mixing core. Unlike the exchange flow, adding a mean flow can break the symmetry. Figure 4.12a shows one example of this: for negative $(\hat{x} - \hat{V}_0\hat{t})/\sqrt{\hat{t}}$ the measured profiles fall slightly below the curve which suggest that the mixing is happening over a slower time scale behind the mixing core. Assuming a symmetric error function fit to the collapsed concentration profiles is still a reasonable leading order approximation, but some aspects of the physical phenomena present are not captured. Secondly, we have experiments which are highly inertial, exhibiting instability and mixing, but for which transverse mixing is incomplete and which are not fully diffusive. For example, see Fig. 4.2 at $\beta = 45°$ and $60°$. Figures 4.12b and c show the similarity scaling for these two experiments, confirming that

the concentration evolution should not be categorized as fully diffusive. The fluctuations in the profiles shown relate to the large scale instabilities that appear intermittently at the interface. A final limit where we do not have diffusive flows is where the layers remain well segregated at the interface, i.e. viscous flows. Figure 4.12d shows again that the averaged concentration profiles do not collapse onto a master curve using the similarity scaling $(\hat{x} - \hat{V}_0\hat{t})/\sqrt{\hat{t}}$. These flows are essentially advective and the profiles collapse instead under a similarity scaling $\hat{x}/\hat{t}$ (see [128]) as is illustrated in the inset of Fig. 4.12d.

We now focus only on those experiments for which we have been able to reliably collapse the data at long times, using the similarity scaling $(\hat{x} - \hat{V}_0\hat{t})/\sqrt{\hat{t}}$, and have been able to estimate a macroscopic diffusion coefficient from the master curve. We call these flows *fully diffusive*. Figure 4.13 plots the measured macroscopic diffusion coefficients for displacement flows at different inclination angles and two Atwood numbers: $At = 0.0035$ and $At = 0.01$. Two clear conclusions are that, within the range of fully diffusive experiments, $\hat{D}_M$ increases with both inclination angle, β, and mean flow speed, $\hat{V}_0$.

None of the above trends are surprising, but they are interesting in suggesting two independent factors contributing to $\hat{D}_M$. The relatively large values of $\hat{D}_M$ confirm that the diffusive transport cannot be molecular in origin, but is due to advection, i.e. this is largely dispersion. The flows are disordered and well-mixed transversely, to all appearances locally turbulent. In such cases we may expect a scaling of the dispersivity with length and velocity scales that are relevant to the eddy structure. This is evidently complex in general, but we might guess that the relevant velocity will scale approximately with either the inertial velocity or the mean flow, depending on the relative strengths of buoyancy or the mean flow in driving the mixing. To explore this, we plot $\hat{D}_M/(\hat{V}_t\hat{D})$ and $\hat{D}_M/(\hat{V}_0\hat{D})$ in the $(Fr, Re\cos\beta/Fr)$-plane (see Fig. 4.14), the axes reflecting the competition between inertia from the mean flow and buoyancy (Fr) and between buoyancy driven motion and viscous dissipation of that motion $(Re\cos\beta/Fr)$, respectively.

A first observation is that our experimental data for fully diffusive experiments closely corresponds to the region of the $(Fr, Re\cos\beta/Fr)$-plane in which the front velocities $\hat{V}_f$ are very close to the mean flow $\hat{V}_0$, e.g. compare with the region in Fig. 4.9b where $V_f \approx 1$. Secondly, we can see that scaling of $\hat{D}_M$ suggest that both mechanisms are responsible for the mixing in different limits. For small Fr, at large $(Re\cos\beta/Fr)$ as we transition out of the

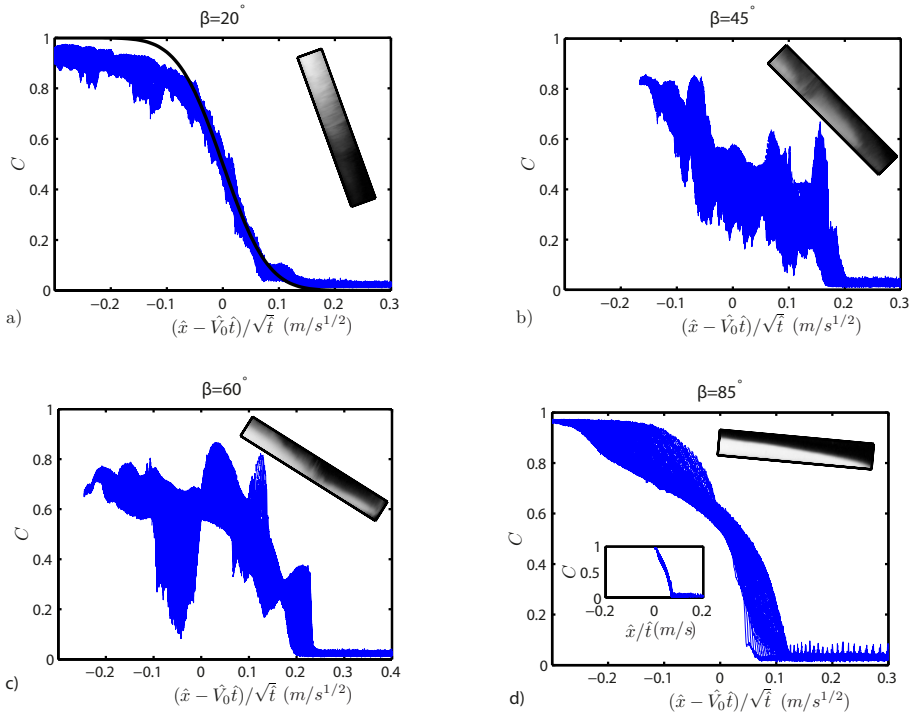

Figure 4.12: Collapse of depth-averaged concentration profiles with $(\hat{x} - \hat{V}_0\hat{t})/\sqrt{\hat{t}}$ for $At = 0.0035$, $\hat{\nu} = 1$ (mm^2/s) and a) $\beta = 20°$, $\hat{V}_0 = 44$ (mm/s) b) $\beta = 45°$, $\hat{V}_0 = 32$ (mm/s) c) $\beta = 60°$, $\hat{V}_0 = 47$ (mm/s) and d) $\beta = 85°$, $\hat{V}_0 = 43$ (mm/s). Note that the mean flow speed in experiments are chosen to be close to each other to make a qualitatively meaningful comparison available (average mean flow speed is $\hat{V}_0 \approx 42$ (mm/s)). The solid line in Fig. 4.12a shows the error-function fit with $\hat{D}_M = 0.002$ (m^2/s). The upper right insets show the qualitative flow pattern in each case. In part d the lower left inset shows the collapse of the concentration profiles when $\hat{x}/\hat{t}$ is used instead of $(\hat{x} - \hat{V}_0\hat{t})/\sqrt{\hat{t}}$.

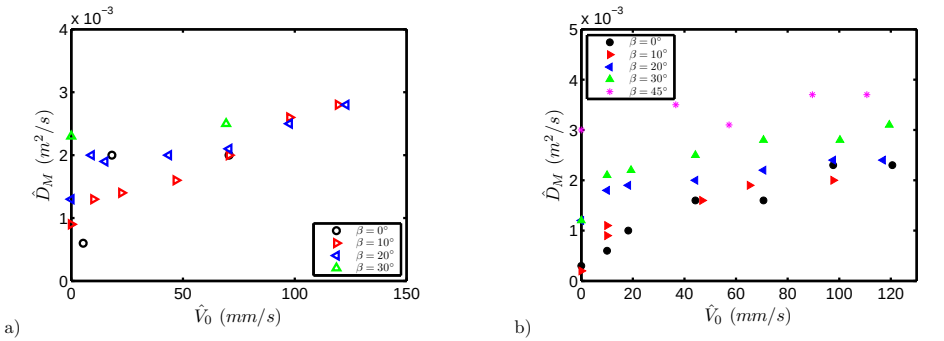

Figure 4.13: Variation of the diffusion coefficient, $\hat{D}_M$ versus mean imposed flow velocity, $\hat{V}_0$ for $\hat{\nu} = 1$ (mm^2/s) and a) $At = 0.0035$ and b) $At = 0.01$.

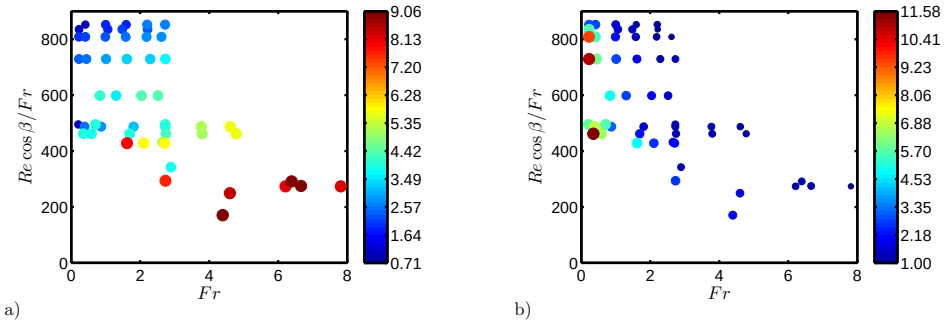

Figure 4.14: Contours of the normalized diffusion coefficient a) $\hat{D}_M/(\hat{V}_t\hat{D})$ and b) $\hat{D}_M/(\hat{V}_0\hat{D})$ versus Fr and $Re\cos\beta/Fr$.

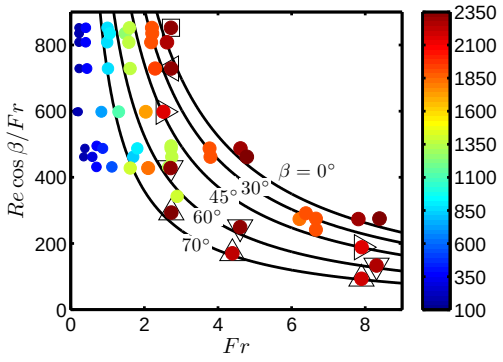

Figure 4.15: Reynolds number, Re, plotted against Fr and $Re\cos\beta/Fr$. The illustrative curves correspond to different inclination angles, β, and are show $Re = Re_{cr} = 2100$. Flows marked by the superposed triangles and/or squares satisfy the criterion $Re > 2100$. The symbols used are for $\beta = 70°$ ($\triangle$), $\beta = 60°$ ($\triangledown$), $\beta = 45°$ ($\triangleright$), $\beta = 30°$ ($\triangleleft$) and $\beta = 0°$ ($\square$).

exchange dominated regime see that $\hat{D}_M/(\hat{V}_t\hat{D})$ appears to become independent of Fr, suggesting buoyancy driven mixing. At the other extreme, for modest $(Re\cos\beta/Fr)$ and as we increase Fr we find $\hat{D}_M/(\hat{V}_0\hat{D}) \approx$ constant, suggesting mixing driven by the mean flow. The pattern of $\hat{D}_M/(\hat{V}_0\hat{D})$ in Fig. 4.14b is suggestive of lines of constant Re, and note that in fully turbulent shear flows the turbulent dispersivity (when scaled with $\hat{V}_0\hat{D}$) has only slow variation with Re. Figure 4.15 shows all our fully diffusive experiments and plots with the colour-scale the Re corresponding to each experiment. Lines of constant Re (keeping all other parameters fixed) would appear as hyperbolae in this plane, and we have included the line $Re = 2100$ for different inclination angles, as a nominal transitional value in the absence of buoyancy effects. Those data points that exceed $Re = 2100$ are highlighted by the superposed symbols. We observe that although some of our data satisfy this criterion, many of the experiments have Re far below 2100, although the mixing behaviour appears fully turbulent. This suggests that buoyancy has a significant role in at least instigating this regime, even for those regimes where the mean flow dominates. It is worth noting that our study has not explored very high Reynolds numbers.

We evaluate the Taylor dispersion coefficient for turbulent pipe flow: $\hat{D}_T = 1.785\hat{V}_0\hat{D}\sqrt{f_f}$, for simplicity using the Nikuradze formula for the

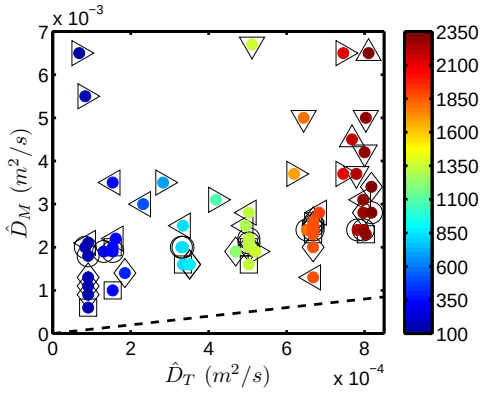

Figure 4.16: Comparison of the experimental macroscopic diffusion coefficient, $\hat{D}_M$, versus Taylor dispersion coefficient, $\hat{D}_T$, for all diffusive experiments shown in Fig. 4.15. The contour values show Reynolds number, Re. The dashed line represents $\hat{D}_M = \hat{D}_T$. The symbols used are for $\beta = 70°$ ($\triangle$), $\beta = 60°$ ($\triangledown$), $\beta = 45°$ ($\triangleright$), $\beta = 30°$ ($\triangleleft$), $\beta = 20°$ (O), $\beta = 10°$ ($\Diamond$) and $\beta = 0°$ ($\square$). The Taylor diffusion coefficient is $\hat{D}_T = 1.785\hat{V}_0\hat{D}\sqrt{f_f}$ for a Newtonian fluid using Nikuradze formula for friction factor, $f_f = 0.266/Re^{1/4}$.

friction factor, $f_f = 0.266/Re^{1/4}$. Figure 4.16 plots for each fully diffusive experiment the measured $\hat{D}_M$ against the calculated $\hat{D}_T$. The colour scale plots again the Reynolds number. We can see that $\hat{D}_M$ exceeds $\hat{D}_T$ by up to an order of magnitude, over the full range of experiments. This is purely comparative of course and no exact agreement is to be expected, due to the relatively low Re. It is well known that the actual dispersion increases rapidly as the turbulence weakens and the viscous wall layers grow thicker; see [42, 47, 140]. Here, although apparently turbulent even at lower Re, the driving force is at least partly buoyancy and we can not expect a classical turbulent velocity profile to drive dispersion. Although we have some velocity data, the UDV system is not ideal for capturing turbulent characteristics of the flow and we feel that making further inference could be beyond the range of reliability of our data. At very high Reynolds numbers, say $Re > 10000$, since all our experiments are at low At we might expect to recover the classical results for turbulent dispersion. However, this is beyond the scope of this study and would be difficult to study in our present apparatus.

4.3 Regime classification and leading order approximations

In the previous section we presented our results in terms of the velocity of the leading displacement front, and in terms of bulk axial diffusivity in the case of fully diffusive flows. We now give a leading order quantitative description of the different flow regimes observed at long times in our experiments, in terms of the 3 dimensionless parameters: (Fr, Re, β). Much of the parametric variation appears to be captured in the $(Fr, Re\cos\beta/Fr)$-plane, as was the case for nearly horizontal displacements studied in [126]. Figure 4.17 shows the experimental points from our study, characterised in terms of flow type. We distinguish flows according to the following criteria: (i) *instantaneous* displacement (if there is no displaced fluid observed above the gate valve); (ii) *fully diffusive* (if we are able to collapse the data at long times via similarity solution of form, $C = 0.5\mathrm{erfc}(\frac{\hat{x}-\hat{V}_0\hat{t}}{2\sqrt{\hat{D}_M\hat{t}}})$; (iii) for *non-diffusive* flows we classify as either, *viscous* flows if there is no instability evident in the spatiotemporal image behind the leading displacement front, and *inertial* otherwise. It can be seen that this classification, although not perfect, does appear to separate the data within the $(Fr, Re\cos\beta/Fr)$-plane.

Two lines are plotted in Fig. 4.17. Firstly, the solid line is the prediction of instantaneous displacements by the lubrication model in [130] ($\chi = \chi_c = 116.32$), as discussed earlier. Below this line only instantaneous displacements may occur, in the viscous limit. The broken line in Fig. 4.17 is given by:

$$\frac{Re\cos\beta}{Fr} = 500 - 50Fr. \tag{4.4}$$

For $\chi > \chi_c$ this line represents the approximate position of the boundary between fully diffusive and non-diffusive flows. The two lines intersect at $Fr \approx 4.62$ and $Re\cos\beta/Fr \approx 270$.

For $\chi < \chi_c$ and sufficiently small flow rates we find viscous dominated flows, characteristically laminar with well defined interfaces separating distinct fluid streams. These flows are an extension of the viscous instantaneous displacements studied in [126, 130], but here we have a higher range of Fr and $Re\cos\beta/Fr$; see Fig. 4.9a. In this regime the viscous stresses generated by the mean flow appear to dominate any destabilizing effects of buoyancy. Using the lubrication/thin-film displacement model in [126, 130] we can compute an approximation to the front velocity, that depends only on the parameter $\chi = 2Re\cos\beta/Fr^2$. Figure 4.18 compares the scaled front velocity values obtained from the current experiments with the predictions

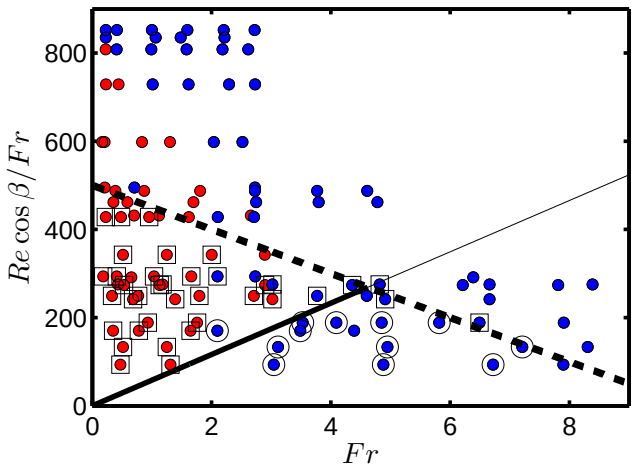

Figure 4.17: Classification of our results for the full range of experiments, presented in the $(Fr, Re\cos\beta/Fr)$-plane: (i) instantaneous displacement flows are colored in blue and non-instantaneous flows in red; (ii) fully diffusive flows have no superposed symbol; (iii) non-diffusive flows are marked as viscous (superposed circles) or inertial (superposed squares). The heavy line represents the prediction of viscous back flows, from the lubrication model in [130], ($\chi = \chi_c = 116.32$). The thick broken line represents $Re\cos\beta/Fr = -50Fr + 500$. The point of intersection of the two lines is $Fr \approx 4.62$ and $Re\cos\beta/Fr \approx 270$.

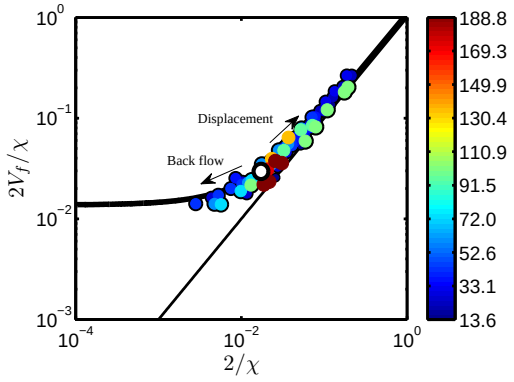

Figure 4.18: Comparison of the front velocity values obtained from experiments classified as viscous with the predictions $V_f(\chi)$ from the lubrication model in [126, 130] (thick solid line). Colour values indicate $Re\cos\beta/Fr$ for each experiment. The data with the solid boundary are for near-horizontal β, taken from [126]. The thick white circle indicates the theoretical transition ($\chi = \chi_c \approx 116.32$). The thin solid line shows $\hat{V}_f = \hat{V}_0$ below which leading front velocities are not possible due to conservation of mass.

$V_f(\chi)$, of the lubrication model. Data from [126], belonging to viscous flows in nearly horizontal experiments, is also included. The lubrication model appears to be effective in predicting the front velocity for our data, i.e. at significantly larger $Re\cos\beta/Fr$ than was previously studied.

On increasing the flow rate (here Fr) the flow transitions from viscous laminar layers to fully diffusive turbulent flow. As we have seen earlier, the fully diffusive regime is driven by a combination of buoyancy and mean flow effects. For $\chi < \chi_c$, we expect that the mean flow effects will be dominant as buoyancy decreases. Although (4.4) appears to capture the transition reasonably well close to the point of interception of the two curves in Fig. 4.17, this relationship cannot be valid as $Re\cos\beta/Fr \to 0$, (e.g. this gives $Fr = 10$ for a horizontal pipe). Instead, we expect a more classical criterion for transition to be valid, primarily based on a Re threshold. We have seen in Fig. 4.15 that the fully diffusive flows observed in this range do have $Re > 1500$, which tends to support our viewpoint. Although not high enough for fully shear driven turbulence, flows at these Re are highly inertial and it is quite conceivable that the transition could be triggered. Firstly, it could be that in the initial stages of the experiment when buoyancy

effects are large, these trigger instability. Secondly, we must admit that our apparatus was not designed for a classical study of shear flow transition, but for observing displacement flows. At high Re, geometric imperfections (e.g. near the gate valve) or entry conditions may play a role in triggering instability. Furthermore, if we consider a long smooth pipe, the viscous flows observed at lower flow rates tend to have an elongating interfacial region that essentially stratifies. The effect of density on the base flow and on the (linear) stability problem is felt only through χ, which decreases like $1/\hat{V}_0$ (i.e. as Re^{-1} increases with flow rate). Thus, the limit of large Re and small χ recovers the single fluid flow. From these perspectives (and in the absence of viscosity differences), we feel that in the regime $\chi < \chi_c$, a better criterion to use as a sufficient condition for transition to the fully-diffusive regime is $Re \gtrsim Re_{cr} = 2100$. Finally, we might reflect on why (4.4) appears to capture this transition so well in the range studied. The main point here is that our experiments are performed using a single pipe diameter and hence Fr simply reflects an increase in $\hat{V}_0$, which is also the main control parameter in varying Re. To distinguish Re and Fr effects would require experiments with a different (identical) viscosity and/or changes in pipe diameter. Here the main focus has been on changing β.

For $\chi > \chi_c$ the flows have a significant inertial component, driven by buoyancy, as well as a contribution from the mean flow. For parameters below the curve (4.4) we have classified these flows as non-diffusive and inertial, but in reality a wide range of behaviours is observed within our data. Firstly, we have seen that for $Fr < 2$ in this range many of the flows have strong back flows and are dominated by buoyancy. We have termed these exchange flow dominated. As $Re\cos\beta/Fr$ is decreased these flows persist down to $Re\cos\beta/Fr \approx 50$, which is outside the range of our data here but covered by the data in [126]. For $Re\cos\beta/Fr \lesssim 50$ (and $\chi > \chi_c$) the flows remain exchange dominated but are now viscous exchange flows; see [126, 130].

Within the exchange dominated range at lower $Re\cos\beta/Fr$ the fluid streams remain fairly distinct and structured, say roughly for $50 \lessapprox Re\cos\beta/Fr \lessapprox 270$. Interfacial instabilities occur, but mixing between the streams is relatively minor. As the flow rate is increased, for $Fr > 2$, buoyancy effects reduce and the countercurrent flow is progressively eliminated as we pass into the regime of instantaneous displacements. These flows laminarise as we cross $\chi = \chi_c$, leading to the counterintuitive observation that increases in flow rate can stabilize the flow; see [129]. The novel result of this study is in determining that stabilisation of exchange dominated inertial flows by the mean flow extends up to $Re\cos\beta/Fr \approx 270$. For $Re\cos\beta/Fr \gtrapprox 270$ ex-

change dominated flows persist. Increasing $Re\cos\beta/Fr$ further destabilises these flows. We progressively observe more intermittency and instability, leading to a greater degree of transverse mixing. Eventually we cross (4.4) into the regime of fully diffusive flows. Equally we traverse (4.4) on increasing Fr, again becoming progressively unstable (i.e. in contrast to the stabilisation by the mean flow observed for $Re\cos\beta/Fr \approx 270$).

For engineering design purposes it is of value to have an approximation to $\hat{V}_f$ governing the flows in the triangular region of Fig. 4.17, that we have classified as non-diffusive inertial flows. In the range of low $Re\cos\beta/Fr$ our study coincides with that of Taghavi *et al.*, who studied near-horizontal pipes and fitted the expression:

$$\hat{V}_f/\hat{V}_t = 0.7 + 0.595Fr + 0.362Fr^2, \tag{4.5}$$

to the available data in these regimes; see [126]. The rationale for the form of expression is that $\hat{V}_t$ is the appropriate velocity scale for inertial/bouyancy-driven flows. The first coefficient coincides with that from extensive exchange flow studies; see [112], and the next coefficients are logical for an expansion in terms of small $\hat{V}_0/\hat{V}_t$ $(= Fr)$. Figure 4.19a plots our experimental front velocity values scaled by inertial velocity $(\hat{V}_f/\hat{V}_t)$, plotted against Fr, and compared with (4.5). We have included data belonging to nearly-horizontal experiments of [126]. The colour scale indicates the value of $Re\cos\beta/Fr$ in each experiment.

Although reasonable, a discernible trend is the deviation from (4.5) at larger values of $Re\cos\beta/Fr$, as well as for higher Fr. The deviation from (4.5) at higher Fr is inevitable since we are moving away from exchange flow dominated regimes. Equally in our near-horizontal flow experiments [126] we were restricted to $Re\cos\beta/Fr < 120$. The leading coefficient 0.7 in (4.5) comes from the exchange flow studies conducted over the approximate range $50 < Re\cos\beta/Fr < 200$; see [112]. We hypothesize that the relationship (4.5) should have a significant dependency on $Re\cos\beta/Fr$, and have developed the following curve fit:

$$\hat{V}_f/\hat{V}_t = Fr + \left(\frac{Re\cos\beta}{Fr} + 50Fr - 500\right)(-0.002337 + 0.002283Fr - 0.002401Fr^2), \tag{4.6}$$

as an improved model. The form of the model is chosen to ensure that $\hat{V}_f/\hat{V}_t = Fr$ on (4.4), i.e. $\hat{V}_f = \hat{V}_0$. Figure 4.19b plots experimental $\hat{V}_f/\hat{V}_t$ values against $\hat{V}_f/\hat{V}_t$ predicted from (4.6), showing close agreement uniformly with $Re\cos\beta/Fr$.

Turning now to the fully diffusive flows, these occur primarily in the region of the $(Fr, Re\cos\beta/Fr)$-plane lying above (4.4). We first note that

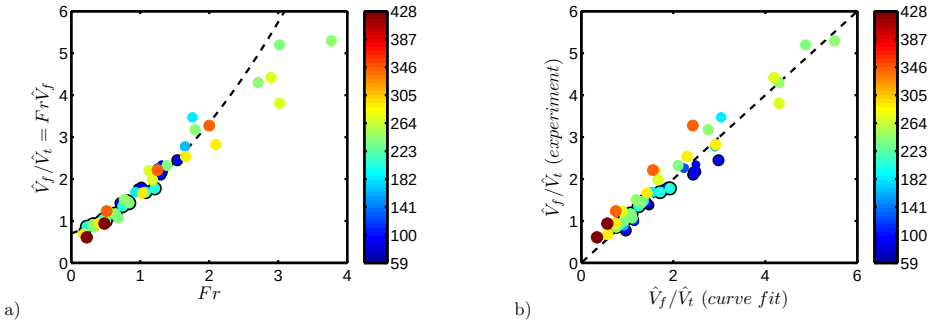

Figure 4.19: a) Scaled front velocity values, $\hat{V}_f/\hat{V}_t$, for intermittent flows shown by squares in Fig. 4.17 plotted versus Fr. The dashed line shows the curve fit (4.5) from [126]. The data with solid line around, belong to nearly horizontal regimes and are taken from [126] b) comparison of experimental and predicted values of $\hat{V}_f/\hat{V}_t$, with the predictions following (4.6). The dashed line in part b indicates $\hat{V}_f/\hat{V}_{t\ (experiment)} = \hat{V}_f/\hat{V}_{t\ (curvefit)}$. The contour values in both figures show the corresponding $Re\cos\beta/Fr$ to each experiment.

there are a good number of data points in Fig. 4.17 that are fully diffusive but not instantaneous displacements. These are found above (4.4) for $Fr < 2$ and $Re\cos\beta/Fr$ extending up to around 800. These are an extension of the exchange dominated flows into the fully diffusive regime. This differs significantly from pure exchange flow studies, driven only by buoyancy. For example, in the data of Debacq *et al.* [33] we can see the onset of fully diffusive flows at $Re\cos\beta/Fr \gtrsim 1000$, for exchange flows in vertical pipes. However, the difference is not surprising as classification of such flows depends partly on the experimental timescale. Our classification scheme here simply means that there is displaced fluid present above the gate valve at the end of our experiment. Given that transverse mixing is very effective for these flows it is unlikely that displaced fluid would persist here over very long timescales, eventually being mixed and washed away.

We have seen earlier that our fully diffusive data (at $\hat{V}_0 = 0$) match well with that from Seon *et al.* data [114], leading to the expression (4.3) for the diffusivity $\hat{D}_{M,Exchange}$. In developing an approximation to the bulk diffusivity $\hat{D}_M$ we have seen in Fig. 4.14b that $\hat{D}_M \sim \hat{D}\hat{V}_0$ for larger Fr. As we expect that the buoyant component is largely predicted by $\hat{D}_{M,Exchange}$, we examine the difference $\hat{D}_M - \hat{D}_{M,Exchange}$, plotted against $\hat{D}\hat{V}_0$; see

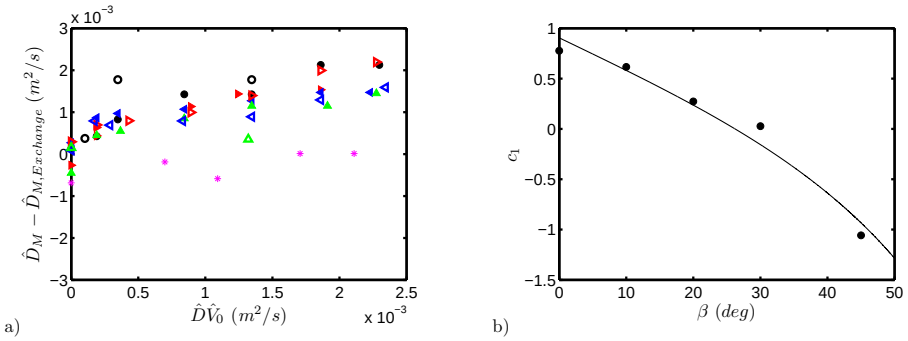

Figure 4.20: a) Variation of the diffusion coefficient $\hat{D}_M - \hat{D}_{M,Exchange}$ with $\hat{D}\hat{V}_0$. Meanings of the symbols are the same as in Fig. 4.13. b) Variation of c_1 in the expression $\hat{D}_M = \hat{D}_{M,Exchange} + \hat{D}\hat{V}_0(c_0 + c_1(\beta)/\sqrt{Fr})$, fitted to our data averaged over each inclination angle, β. Note that $c_0 = 0.6618$ is determined from our high Reynolds number experiments $Re > 2100$.

Fig. 4.20a. We see that the data for each pipe inclination β appears to follow an individual curve. Variation with β should correspond to a buoyancy effect, rather than simply a mean flow effect. To incorporate this, we have looked for a relationship of form:

$$\hat{D}_M = \hat{D}_{M,Exchange} + \hat{D}\hat{V}_0(c_0 + c_1(\beta)/\sqrt{Fr}) \tag{4.7}$$

At high Re we expect $\hat{D}_M \sim \hat{D}\hat{V}_0$ from the Taylor dispersion analysis, where Re dependency through the friction factor is weak. We have therefore used our data for high Reynolds number experiments $Re > 2100$, to fit $c_0 = 0.6618$, and then have used the average data values over each inclination, to fit $c_1(\beta) = 0.9054 - 1.838 \tan\beta$. This fit is illustrated in Fig. 4.20b.

The effectiveness of the expression in (4.7) in approximating $\hat{D}_M$ is illustrated in Fig. 4.21. Although reasonable as a prediction, there is some spread in the data. We believe this variability is at least partly due to variability in the measurement procedure, leading to fitting of $\hat{D}_M$. In each experiment we wait for long times to fit $\hat{D}_M$. However, as these are (mostly) instantaneous displacements the time of sampling of each experiment is related to the transit time along the pipe (an advective timescale), i.e. if you wait too long the data has left the pipe. If the flow development is diffusively controlled, ideally one should sample at times that are equally significant diffusively.

Finally, we consider the appropriate front velocity for the diffusive regime.

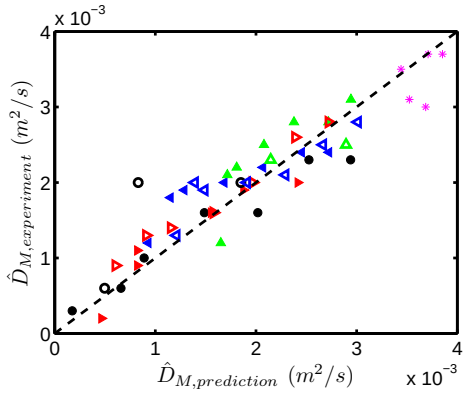

Figure 4.21: Comparison of the experimental macroscopic diffusion diffusion coefficient, $\hat{D}_{M,exp}$, against the prediction of (4.7). The broken line shows $\hat{D}_{M,experiment} = \hat{D}_{M,prediction}$. Meanings of the symbols are the same as in Fig. 4.13.

We have used $(\hat{x} - \hat{V}_0\hat{t})/\sqrt{\hat{t}}$ as a similarity scaling for the concentration profiles in fitting $\hat{D}_M$. This implicitly assumes a speed $\hat{V}_0$ for the advective transport. We can also however proceed in the reverse direction for any given $\hat{D}_M$, to find the front velocity. Our procedure for finding the front velocity relies on tracking the concentration profiles at later times in our experiment. However, for fully diffusive flows part of the evolution of the concentration is driven by axial diffusion. For given $\hat{D}_M$ we therefore use the assumed erfc form of solution to compute the speed of the front at $C = 0.1$, purely due to diffusion as the mean front is about to exit the pipe, say $\hat{V}_{f,D}$. We subtract this effect from the measured $\hat{V}_f$ of fully diffusive experiments to recover the advective component of $\hat{V}_f$. This is plotted against $\hat{V}_0$ in Fig. 4.22. For $\hat{V}_{f,D}$ we have used both $\hat{D}_M$ and an estimate of the effects of the initial transients in each experiment, also expressed as a diffusivity. We can see that the advective component of $\hat{V}_f$ is very close to the mean velocity.

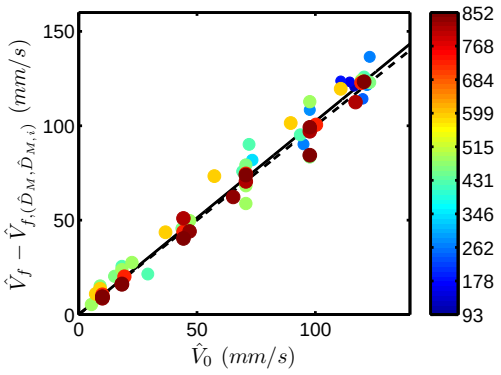

Figure 4.22: Front velocity values, $\hat{V}_f - \hat{V}_{f,D}$, plotted against the mean flow velocity, $\hat{V}_0$ for all fully diffusive experiments shown in Fig. 4.17. The colour values show the corresponding $Re\cos\beta/Fr$. The solid line is the linear fit $\hat{V}_f - \hat{V}_{f,D} = 1.024\hat{V}_0$. The broken line represents $\hat{V}_f - \hat{V}_{f,D} = \hat{V}_0$.

4.4 Discussion points

Displacement flow of two miscible iso-viscous Newtonian fluids in an inclined pipe has been investigated experimentally in the case where the displacing fluid is denser than the displaced fluid (i.e. density unstable). Our experiments have covered a broad range of the governing dimensionless parameter space (β, Re, Fr), not covered before in any experimental study.

We have classified flows as fully diffusive, instantaneous, inertial and viscous. For each classification we have provided a qualitative description of each and delineated where each flow can be found in the dimensionless plane of Fr and $Re\cos\beta/Fr$. It was also found that due to strong mixing at inclinations close to vertical, instantaneous displacements can still exist at values of χ higher than the predictions of the lubrication model ($\chi_c = 116.32$). For low $Re\cos\beta/Fr$ our results form a natural extension of those of [126], but the range of phenomena observed is significantly different here, as the pipe inclination is changed.

For each type of flow we have produced a closure approximation to the front velocity $\hat{V}_f$ and to the bulk axial diffusivity $\hat{D}_M$, that can be used for engineering calculations. When the flow is viscous the lubrication model [128] can be an effective tool to predict $\hat{V}_f$. In this case no bulk diffusion coefficient can be defined for the flow. On the other hand when the flow is

fully diffusive, the front velocity is very close to the mean imposed velocity $\hat{V}_f \approx \hat{V}_0$. It was also found that among the diffusive flows $\hat{D}_M$ exceeds the Taylor dispersion coefficient, $\hat{D}_T$, by up to an order of magnitude, over the full range of experiments. However, we must consider that buoyancy is largely responsible for enhancing the mixing, which evolves in such a way as to spread density gradients axially along the pipe. The experimental apparatus used in this study is limited in length and therefore transit time. In an oil well and over significantly longer times than possible in our experiments, one might expect that the dispersing mixture would eventually spread to such an extent that either the flow might re-laminarize or (if turbulent) would approach the turbulent Taylor dispersion coefficient from a single phase flow. Therefore, it is important to cautiously consider Taylor dispersion as a lower limit for the axial spreading.

Another important contribution of this work is in broadening our knowledge of the stabilizing/de-stabilizing effect of the mean flow on the well-studied exchange flows [111–115]. The effect of the mean flow is investigated over all inclination angles. Interestingly we have found that the imposed velocity can have quite different effects (stabilizing and/or de-stabilizing) on the flow, all controlled by the parameter $Re\cos\beta/Fr$. In particular we found that the stabilizing effect of the mean flow found in [129] is valid up to $Re\cos\beta/Fr \approx 270$. Above this limit the imposed flow was found to progressively destabilize the flow up to $Re\cos\beta/Fr \approx 500$. Above this limit the imposed flow has a neutral effect on the flow since the degree of mixing is already sufficiently high for the exchange-dominated regime to become fully diffusive.

Chapter 5

Miscible density unstable displacement flows in inclined channels: Numerical simulations

In the previous chapter we looked into the iso-viscous density unstable displacement fluids in pipe through an experimental approach. Here, as a second displacement flow geometry we consider a plane channel instead of the pipe, but keeping all the rest of the dimensionless parameters in a similar range same. This allows us to understand better whether the results we have derived experimentally are at least qualitatively universal across a range of different duct geometries. Carrying out a detailed computational study of the type of pipe flows that we have observed would necessarily require three-dimensional computations, which are prohibitively slow if one is to study wide parametric variations. The plane channel computations are two-dimensional, which has distinct advantages in terms of computational speed. Furthermore, the simpler geometry allows room for both data analysis and development of modeling approaches (see chapter 6) that would be too complex in the pipe geometry. Therefore, one can either consider the plane channel as an independent study or as one which allows new perspectives on the pipe displacement flow.

Figure 5.1 shows the geometry and notation used in the current chapter. The fluids have the same viscosity but different densities. The displacing fluid is denser than the displaced fluid. Three dimensionless groups largely describe these flows: densimetric Froude number Fr, Reynolds number Re and duct inclination β. Following the approach in [123], we are motivated to classify the different observed regimes phenomenologically in the two-dimensional $(Fr, Re\cos\beta/Fr)$-plane. We also aim to provide leading order approximations for the transitions between different regimes. The effect of the imposed flow on macroscopic diffusion is also investigated for flows

that mix significantly. Finally, stabilizing and/or de-stabilizing effects of the mean flow on buoyant exchange flows are given for a broad range of dimensionless parameters.

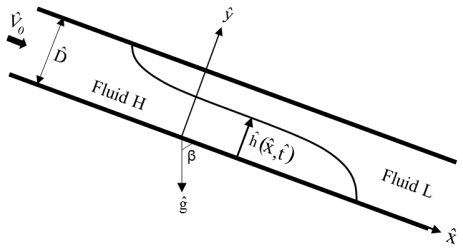

Figure 5.1: Schematic view of the numerical domain used.

Before presenting our results, we note that some caution is needed in making inferences regarding the pipe flow from the channel flow results. For example [62] studied pure exchange flows in pipes and channels in the inertially dominated regime, when the fluids mix, and have shown distinct differences in the flow structures observed. Therefore, direct comparisons are only like to be valid in regimes where viscous forces dominate in balancing buoyant and imposed pressure drops. In other cases, we emphasize that we are studying two-dimensional mixing and instability processes.

5.0.1 Parameter range

Approximately 180 simulations have been carried out covering the parameter ranges indicated in Table 5.1. We have selected a range of dimensional parameters that is similar in scope to those of our pipe flow experiments. However, one restriction is that we have not explored very high Re (typically $Re \leq 500$ for our simulations). At larger Re we would expect to enter a fully mixed turbulent regime, for which we have not explored the performance of our code. It is worth noting that in a few cases we did push up to $Re = 800$ in order to cover a wider range in dimensionless planes and better understand the flow dynamics. However most of the simulations were carried for $Re \leq 500$.

Our numerical study is complementary to that in chapter 4 in studying pipe inclinations that are far from horizontal. The dimensionless parameters governing the flow are defined exactly as for those presented in the previ-

Parameter	Range
At	$0.001,\ 0.0035,\ 0.01$
$\hat{V}_0$	$0 - 27$ (mm/s)
$\hat{\nu}$	1 (mm^2/s)
β	$[0, 10, ..., 80, 90]$ (deg)
Re	$50 - 500$
Fr	$0 - 1.92$

Table 5.1: Parameter range of our numerical study.

ous chapter for pipe flow except that $\hat{D}$ now denotes the channel thickness instead of the pipe diameter. The 3 principal parameters are the Atwood number, At, the Froude number, Fr, inclination angle, β, the Reynolds number, Re and the Péclet number, Pe. Again we have $At > 0$ since $\hat{\rho}_H > \hat{\rho}_L$ (heavy fluid displacing the light fluid in the downwards direction). Our simulations are all run for small At, where the Boussinesq approximation is valid. Finally, since our fluids are miscible there is the potential for the Péclet number $Pe = \hat{V}_0\hat{D}/\hat{D}_m$ to influence the flow (here $\hat{D}_m$ is the molecular diffusivity). Typically, for the range of flow rates in our channel and the working fluids in reality we have $Pe \gg 1$. This suggests that molecular diffusivity does not play a major role in flows studied. The range of dimensionless parameters is also shown in Table 5.1. The three most relevant dimensionless parameters are β, Re and Fr, (assuming that $At \ll 1$ and $Pe \gg 1$, as for the experimental study).

5.0.2 Simulation overview

The computations that we have carried out are fully inertial, solving the full 2D Navier-Stokes equations with liquid species modeled via a scalar concentration, c. Details of the computational methodology and the governing system of equations are given in appendix A, as well as a discussion of calibration and convergence studies for the particular code we have used. In summary, the momentum and diffusion coefficients have been discretised using a mixed finite element/finite volume method. In order to check the accuracy of the code, various simple test problems have been implemented. These include quantitative comparisons with the computational work of Sahu *et al.* [106] for displacement flows, and with Hallez & Magnaudet [62] for exchange flows in 2D channels. The same code has been used extensively in [71] for miscible core-annular Newtonian flows of differ-

ing viscosities in which pearl and mushroom shaped instabilities develop. The results therein have been benchmarked against the recent experiments of [37, 38].

As explained in appendix A in our computational work we are mostly interested in predicting global features of the displacement flow such as the flow instability, instantaneous/non-instantaneous displacements, etc., (see chapter 4 for more details). For the meshes in most of the computations we used 28 cells across the channel, refined slightly towards the walls, and 400 cells along the length of the channel. The meshes used are relatively coarse for quantitatively studying small scale features of the displacement flows, but here we want to see if the large scale features of the flow depend significantly on the mesh size. Figures 5.2a,b show the dependency of $(1-\bar{C}(\hat{t}))/(1-\bar{C}(0))$ and the position of the displacing front, $\hat{x}_{front}$, on different mesh sizes respectively.[4] The parameters used are $\beta = 40°$, $At = 0.0035$, $\hat{V}_0 = 2.6$ (mm/s) and $\hat{\nu} = 1$ (mm^2/s). The term $\bar{C}(\hat{t})$ is the average concentration over the entire computational domain at time $\hat{t}$. Naturally at $\hat{t} = 0$ (s) the quantity $(1-\bar{C}(\hat{t}))/(1-\bar{C}(0))$ approaches 1 and decreases with time as more displacing fluid (with $C = 1$) is introduced into the computational domain. The importance of this large scale measurement is that it shows how fast and efficient the displacement is i.e. how successfully the displaced fluid is being removed front the domain by the displacing liquid. The faster that $(1-\bar{C}(\hat{t}))/(1-\bar{C}(0)) \to 0$ with time, the better the displacement is. In Fig. 5.2a it is shown this large scale feature of the flow does not depend on the mesh size significantly.

The position of the displacing front $\hat{x}_{front}$ with time is given in Fig. 5.2b for the same range of mesh sizes. First of all we can see that for this particular simulation, the rate of increase of the front position experiences a different behaviour at $\hat{t} \approx 6.5$ (s) (indicated by red vertical dashed-line). Initially, mixing is controlled by inertia due to the very strong buoyancy forces. This is the reason why the front accelerates faster at the beginning. Over time, viscous forces come into balance with inertia and buoyancy and the movement of the front becomes more steady. See also [115] and [23] for transient behaviour of similar gravity currents. Secondly, we can see that the position of the front from which the front velocity can be calculated does vary slightly with the mesh size. This is because, the mixing flows would be better resolved in fine mesh sizes than the rough ones. The relative error in final front velocity value is estimated to be of order 6 %.

[4] The mesh size 28×400 for instance means 28 cells are used across the channel and 400 cells are used along it.

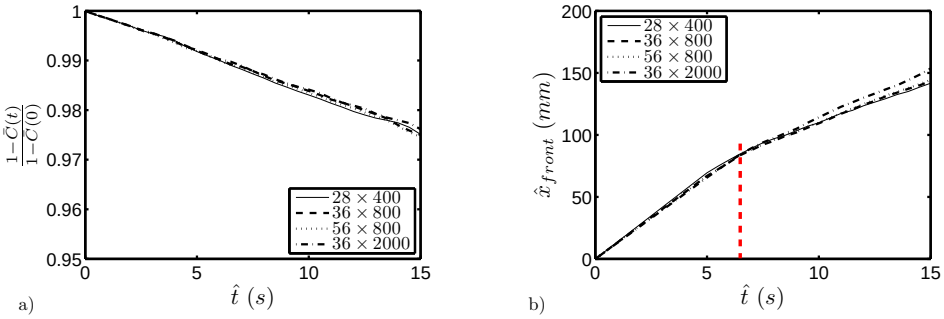

Figure 5.2: a) Evolution of $(1 - \bar{C}(\hat{t}))/(1 - \bar{C}(0))$ with time for different mesh sizes for $\beta = 40°$, $At = 0.0035$, $\hat{V}_0 = 2.6$ (mm/s) and $\hat{\nu} = 1$ (mm^2/s). Note that $\bar{C}(\hat{t})$ is the average concentration over the whole computational domain computed at time $\hat{t}$. b) The evolution of the displacing front position, $\hat{x}_{front}$, with time for different mesh sizes for the same parameters as part a. The red dashed line shows the transition between different phases of the displacement.

In the results that follow we have mostly used mesh size 28×400, in order to generate a broad data set of simulations covering the key parameters. This resolution is also consistent with a previous study (see [125]), enabling direct comparison but for a fuller range of channel inclinations. To directly study particular features of interest, e.g. the formation of the Rayleigh-Taylor mushrooms at higher inclinations, we have used a finer mesh to ensure accuracy. It was however found that although the fine mesh simulations for these flows were different from the rough mesh ones from the quantitative point of the view, the large scale and qualitative features remained the same.

5.1 Results

We now present the computational results. We first give a broad phenomenological description of the main regimes we have observed in our displacement flow simulations ($\hat{V}_0 > 0$) in §5.1.1 and 5.1.2. These flow regimes are studied through numerous tools e.g. spatiotemporal plots, velocity fields, time dependent interface evolution profiles etc. This leads to a delineation of the observed flows into a number of regimes, the boundaries of which we are able to identify in terms of the main dimensionless groups (Re, Fr, β). In the case of transversely mixed flows we analyze the effective axial dif-

fusivity (or dispersivity), from measured concentration profiles in §5.1.5. Finally in §5.1.6, we locate different flow regimes on the non-dimensional $(Fr, Re\cos\beta/Fr)$-plane, as an effective way of comparing channel and pipe flows. This enables us to better understand the essential physical mechanisms governing displacement flows over a wide range of parameters.

5.1.1 Displacement flows: main qualitative features

We first address the most basic question: namely is the global qualitative behaviour observed for pipe displacement flows ($\hat{V}_0 > 0$), as shown in the previous chapter, significantly affected by introducing the new geometry. Figure 5.3 shows typical results from our simulations, primarily illustrating the effect of inclination angle β on the flow pattern. The concentration values in the numerical simulations shown in Fig. 5.3 are calibrated so that they vary between 0 (displaced fluid) and 1 (displacing fluid). The data shown are obtained for $At = 0.0035$ and kinematic viscosity $\hat{\nu} = 1$ (mm^2/s), all with a mean imposed velocity $\hat{V}_0 = 15.7$ (mm/s). Upon comparing with Fig. 4.2 in the previous chapter, this suggests that the channel flow displacement seems to destabilize more than the pipe flows. The degree of mixing even in close to horizontal ducts seems to be much higher in channels than in analogous pipe flows.

Another key difference between channel and pipe flow displacements is that the slumping pattern is more pronounced in the latter. In fact we always observe a two-layer flow in our experiments whereas in channel flow simulations the two-layer structure is not observed as frequently. In fact the channel flows computed are more similar to a three-layer structure than to a slumping two-layer flow. This can be purely due to the geometry effects. Possibly in pipe flows, as the displacing liquid moves downstream, it squeezes the displaced layer around the pipe. This in turn helps the displaced layer to direct the displacing fluid down towards the lower pipe walls (strengthening the slumping effect). However, in channel geometry there is no such geometrical limitation that generates azimuthal motions, i.e. the flow is 2D and thus the displacing liquid can not squeeze the displaced layer towards the upper wall in the same way as in pipe. It is also worth noting that similar to the pipe exchange flows of [113], the degree of mixing and disorder in the system increases as we move towards the vertical ($\beta \to 0^\circ$). The flow pattern for more horizontal inclinations remains qualitatively similar to viscous flows of two separated layers; see $\beta = 90^\circ$ in Fig. 5.3. Note that in the case of viscous flows detecting an *interface* between the fluids is much easier than the case where mixing and instabilities are strong.

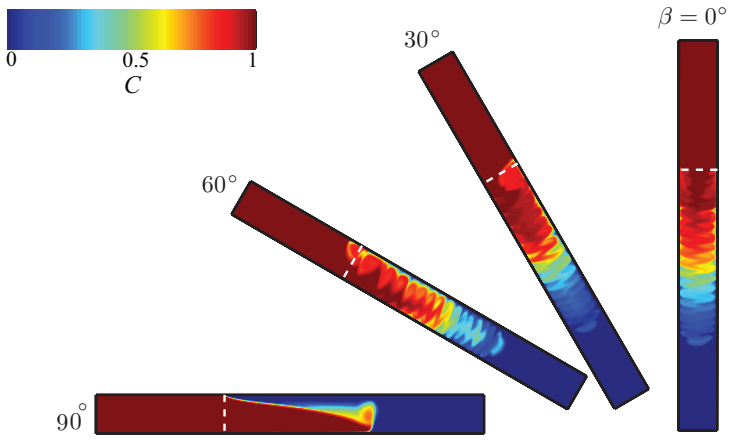

Figure 5.3: Change in iso-viscous displacement flows with β for $At = 0.0035$ and kinematic viscosity $\hat{\nu} = 1$ (mm^2/s). Mean flow speed is $\hat{V}_0 = 15.7$ (mm/s). The field of view is 1428×19.05 (mm^2) with the white dashed lines indicating the position of the imaginary gate valve. The color bar at the top left of the figure shows the corresponding concentration value, C, with 0 referring to the pure displaced fluid and 1 to the pure displacing fluid. The snapshots are taken at $\hat{t} = 25$ (s).

By interface we mean a point or points at a streamwise location where the concentration gradient transversely is high and the two fluids meet and interact. As discussed previously, since our fluids are miscible we always have a diffusive interface with concentration varying between that of the displaced and displacing fluids. However due to the large Péclet number limit we consider throughout this thesis, we can assume that the interface between the two fluids stay sharp at least when there is not a strong mixing present.

Similar to the previous chapter for pipe displacement we now try to investigate the physical features of the flows shown in Fig. 5.3 from different aspects. Figure 5.4 shows the spatiotemporal diagrams constructed from concentration fields for the same simulations as shown in Fig. 5.3. The depth-averaged concentration value $C(x,t)$ is simply the mean value of the fluid concentration averaged across the pipe at location $\hat{x}$ and time $\hat{t}$, which can be used to estimate the degree of mixing inside the pipe. As can be seen in Figs. 5.4a-d the flow stability increases as we move toward nearly horizontal inclinations. In principle we could extract statistical data on the wavelengths and growth rates of the instabilities from this data, but this is

not the aim of the present study.

In contrast to the experimental spatiotemporal diagrams shown previously, when the degree of mixing is high it is not very difficult to distinguish the front between two fluids in simulations. Of course, when the fluids become more separated the location of the advancing displacement front can be recognized clearly (Fig. 5.4d). The inverse slope of the line bounding the blue region in the spatiotemporal diagram is minus the front velocity (see the dashed line in Fig. 5.4d). This boundary can be either obtained through standard image processing methods or through the concentration evolutions profiles discussed later in Fig. 5.8. Another difference with the pipe experiments is that there is hardly any noticeable change in the spatiotemporal diagrams when the channel is inclined away from horizontal (Fig. 5.4a-c), in the sense that most of the flows shown are unstable and the mixing patterns seem to be almost the same at different inclinations.

To gain additional insight into the flow dynamics, the characteristic contours of streamwise velocity profile in the midst of computational domain ($\hat{x} = 476$ (mm) measured from the gate valve) are plotted in Fig. 5.5. the location is chosen such that the flow has had enough time to develop over time and can give information about long time behaviors which we are interested in. This way of presenting the velocity profiles mimics using an ultrasonic Doppler velocimeter (UDV) probe in the experiments (see chapter 4 for UDV measurements) and can give us better insight to the flow dynamics and its development after the start of the displacement. In all cases shown, the flow seems to develop the same over time before the displacing front reaches the probe position in the channel (see the results for $0\ s < \hat{t} \lesssim 15$ (s) for instance). Before the displacing front reaches the measurement point the flow has mostly developed to a Poiseuille-like profile.

Once the front passes the middle of the channel different patterns can form depending on the inclination angle. for instance Figs. 5.5a-c show the velocity profile across the channel for a type of flow that mixes fairly strongly across the channel. Note the positive and negative regions of velocity in these figures. The negative regions suggest that the flow is backward in those areas i.e. we have local back flows. Figure 5.5d in return confirms a slumping-type flow pattern by showing the separated positive and negative (or close-to-zero) regions of velocity. These positive and negative (or close-to-zero) regions correspond to the displacing and displaced layers respectively (see also Fig. 5.3 for $\beta = 90°$). In contrast to the experiments, even though the mixing is significant, (see Fig. 5.3 for $\beta = 0°$ for instance), the velocity profile is still not Poiseuille-like, as would be expected if the transverse mixing was complete.

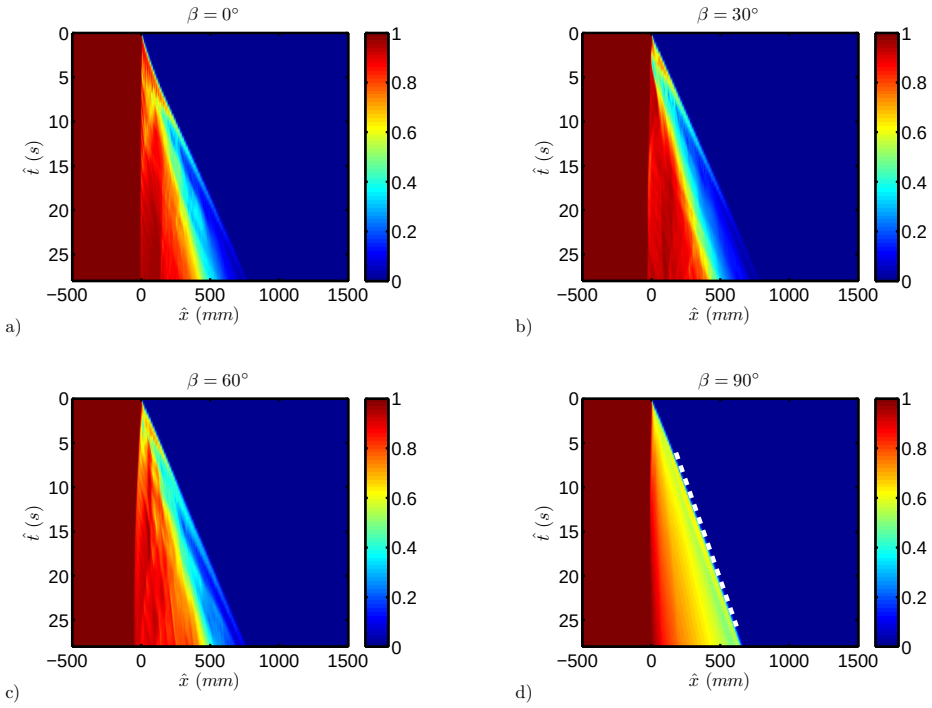

Figure 5.4: spatiotemporal diagrams of the depth-averaged concentration field obtained for the same simulations as shown in Fig. 5.3 for a) $\beta = 0°$, b) $\beta = 30°$, c) $\beta = 60°$ and d) $\beta = 90°$. The dashed line in part d indicates the position of the displacing front and its slope is $-1/\hat{V}_f$. In this case the spatiotemporal diagram gives $\hat{V}_f = 22.7$ (mm/s) and the method to be explained later in Fig. 5.8 predicts $\hat{V}_f = 22.5$ (mm/s).

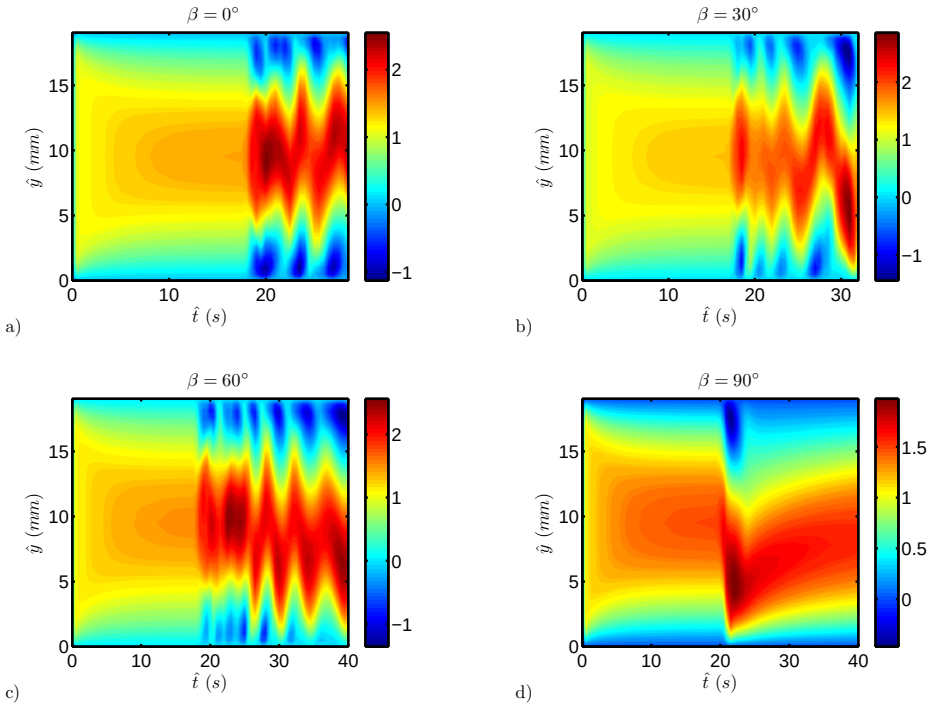

Figure 5.5: The variation of the streamwise scaled velocity component in the midst of computational domain $\hat{x} = 476$ (mm) with time $\hat{t}$ and depthwise location $\hat{y}$ for the same simulations as shown in Figs. 5.3 and 5.4 a) $\beta = 0°$, b) $\beta = 30°$, c) $\beta = 60°$ and d) $\beta = 90°$.

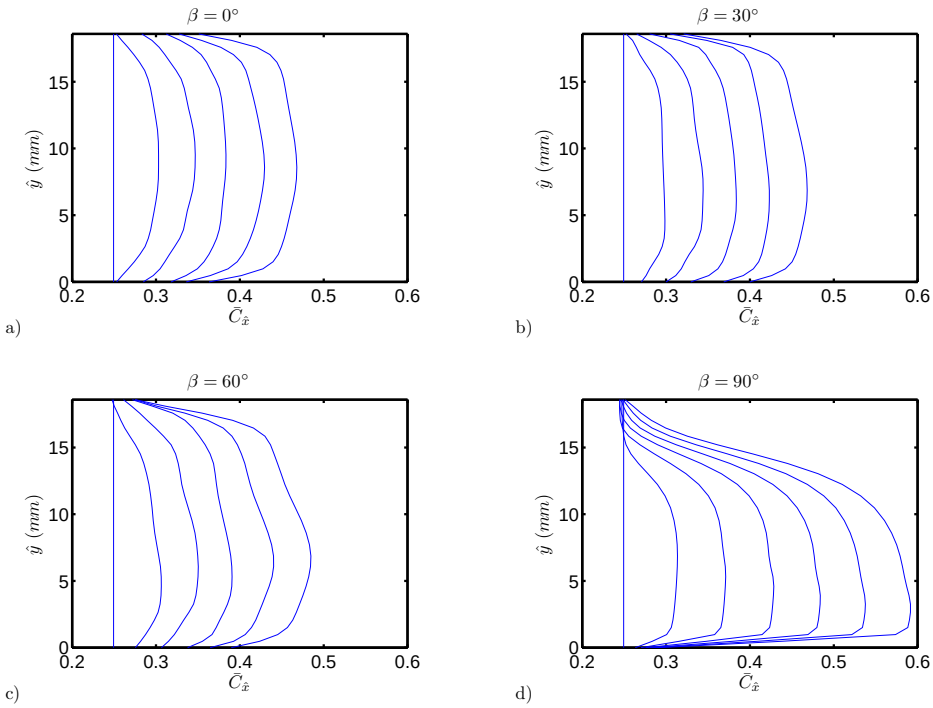

Figure 5.6: The averaged concentration, $\bar{C}_{\hat{x}}$, along the length of the computational domain plotted at different times $\hat{t} = [0, 5, ..25]$ (s) for the same simulations as shown in Figs. 5.3 and 5.4 a) $\beta = 0°$, b) $\beta = 30°$, c) $\beta = 60°$ and d) $\beta = 90°$.

The snapshots of the simulations and the velocity profiles shown in Figs. 5.3 ($\beta = 0, 30, 60°$) and 5.5a-c did not reveal much difference between the flows at different inclination angles. In the spatiotemporal diagrams the concentration values were averaged across the pipe and at each streamwise location. If we instead average the concentration values along the channel at each depthwise location, a different quantity can be obtained called $\bar{C}_{\hat{x}}$ which can give useful insight to the displacement flows. Figure shows the averaged concentration values along the channel for the same simulations shown in Fig. 5.3 at different times. It can be seen that from a-d the value of the $\bar{C}_{\hat{x}}$ increases towards the lower wall $\hat{y} = 0$ (mm) suggesting increased slumping as the channel becomes more horizontal. When the mixing is highest in Fig. 5.1.1a, the profiles of $\bar{C}_{\hat{x}}$ become nearly symmetric across the channel, which means the mixing has acted efficiently.

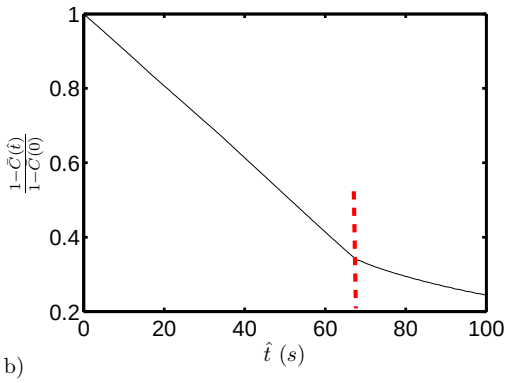

Figure 5.7: Evolution of $(1 - \bar{C}(\hat{t}))/(1 - \bar{C}(0))$ with time for the same simulation as in Fig. 5.3 ($\beta = 90°$). At $\hat{t} \approx 68$ (s), indicated by red dashed line, the displacing front reaches the end of the computational domain.

Now that we have observed the typical behaviours of the concentration values, when averaged both along the channel and across it, the next step is to consider the concentration averaged over the entire domain to obtain $\bar{C}$. As shown earlier in Fig. 5.2a, we usually translate this into a residual fraction $(1 - \bar{C}(\hat{t}))/(1 - \bar{C}(0))$. Figure 5.7 shows the residual fraction of displaced fluid for the same simulation shown in Fig. 5.3 for $\beta = 90°$. It can be seen that the slope of the average concentration quantity changes at some critical time (here $\hat{t} \approx 68$ (s)), called the breakthrough time. This change in slope happens when the displacing front reaches the end of the computational domain. After the breakthrough time the only mechanisms through which the displaced layer is removed from the channel are by the action of the displacing fluid on the displaced fluid. In the viscous regime this is by dragging the residual layers along the wall, through a combination of viscous and pressure gradient effects. In the case of unstable flows this is augmented by mixing effects.

5.1.2 Front velocity measurement and characteristics

In a long channel, the ratio of the mean flow speed to the leading front velocity, $\hat{V}_0/\hat{V}_f$, indicates the proportion of the channel displaced in an experiment or a simulation, i.e. the displacement efficiency. Consequently, it becomes important to measure $\hat{V}_f$ in a consistent and repeatable way, regardless of the degree of mixing. Whereas edge detection and calculation

of the slope from the spatiotemporal diagram has proven effective in inclinations close to horizontal (see [126]), strong transverse mixing such as in Fig. 5.3 for $\beta = 0^\circ$ (Fig. 5.4a) makes this method less reliable. Figure 5.8a shows the concentration profiles at instants of time along channel length for the same simulation as shown in Fig. 5.4c. Note that the profiles of concentration shown in Fig. 5.8a and the spatiotemporal diagram data in Fig. 5.4c are interchangeable. In contrast to the experiments where there was noise in the measured concentrations close to the lower wall of the pipe, we do not have such problem in the numerical solutions. However, to avoid very diffuse concentrations, we estimate the speed of the displacement front by the velocity of the concentration level set $C = 0.01$, (see the dashed line in Fig. 5.8a). Note that this value was chosen to be $C = 0.1$ in the experiments of the previous chapter due to image processing noise close to the lower wall of the pipe (Fig. 4.5).

Figure 5.8b shows the variation of the front velocity, $\hat{V}_f$ with time, which is quite typical of most of our simulations. Similar to the experiments, initially the front velocity accelerates as the flow initiates due to the existing large buoyancy forces. As time passes by the viscous and inertial forces start to balance the buoyant forces. This figure also shows that the choice of concentration threshold used to compute $\hat{V}_f$ does not influence the front velocity significantly.

In those cases that instability and mixing causes slow oscillation and noise in the profile of front velocity with time, or the front velocity slightly decreases or increases with time, an average value is adopted taken over long times so that the flow is well developed. Figures 5.9a,b show examples where the front velocity slightly increases and decreases with time, respectively. In such cases a long time average value is calculated, with the idea that in quantifying the front velocity, we want to compute a global value representative of the long term behaviour of system, e.g. after initial transients related to rapid mixing, buoyancy, etc have developed. We will use the measured front velocity value to understand the large scale features of the flow and the dominant dynamical trends in the system, as will be seen later.

We now explore the main characteristics of front velocity measurements across our numerical range, where we have varied inclination angles, β, density differences, At, and mean flow speeds $\hat{V}_0$. Figures 5.10a-c show $\hat{V}_f$ for simulations conducted with $At = 0.001$, $At = 0.0035$ and $At = 0.01$, respectively. Note that the front velocities are always higher than $\hat{V}_0$, due to mass conservation. For inclinations close to the horizontal, the front velocity seems to increase with β at lower $\hat{V}_0$. This effect is amplified by At.

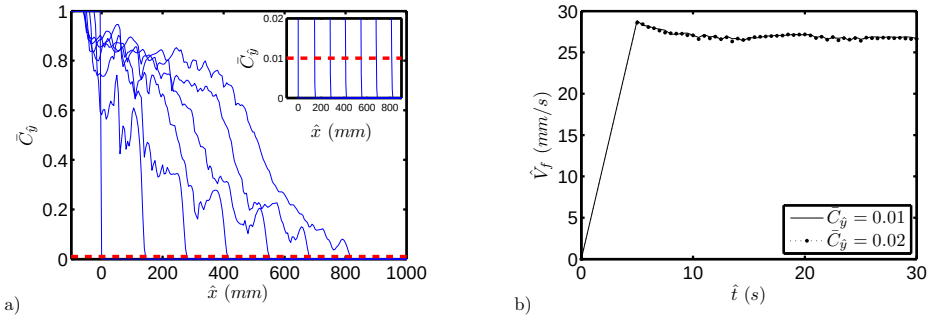

Figure 5.8: a) Evolution of the depth-averaged concentration field, $\bar{C}_{\hat{y}}$ with time, $\hat{t} = [0, 5, ..., 30]$ (s), and streamwise location, $\hat{x}$, measured from the gate valve for the same simulation as in Figs. 5.3 ($\beta = 60°$, $At = 0.0035$, $\hat{V}_0 = 15.7$ (mm/s)) and 5.4c. The dashed line shows $\bar{C}_{\hat{y}} = 0.01$ which is used for measuring the displacing front velocity, $\hat{V}_f$. The inset shows the same figure but focuses on the region $0 < \bar{C}_{\hat{y}} < 0.02$ where the interface evolution profiles intersecting with $\bar{C}_{\hat{y}} = 0.01$ can be better seen. b) The evolution of the front velocity value, $\hat{V}_f$, with time for the same simulation as part a for two different choices of intersection values namely $\bar{C}_{\hat{y}} = 0.01$ and $\bar{C}_{\hat{y}} = 0.02$. The measured front velocity value is $\hat{V}_f = 26.8$ (mm/s) in this case.

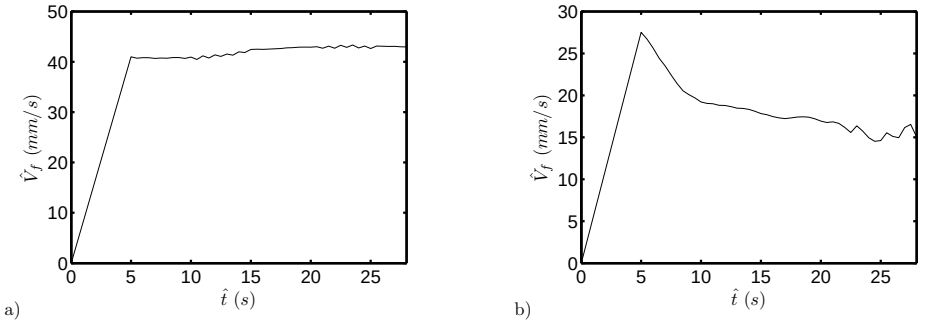

Figure 5.9: The evolution of the front velocity value, $\hat{V}_f$, with time for a) $\beta = 70°$, $At = 0.0035$, $\hat{V}_0 = 26.2$ (mm/s) and b) $\beta = 20°$, $At = 0.01$, $\hat{V}_0 = 10.5$ (mm/s) showing increase and decrease in $\hat{V}_f$ with time respectively.

Due to higher density difference of the fluids in this case, the displaced layer is pushed backwards but because of the strong stabilizing (and separating) component of the buoyancy at the interface the fluids do not mix significantly (i.e. viscous flows) and we get an overall high front velocity value. In contrast, for the larger $\hat{V}_0$ we see a slight decrease in front velocity as the channel becomes progressively horizontal. Although these trends are evident, the variations in front velocity with β are relatively modest and for $\beta < 45^\circ$ the front velocity appears to be essentially constant.

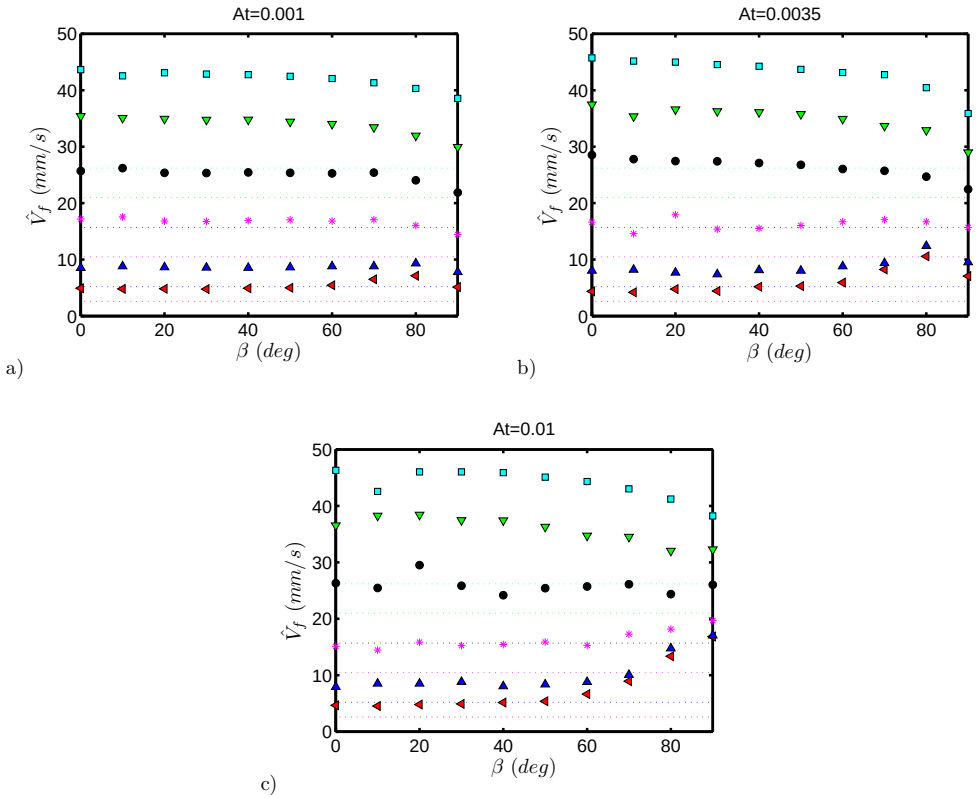

Figure 5.10: Change in displacing front velocity, $\hat{V}_f$ with inclination angle, β, and imposed velocity, $\hat{V}_0$ for $\hat{\nu} = 1$ (mm^2/s) and a) $At = 0.001$, b) $At = 0.0035$ and c) $At = 0.01$. Different markers represent $\hat{V}_0 = 2.6$ (mm/s) (◀), 5.2 (▲), 10.5 (∗), 15.7 (●), 21 (▼) and 26.2 (mm/s) (■). Thin broken lines indicate $\hat{V}_0$.

As mentioned earlier, the channel displacement flows show more instability and mixing compared to those in the pipe geometry. In the case of

the pipe displacement when the mixing is efficient, the front velocity value is very close to that of the mean flow i.e. $\hat{V}_f \approx \hat{V}_0$. However this seems to be quite different for channel flow. In fact when the fluids mix significantly, the displacing front still advances close to the channel center; see Fig. 5.3 for example. One then expects to have $\hat{V}_f \approx 1.5\hat{V}_0$ (by analogy with the Poiseuille flow). We have subtracted the front velocity values by $1.5\hat{V}_0$ and plotted the results in Fig. 5.11. At small At and lower $\hat{V}_0$ the plateau values for lower β agree well. As a side note, if we were to run the simulations over longer channel length and at larger times, the mixing could have been stronger and more complete transversely. In that case the front velocity value would be much closer to the mean flow speed $\hat{V}_f \approx \hat{V}_0$ similar to the pipe flow experiments (chapter 4).

We now proceed with a dimensionless analysis of the results, focusing on the normalized front velocity $V_f = \hat{V}_f/\hat{V}_0$. In our previous study of near-horizontal displacements [126], we were able to classify all flows in the $(Fr, Re\cos\beta/Fr)$-plane, and therefore start with this description. Figure 5.12 shows the normalized front velocity $V_f = \hat{V}_f/\hat{V}_0$, plotted against Fr and $Re\cos\beta/Fr$, for all simulations run in this study. The scale is adjusted up to $V_f = 2$. The parameter regime studied by Taghavi *et al.* [126] is marked by the broken line: $0 < Re\cos\beta/Fr < 80$ and $0 < Fr < 2$. It can be seen that the present study covers a much wider parameter range (primarily due to variations in β).

The parameter $Re\cos\beta/Fr$ is independent of $\hat{V}_0$, so that as $Fr \to 0$ we approach the exchange flow limit. For small Fr we observe a number of flows for which $V_f > 2$. We refer to these as *exchange flow dominated* similar to the pipe flow experiments and note that since we have scaled with the mean flow velocity, large $V_f > 2$ strongly suggests that some part of the velocity field is moving backwards against the mean flow, driven by buoyancy.

Another interesting comparison that can be made against the pipe experiments concerns fully mixed regions. Experimentally, it was found that $\hat{V}_f \approx \hat{V}_0$ for the unstable and diffusive flows. These flows usually appeared at high $Re\cos\beta/Fr$ or Fr values. We can see that for similar ranges of $Re\cos\beta/Fr$ or Fr in channel flow the front velocity is not close to $\hat{V}_0$ because of the different nature of the displacing front in the channel (the displacing front moves close to the channel centerline even in the cases that mixing is high).

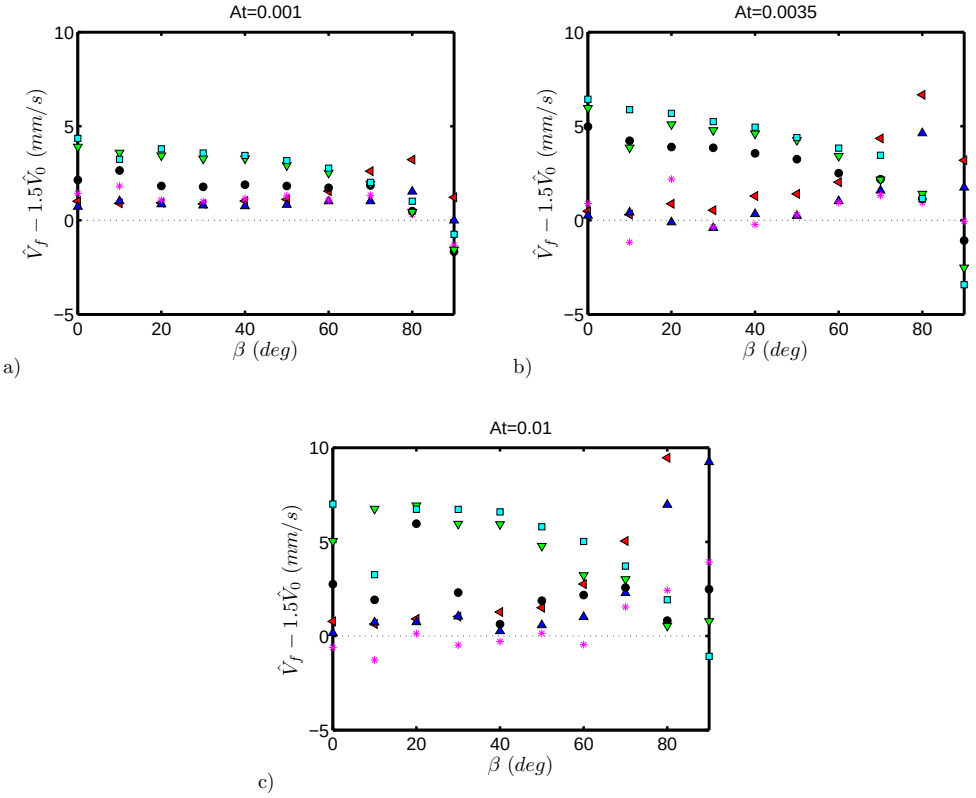

Figure 5.11: Change in $\hat{V}_f - 1.5\hat{V}_0$ with tilt angle, β, and imposed velocity, $\hat{V}_0$ for the same simulations as shown in Fig. 5.10 a) $At = 0.001$, b)$At = 0.0035$ and c)$At = 0.01$. Different markers represent $\hat{V}_0 = 2.6$ (mm/s) (◀), 5.2 (▲), 10.5 (∗), 15.7 (●), 21 (▼) and 26.2 (mm/s) (■). The dashed lines show $\hat{V}_f - 1.5\hat{V}_0 = 0$ (mm/s).

5.1.3 Instantaneous and non-instantaneous displacements

An important large scale feature of the displacement flows is whether they are instantaneous or not. By instantaneous displacement we mean that the displaced fluid does not travel upstream of the gate valve once the simulation/experiment starts. If the displacement is non-instantaneous we have inevitably had a back-flow of the displaced fluid layer. From the industrial point of view this characteristic is very important if it is sustained, as it implies a residual of displaced fluid. Ideally we want to always displace instantaneously and avoid back flow. Taghavi *et al.* [130] looked into flows with back flow in detail, for nearly horizontal channels. It was found that

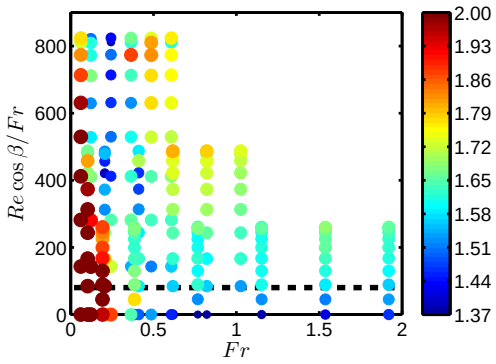

Figure 5.12: Presentation of our results for the full range of simulations: normalized front velocity $\hat{V}_f/\hat{V}_0$, plotted against Fr and $Re\cos\beta/Fr$. The rectangular area ($0 < Re\cos\beta/Fr < 80$, $0 < Fr < 2$) indicated by dashed lines, locates the range of nearly horizontal simulations and is studied in full details in [126] (also see Fig. 5.14a).

the *trailing front* can show different behaviours as the imposed velocity was varied. The trailing front is the one that moves close to the upper wall of the channel and is slower than the leading front, which is close to the lower wall. The possible movements of the trailing front can yield to instantaneous displacements, stationary layers, temporary and sustained back flows. By slowly increasing the mean flow from 0 different patterns can arise. For very low values of imposed velocity the trailing front keeps moving upstream of the gate valve due to the strong buoyancy force relative to that of the imposed flow. If the imposed flow is further increased the trailing front moves upstream of the gate valve but then stops at some location $\hat{x}$. The trailing front may remain stationary, at a critical $\hat{V}_0$, but for slightly larger $\hat{V}_0$ the trailing front returns back downstream after some time $\hat{t}$. Finally, if the mean flow is sufficiently high, the trailing front is displaced instantly by not flowing backwards, upstream of the gate valve at all.

Channel displacement flows at higher inclinations have not been studied from the perspective of the trailing front so far. Here we aim to see if stationary layers also exist at larger inclinations where the degree of mixing and instability is higher. Figures 5.13a-c show respectively snapshots, spatiotemporal diagram and the velocity field of a simulation with parameters $\beta = 60°$, $At = 0.0035$, $\hat{\nu} = 1$ (mm^2/s) and $\hat{V}_0 = 15.7$ (mm/s). Parts a and

b show that the trailing front moves upstream of the gate valve and stays at a location $\hat{x} \approx -90$ (mm) for relatively long times, up to $\hat{t} = 80$ (s). The broken line in Fig. 5.13b shows where the trailing front stops over time. Figure 5.13c shows the corresponding velocity fields to the snapshots shown in part a focusing on the above-the-gate-valve area. in the last velocity field shown, the average position of the interface between the two fluids is added, from Fig. 5.13a $h \approx 0.6$ showing the counter-current motion within the displaced layer. In fact although the interface has a positive speed towards downstream of the flow, the displaced layer has negative speed (back flow) in some parts to balance the mass flow rate to zero and ensure a stationary layer. Note that for this simulation shown a fine mesh size 56×1000 is used. The very same simulation is also run for usual 28×400 mesh size and no qualitative difference was observed. In contrast to the pipe flow experiments, we do see a significant degree of mixing in the stationary upper layer.

We now classify our displacement flows in terms of being instantaneous or non-instantaneous, over the range of parameters computed. Figure 5.14 shows such a classification in the dimensionless plane of Fr and $Re\cos\beta/Fr$. Figure 5.14a is taken from [126] and focuses only on nearly horizontal simulations. In this figure the different trailing front behaviours (sustained back flow, stationary interface, temporary back and instantaneous displacement) are all classified. Figure 5.14b on the other hand shows the results for higher inclination angles and we adopt a simpler classification: the blue data in this figure indicate instantaneous displacement and all others are non-instantaneous flows. Note that non-instantaneous displacement flows can exist sustained back flow, stationary layer and the temporary back flow as sub-categories. The prediction from the lubrication model of [128] is also added as a line to the graph.

First note that the lubrication model wrongly predicts some flows to displace instantaneously ($Re\cos\beta/Fr = 0$ and $Fr \lesssim 0.6$). in fact these flows are temporary back flows as better shown in Fig. 5.14a. Due to the wider range of parameters in the current study we can not have the same data resolution as in Fig. 5.14a. Secondly, the pattern shown in Fig. 5.14 is qualitatively similar to that of the experimental study presented in the previous chapter. As Fr increases the flows transition from non-instantaneous to instantaneous. The required Froude number for this transition decreases with $Re\cos\beta/Fr$ at least when away from nearly horizontal displacements (small $Re\cos\beta/Fr$). This is because although the inclination angle is getting closer to the vertical (enhancing counter-current flow tendencies), the increased instability and transverse mixing in the system does not allow the

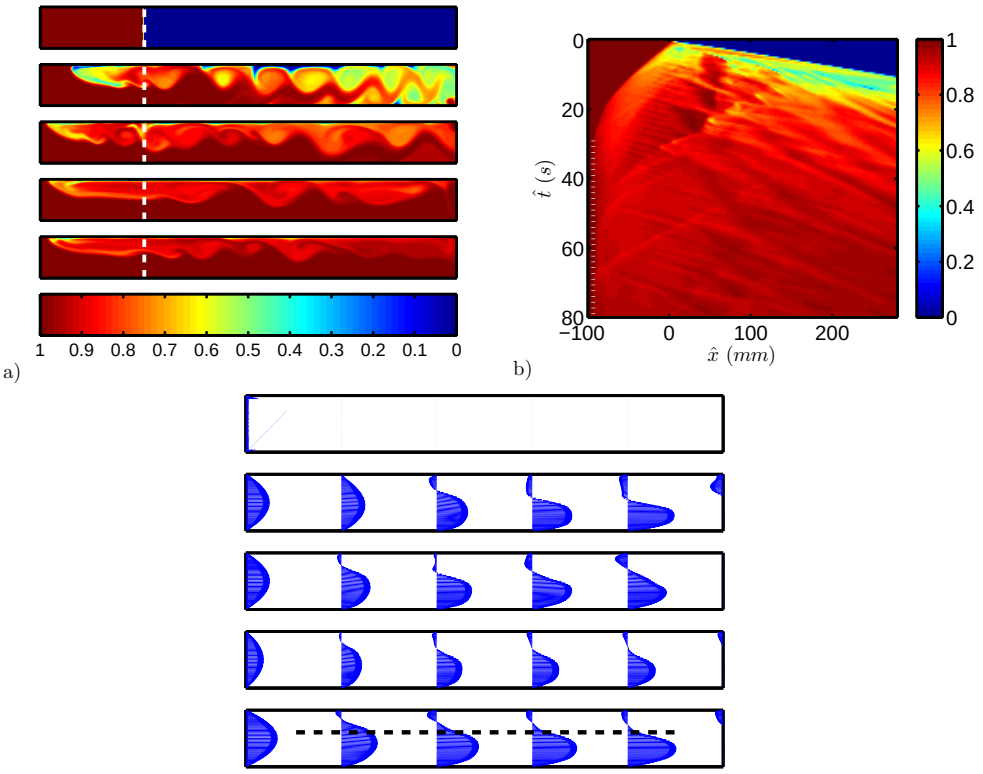

Figure 5.13: a) Snapshots of the numerical simulations at times $\hat{t} = [0, 16, ..., 64]$ (s) run for $\beta = 60°$, $At = 0.0035$, $\hat{\nu} = 1$ (mm^2/s) and $\hat{V}_0 = 15.7$ (mm/s). The last image at the bottom of the figure is the colourbar of the concentration values. The size of the domain shown is 19×400 (mm^2). The dashed lines in figure a shows the position of the imaginary gate valve b) Spatiotemporal diagram of the depth-averaged concentration field for the same simulation as part a. The white dotted line indicates the location at which the trailing front stops c) Vectors of velocity field with time for the same snapshots shown in part a for the area above gate valve. The dashed line in figure c shows the average position of the interface $h \approx 0.6$ taken from part a. We clearly see the counter-current motion within the displaced layer.

displaced layer to travel upwards.

One exotic behavior that was not observed before for nearly horizontal simulations is having back flows that repeat more than *once*. Figure 5.15

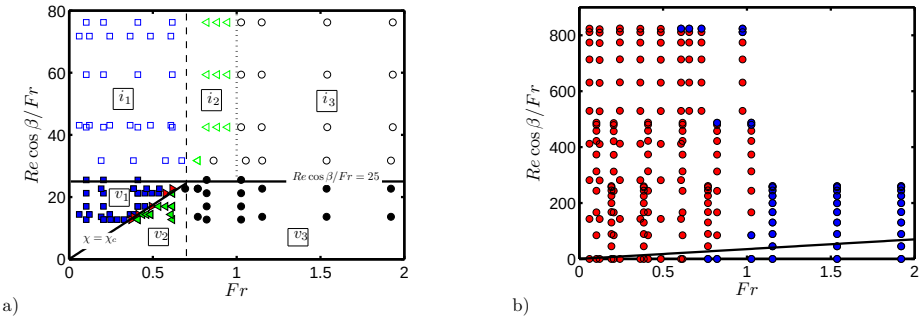

Figure 5.14: a) Classification of the results for the full range of simulations with laminar imposed flows taken from nearly horizontal data of [126]: sustained back flow (■, □), stationary interface (▶), temporary back flow (◀, ◁) and instantaneous displacement (●, ○). Data point with filled symbols are viscous and with hollow symbols are inertial. The horizontal bold line shows the first order approximation to the inertial-viscous transition ($Re\cos\beta/Fr = 25$, from [112] or [126]). The angled heavy line represents the prediction of the stationary interface from the two-layer lubrication model: $\chi = \chi_c = 69.94$. The vertical dashed-line is $\hat{V}_0/\hat{V}_t = 0.7$ and the dotted-line is $\hat{V}_0/\hat{V}_t = 1$. Regions marked with v_j and i_j (j=1, 2, 3) are viscous and inertial, respectively, with j=1, 2, 3 corresponding respectively to sustained back flow, temporary and instantaneous displacement flows. b) Classification of our results for the full range of simulations plotted in the plane of Fr and $Re\cos\beta/Fr$. The instantaneous displacement flows are colored in blue and non-instantaneous ones in red. The heavy line represents the prediction of the lubrication model for the stationary interface ($\chi_c = 2Re\cos\beta/Fr^2 = 69.94$).

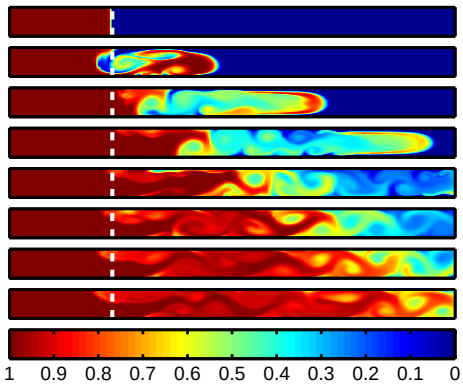

Figure 5.15: Snapshots of the numerical simulation at times $\hat{t} = [0, 2, ..., 14]$ (s) run for $\beta = 10°$, $At = 0.01$, $\hat{\nu} = 1$ (mm^2/s) and $\hat{V}_0 = 15.7$ (mm/s). The last image at the bottom of the figure is the colourbar of the concentration values. The size of the domain shown is 19×260 (mm^2). The dashed lines show the imaginary position of the gate valve in both figures. Initially there is a strong back flow that disappears around $\hat{t} \approx 4$ (s) and then reforms for $\hat{t} > 4$ (s) due to the strong back flow.

shows snapshots of a simulation for $\beta = 10°$, $At = 0.01$, $\hat{\nu} = 1$ (mm^2/s) and $\hat{V}_0 = 15.7$ (mm/s) in which the trailing front first goes upstream of the gate valve, gets displaced later ($\hat{t} \approx 4$ (s)) and then comes back up again ($\hat{t} > 4$ (s)). For temporary back flows observed before we had the trailing front going up the gate valve first and then being displaced towards downstream. In the current case it seems as if the initial buoyancy force in the streamwise direction is so large that causes a backwards burst of the displaced liquid initially. Once the flow develops over time, viscous forces can dominate the initial buoyant force and drag the displaced fluid downstream, at least temporarily. The counter current motion within the light displaced layer again starts to strengthen and thus pushes the displaced layer upstream above the initial position of the interface. Note that the mesh size used in Fig. 5.15 is 56×1000, for better resolution of the phenomenon. The simulation was also run for 28×400, where no significant qualitative difference was observed.

5.1.4 Displacing front phenomena

In the case of iso-viscous Newtonian displacement flow in pipe (chapter 4), the leading displacement front remained connected to the bulk of the displacing fluid. Even in the case of mixing and instability, although waves appeared at the interface between the fluids there was no *cutting* of the stream between the displacement front and the rest of the displacing liquid. In the case of channel displacements, we have observed a number of different phenomena at different inclination angles and/or flow rates. In this section we describe these phenomena and specify their location in the $(Fr, Re\cos\beta/Fr)$-plane.

Front detachment

One of the most common behaviors observed throughout the numerical simulation results was that the displacement front seemed to be *cut* from the rest of the displacing layer. Figure 5.16 shows an example of this for $\beta = 20°$, $At = 0.001$, $\hat{\nu} = 1$ (mm^2/s) and $\hat{V}_0 = 26.2$ (mm/s). Figure 5.16a shows the snapshots of the concentration field at different times. As shown in the figure the front initially is attached to the larger body of displacing fluid, but over time as instabilities start to form, it is cut off from the rest of the displacing layer. Evidently, as well as the instability mechanism to cut the displacing fluid stream the detached front appears to move faster than the bulk, being analogous to a falling droplet.

Figure 5.16b shows the velocity vectors corresponding to the same snapshots as in part a. Although there is an apparent change in concentration close to the frontal region, evident from the snapshots, the velocity field seems to be vary smoothly in that region. Also note the unstable nature of the velocity field in this case. Figure 5.16b shows that due to the instabilities the depthwise component of the velocity changes sign over time at a location, (observe e.g. the highlighted box in this figure). Although the front is separated from the bulk of the displacing fluid initially, it mixes with the displaced fluid over longer times and finally diminishes (Fig. 5.16a). In order to better understand the formation and diminishing processes, the concentration values are averaged across the channel at each location and are plotted in Fig. 5.16a. These profiles correspond to the same instants of time as in parts a and b. It can be seen that there is an obvious change in concentration close to the frontal region as the displacing front is cut by the instabilities.

The type of instabilities observed in Figs. 5.3 and 5.16a are quite com-

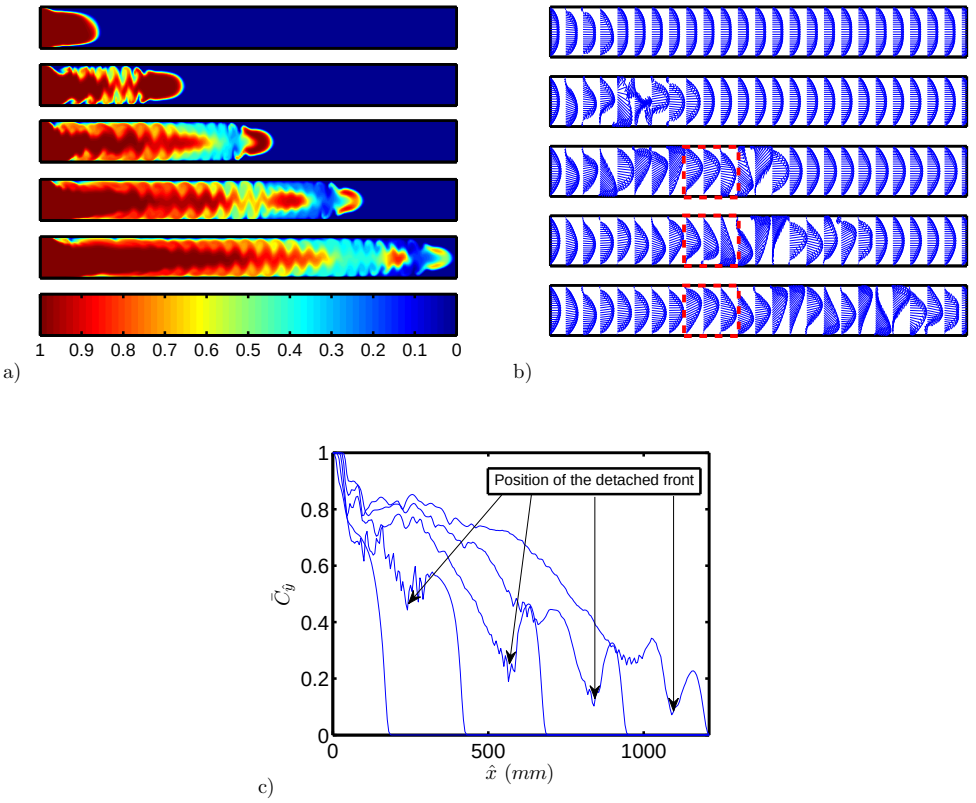

Figure 5.16: a) Snapshots of the numerical simulation at times $\hat{t} = [5, 13, ..., 29]$ (s) run for $\beta = 20°$, $At = 0.001$, $\hat{\nu} = 1$ (mm^2/s) and $\hat{V}_0 = 26.2$ (mm/s) showing the detachment of the front from the displacing fluid layer. The last image at the bottom of the figure is the colourbar of the concentration values. The size of the domain shown is 19×1210 (mm^2) starting from gate valve position $\hat{x} = 0$ (mm). b) Vectors of velocity field with time for the same simulations shown in part a. The dashed red boxes added show the oscillating behavior of the flow better. c) Evolution of the depth-averaged concentration field, $\bar{C}_{\hat{y}}$, with time and streamwise location for the same simulation as in parts a and b. The arrows point the position of the detached front that disappears over time.

mon in channel displacement flows. Due to this we have decided to take a closer look at these instabilities and extract more physical information from the available data. Figure 5.17 shows a representative case from the same numerical simulation as Fig. 5.16 except at time $\hat{t} = 29$ (s). Figure

5.17a is basically the last snapshot in Fig. 5.16a plotted on a larger scale for convenience. Figure 5.17b shows the contour of the speed $\hat{V} = \sqrt{\hat{V}_x^2 + \hat{V}_y^2}$ (here $\hat{V}_x$ and $\hat{V}_y$ are the dimensional streamwise and depthwise velocity components respectively). We can see that although the velocity is far from a Poiseuille profile, the high speed regions remain towards the centre of the channel, with unstable oscillations mimicking those in the concentration.

Figure 5.17c shows the vorticity contours, $\hat{\omega}$, for the same snapshot as in part a:

$$\hat{\omega} = \frac{\partial \hat{V}_y}{\partial \hat{x}} - \frac{\partial \hat{V}_x}{\partial \hat{y}}.$$

We see that positive vorticity is mostly located on the upper half of the channel whereas the negative vorticity is in the lower half, as would be expected for a channel flow. However, on close inspection we see that there are also positive values of $\hat{\omega}$ close to the lower wall and negative values close to the top wall, which is not expected. This indicates the existence of tiny rotational regions of current causing local back flow and mixing. The main cause of these local back flows must be the instabilities close to the interface and within the fluid layers. To see this interesting effect better we have plotted in Fig. 5.17d the velocity vectors focusing on this back-flow area highlighted in Fig. 5.17c. The figure clearly shows the velocity reversal close to the lower wall of the channel causing positive vorticity. Just an additional comment is to note that the type of instabilities and the related mechanisms are very similar when either fine or rough meshes are used.

Leaking front

Another interesting phenomenon observed in a few simulations was the formation of a second displacing front from within the displacing fluid region. Figure 5.18 shows an example of this for $\beta = 80°$, $At = 0.0035$, $\hat{\nu} = 1$ (mm^2/s) and $\hat{V}_0 = 15.7$ (mm/s). Figure 5.18a shows the snapshot of the simulations at successive times. At time $\hat{t} \approx 22.5$ (s) an extra tip region starts to form at the displacing front. We call this a *leaking front*, as displacing fluid appears to *leak* from the main front into this region. Figure 5.18b shows the interface evolution profiles for the same snapshots as in part a. The figure clearly shows that a jump in the averaged concentration value starts to form close to the front. In contrast to the detached front discussed earlier, the leaking front seems to strengthen and enlarge over time but does not detach and appears to also dissipate via diffusive mixing.

Again the results presented in Fig. 5.18 are for a finer mesh of size

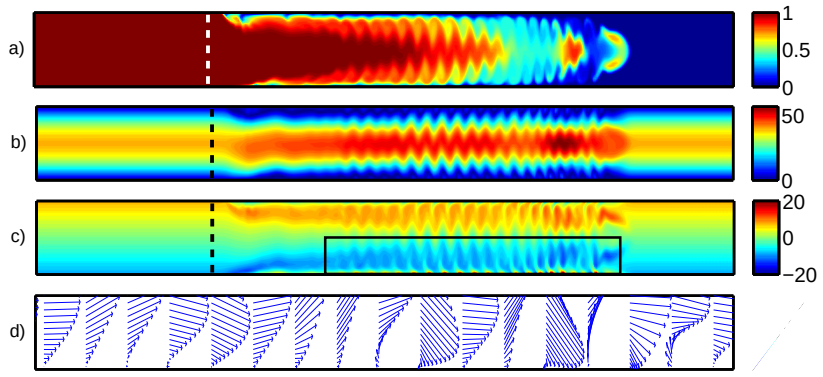

Figure 5.17: a) Snapshot of the numerical simulation at time $\hat{t} = 29$ (s) run for the same parameters as in Fig. 5.16. The field of view in parts a)-c) is 19×2000 (mm^2) and the broken vertical line shows the imaginary position of the gate valve $\hat{x} = 0$ (mm). b) contours of the speed $\hat{V} = \sqrt{\hat{V}_x^2 + \hat{V}_y^2}$ in mm/s. c) contours of vorticity in $1/s$ defined as $\hat{\omega} = \partial\hat{V}_y/\partial\hat{x} - \partial\hat{V}_x/\partial\hat{y}$. The solid box shows the region magnified below in part d. d) Vectors of the velocity field for the boxed-region shown in part c showing back flow close to the lower wall.

56×1000. However, qualitative similar results were obtained for the coarser usual mesh size of 28×400.

Dispersive spike formation

In the case when the channel was inclined strictly horizontally, another interesting displacement front pattern was observed. Figure 5.19 shows the existence of a dispersive spike-like region at the frontal region. Figure 5.19a shows snapshots of a typical simulation carried out for $\beta = 90°$, $At = 0.001$, $\hat{\nu} = 1$ (mm^2/s) and $\hat{V}_0 = 10.5$ (mm/s). At time $\hat{t} \approx 36$ (s) the spike starts to form and extends progressively. Always about the interface we have secondary flows that tend to disperse fluid that diffuses. Here the front is slumped towards the bottom of the channel, but the secondary flow forms a dispersive tip above and slightly ahead of the advancing front. The profiles of depth-averaged concentration are given in Fig. 5.19b, and appear as a small spike, just ahead of the main front. The inset in Fig. 5.19b focuses on the range $0 < \bar{C}_{\hat{y}} < 0.01$ to show the formation of the spike better. It

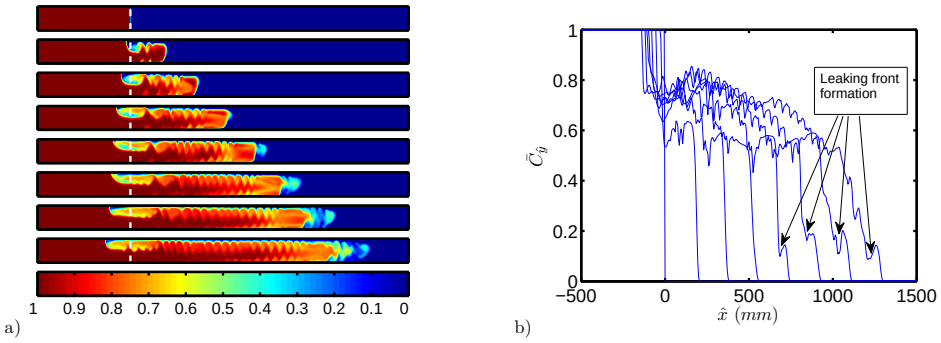

Figure 5.18: a) Snapshots of the numerical simulation at times $\hat{t} = [0, 7.5, ..., 52.5]$ (s) run for $\beta = 80°$, $At = 0.0035$, $\hat{\nu} = 1$ (mm^2/s) and $\hat{V}_0 = 15.7$ (mm/s) showing the acceleration of the tip of the displacement front and finally its separation from the displacing layer. The last image at the bottom of the figure is the colourbar of the concentration values. The size of the domain shown is 19×2000 (mm^2). The broken lines indicate the position of the imaginary gate valve $\hat{x} = 0$ (mm). b) Evolution of the depth-averaged concentration field, $\bar{C}_{\hat{y}}$, with time and streamwise location for the same simulation as in parts a. the acceleration and tip separation effect is also evident from the evolution profiles.

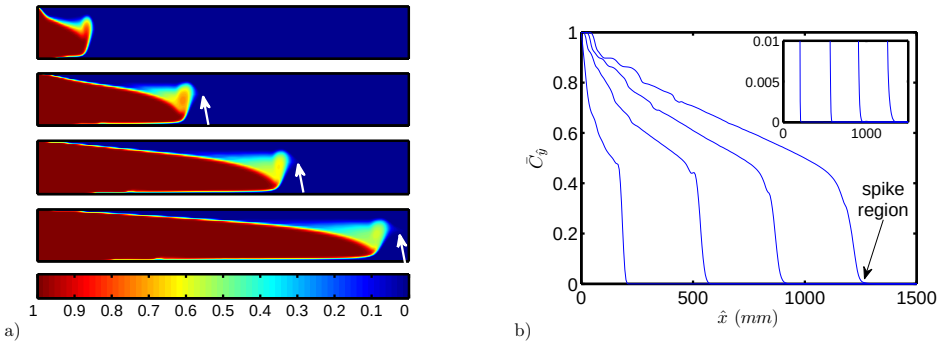

Figure 5.19: a) Snapshots of the numerical simulation at times $\hat{t} = [12, 36, 60, 84]$ (s) run for $\beta = 90°$, $At = 0.001$, $\hat{\nu} = 1$ (mm^2/s) and $\hat{V}_0 = 10.5$ (mm/s) showing the appearance of spike at the displacement tip. The last image at the bottom of the figure is the colourbar of the concentration values. The size of the domain shown is 19×1307 (mm^2) starting from the gate valve on the left $\hat{x} = 0$ (mm). b) Evolution of the depth-averaged concentration field, $\bar{C}_{\hat{y}}$, with time and streamwise location for the same simulation as in parts a. The inset focuss on the region $0 < \bar{C}_{\hat{y}} < 0.01$ to show the spike effect better.

is worth noting that the spike formation at the displacement front was not observed in density unstable pipe experiments. A similar dispersive spike phenomenon was observed in density stable iso-viscous Newtonian flows at strictly vertical inclination angles, as discussed in chapter 3. Note that the results presented in Fig. 5.19 were obtained for a fine mesh size: 56×1000. Qualitatively similar results were observed in simulations run for the usual mesh size of 28×400.

Overall displacing front classification

In the previous section different phenomena related to the displacement front were explained namely the front detachment, leaking front and dispersive spikes. Now let us see where these flows are located on the dimensionless plane of Fr and $Re\cos\beta/Fr$. Figure 5.20 shows this classification. The first thing to note is that in a large number of simulations front detachment has been observed. There are only a few cases with leaking front and the dispersive spike-like fronts appear only for $Re\cos\beta/Fr = 0$, meaning strictly horizontal displacements. It seems as if these flows can be septated from the rest of the flows (in which no particular pattern is observed at the front) by

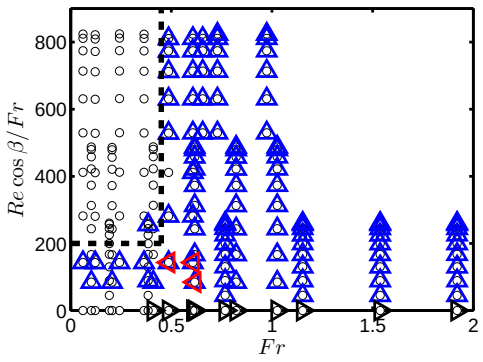

Figure 5.20: Classification of our results for the full range of simulations plotted in the plane of Fr and $Re\cos\beta/Fr$. The flows in which front detachment occurs are marked by ($\triangle$). Data with accelerating fronts that form a dispersive spike are marked by ($\triangleright$) and flows with leaking front are shown by ($\triangleleft$). The heavy dashed lines, $Fr = 0.45$ and $Re\cos\beta/Fr = 200$, roughly separate these flows from the rest.

the lines $Fr = 0.45$ and $Re\cos\beta/Fr = 200$. It is also interesting to note that the leaking front flows lie between dispersive spike and detached-front flows. The area in which none of these frontal phenomena are observed ($Fr < 0.45$ and $Re\cos\beta/Fr > 200$) seems to include mostly the exchange dominated flows; compare with Fig. 5.14. We usually have high degree of mixing in this flows.

The Rayleigh-Taylor limit

Given the fact that the displacement configuration in our study is density unstable i.e. heavy fluid on top of the light, we expect to observe flows that are phenomenologically similar to Rayleigh-Taylor type instabilities in some limits of our parameter space. These are characterised by the formation of mushroom-like plumes within the heavy upper layer; see e.g. [13]. Figure 5.21a shows snapshots of a displacement flow in a strictly vertical channel ($\beta = 0°$) for $At = 0.001$, $\hat{\nu} = 1$ (mm^2/s) and $\hat{V}_0 = 2.6$ (mm/s). The figure clearly shows the formation of Rayleigh-Taylor mushroom structure as time evolves. This is for a relatively low imposed flow rate. Due to both mixing and the imposed flow, the mushroom-like structure is not sustained over longer times. Figure 5.21b shows the corresponding velocity fields to the

snapshots depicted in part a. It is interesting to note the backward velocity vectors close to the gate valve where the mushroom initially forms.

The mushroom patterns shown in Fig. 5.21a & b were obtained for a strictly vertical channel. It is interesting to see if the same effect is observed at small inclinations away from the vertical. Figure 5.21c shows snapshots of simulations obtained for the same parameters as in Fig. 5.21a except for $\beta = 10^\circ$. We see that due to the effects of slumping the Rayleigh-Taylor mushroom pattern does not form anymore, i.e. symmetry is broken in the initial onset of flow, even though β is very small. Figure 5.21d shows the corresponding velocity vectors, with an upstream component to the velocity when close to the gate valve. Note that the simulations shown in Fig. 5.21 were obtained for a mesh size 56×1000. The same qualitative patterns were observed for the usual mesh size of 28×400.

Cutting of the fluid streams

As mentioned earlier, channel flow displacements in the current study were run over a range of imposed velocities $\hat{V}_0 \in [0 - 27]$ (mm/s). For small imposed velocities we inevitably recover results close to the exchange flow of two fluids; see [111–115] and [62–64] for exchange flow experiments and numerical simulations, respectively. Hallez *et al.* looked into the exchange flows in both channel [63] and pipe [62, 64], using direct numerical simulations. They discovered that there are essential differences in 2D and 3D flows which arise from different dynamic vorticity fields. From this perspective, strong and coherent vortices found in channel flows enables the vortices to cut the layers of pure fluid that feeds the fronts in a *periodic* manner. In contrast the vortical motions in 3D are such that they promote segregation effect and thus avoid completely cutting the pure fluid layers; see [62]. In our numerical simulation for channel displacement flows we also observed this type of oscillatory behavior in the leading front velocity. Figure 5.22 shows a representative case obtained for $\beta = 20^\circ$, $At = 0.01$, $\hat{\nu} = 1$ (mm^2/s) and $\hat{V}_0 = 2.6$ (mm/s). Figure 5.22a shows the snapshots of the simulations where the mixing is fairly strong. Due to the low imposed velocity in this case ($\hat{V}_0 = 2.6$ (mm/s)), it is very likely that we are in exchange dominated regime. The flow instability and back flow are common features of such flows a least at higher inclination angles. Figure 5.22b shows the corresponding spatiotemporal diagram of the same simulations. The figure shows unevenness in the boundaries of the two displacement front, due to oscillation. Note that the image contrast is adjusted here to show the slight variation and unevenness in concentration values better. The uneven os-

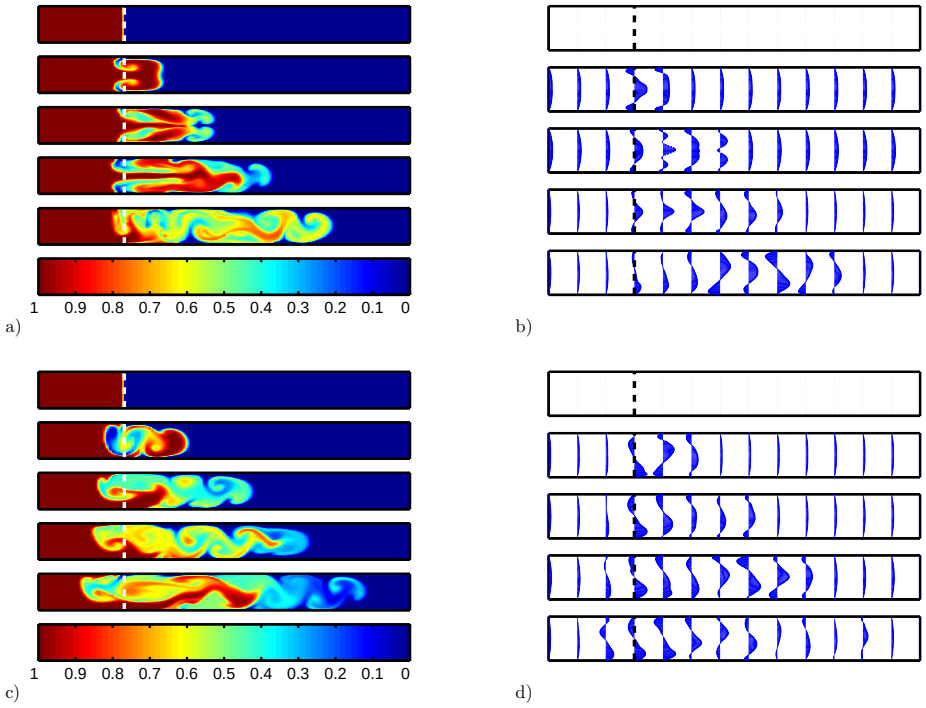

Figure 5.21: a) Snapshots of the numerical simulation at times $\hat{t} = [0, 6.5, ..., 26]$ (s) run for $\beta = 0°$, $At = 0.001$, $\hat{\nu} = 1$ (mm^2/s) and $\hat{V}_0 = 2.6$ (mm/s) showing the formation of Rayleigh-Taylor instability. The last image at the bottom of the figure is the colourbar of the concentration values. The size of the domain shown is 19×260 (mm^2). b) Velocity vector-field with time for the same simulations shown in part a. The dashed lines show the imaginary position of the gate valve in both figures. Figures c and d are run for the exact same parameters as to a and b except $\beta = 10°$.

cillations in the depth-averaged concentration shown in Fig. 5.22b reflect the oscillations present in the front velocity due to the vortical structures. Figures 5.22c,d show the leading and trailing front velocities, which exhibit clear oscillations. As shown in Fig. 5.22c, at longer the value of the leading front velocity fluctuates around an almost-constant value ($\hat{V}_f \approx 5$ (mm/s)) as time passes by. The oscillations observed repetitively cut the pure fluid layers feeding the fronts. This cut-off in the feeding layers can accelerate and/or decelerate the front (see [62] for similar effects in exchange flows). Figure 5.22d shows a similar phenomenon at the trailing front, where also the pure fluid layers are cut. Note that here we have a small imposed velocity that breaks the symmetry of the two fronts. As before, the simulations in Fig. 5.22 were obtained for a mesh size 56×1000, but with a qualitatively similar oscillatory pattern in front velocity observed for coarser mesh size of 28×400.

It is now interesting to understand to what extent the oscillatory pattern in front velocity persists as the imposed velocity, $\hat{V}_0$, increases. Figure 5.23 shows that these flows can be observed over almost all values of $Re\cos\beta/Fr$ (or equivalently inclination angles). Secondly, we can see that the oscillation in front velocity stops for $Fr \gtrsim 0.3$. In fact there can be drawn an almost clear boundary between oscillatory and non-oscillatory flows in dimensionless plane of Fr and $Re\cos\beta/Fr$. It is interesting to note that most of the flows that were not marked as detached fronts, leaking fronts or dispersive spikes in Fig. 5.20 fall in the oscillating flow boundaries in Fig. 5.23.

5.1.5 Macroscopic diffusion

Similar to the previous chapter for pipe displacement flows, in this section we focus on those simulations where the degree of transverse mixing is high. In such cases we expect that advective transport due to the mean flow will be supplemented by diffusive spreading along the pipe. Debacq *et al.* [33, 34] used a similarity scaling for exchange flows in vertical pipes to collapse profiles of the cross-sectionally averaged concentration C, measured at each location $\hat{x}$ and time $\hat{t}$, onto a master curve defined with respect to $\hat{x}/\sqrt{\hat{t}}$. On fitting the master curve to an error function form, estimates were derived for the macroscopic diffusion of the mean concentration along the pipe. Seon *et al.* [114] followed the same approach for inclined pipes (as have we in the previous chapter) and we adopt an analogous approach here for channel flows.

In the presence of a mean flow ($\hat{V}_0$), when the flows fully mix transversely it is logical to assume a core of the mixture traveling with the speed $\hat{V}_0$

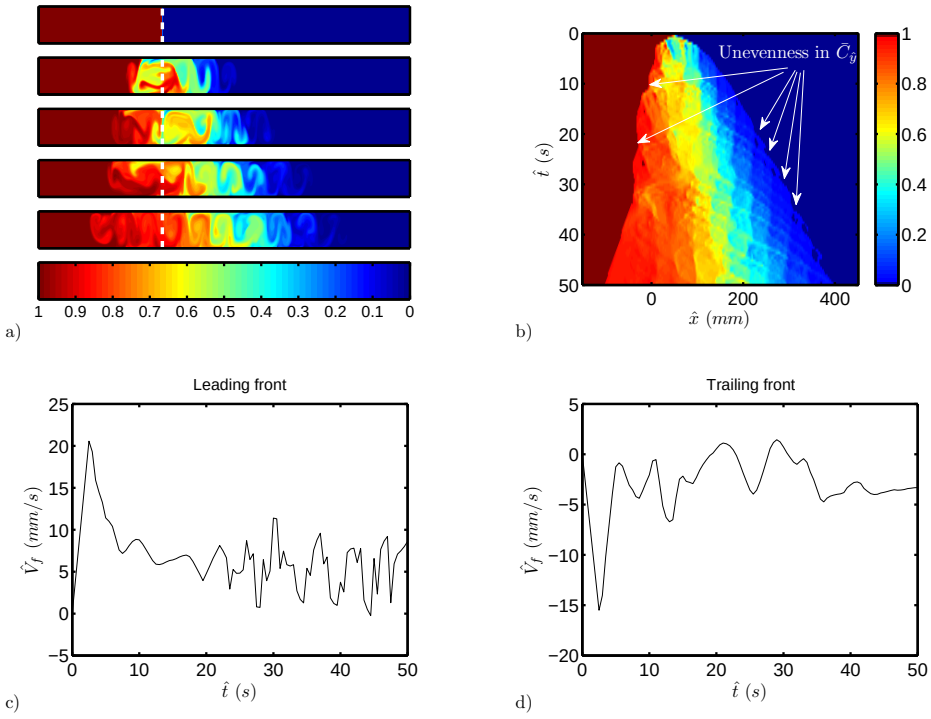

Figure 5.22: a) Snapshots of the numerical simulation at times $\hat{t} = [0, 10, ..., 40]$ (s) run for $\beta = 20°$, $At = 0.01$, $\hat{\nu} = 1$ (mm^2/s) and $\hat{V}_0 = 2.6$ (mm/s). The last image at the bottom of the figure is the colourbar of the concentration values. The size of the domain shown is 19×600 (mm^2). b) Spatiotemporal diagram of the averaged concentration values, $\bar{C}_{\hat{y}}$ for the same simulation as part a. Note that the image contrast is adjusted to show the slight variation and unevenness in concentration values better. c, d) The evolution of the leading and trailing front velocity values respectively with time for the same simulation as part a showing oscillation with time.

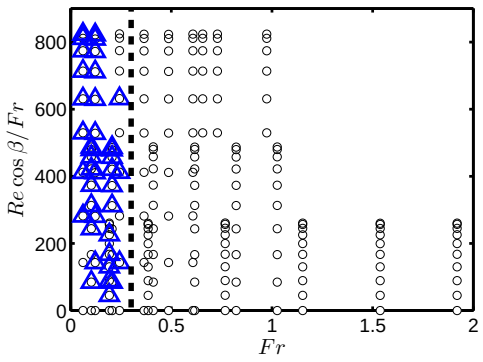

Figure 5.23: Classification of our results for the full range of simulations plotted in the plane of Fr and $Re\cos\beta/Fr$. The flows with oscillatory behavior in the front velocity are marked with superposed triangles. The heavy dashed line, $Fr = 0.3$ roughly indicates the boundary between oscillatory and non-oscillatory flows.

and therefore use $(\hat{x} - \hat{V}_0\hat{t})/\sqrt{\hat{t}}$ as a similarity scaling. Figure 5.24 shows two examples of this for $\beta = 20°$, $At = 0.01$ and $\hat{\nu} = 1$ (mm^2/s). In Fig. 5.24a,b the mean flow speeds are $\hat{V}_0 = 5.3$, 10.5 (mm/s) respectively. We can see that all the concentration evolution profiles have collapsed onto one curve. The solid line shows a curve fit of the form $C = 0.5\text{erfc}(\frac{\hat{x}-\hat{V}_0\hat{t}}{2\sqrt{\hat{D}_M\hat{t}}})$, motivated by the analytical solution to the linear diffusion equation. In Fig. 5.24a we find $\hat{D}_M = 1.09 \times 10^{-4}$ (m^2/s) and in Fig. 5.24b we find $\hat{D}_M = 1.97 \times 10^{-4}$ (m^2/s). Here $\hat{D}_M$ is the macroscopic diffusion coefficient. Note that similar to the pipe flow experimental findings in chapter 4, the macroscopic diffusion coefficient for channel flow also seems to increases with mean flow speed, as shown in Figs. 5.24a and b. Again it is worth noting that for quantitative measurement of the macroscopic diffusion coefficient a much finer mesh is advisable. However, here we are looking only for the main qualitative for trends: the large scale features and a physical interpretation of the results.

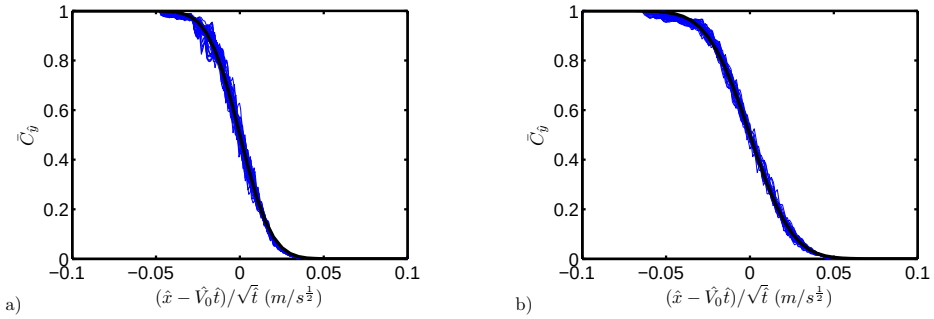

Figure 5.24: Collapse of depth-averaged concentration profiles with $(\hat{x} - \hat{V}_0\hat{t})/\sqrt{\hat{t}}$ for $\beta = 20°$, $At = 0.01$, $\hat{\nu} = 1$ (mm^2/s) and a) $\hat{V}_0 = 5.3$ (mm/s) b) $\hat{V}_0 = 10.5$ (mm/s). The solid lines show the error-function fit obtained for $\hat{D}_M = 1.09 \times 10^{-4}$ (m^2/s) and $\hat{D}_M = 1.97 \times 10^{-4}$ (m^2/s) for parts a and b respectively.

We now consider the variation in diffusive regime with different inclination angles. Figures 5.25a-d show the collapse of depth-averaged concentration profiles with $(\hat{x}-\hat{V}_0\hat{t})/\sqrt{\hat{t}}$ for the same simulations as shown in Figs. 5.3 and 5.4. Snapshots are also added to the figures as inset for better understanding the flows. It can be seen that when the mixing is very strong and efficient ($\beta = 0°$ in Fig. 5.25), the collapsed profiles fall into an almost exact error-function shape. Waves and slight deviations from the fitted curve are due to short time behavior and the initial stages of mixing which we have seen can be quite structured. At longer times we perhaps will observe a smoother fit for diffusive flows. As we move away from the strictly vertical channel (weaker mixing, more slumping) the collapsed profiles start to deviate from the diffusive flow fit function. This deviation appears mostly in the form of a drop in concentration values for $(\hat{x} - \hat{V}_0\hat{t})/\sqrt{\hat{t}} < 0$, meaning the region upstream the mixing core (see Figs. 5.25b,c). The deviation from the symmetric error function fit means that the mixing downstream and upstream of the mixing core has different qualities. In fact in most of the diffusive simulations observed, the downstream zone of the mixing core was found to be more diffusive than the upstream region. In other words, mixing close to the leading front is stronger than that close to the trailing front (see Fig. 5.3 for $\beta = 30°$ or $\beta = 60°$ for instance). For the (nearly) horizontal cases where the flow is more segregated at the interface and the mixing is not as strong, the profiles do not collapse well onto the error function fit at all, but are more advective; see Fig. 5.25d. In this case a more sensible

scaling parameter to use is $\hat{x}/\hat{t}$ rather than $(\hat{x} - \hat{V}_0\hat{t})/\sqrt{\hat{t}}$, as shown in the inset to Fig. 5.25d.

We now focus only on those simulations for which we have been able to reliably collapse the data at long times, using the similarity scaling $(\hat{x} - \hat{V}_0\hat{t})/\sqrt{\hat{t}}$, and have been able to estimate a macroscopic diffusion coefficient from the master curve. We call these flows *fully diffusive*. Figure 5.26 plots the measured macroscopic diffusion coefficients for displacement flows at different inclination angles and for the three Atwood numbers: $At = 0.001$, $At = 0.0035$ and $At = 0.01$. Two clear conclusions can be made, similar to the experimental study for pipe flow displacements: within the range of fully diffusive experiments, $\hat{D}_M$ increases with both inclination angle, β, and mean flow speed, $\hat{V}_0$. Also note that due to the more unstable nature of the flow in channel displacement over the pipe, fully diffusive flows can also be found for smaller At number. In the case of pipe flow, the fully diffusive flows were only found for $At > 0.0035$ keeping all the other parameters the same, Fig. 4.13.

The trends shown in Figs. 5.26a-c are interesting in suggesting two independent factors contributing to $\hat{D}_M$. The relatively large values of $\hat{D}_M$ confirms that the diffusive transport cannot be molecular in origin, but is due to advection, i.e. this is largely dispersion. The flows are disordered and relatively well-mixed transversely, to all appearances locally turbulent. In such cases a scaling of the dispersivity with length and velocity scales is expected that are relevant to the eddy structure. This is evidently complex in general, but we might guess that the relevant velocity will scale approximately with either the inertial velocity or the mean flow, depending on the relative strengths of buoyancy or the mean flow in driving the mixing. To explore this, we plot $\hat{D}_M/(\hat{V}_t\hat{D})$ and $\hat{D}_M/(\hat{V}_0\hat{D})$ in the $(Fr, Re\cos\beta/Fr)$-plane (see Fig. 5.27), the two axes reflecting the competition between inertia from the mean flow and buoyancy (Fr) and between buoyancy driven motion and viscous dissipation of that motion $(Re\cos\beta/Fr)$, respectively. Note that $\hat{V}_t$ is a velocity scale obtained by the balance between inertia and buoyancy $(\hat{V}_t = \sqrt{At\hat{g}\hat{D}})$.

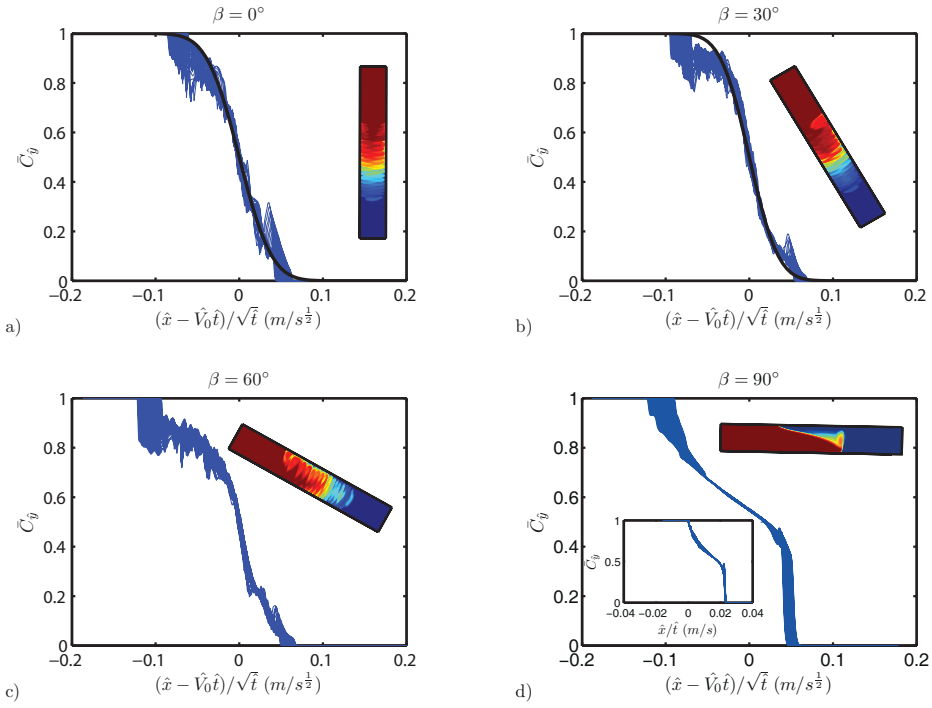

Figure 5.25: Collapse of depth-averaged concentration profiles with $(\hat{x} - \hat{V}_0\hat{t})/\sqrt{\hat{t}}$ for the same simulations as shown in Figs. 5.3 and 5.4 a) $\beta = 0°$, b) $\beta = 30°$, c) $\beta = 60°$ and d) $\beta = 90°$. The solid line in Figs. 5.25a and b show the error-function fits with $\hat{D}_M = 4.6 \times 10^{-4}$ (m^2/s) and $\hat{D}_M = 3.7 \times 10^{-4}$ (m^2/s) respectively. The upper right insets show the qualitative flow pattern in each case already shown in Fig. 5.3. In part d the lower left inset shows the collapse of the concentration profiles when $\hat{x}/\hat{t}$ is used instead of $(\hat{x} - \hat{V}_0\hat{t})/\sqrt{\hat{t}}$.

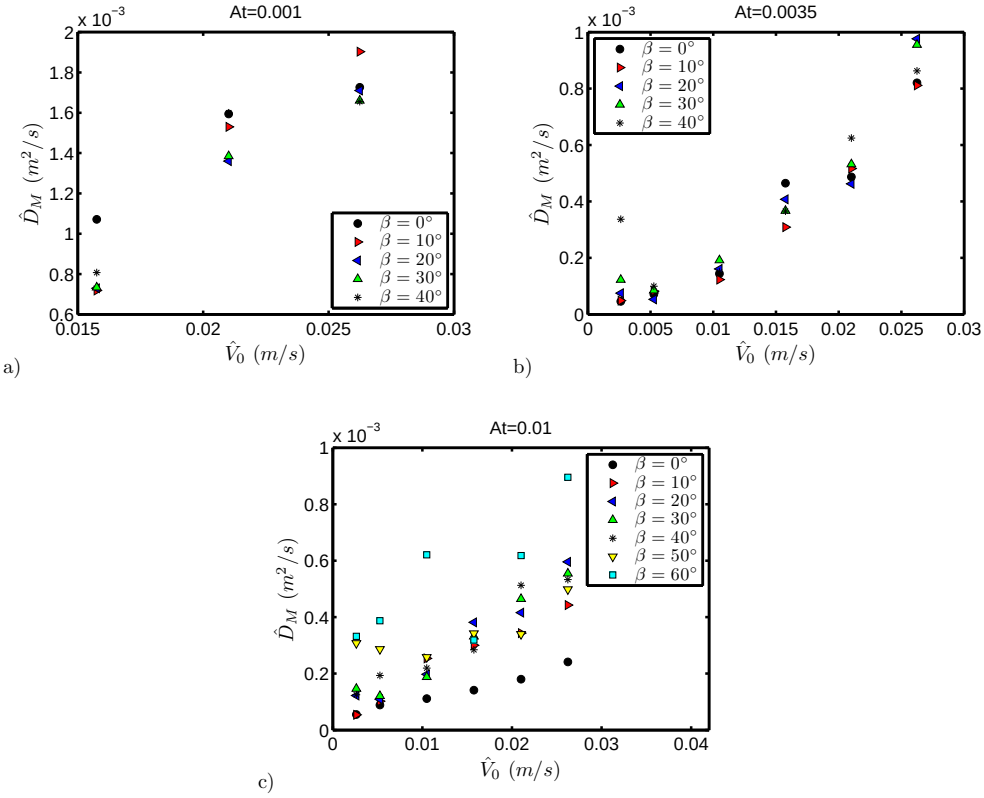

Figure 5.26: Change in macroscopic diffusion coefficient, $\hat{D}_M$ with mean imposed velocity $\hat{V}_0$ and tilt angle, β, for $\hat{\nu} = 1$ (mm^2/s) and a) $At = 0.001$, b) $At = 0.0035$ and c) $At = 0.01$.

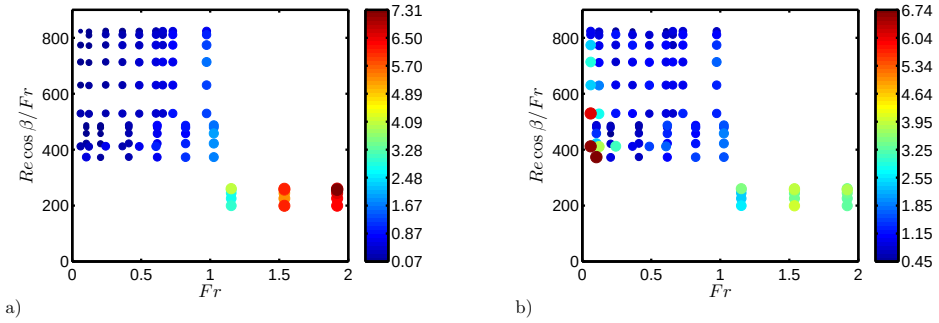

Figure 5.27: Contours of the normalized diffusion coefficient a) $\hat{D}_M/(\hat{V}_t\hat{D})$ and b) $\hat{D}_M/(\hat{V}_0\hat{D})$ versus Fr and $Re\cos\beta/Fr$.

We can see that scaling of $\hat{D}_M$ suggest that both mechanisms are responsible for the mixing in different limits. For small Fr, at large $(Re\cos\beta/Fr)$ as we transition out of the exchange dominated regime see that $\hat{D}_M/(\hat{V}_t\hat{D})$ appears to become independent of Fr, suggesting buoyancy driven mixing. At the other extreme, for modest $(Re\cos\beta/Fr)$ and as we increase Fr we find $\hat{D}_M/(\hat{V}_0\hat{D}) \approx$ constant, suggesting mixing driven by the mean flow.

5.1.6 Overall regime classification

In the previous sections we presented our results in terms of the velocity of the leading displacement front, and in terms of bulk axial diffusivity in the case of fully diffusive flows. We now try to give a qualitative description of the different flow regimes observed at long times in our simulations, in terms of the 3 dimensionless parameters: (Fr, Re, β). Much of the parametric variation appears to be captured in the $(Fr, Re\cos\beta/Fr)$-plane, as was the case for displacement flow experiments in pipe (chapter 4). Figure 5.28 shows the numerical points from our study, characterised in terms of flow type. We distinguish flows according to the following criteria: (i) *instantaneous* displacement (if there is no displaced fluid observed above the gate valve); (ii) *fully diffusive* (if we are able to collapse the data at long times via similarity solution of form, $C = 0.5\mathrm{erfc}(\frac{\hat{x}-\hat{V}_0\hat{t}}{2\sqrt{\hat{D}_M\hat{t}}})$; (iii) for *non-diffusive* flows we classify as either, *viscous* flows if there is no instability evident in the spatiotemporal image behind the leading displacement front, and *inertial* otherwise. It can be seen that this classification, although not perfect, does appear to separate the data within the $(Fr, Re\cos\beta/Fr)$-plane.

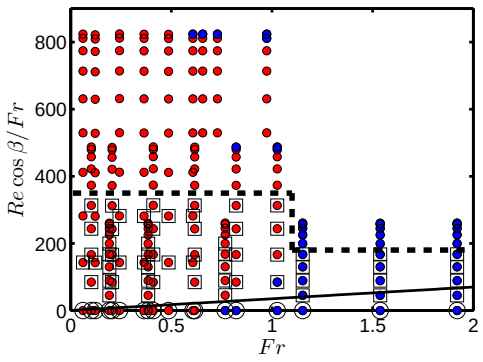

Figure 5.28: Classification of our results for the full range of simulations plotted in the plane of Fr and $Re\cos\beta/Fr$. The instantaneous displacement flows are colored in blue and non-instantaneous ones in red. The heavy line represents the prediction of the lubrication model for the stationary interface. The thick dashed lines show the boundary between diffusive and non-diffusive flows. The horizontal dashed lines are drawn at $Re\cos\beta/Fr = 350$ and $Re\cos\beta/Fr = 180$ and the vertical dashed line is at $Fr = 1.1$. Non-diffusive flows are marked by either the superposed circles (viscous flows) or squares (intermittent flows). The transition between viscous and inertial regimes is re-confirmed to occur at $Re\cos\beta/Fr = 25$ (see also [126]).

The first thing to note is that compared to the pipe displacement flow results in chapter 4, viscous flows in the channel are found over a rather narrow range $Re\cos\beta/Fr \lesssim 25$. The boundary between the diffusive and non-diffusive flows can be drawn using $Re\cos\beta/Fr = 350$, $Re\cos\beta/Fr = 180$ and $Fr = 1.1$ line (Fig. 5.28). In contrast to pipe displacement flows where the imposed flow had a significant influence on the stability of the flows, in the channel geometry it seems not to be as influential. For instance, the viscous flows found seem to remain viscous on increasing Fr number (or increasing $\hat{V}_0$ equivalently). The inertial non-diffusive flows within the range $25 \lesssim Re\cos\beta/Fr \lesssim 180$ also stay unaffected by the imposed flow. For data with $Re\cos\beta/Fr \gtrsim 350$ the flows are already diffusive for even small Fr numbers (or small $\hat{V}_0$ values). Increasing Fr in this range does not change the qualitative characteristics of the flow.

The only range of $Re\cos\beta/Fr$ in which the imposed flow seem to have an effect on the flow stability is $180 \lesssim Re\cos\beta/Fr \lesssim 350$. In this range the inertial non-diffusive flows transform into fully diffusive flows at $Fr \approx 1.1$.

Note that although the influence of the imposed flow on flow stability is not very pronounced in the case of the channel flows studied, it still has a large impact on making displacement flows transition to instantaneous from non-instantaneous. Note the non-instantaneous (red) data points that transform to instantaneous flows (blue) under the influence of increasing Fr. Compared to the pipe flow experiments, the range of dimensionless parameters studied is a bit limited as we have restricted the range of Re.

5.2 Discussion points

Displacement flow of two miscible iso-viscous Newtonian fluids in an inclined channel has been investigated numerically in the case where the displacing fluid is denser than the displaced fluid (i.e. density unstable). Our simulations have covered a broad range of the governing dimensionless parameter space (β, Re, Fr), not covered before in any numerical study. The qualitative features of the flow at different inclination angles were investigated through the concentration field snapshots, spatiotemporal diagrams of the averaged concentration and also the contours of the velocity field. As we move on closer to vertical and higher inclination angles the mixing and instability increase within the flow.

Similar to the pipe flow experiments, the two important quantities to measure in channel flow simulations are front velocity and macroscopic diffusion coefficient. Note that the latter was measured only for fully diffusive flows. similar to the experimental study for pipe flow displacements $\hat{D}_M$ increases with both inclination angle, β, and mean flow speed, $\hat{V}_0$. In the case of the pipe displacement when the mixing is efficient, the front velocity value was found to be very close to that of the mean flow i.e. $\hat{V}_f \approx \hat{V}_0$. However, for channel flow even when the fluids mix significantly the displacing front still advances close to the channel center; resulting in $\hat{V}_f \approx 1.5\hat{V}_0$ (by analogy with the Poiseuille flow). Note that if the simulations were run over a longer channel length and at larger times, the mixing could have been stronger and more complete transversely ($\hat{V}_f \approx \hat{V}_0$).

Different interesting patterns were observed at the tip of the displacing front, namely front detachment, leaking and dispersive spike fronts. These phenomena were explained physically and then have been located on dimensionless flow regime maps. Similarly, we took a similar approach with exchange dominated flows that exhibited some oscillatory-type pattern in the front velocity. These flows were found over the whole range of $Re\cos\beta/Fr$ and for $Fr < 0.3$.

The Rayleigh-Taylor mushroom structure was found for strictly vertical case for relatively low imposed flow rate and density difference. Due to both mixing and the imposed flow, the mushroom-like structure is not sustained over longer times. For inclinations slightly away from the vertical, the mushroom pattern was not observed due to the effects of slumping, i.e. symmetry is broken in the initial onset of flow, even though β is very small.

Finally, we have classified flows as fully diffusive, instantaneous, inertial and viscous, providing a qualitative description of each and delineating where each flow can be found in the dimensionless planes of Fr and $Re\cos\beta/Fr$. Viscous flows in the channel were found over a rather narrow range $Re\cos\beta/Fr \lesssim 25$. The boundary between the diffusive and non-diffusive flows was drawn using $Re\cos\beta/Fr = 350$, $Re\cos\beta/Fr = 180$ and $Fr = 1.1$ line. In contrast to pipe displacement flows where the imposed flow had a significant influence on the stability of the flows, in the channel geometry it seems not to be as influential.For low $Re\cos\beta/Fr$ our results form a natural extension of those of [126], but the range of phenomena observed is significantly different here, as the channel inclination is changed.

Chapter 6

Weighted residual method for two-layer non-Newtonian channel flows

In this chapter[5] we study buoyant displacement flows in a plane channel with two stratified fluid layers, in the long wavelength limit and including the effects of weak inertia. The motivation for this comes from the results of chapters 4 & 5 as well as from the earlier studies of [126]. Broadly speaking, in the flows we have studied we have observed flows that range from structured viscous streams, through instability and partial mixing to flows that are fully mixed in the transverse direction and diffuse/disperse axially. Although we have developed semi-empirical expressions that to some extent describe our results and approximate bulk flow quantities (e.g. front velocity), we do not have any predictive methodology for these flow transitions, nor a methodology that generalizes to other fluid combinations than we have studied. The aim of this chapter is to develop such a methodology.

We have characterized our observed flows in the $(Fr, Re\cos\beta/Fr)$-plane. Broadly speaking, instabilities and inertial flows have been observed in three main regimes: (i) beyond a critical ratio of axial buoyancy stress to viscous stress (χ); (ii) beyond a critical ratio of inertial ($\hat{V}_t$) to viscous ($\hat{V}_\nu$) velocity scales (at lower mean displacement velocities $\hat{V}_0$); (iii) due to shear-flow turbulent transition at high Reynolds numbers, possibly aided by buoyancy. As β is decreased the axial component of the buoyancy force increases and the stabilizing transverse component decreases. Although we associate reduced inclination β with inertial instability, it must be noted that this depends strongly on the buoyancy and viscous forces present. Of all these transitions, the one most amenable to any form of analysis is the loss of stability of the viscous stratified flows.

[5] A version of this chapter has been submitted for publication: **K. Alba**, S.M. Taghavi and I.A. Frigaard. *Weighted residual method for two-layer non-Newtonian channel flows: steady state results and their stability.*

Although we have studied only Newtonian iso-viscous flows so far in the thesis, the range of industrial fluids used in primary cementing (and other processes) will typically have viscosity differences and also non-Newtonian rheologies. In particular we are interested in non-Newtonian fluids described by the Herschel-Bulkley fluid model. These fluids have a yield stress, below which the rate of strain is zero, and also exhibit shear-thinning behaviour. Once this wider range of fluids is studied, we might also expect to add a 4th instability mechanism to (i)-(iii) above, namely due to viscosity/rheology difference at the interface. Although there will undoubtedly be further differences when we come to study non-Newtonian displacement flows, some of our previous studies (e.g. [125]) suggest that there are also qualitative similarities, e.g. we also expect a transition from viscous to inertial regimes.

Rather than consider stratified pipe geometries, for simplicity we consider only a two-layer channel flow. Although this channel flow configuration does not relate directly to the pipe flow experiments presented in chapter 4, the results might still be used to draw qualitative conclusions about the effect of different physical parameters. The pipe geometry introduces complexities in any form of simplified modeling, as soon as non-Newtonian fluids are considered, necessitating simplifying approximations if progress is to be made, e.g. [87], whereas the two-layer channel flow is tractable analytically, although also complex.

On the other hand, computational results presented in chapter 5 for a channel geometry commonly showed that the displacing fluid layer advances along the middle of the channel, through the displaced layer rather than slumping underneath it, unless the inclination is very close to horizontal. Thus, in selecting a two-layer channel flow configuration our focus is mainly on developing qualitative understanding for both pipe and channel geometries. A common situation is that the interface elongates during the displacement, due to both the mean flow and buoyancy. We are interested in exploiting this long-thin aspect ratio of the flow to reduce the dimensionality of the problem. Two-layer thin film/lubrication models have already been developed in [126, 128] and used to predict the front velocity in displacement flows for both pipes and channels. However, inertial effects are absent at leading order in these models and must be included in any realistic analysis of instability.

In general our interest lies in miscible flows for which the (molecular) Péclet number is very large, which occur widely in the applications considered. In these flows the fluids do not mix significantly on the timescale of the flow, unless there is some form of flow instability to drive the mixing. Thus, we describe the flow as having a distinct interface. We take

account of weak inertial effects by developing a weighted residual method. This method is developed to give a first order accurate approximation to the interface height and flux functions in each layer. As the fluids are shear-thinning and have a yield stress, to retain a formulation that can be resolved analytically requires the development of a system of special functions for the weight functions and various integral expressions. This formulation is a large part of the contribution of this chapter.

Secondly, we study the stability of these systems via both a linear temporal analysis and a numerical spatiotemporal method. These results are compared with an analysis of the Orr-Sommerfeld equations, for two generalized non-Newtonian fluids following Herschel-Bulkley. Analytical expressions for the growth rate and wave speed are obtained in the long wavelength limit. The predictions of linear analysis based on weighted residual method shows excellent agreement with the Orr-Sommerfeld approach for Newtonian and non-Newtonian fluids. For displacement flows in unstable parameter ranges we do observe growth of interfacial waves that saturate nonlinearly and disperse. The observed waves have qualitatively similar characteristics to those observed experimentally in pipe flow displacements.

Asymptotic methods and simplified modeling approaches have a long history of application. In environmental and geophysical flow contexts, two main strands of research are relevant. Firstly coming from the inviscid direction, the shallow water equations have been used extensively in studying wave dynamics. Here viscous effects typically enter only in the specification of a drag law and in modeling the axial dissipation. As we consider non-Newtonian fluids the precise nature of the viscous terms is of importance. Secondly, researchers have taken classical thin-film/lubrication theory models and attempted to extend them to (weakly) inertial flows. It is this latter approach that we adopt.

The spirit of our derivation follows that of [8] in that our weighted residual approach is aimed at a first order accurate prediction of the interface height and fluxes in the two fluid layers (see §6.2). Unlike Newtonian fluids the base flows are generally not polynomials given in terms of the transverse coordinate y, slaved to the interface height h. Thus, the more elaborate expansions to higher order found in e.g. [8], are hard to write down in simple terms. In any case, there are considerable complications at an algebraic level to overcome. As we shall see below, this can be achieved but involves developing a systematic calculus for the integral functions that must be evaluated. Development of this algebraic framework is the objective of the first part of this chapter. In the second part we consider the stability of these flows, first comparing against long wavelength Orr-Sommerfeld results for

parallel flows and then examining displacement flows numerically (see §6.4). Note again that although our interest is in studying displacement flows, the formulation developed in this chapter can be easily used for similar two-layer flows e.g. co-extrusion flows.

6.1 Displacement flow in channel

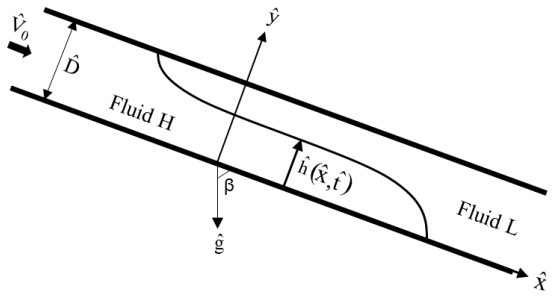

Figure 6.1: Schematic of displacement geometry. Note that dimensional notations are used in the figure and the interface shape is illustrative only.

The starting point for the model is a fully 2D plane channel miscible displacement flow in the immiscible large Péclet number limit. In general it will be assumed that the displacing fluid (fluid H) is heavier than the displaced (fluid L), so that the configuration is density unstable (see figure 6.1). The Navier-Stokes equations are made dimensionless using the channel height $\hat{D}$ as length-scale and the mean displacement velocity $\hat{V}_0$ as velocity scale. The model equations are:

$$[1 \pm At]\,[\mathbf{u}_t + \mathbf{u}\cdot\nabla\mathbf{u}] = -\nabla p + \frac{1}{Re}\nabla\cdot\tau \pm \frac{1}{Fr^2}\mathbf{e}_g, \tag{6.1}$$

$$\nabla\cdot\mathbf{u} = 0, \tag{6.2}$$

$$h_t + \mathbf{u}\cdot\nabla(h-y) = 0. \tag{6.3}$$

Here $\mathbf{e}_g = (\cos\beta, -\sin\beta)$ in directions (x, y) and the $\pm$ refers to the heavy/light fluid layers, respectively. The mean static pressure gradient has been subtracted from the pressure before scaling. The interface height is denoted by

$y = h(x,t)$. For $t > 0$, no slip boundary conditions are satisfied at the solid walls and outflow conditions imposed at the channel exit. At the inflow, pure heavy fluid is pumped at mean velocity $\hat{V}_0$. Apart from the angle of inclination β and Atwood number, $At = (\hat{\rho}_H - \hat{\rho}_L)/(\hat{\rho}_H + \hat{\rho}_L)$, two other dimensionless parameters appearing in (6.1) are the Reynolds number, Re, and the (densimetric) Froude number, Fr:

$$Re \equiv \frac{\hat{V}_0 \hat{D}}{\hat{\nu}}, \quad Fr \equiv \frac{\hat{V}_0}{\sqrt{At\hat{g}\hat{D}}}. \tag{6.4}$$

Here $\hat{\nu}$ is defined using the mean density $\hat{\rho} = (\hat{\rho}_H + \hat{\rho}_L)/2$ and a viscosity scale that will be derived from the rheological properties of the pure displacing fluid (fluid H). We see that for small At the flow is essentially governed by the 3 parameters β, Re & Fr. A dimensionless combination of these that arises naturally in thin layer flows is

$$\chi = \frac{2Re\cos\beta}{Fr^2}, \tag{6.5}$$

which represents the balance of axial buoyancy stresses and viscous stresses due to the imposed flow.

6.1.1 Constitutive equations considered

The fluids are assumed to be Herschel-Bulkley fluids, which incorporates also the simpler Bingham, power law and Newtonian models. Herschel-Bulkley fluids are described by 3 (dimensional) parameters: a fluid consistency $\hat{\kappa}$, a yield stress $\hat{\tau}_Y$ and a power law index, n. Dimensionless constitutive laws for pure fluid k are:

$$\dot{\gamma}(\mathbf{u}) = 0 \iff \tau_k(\mathbf{u}) \le B_k, \tag{6.6}$$

$$\tau_{k,ij}(\mathbf{u}) = \left[\kappa_k \dot{\gamma}^{n_k - 1}(\mathbf{u}) + \frac{B_k}{\dot{\gamma}(\mathbf{u})}\right] \dot{\gamma}_{ij}(\mathbf{u}) \iff \tau_k(\mathbf{u}) > B_k \tag{6.7}$$

where the strain rate tensor has components:

$$\dot{\gamma}_{ij}(\mathbf{u}) = \frac{\partial u_i}{\partial x_j} + \frac{\partial u_j}{\partial x_i}, \tag{6.8}$$

and the norms of these tensors, $\dot{\gamma}(\mathbf{u})$ and $\tau_k(\mathbf{u})$, are defined by:

$$\dot{\gamma}(\mathbf{u}) = \left[\frac{1}{2}\sum_{i,j=1}^{2} [\dot{\gamma}_{ij}(\mathbf{u})]^2\right]^{1/2}, \qquad \tau_k(\mathbf{u}) = \left[\frac{1}{2}\sum_{i,j=1}^{2} [\tau_{k,ij}(\mathbf{u})]^2\right]^{1/2}. \tag{6.9}$$

Here, subscripts $k = H, L$ are used to distinguish the fluids. The parameter $\kappa_H = 1$ and κ_L is the viscosity ratio m, equal to:

$$m \equiv \frac{\hat{\mu}_L}{\hat{\mu}_H} = \frac{\hat{\kappa}_L[\hat{V}_0/\hat{D}]^{n_L-1}}{\hat{\kappa}_H[\hat{V}_0/\hat{D}]^{n_H-1}}, \tag{6.10}$$

where $\hat{\mu}_L$ is a viscosity scale for fluid 2 (the less dense fluid). Note that in the case of 2 Newtonian fluids, $\hat{\mu}_k = \hat{\kappa}_k$. The Bingham numbers B_k are defined as:

$$B_k \equiv \frac{\hat{\tau}_{k,Y}}{\hat{\kappa}_H[\hat{V}_0/\hat{D}]^{n_H}}. \tag{6.11}$$

For each fluid we shall work with two viscosity functions η_k and $\eta_{k,t}$, defined as:

$$\eta_k = \left[\kappa_k \dot{\gamma}^{n_k-1}(\mathbf{u}) + \frac{B_k}{\dot{\gamma}(\mathbf{u})}\right], \tag{6.12}$$

$$\eta_{k,t} = \eta_k + \dot{\gamma}\frac{\partial \eta_k}{\partial \dot{\gamma}} = n_k \kappa_k \dot{\gamma}^{n_k-1}(\mathbf{u}). \tag{6.13}$$

The first of these is the *effective* viscosity (often called the apparent viscosity). The second of these is referred to as the *tangent* viscosity. Both viscosity functions are used practically in interpreting flow curves (rheograms) of viscometric flows; see e.g. [108]. Simply put, the flow curve $\tau = \dot{\gamma}\eta_k(\dot{\gamma})$, defines η_k for generalised Newtonian fluids, while $\eta_{k,t} = \frac{\mathrm{d}\tau}{\mathrm{d}\dot{\gamma}}$ is the viscosity measured as the tangent to the flow curve. The tangent viscosity also arises naturally in problems involving perturbations of shear flows of generalised Newtonian fluids: it is the difference between effective and tangent viscosities that gives a measure of the shear-induced anisotropy present in linear stability problems; see [91]. For shear thinning fluids the tangent viscosity is always less than the effective viscosity. These viscosity functions arise naturally in the analysis below.

6.1.2 Parallel flow solution

For any $h \in [0, 1]$ we are able to find a parallel two-layer solution of (6.1)-(6.3): $\mathbf{u} = (U_p(y), 0)$, $p = P_p(x, y)$, from the following system

$$\frac{\mathrm{d}}{\mathrm{dy}}\tau_{H,xy} = -f_p, \qquad y \in (0, h), \tag{6.14}$$

$$\frac{\mathrm{d}}{\mathrm{dy}}\tau_{L,xy} = \chi - f_p, \qquad y \in (h, 1), \tag{6.15}$$

with boundary and interface conditions:

$$U_p(0) = 0,\ U_p(h^-) = U_p(h^+),\ \tau_{H,xy}(h^-) = \tau_{L,xy}(h^-),\ U_p(1) = 0, \quad (6.16)$$

and flow constraint

$$\int_0^1 U_p(y)\ \mathrm{dy} = 1. \quad (6.17)$$

The pressure field P_p is defined by the modified pressure gradient f_p via:

$$P_p(x,y) = \begin{cases} \dfrac{1}{Re}\left[-f_p x + \dfrac{\chi}{2}x - \dfrac{\chi\tan\beta}{2}y\right], & 0 \le y \le h, \\ \dfrac{1}{Re}\left[-f_p x + \dfrac{\chi}{2}x - \dfrac{\chi\tan\beta}{2}(2h-y)\right], & h < y \le 1, \end{cases} \quad (6.18)$$

up to an arbitrary additive constant.

For any of the fluids that are not Newtonian, the problem (6.14)-(6.17), is nonlinear. Since there is a single non-zero component of the strain rate and deviatoric stress, the constitutive laws are given in terms of simple algebraic relations. The approach taken to solve these equations in [128] is to define the shear stresses $\tau_{H,xy}$ & $\tau_{L,xy}$ in each layer, in terms of f_p and the interfacial stress τ_i. A single monotone equation is then derived for the interfacial velocity, by integrating outwards from each wall, and this equation is solved iteratively to give τ_i. In an outer iteration, we find the modified pressure gradient f_p, such that (6.17) is satisfied, (the flow rate increases monotonically with f_p).

Although iterative, this procedure is relatively quick and convergence to any given tolerance can be guaranteed. Note that the solution computed in this way includes f_p. We consider the rheological parameters (m, n_H, n_L, B_H, B_L) as fixed for any such computation. The main parametric dependency therefore is on (h, χ), and we write:

$$U_p(y) = U_p(y; h, \chi), \qquad f_p = f_p(h, \chi). \quad (6.19)$$

Figure 6.2a shows some examples of the base multi-layer velocity solution for $(h, \chi) = (0.8, 10)$. The lower fluid is Newtonian and the upper fluid is a Bingham fluid. For increasing B_L we observe that the upper layer velocity decreases progressively until eventually the layer becomes static, held by the yield stress of fluid L. Figure 6.2b shows further examples for $(h, \chi) = (0.5, 0)$. The lower fluid is Newtonian and the upper fluid is a power-law fluid. For decreasing n_L we observe that the upper layer velocity

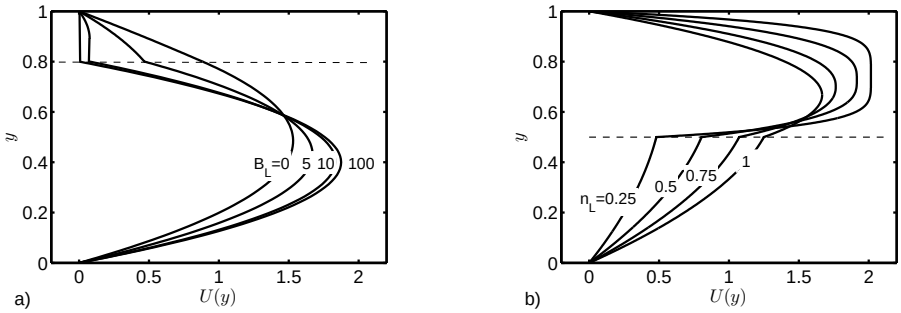

Figure 6.2: Change in the base flow velocity profile, $U_p(y)$, with a) upper layer Bingham number, B_L, for $B_H = 0$, $m = 1$, $n_L = 1$, $n_H = 1$ and $\chi = 10$, b) upper layer power-law index, n_L, for $B_L = 0$, $B_H = 0$, $m = 0.2$, $n_H = 1$ and $\chi = 0$. The broken lines in figures a and b indicate the position of the interface, $h = 0.8$ and $h = 0.5$ respectively.

increases, at the expense of that in the lower layer. This is a due to shear-thinning. The light fluid velocity profile also becomes increasingly plug-like, although there is in fact always a single maximum.

We now introduce some notational shorthand that will become useful for the algebraic manipulations later in the paper. Let us suppose that we have iterated to find τ_i and f_p for a parallel flow solution that is defined by parameters (h, χ). The shear stresses vary linearly across each fluid layer and can be defined most simply by the values at the ends of each layer:

$$\tau_{H,xy}(y) = \tau_H \left(1 - \frac{y}{h}\right) + \tau_i \frac{y}{h}, \quad y \in (0, h), \tag{6.20}$$

$$\tau_{L,xy}(y) = \tau_L \frac{h - y}{h - 1} + \tau_i \frac{1 - y}{1 - h}, \quad y \in (h, 1), \tag{6.21}$$

where $\tau_H = \tau_i + f_p h$ and $\tau_L = \tau_i + (1 - h)(\chi - f_p)$. To make the algebra more compact, we will denote the positive part of a function $v(x)$ by the notation $(v(x))_+$, i.e.

$$(v(x))_+ = \max\{0, v(x)\}.$$

Note that the strain rate of the parallel flow solution, say $\dot{\gamma}_0$ is given in fluid k by:

$$\dot{\gamma}_0(y) = \left| \frac{\partial U_p}{\partial y}(y) \right| = \frac{(|\tau_{k,xy}|(y) - B_k)_+^{m_k}}{\kappa_k^{m_k}}, \tag{6.22}$$

and the velocity gradient in fluid k is:

$$\frac{\partial U_p}{\partial y}(y) = \mathrm{sgn}(\tau_{\mathrm{k,xy}})\frac{(|\tau_{\mathrm{k,xy}}|(\mathrm{y}) - \mathrm{B_k})_+^{\mathrm{m_k}}}{\kappa_{\mathrm{k}}^{\mathrm{m_k}}}, \tag{6.23}$$

where $m_k = 1/n_k$. To construct the solution (and various other quantities of importance) we need to integrate this type of quantity across the fluid layers. To deal with these expressions in a systematic fashion we define the following integral expressions:

$$I_{H,p}(y) = m_H \int_0^y \frac{(|\tau_{H,xy}|(\tilde{y}) - B_H)_+^p}{\kappa_H^{m_H}}\ \mathrm{d\tilde{y}}, \tag{6.24}$$

$$J_{H,p}(y) = m_H \int_0^y \mathrm{sgn}(\tau_{\mathrm{H,xy}})\frac{(|\tau_{\mathrm{H,xy}}|(\tilde{\mathrm{y}}) - \mathrm{B_H})_+^{\mathrm{p}}}{\kappa_{\mathrm{H}}^{\mathrm{m_H}}}\ \mathrm{d\tilde{y}}, \tag{6.25}$$

$$I_{L,p}(y) = m_L \int_y^1 \frac{(|\tau_{L,xy}|(\tilde{y}) - B_L)_+^p}{\kappa_L^{m_L}}\ \mathrm{d\tilde{y}}, \tag{6.26}$$

$$J_{L,p}(y) = m_L \int_y^1 \mathrm{sgn}(\tau_{\mathrm{L,xy}})\frac{(|\tau_{\mathrm{L,xy}}|(\tilde{\mathrm{y}}) - \mathrm{B_L})_+^{\mathrm{p}}}{\kappa_{\mathrm{L}}^{\mathrm{m_L}}}\ \mathrm{d\tilde{y}}. \tag{6.27}$$

These functions can be evaluated directly for $p > -1$. The basic method involves change of the independent variable from y to $\tau_{k,xy}$ after which the integrals become tractable. This methodology is commonly used in calculating hydraulics quantities for generalized Newtonian fluids. Later we shall also integrate these functions and various products of these functions over the intervals $[0, h]$ & $[h, 1]$. Algebraic expressions for the $I_{k,p}$ and $J_{k,p}$ functions are described fully in appendix C.

With the aid of the above functions, the velocity in each fluid layer is given simply by:

$$U_p(y) = \int_0^y \frac{\partial U_p}{\partial y}(\tilde{y})\ \mathrm{d\tilde{y}} = \frac{\mathrm{J_{H,m_H}(y)}}{\mathrm{m_H}}, \qquad \mathrm{y} \in [0, \mathrm{h}], \tag{6.28}$$

$$U_p(y) = \int_1^y \frac{\partial U_p}{\partial y}(\tilde{y})\ \mathrm{d\tilde{y}} = -\frac{\mathrm{J_{L,m_L}(y)}}{\mathrm{m_L}}, \qquad \mathrm{y} \in (\mathrm{h}, 1]. \tag{6.29}$$

and note that the parameters τ_i and f_p have been computed in such a way that the velocity is continuous at the interface: $m_L J_{H,m_H}(h) = -m_H J_{L,m_L}(h)$.

6.1.3 Long-thin flows

Our paper focuses wholly on flows that have a long-thin aspect ratio. Accordingly, it is assumed that after an initial time the flow develops axially

over a length-scale $\delta^{-1} \gg 1$. For example, the heavier fluid slumps towards the lower side of the channel and elongates axially with the two fluids separated by a single interface, $y = h(x,t)$. For now we simply regard δ as an arbitrary small aspect ratio, assume that the channel is effectively infinite and adopt a lubrication/thin-film type rescaling:

$$\delta(x - x_0) = \xi, \qquad \delta t = T, \qquad \delta p = P, \qquad u = U, \qquad v = \delta V,$$

where the initial interface is centred at $x = x_0$. The overall aim is to derive a perturbation approximation. We start with a general expansion:

$$(U, V, P) = (U_0, V_0, P_0) + \delta(U_1, V_1, P_1) + \delta^2(U_2, V_2, P_2) + ...$$

which we insert in the equations of motion and expand to order δ. We do not include h in this expansion as we shall anyway assume that the interface position is accurate to first order in δ. We follow the usual thin-film/lubrication practice of eliminating the pressure by integrating the y-momentum equations:

$$P_0 + \delta P_1 = \begin{cases} \dfrac{\chi}{2}\xi - \displaystyle\int_0^{\xi} f_0(\tilde{\xi}) + \delta f_1(\tilde{\xi})\ \mathrm{d}\tilde{\xi} - \dfrac{\mathrm{y}\delta}{2}\chi\tan\beta, & y \in [0,h] \\ \dfrac{\chi}{2}\xi - \displaystyle\int_0^{\xi} f_0(\tilde{\xi}) + \delta f_1(\tilde{\xi})\ \mathrm{d}\tilde{\xi} - \dfrac{(2\mathrm{h} - \mathrm{y})\delta}{2}\chi\tan\beta, & y \in [h,1] \end{cases} \tag{6.30}$$

where $f_0(\xi,T)+\delta f_1(\xi,T)$ is the modified pressure gradient along the bottom wall of the channel. Insertion into the x-momentum equations gives the following equations valid to first order in δ:

$$\begin{aligned} \delta Re\,[1 + At]\left[\frac{\partial U_0}{\partial T} + U_0\frac{\partial U_0}{\partial \xi} + V_0\frac{\partial U_0}{\partial y}\right] &= f_0 + \frac{\partial}{\partial y}\left[\eta_H(\dot{\gamma}_0)\frac{\partial U_0}{\partial y}\right] + \delta f_1 \\ &\quad + \delta\frac{\partial}{\partial y}\left[\eta_{H,t}(\dot{\gamma}_0)\frac{\partial U_1}{\partial y}\right], \end{aligned} \tag{6.31}$$

within the heavy layer, $y \in (0,h)$. Within the light fluid layer, for $y \in (h,1)$ we have

$$\begin{aligned} \delta Re\,[1 - At]\left[\frac{\partial U_0}{\partial T} + U_0\frac{\partial U_0}{\partial \xi} + V_0\frac{\partial U_0}{\partial y}\right] &= f_0 - \chi + \frac{\partial}{\partial y}\left[\eta_L(\dot{\gamma}_0)\frac{\partial U_0}{\partial y}\right] \\ + \delta f_1 + \delta\frac{\partial}{\partial y}\left[\eta_{L,t}(\dot{\gamma}_0)\frac{\partial U_1}{\partial y}\right] + \delta\chi\tan\beta\frac{\partial h}{\partial \xi}. & \end{aligned} \tag{6.32}$$

Note that the effects of buoyancy are felt in the two terms involving χ. The first of these (χ) is the effect of the axial buoyancy force whereas the second

models the transverse buoyancy force, which manifests through the slope of the interface. This second term may be of the same order as the first. For example, we might assume that spreading of the interface, relative to the mean flow, is driven by buoyant stresses which have size: $(\hat{\rho}_H - \hat{\rho}_L)\hat{g}\sin\beta\hat{D}$, which act via the slope of the interface $\hat{D}/\hat{L}$, and that these are balanced by viscous stresses, leading to:

$$\delta^{-1} = \frac{\hat{L}}{\hat{D}} = \frac{(\hat{\rho}_H - \hat{\rho}_L)\hat{g}\sin\beta\hat{D}^2}{\hat{\mu}\hat{V}_0} = \chi\tan\beta, \tag{6.33}$$

see e.g. [128]. This situation is most likely in strongly inclined channels.

Both fluids are incompressible and the interface is advected via a kinematic condition:

$$\frac{\partial U_0}{\partial\xi} + \frac{\partial V_0}{\partial y} + \delta\left[\frac{\partial U_1}{\partial\xi} + \frac{\partial V_1}{\partial y}\right] = 0, \tag{6.34}$$

$$\frac{\partial h}{\partial T} + (U_0 + \delta U_1)\frac{\partial h}{\partial\xi} = V_0 + \delta V_1. \tag{6.35}$$

No slip conditions are satisfied at each wall and the net flux of fluid along the channel is equal to unity, due to scaling with the mean flow:

$$1 = \int_0^1 U\ \mathrm{dy} \quad \Rightarrow \quad 1 = \int_0^1 \mathrm{U}_0\ \mathrm{dy}, \quad 0 = \int_0^1 \mathrm{U}_1\ \mathrm{dy}. \tag{6.36}$$

Combining the incompressibility condition with the kinematic condition, we arrive at the standard thin-film equation:

$$\frac{\partial h}{\partial T} + \frac{\partial}{\partial\xi}q = 0, \qquad q = \int_0^h U_0 + \delta U_1\ \mathrm{dy}. \tag{6.37}$$

6.1.4 Standard thin-film approach

The standard thin-film approach now considers the formal limit Re fixed as $\delta \to 0$ in which both inertial and first order viscous and pressure gradient perturbations vanish. The term involving the slope of the interface may be retained at leading order (usually according to the inclination of the channel), as discussed above. We note that in this formal limit, (6.31) and (6.32) reduce considerably. The leading order velocity is defined by a system analogous to that of the parallel flow solution in §6.1.2. In the notation of §6.1.2, we have

$$U_0(y) = U_p(y, h, \chi - \delta\chi\tan\beta\frac{\partial h}{\partial\xi}), \qquad f_0 = f_p(h, \chi - \delta\chi\tan\beta\frac{\partial h}{\partial\xi}).$$

The flux function q is given simply by:

$$q \;=\; q(h, \chi - \delta\chi \tan\beta \frac{\partial h}{\partial \xi}) = \int_0^h U_p(y, h, \chi - \delta\chi \tan\beta \frac{\partial h}{\partial \xi})\ \mathrm{dy} \quad (6.38)$$

In general, from (6.28) we can evaluate:

$$q = \int_0^h \frac{J_{H,m_H}(y)}{m_H}\ \mathrm{dy} \;=\; \frac{hI_{H,m_H+1}(h)}{m_H(m_H+1)(\tau_i - \tau_H)} - \frac{h^2(|\tau_H| - B_H)_+^{m_H+1}}{(m_H+1)\kappa_H^{m_H}(\tau_i - \tau_H)} \quad (6.39)$$

Algebraic expressions evaluating the terms above are described fully in appendices B and C. We see that the standard thin-film approach yields the evolution equation (6.37), with q given semi-analytically. This equation has been studied extensively by [128].

6.2 Weighted residual approximation

We wish to develop simplified equations for our zero-th order perturbation in such a way that it approximates certain flow quantities to first order. It is clear that achieving a first order approximation to local quantities is unlikely with the zero-th order terms alone. Instead we aim to approximate certain integral quantities to first order: namely the interface height and the volumetric fluxes of the individual fluid layers. Consistent with this objective, we have not expanded h in terms of δ, as only leading order terms occur. Now we see that if the leading order solution U_0 is to give a first order accurate approximation to h via the evolution equation (6.37), we require that:

$$q = \int_0^h U_0\ \mathrm{dy} + \mathrm{O}(\delta^2) \quad \Rightarrow \int_0^{\mathrm{h}} \mathrm{U}_1\ \mathrm{dy} = 0. \quad (6.40)$$

Equally, since the net flux of U_1 is zero we have also the constraint that

$$\int_h^1 U_1\ \mathrm{dy} = 0. \quad (6.41)$$

The motivation for studying (6.31) and (6.32) is that they contain the leading order effects of inertia, at first order in δ, but are far simpler than a fully 2D Navier-Stokes system. The challenge is to retain this leading order inertial effect without the additional complexity of computing the first order perturbation solution, i.e. (U_1, V_1) and f_1. The idea of the weighted residual method is to determine weight functions, $g_H(y)$ and $g_L(y)$, such that when

we multiply (6.31) by $g_H(y)$ and (6.32) by $g_L(y)$, then integrate across the 2 intervals and sum, the first order terms that involve (U_1, f_1) should vanish, leaving behind terms that represent evolution of the leading order inertial terms.

Determining which terms should vanish is not decided by the size of the terms (e.g. formally the inertial terms are also first order), but is determined by the criterion of closure and solvability of the residual equations. For example, the term $(\delta\chi \tan\beta \frac{\partial h}{\partial \xi})$ depends only on zero-th order variables and there is consequently no need for this to vanish. Equally, we have seen that this term may in some circumstances be of zero-th order, in strongly inclined channels.

The above requirements help to define the weight functions. Explicitly we require:

$$\begin{aligned} 0 = &\int_0^h g_H \left[\frac{\partial}{\partial y}\left[\eta_{H,t}(\dot\gamma_0)\frac{\partial U_1}{\partial y}\right] + f_1\right]\ \mathrm{dy} \\ &+ \int_h^1 g_L \left[\frac{\partial}{\partial y}\left[\eta_{L,t}(\dot\gamma_0)\frac{\partial U_1}{\partial y}\right] + f_1\right]\ \mathrm{dy}. \end{aligned} \tag{6.42}$$

Note that f_1 does not vary with y. On integrating by parts we have:

$$\begin{aligned} 0 \;=\; & \int_0^h U_1 \frac{\partial}{\partial y}\left[\eta_{H,t}(\dot\gamma_0)\frac{\partial g_H}{\partial y}\right]\ \mathrm{dy} + \int_\mathrm{h}^1 \mathrm{U_1}\frac{\partial}{\partial \mathrm{y}}\left[\eta_{\mathrm{L,t}}(\dot\gamma_0)\frac{\partial \mathrm{g_L}}{\partial \mathrm{y}}\right]\mathrm{dy} \\ + \; & \left[g_H \eta_{H,t}(\dot\gamma_0)\frac{\partial U_1}{\partial y} - U_1\eta_{H,t}(\dot\gamma_0)\frac{\partial g_H}{\partial y}\right]_0^h \\ + \; & \left[g_L \eta_{L,t}(\dot\gamma_0)\frac{\partial U_1}{\partial y} - U_1\eta_{L,t}(\dot\gamma_0)\frac{\partial g_L}{\partial y}\right]_h^1 \\ + \; & f_1\left(\int_0^h g_H\ \mathrm{dy} + \int_\mathrm{h}^1 \mathrm{g_L}\ \mathrm{dy}\right) \end{aligned} \tag{6.43}$$

From the perturbation expansion of the usual conditions of continuity of velocity and stress at the interface, we may expect that the first order perturbation satisfies:

$$U_1(\xi, h^-, T) = U_1(\xi, h^+, T), \quad \eta_{H,t}(\dot\gamma_0)\frac{\partial U_1}{\partial y}(\xi, h^-, T) = \eta_{L,t}(\dot\gamma_0)\frac{\partial U_1}{\partial y}(\xi, h^+, T) \tag{6.44}$$

as well as U_1 vanishing at the 2 solid walls. For the weight functions $g_H(y)$ and $g_L(y)$ we impose equivalent conditions:

$$g_H(0) \;=\; 0, \tag{6.45}$$

$$g_H(h) = g_L(h), \tag{6.46}$$

$$\eta_{H,t}(\dot{\gamma}_0)\frac{\partial g_H}{\partial y}(h) = \eta_{L,t}(\dot{\gamma}_0)\frac{\partial g_L}{\partial y}(h), \tag{6.47}$$

$$g_L(1) = 0, \tag{6.48}$$

which ensure that the boundary terms in (6.43) vanish. To complete the specification, we define $g_H(y)$ and $g_L(y)$ as the solutions of the following boundary value problem:

$$\frac{\partial}{\partial y}\left[\eta_{H,t}(\dot{\gamma}_0)\frac{\partial g_H}{\partial y}\right] = -a, \quad y \in (0,h) \tag{6.49}$$

$$\frac{\partial}{\partial y}\left[\eta_{L,t}(\dot{\gamma}_0)\frac{\partial g_L}{\partial y}\right] = 1-a, \quad y \in (h,1) \tag{6.50}$$

with boundary and jump conditions (6.45) - (6.48). The constant $a \in [0,1]$ is again uniquely determined by the condition that:

$$\int_0^h g_H \ \mathrm{dy} + \int_{\mathrm{h}}^1 \mathrm{g_L} \ \mathrm{dy} = 0. \tag{6.51}$$

Observe that the first two terms in (6.43) now vanish due to the definition of $g_H(y)$ and $g_L(y)$ in the above boundary value problem, combined with the individual flux conditions, (6.40) & (6.41). The final pressure gradient term also vanishes due to (6.51). The choice of constants $-a$ and $1-a$, on the right-hand sides of (6.49) & (6.50), firstly normalizes the weight functions and secondly (via (6.51)) ensures that the flux of g_H is positive and that of g_L is negative. We shall deal below in §6.2.3 with solution of (6.45)-(6.51).

6.2.1 Velocity closure

To progress with (6.31) and (6.32), we must assume a functional form for the leading order velocity, U_0. To this end we assume that the leading order shear stress in each fluid layer varies at most linearly with y at each (ξ, T). Thus, we assume that the two-layer flow satisfies the equations:

$$\frac{\partial}{\partial y}\left[\eta_H(\dot{\gamma}_0)\frac{\partial U_0}{\partial y}\right] = \frac{\mathrm{d}}{\mathrm{dy}}\tau_{H,xy,0} = -f(\xi,T), \quad y \in [0,h), \tag{6.52}$$

$$\frac{\partial}{\partial y}\left[\eta_L(\dot{\gamma}_0)\frac{\partial U_0}{\partial y}\right] = \frac{\mathrm{d}}{\mathrm{dy}}\tau_{L,xy,0} = b(\xi,T) - f(\xi,T), \quad y \in (h,1], \tag{6.53}$$

plus no-slip conditions at the walls and continuity of velocity and shear stress at $y = h$. Note that this is not very different in form from the multi-layer weighted residual approach of [8], who assume a quadratic form for the

velocity, i.e. solving for the base flow from (6.52) & (6.53) for 2 Newtonian fluids would also lead to quadratic expressions in y. Once the boundary and interface conditions are implemented in [8] there is also only a single free variable, equivalent to $b(\xi, T)$. The point is that for the more complex fluids considered here, parallel shear flow velocities are not typically polynomial in y and it would be incorrect to use a polynomial expression as the first term in an approximation to the velocity. Instead the form of closure (6.52) & (6.53) corresponds to that of the parallel flow solutions in §6.1.2.

Just as in the standard thin-film approach of §6.1.4, where the leading order velocity is *slaved* to the interface height h, in the weighted residual approach the leading order velocity is slaved to both h and a second primary variable. The choice of primary variables that has been made for Newtonian fluid combinations is (h, q), e.g. [1, 8, 126]. There is nothing wrong with that choice here, but it is more natural to work with (h, b) as our primary variables, i.e. due to the velocity closure (6.52) & (6.53). In the appendix of [128] it is shown that q increases monotonically with b, so that (h, b) is formally equivalent to (h, q). Use of (h, q) is possible, but would entail the additional (computational) evaluation of the mapping $b \mapsto q$ which is time consuming in numerical implementation. For Newtonian problems this mapping would be linear and there is essentially no computational penalty of working with (h, q).

Therefore as velocity closure, for any value of (h, b) we formally compute the parallel flow solution described in §6.1.2; U_0 and f are uniquely determined as:

$$f = f_p(h, b), \qquad U_0(y) = U_p(y; h, b).$$

Note that in this way f is also slaved to (h, b) and has the physical meaning of a leading order modified pressure gradient, although it is not necessary that $f = f_0$. However, if we wish to resolve the limit $Re \to 0$ consistently in our approximation, we need to base our velocity closure on the form of the solution found in the thin-film limit. Consistency as $Re \to 0$ is found provided that

$$b = \chi - \delta\chi \tan\beta \frac{\partial h}{\partial \xi}, \qquad f = f_p(h, \chi - \delta\chi \tan\beta \frac{\partial h}{\partial \xi}) = f_0, \quad \text{as} \quad Re \to 0.$$

This solution has been discussed in §6.1.4.

6.2.2 Weighted residual equation

An evolution equation for $b(\xi, T)$ is needed, to couple to (6.37) for $h(\xi, T)$. We multiply (6.31) by $g_H(y)$ and (6.32) by $g_L(y)$, integrate across the 2

intervals and sum the expressions. Due to the chosen form of weight functions, the terms involving (U_1, f_1) vanish. Substituting (6.52) & (6.53) for the leading order shear stresses leads to a term $(f_0 - f)$ in each of (6.31) and (6.32), which also vanishes due to (6.51). The remaining expressions in the residual equation are:

$$\begin{aligned} 0 &= \delta Re\,[1+At]\int_0^h \frac{\partial U_0}{\partial T} g_H \;\mathrm{dy} + \delta \mathrm{Re}\,[1-\mathrm{At}]\int_{\mathrm{h}}^1 \frac{\partial \mathrm{U_0}}{\partial \mathrm{T}} \mathrm{g_L}\;\mathrm{dy} \\ &\quad + \delta Re\,[1+At]\int_0^h \frac{\partial U_0}{\partial \xi}\left[U_0 g_H - \int_0^h \frac{\partial U_0}{\partial y} g_H \;\mathrm{d\tilde{y}} + \int_0^{\mathrm{y}} \frac{\partial \mathrm{U_0}}{\partial \mathrm{y}} \mathrm{g_H}\;\mathrm{d\tilde{y}}\right]\;\mathrm{dy} \\ &\quad + \delta Re\,[1-At]\int_h^1 \frac{\partial U_0}{\partial \xi}\left[U_0 g_L + \int_h^1 \frac{\partial U_0}{\partial y} g_L \;\mathrm{d\tilde{y}} - \int_{\mathrm{y}}^1 \frac{\partial \mathrm{U_0}}{\partial \mathrm{y}} \mathrm{g_L}\;\mathrm{d\tilde{y}}\right]\;\mathrm{dy} \\ &\quad + \left[\left(\chi - \delta\chi \tan\beta \frac{\partial h}{\partial \xi}\right) - b(\xi, T)\right]\int_h^1 g_L(y)\;\mathrm{dy} \end{aligned} \tag{6.54}$$

Note that we have used integration by parts and the continuity equation to eliminate V_0. Since U_0 is uniquely determined by (h, b), (6.54) can be regarded an evolution equation for $b(\xi, T)$, of the form:

$$0 = A^h \frac{\partial h}{\partial T} + A^b \frac{\partial b}{\partial T} + C^h \frac{\partial h}{\partial \xi} + C^b \frac{\partial b}{\partial \xi} + \left[\left(\chi - \delta\chi \tan\beta \frac{\partial h}{\partial \xi}\right) - b\right] S \tag{6.55}$$

where

$$A^h(h,b) = \delta Re\,[1+At]\int_0^h \frac{\partial U_0}{\partial h} g_H \;\mathrm{dy} + \delta \mathrm{Re}\,[1-\mathrm{At}]\int_{\mathrm{h}}^1 \frac{\partial \mathrm{U_0}}{\partial \mathrm{h}} \mathrm{g_L}\;\mathrm{dy} \tag{6.56}$$

$$A^b(h,b) = \delta Re\,[1+At]\int_0^h \frac{\partial U_0}{\partial b} g_H \;\mathrm{dy} + \delta \mathrm{Re}\,[1-\mathrm{At}]\int_{\mathrm{h}}^1 \frac{\partial \mathrm{U_0}}{\partial \mathrm{b}} \mathrm{g_L}\;\mathrm{dy} \tag{6.57}$$

$$\begin{aligned} C^h(h,b) &= \delta Re\,[1+At]\int_0^h \frac{\partial U_0}{\partial h}\left[U_0 g_H - \int_0^h \frac{\partial U_0}{\partial y} g_H \;\mathrm{d\tilde{y}} + \int_0^{\mathrm{y}} \frac{\partial \mathrm{U_0}}{\partial \mathrm{y}} \mathrm{g_H}\;\mathrm{d\tilde{y}}\right]\;\mathrm{dy} \\ &+ \delta Re\,[1-At]\int_h^1 \frac{\partial U_0}{\partial h}\left[U_0 g_L + \int_h^1 \frac{\partial U_0}{\partial y} g_L \;\mathrm{d\tilde{y}} - \int_{\mathrm{y}}^1 \frac{\partial \mathrm{U_0}}{\partial \mathrm{y}} \mathrm{g_L}\;\mathrm{d\tilde{y}}\right]\;\mathrm{dy} \end{aligned} \tag{6.58}$$

$$\begin{aligned} C^b(h,b) &= \delta Re\,[1+At]\int_0^h \frac{\partial U_0}{\partial b}\left[U_0 g_H - \int_0^h \frac{\partial U_0}{\partial y} g_H \;\mathrm{d\tilde{y}} + \int_0^{\mathrm{y}} \frac{\partial \mathrm{U_0}}{\partial \mathrm{y}} \mathrm{g_H}\;\mathrm{d\tilde{y}}\right]\;\mathrm{dy} \\ &+ \delta Re\,[1-At]\int_h^1 \frac{\partial U_0}{\partial b}\left[U_0 g_L + \int_h^1 \frac{\partial U_0}{\partial y} g_L \;\mathrm{d\tilde{y}} - \int_{\mathrm{y}}^1 \frac{\partial \mathrm{U_0}}{\partial \mathrm{y}} \mathrm{g_L}\;\mathrm{d\tilde{y}}\right]\;\mathrm{dy} \end{aligned} \tag{6.59}$$

$$S(h,b) = \int_h^1 g_L(y)\;\mathrm{dy} \tag{6.60}$$

6.2.3 Calculating the weight functions and terms in the residual equation (6.55)

The weight functions are defined by the problem (6.45) - (6.51). Unlike the Newtonian problem, the tangent viscosity functions that appear in (6.49) & (6.50) depend on the local rate of strain $\dot{\gamma}_0$. This means that the weight functions will depend on b as well as h. At first glance the problem (6.45) - (6.51) appears to be just as formidable as computing $U_0(y)$. However, in fact the weight functions can be determined analytically from the zeroth order solution $U_0(y)$, because the problem is linear in $g_k(y)$.

First, let's observe that the problem (6.45) - (6.51) for the weight functions is an exchange flow problem for two fluids, with y-varying viscosities given by the tangent viscosities in each layer. Considering (6.47) we denote by $\tau_{w,i}$ the common value of the weight function *shear stress* at the interface, i.e.

$$\tau_{w,i} = \eta_{H,t}(\dot{\gamma}_0)\frac{\partial g_H}{\partial y}(h) = \eta_{L,t}(\dot{\gamma}_0)\frac{\partial g_L}{\partial y}(h),$$

and now integrate (6.49) & (6.50) out from $y = h$:

$$\eta_{H,t}(\dot{\gamma}_0)\frac{\partial g_H}{\partial y} = \tau_{w,i} - a(y-h), \qquad y \in (0,h), \tag{6.61}$$

$$\eta_{L,t}(\dot{\gamma}_0)\frac{\partial g_L}{\partial y} = \tau_{w,i} + (1-a)(y-h), \qquad y \in (h,1). \tag{6.62}$$

The right hand sides of (6.61) & (6.62) are linear in y, but $\eta_{k,t}(\dot{\gamma}_0) \propto \dot{\gamma}_0^{n_k-1}$, which is not a linear function of y. However, $\dot{\gamma}_0^{n_k}$ is a linear function of y, and it therefore appears that the derivatives of g_k must mimic the behaviour of $\dot{\gamma}_0$ in order to satisfy (6.61) & (6.62). In any yielded region of flow, $\dot{\gamma}_0^{n_k}$ is proportional to the shear stress, minus the yield stress. This strongly suggests that for $k = H,\ L$ the quantity

$$\eta_{k,t}(\dot{\gamma}_0)\frac{\partial g_k}{\partial y}$$

must be a linear function of the shear stress $\tau_{k,xy}(y)$, in layer k. By comparing with (6.61) & (6.62) these linear relations are easily determined, leading to:

$$\frac{\partial g_H}{\partial y} = \frac{\frac{a}{f}[\tau_{H,xy}(y) - \tau_i] + \tau_{w,i}}{\eta_{H,t}(\dot{\gamma}_0)}, \qquad y \in (0,h), \tag{6.63}$$

$$\frac{\partial g_L}{\partial y} = \frac{\frac{1-a}{b-f}[\tau_{L,xy}(y) - \tau_i] + \tau_{w,i}}{\eta_{L,t}(\dot{\gamma}_0)}, \qquad y \in (h,1). \tag{6.64}$$

Note that f and τ_i are already determined as part of the velocity closure, slaved to (h, b). We therefore have two unknown constants to determine: $\tau_{w,i}$ and a. These are effectively an interfacial stress and modified pressure gradient for the weight function problem. These two constants will be determined via (6.46) and (6.51), respectively.

First we integrate (6.63) from the lower wall, where we impose (6.45). After some algebra we find:

$$\begin{aligned} g_H(y) &= \frac{a}{f}J_{H,m_H}(y) + \left[\tau_{w,i} - \frac{a}{f}\tau_i\right] I_{H,m_H-1}(y) + \frac{aB_H}{f}J_{H,m_H-1}(y), \\ &= ah[I_{H,m_H-1}(y) - L_{H,m_H}(y)] + \tau_{w,i}I_{H,m_H-1}(y), \end{aligned} \tag{6.65}$$

where we define:

$$L_{k,m_k} = \frac{J_{k,m_k}(y) + B_k J_{k,m_k-1}(y) - \tau_k I_{k,m_k-1}(y)}{\tau_i - \tau_k}, \qquad k = H, L. \tag{6.66}$$

The advantage of using the function L_{k,m_k} is that this combination of the functions J_{k,m_k}, J_{k,m_k-1} and I_{k,m_k-1} does not become singular as $\tau_i \to \tau_k$. Similarly, we integrate (6.64) out from the upper wall, where we impose (6.48) and find:

$$\begin{aligned} g_L(y) &= -\frac{(1-a)}{(b-f)}J_{L,m_L}(y) - \left[\tau_{w,i} - \frac{(1-a)}{(b-f)}\tau_i\right] I_{L,m_L-1}(y) \\ &- \frac{(1-a)B_L}{(b-f)}J_{L,m_L-1}(y). \end{aligned} \tag{6.67}$$

Equating the two weight functions at the interface, i.e. imposing (6.46), gives one linear equation relating $\tau_{w,i}$ and a:

$$\tau_{w,i} = \frac{ah[L_{H,m_H-1}(h) - I_{H,m_H}(h)] + (1-a)(1-h)[L_{L,m_L}(h) - I_{L,m_L-1}(h)]}{[I_{H,m_H-1}(h) + I_{L,m_L-1}(h)]}. \tag{6.68}$$

Note that $[I_{H,m_H-1}(h) + I_{L,m_L-1}(h)] > 0$. We determine a by satisfying (6.51). For this we need to compute the fluxes of the weight functions. Algebraic expressions for the integrals of the functions $I_{k,p}$, $J_{k,p}$ and $L_{k,p}$ are given in appendix C. Having eliminated $\tau_{w,i}$, this results in single linear equation for a. The complete solution is given in appendix B.

Figure 6.3 shows examples of the weight functions $g_H(y)$ and $g_L(y)$ for the same base flow solutions as in Fig. 6.2. In Fig. 6.3a as B_L is increased we have seen in Fig. 6.2a that $U(y) \to 0$ in the upper layer. In this limit we find also that $g_L(y) \to 0$, and since the net flux is zero, we also have

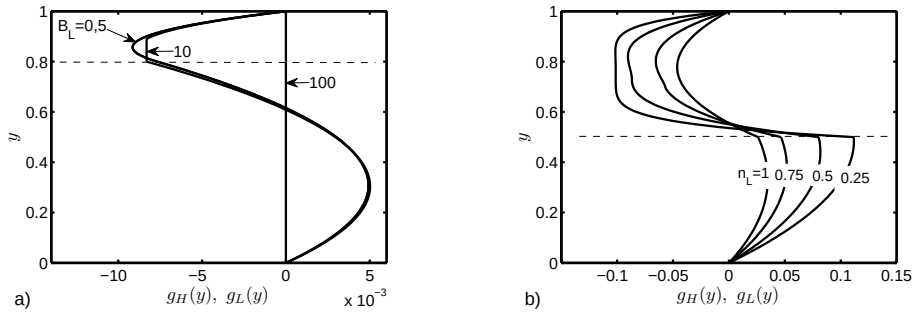

Figure 6.3: a) Examples of heavy and light fluid weight functions, $g_H(y)$ and $g_L(y)$, varying with B_L for $B_H = 0$, $m = 1$, $n_L = 1$, $n_H = 1$ and $b = 10$. The broken line indicates the position of the interface ($h = 0.8$). b) Change in $g_H(y)$ and $g_L(y)$, with n_L. The parameters used are $B_L = 0$, $B_H = 0$, $m = 0.2$, $n_H = 1$ and $b = 0$. The broken line indicates the position of the interface ($h = 0.5$).

$g_H(y) \to 0$. This flow, when the upper layer is stationary is simply that of a single fluid in a channel of reduced constant width. In this situation, neither h nor b evolves and $q = 1$, since all the fluid passes in the lower layer.

In Fig. 6.3b we see a progressively plug-like profile for g_L as n_L decreases, due to the progressively singular tangent viscosity of the base flow. Undulations are evident in $g_L(y)$ for $n_L = 0.75$ and $n_L = 0.5$, but are also there for $n_L = 0.25$ if one zooms in. These are physical and can be explained as follows. First we have from (6.62) that:

$$\frac{\partial g_L}{\partial y} = \frac{\tau_{w,i} + (1-a)(y-h)}{\eta_{L,t}(\dot{\gamma}_0)},$$

Since the net flux of the weight functions is zero, we may expect a maximum in $g_H(y)$ and a minimum in $g_L(y)$. The minimum in $g_L(y)$ is where $\tau_{w,i} + (1-a)(y-h) = 0$. If fluid L is shear-thinning ($n_L < 1$) we may also have a maximum in $U_0(y)$ (see Fig. 6.2b), at which we have $\eta_{L,t}(\dot{\gamma}_0) \to 0$. We see that the maximum in $U_0(y)$ implies a second stationary point of $g_L(y)$. At the second stationary point, $\frac{\partial g_L}{\partial y} \to 0$, but does not generally change sign, which results in an inflection point.

Calculation of the various terms in the residual equation (6.55) is described fully in appendix B. In outline the procedure is as follows. We first develop expressions for the partial derivatives of U_0 with respect to h

and b. These expressions are linear combinations of the functions $I_{k,p}$ and $J_{k,p}$, in each fluid k layer. The terms contributing to A^h and A^b are consequently comprised of linear combinations of integrals across each fluid layer of quadratic products of the $I_{k,p}$ and $J_{k,p}$ functions. For the terms contributing to C^h and C^b there are additional products with U_0 and derivatives of U_0. These can also be expressed as linear combinations of the $I_{k,p}$ and $J_{k,p}$ functions. Consequently, the terms contributing to C^h and C^b are comprised of linear combinations of integrals across each fluid layer of cubic products of the $I_{k,p}$ and $J_{k,p}$ functions. Algebraic expressions for the integrals of quadratic and cubic products of the $I_{k,p}$ and $J_{k,p}$ functions is described fully in appendix C. Aside from lengthy algebra (which can be largely automated in computation) there is no essential difficulty in resolving these expressions algebraically.

Examples of the inertial coefficients are shown in Fig. 6.4, plotted against (h, b). For two identical Newtonian fluids we see in Fig. 6.4 that the contours of these functions exhibit strong symmetry. This symmetry is no longer present when one of the fluids is rheologically different from the other. In each case, all the coefficients A^h, A^b, C^h and C^b vanish near the walls of the channel, returning the problem to a single fluid problem.

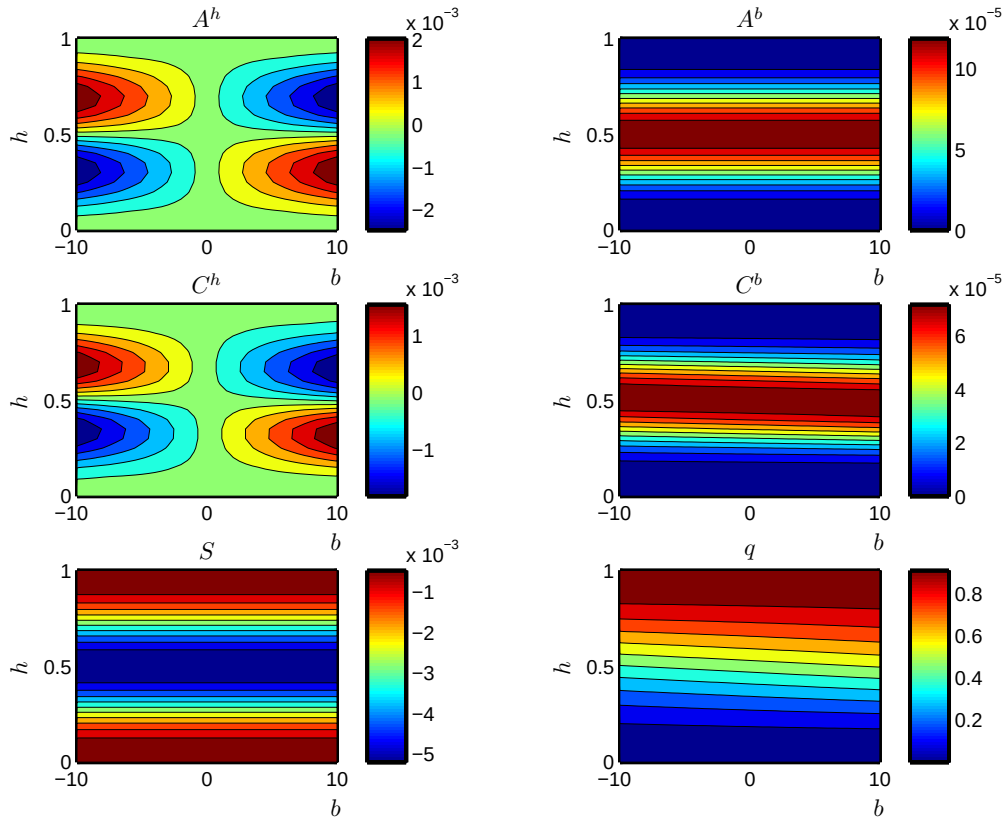

Figure 6.4: Contours of the inertial coefficients, A^h, A^b, C^h, C^b, S and q, in (b,h)-plane. Parameters used are $B_L = 0$, $B_H = 0$, $m = 1$, $n_L = 1$, $n_H = 1$, $At = 0$ and $\delta Re = 1$.

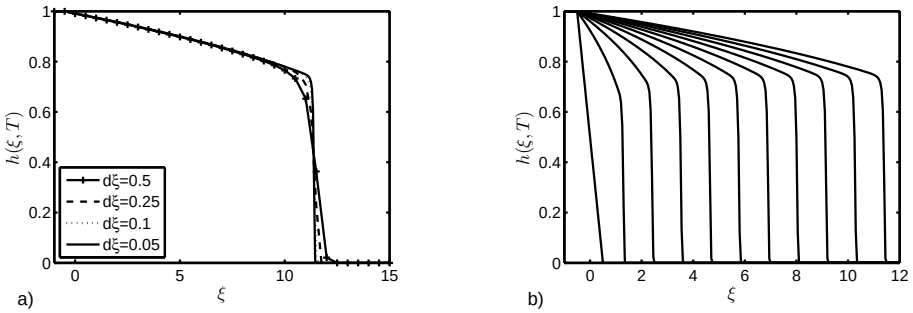

Figure 6.5: a) Dependency of the interface evolution on mesh size. The parameters used are $B_H = 0$, $B_L = 0$, $m = 1$, $n_H = 1$, $n_L = 1$, $\chi = 0$, $\delta Re = 0$ and the solutions are compared at $T = 10$. b) Evolution of the interface height with time ($T = [0, 1, 2, .., 10]$) for the parameters as in part a.

6.3 Results: displacement flows

Our reduced model consists of (6.37) and (6.55), which determine the evolution of (h, b), providing a first order accurate approximation to h and the volumetric fluxes in each layer. When furnished with appropriate initial and boundary conditions these equations can model the long-time dynamics of a slumping displacement flow in the weakly inertial regime.

For numerical solution of these equations, we suppose fully developed flows of pure fluid H as $\xi \to -\infty$ and of fluid L as $\xi \to \infty$. As initial condition we take a linear profile ($h(\xi, 0) = 0.5 - \xi$) separating fluid H and fluid L. The kinematic condition (6.37) is discretized in conservative form, second-order in space and first-order explicitly in time. It is integrated using a Van Leer flux limiter scheme (see e.g. [151]) for shock capturing. For the depth-averaged momentum equation (6.55) the same flux limiter scheme has been used. However, (6.37) and (6.55) are solved sequentially and we have used updated values for h in the solution of (6.55), making the scheme semi-implicit. Iterations continue up to the desired end time of the computation.

To explore the performance of the numerical procedure we examine convergence with varying spatial mesh step $d\xi$, in Fig. 6.5a. The results are in full agreement with those presented in [128] as $\delta Re \to 0$. Computations performed for the rest of the paper use $d\xi = 0.05$. A typical displacement flow computation is shown in Fig. 6.5b, for the same parameters as in Fig. 6.5a.

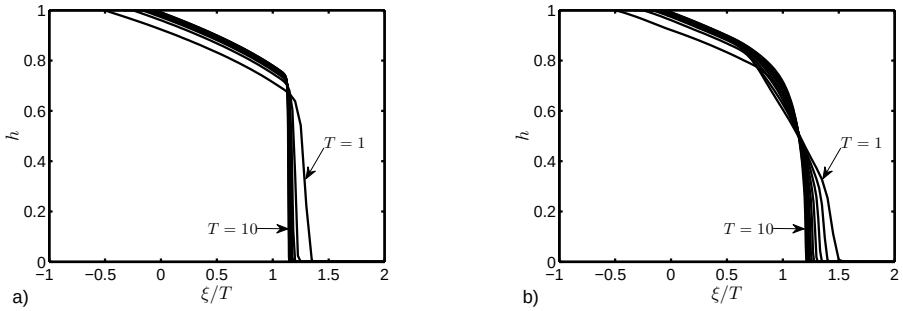

Figure 6.6: Collapse of the interface heights, h, by using ξ/T instead of ξ for $T = [1, 2, ...10]$. The parameters used are $B_H = 0$, $B_L = 0$, $m = 1$, $n_H = 1$, $n_L = 1$, $\chi = 0$ and a) $\delta Re = 0$, b) $\delta Re = 50$.

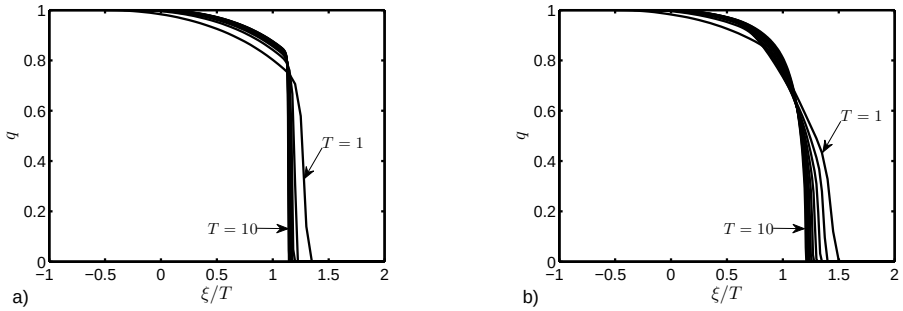

Figure 6.7: Self-similarity of $q(h, b)$, plotted against ξ/T instead of ξ, for $T = [1, 2, ...10]$; parameters as in Fig. 6.6: a) $\delta Re = 0$, b) $\delta Re = 50$.

The interface evolution observed in Fig. 6.5b for $\delta Re = 0$ results in a steadily advancing displacement front, stretching out other parts of the interface. At longer times the interface profiles collapse onto a single curve when rescaled with ξ/T, as shown in Fig. 6.6a. When inertia is introduced we still find the interface evolving to a similarity solution (see Fig. 6.6b), but it can be seen that both the final shape of the scaled interface is different and that inertia delays convergence of the interface to the self-similar profile. It is not only the interface height that approaches a similarity shape. All the process variables appear to follow the convergence of the interface. As an example, we plot the volumetric flux $q(h, b)$ in Fig. 6.7, for the same flows as in Fig. 6.6.

Although convergence to the similarity solution is slower with inertia than without, we have found that the converged solution is well approximated by the solution at $T = 10$ in all cases examined. Therefore, in order to examine the effects of the different parameters on the similarity shape of the interface, we have simply plotted $h(\xi, T)$ at $T = 10$ as a function of ξ/T. An alternative to this procedure would be to reformulate (6.37) and (6.55) in terms of $h(\xi/T)$ and $b(\xi/T)$ and try to compute directly. However, this procedure is rather complex. In the self-similar profiles presented in e.g. Fig. 6.6b, note that a vertical segment of $h(\xi/T)$ simply indicates a part of the interface advancing at constant speed and not a shock. In the thin-film/lubrication limit of $\delta Re = 0$ shocks only arise for the pure advective case, where the slope of the interface is negelected. Normally, in the frontal region of the propagating interface the diffusive term $h_{\xi\xi}$ (due to gravitational spreading) is active in smoothing the interface; see the discussion in [128]. We suspect that there is similar gravitational spreading here, when inertia is present.

Figure 6.8 presents general effects on displacement for a range of parametric variations, all for fluids with no yield stress ($B_H = 0$, $B_L = 0$). Inertia is usually found to result in marginally faster interface speeds of the leading displacement front (of the order of a few percent); see Fig. 6.8a. In [126] we have shown that an inertialess lubrication/thin film model underpredicts the front velocity measured in our experiments by a similarly small amount. Together with the faster frontal speed, the front height is lower and $h(\xi/T)$ generally appears more rounded with inertial effects than without. Note that the small difference in $h(\xi/T)$, evident above, are amplified in the $h(\xi, T)$ representation, so that it is incorrect to assume that e.g. inertial effects are negligible.

The effects of viscosity ratio are shown in Figs. 6.8b & d. If the displaced fluid L is less viscous $m < 1$ we observe that the front height is higher and the

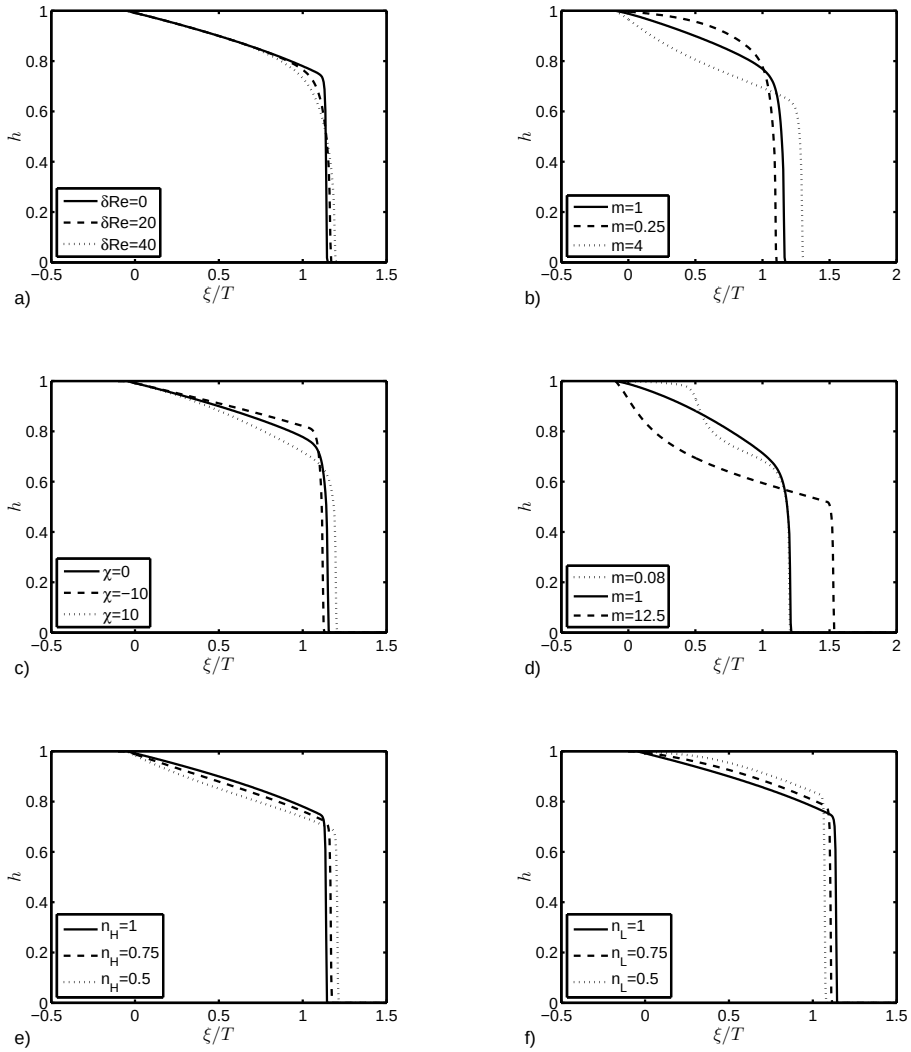

Figure 6.8: Effects of various parameters on similarity shape of the interface, $h(\xi, T)$ at $T = 10$ as a function of ξ/T: a) δRe varying for $m = 1$, $n_H = 1$, $n_L = 1$, $\chi = 0$; b) m varying for $n_H = 1$, $n_L = 1$, $\chi = 0$, $\delta Re = 10$; c) χ varying for m, $n_H = 1$, $n_L = 1$, $\delta Re = 10$; d) m varying for $n_H = 1$, $n_L = 1$, $\chi = 10$, $\delta Re = 10$; e) n_H varying for $m = 1$, $n_L = 1$, $\chi = 0$, $\delta Re = 10$; f) n_L varying for $m = 1$, $n_H = 1$, $\chi = 0$, $\delta Re = 10$. For all results $B_H = 0$, $B_L = 0$.

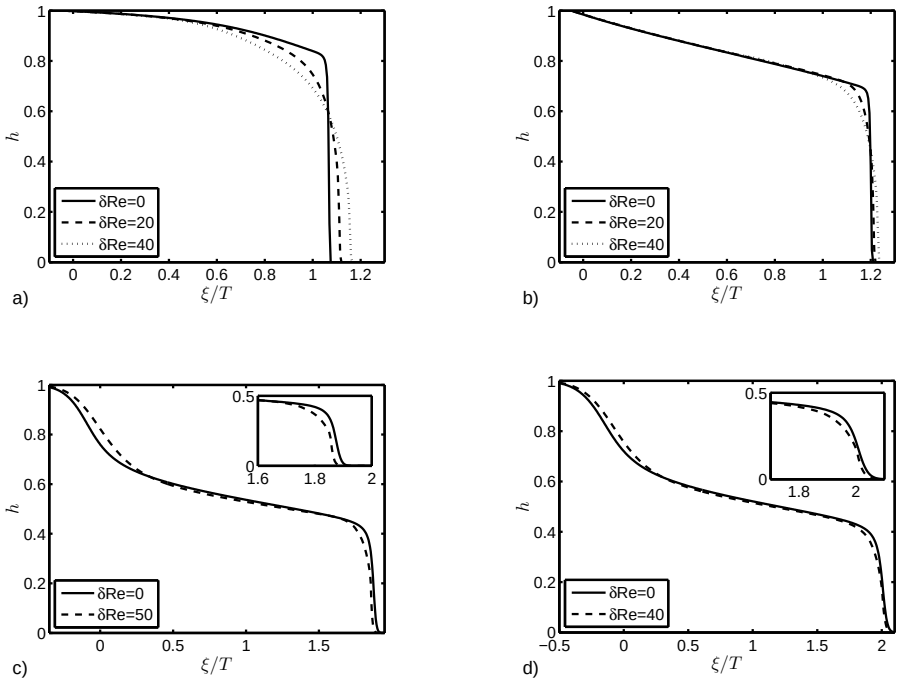

Figure 6.9: Effects of varying inertia (δRe) on similarity shape of the interface, $h(\xi, T)$ at $T = 10$ as a function of ξ/T: a) $\chi = 0$, $m = 0.25$; b) $\chi = 0$, $m = 2$; c) $\chi = 100$, $m = 10$; d) $\chi = 120$, $m = 12.5$. The inset in parts c and d zoom in on the displacement fronts for easier comparison of profiles. For all results $B_H = 0$, $B_L = 0$, $n_L = 1$, $n_H = 1$.

front speed is slower, meaning that the displacement is more effective. On the other hand, for $m > 1$ the front moves more rapidly through fluid L and displacement efficiency is reduced. The effects of buoyancy manifest through χ (Fig. 6.8c). For a positive value of χ buoyancy pushes fluid L backwards against the mean flow. A negative value of χ would correspond to displacing uphill, where buoyancy forces act to push fluid L in the same direction as the mean flow. Perhaps intuitively, front height increases and the displacement becomes more effective as χ is decreased. Figure 6.8d shows the effects of positive χ with viscosity ratio. Here for $m = 0.08$ we observe two frontal regions. At low viscosities the buoyancy is becoming increasingly effective at retarding the light fluid layer, which competes against the positive effects of the viscosity ratio.

Figures 6.8e & f show the effects of varying the two power law indices. The effects are fairly intuitive and can be understood as a viscous effect. Smaller n_k shear-thins fluid k, which reduces the effective viscosity. Parameters that reduce the viscosity of the displacing fluid with respect to the displaced fluid also result in faster and lower fronts, reducing the displacement efficiency, e.g. reducing n_H. Reducing n_L improves the displacement efficiency.

Further examination of the effects of varying inertia (δRe) is presented in Fig. 6.9 for two Newtonian fluids of different viscosity ratio. In the absence of buoyancy (Figs. 6.9a & b) we see faster interface speeds of the leading displacement front, lower frontal heights and less efficient displacement. However, there are ranges of parameters at larger χ for which inertia apparently can reduce the speed of the leading displacement front, albeit marginally, as illustrated in Figs. 6.9c & d.

6.4 Stability of 2-layer flows

One of the main motivations for using the weighted residual approach is that it has proven effective in predicting long wavelength instabilities for weakly inertial thin film flows ([104]) and multi-layer flows ([8]). Here we explore whether this effectiveness carries over to multi-layer non-Newtonian fluid flows. First we make a comparison between a linear stability analysis of the weighted residual approach for a uniform layer and that for a parallel two-layer shear flow, leading to an Orr-Sommerfeld formulation. Secondly, we use the weighted residual approach to study the stability of various scenarios, including those that result during displacements.

6.4.1 Weighted residual method stability of a parallel flow

The governing equations of the weighted residual method are (6.37) and (6.55), which model evolution of (h, b). To compare with a more classical Orr-Sommerfeld approach we carry out a linear stability analysis of a uniform steady solution: $(h_0, b_0) =$ constant. A constant uniform solution of (6.37) and (6.55) is also a two-layer parallel solution of the full Navier-Stokes system, as has been described in §6.1.2. Any $h_0 \in [0, 1]$ may be considered, but steady constant b_0 must satisfy:

$$b_0 = \chi. \tag{6.69}$$

Recall that χ gives the ratio of viscous forces to buoyancy forces (along the channel). The base velocity U_0 and modified pressure gradient f_0 then coincide exactly with the parallel flow solution, i.e.

$$U_0(y) = U_p(y; h_0, \chi), \qquad f = f_0 = f_p(h_0, b_0), \tag{6.70}$$

with $P_0(x, y) = P_p(x, y; h_0, \chi)$ defined from (6.18). The same base solution is used for the Orr-Sommerfeld analysis to follow.

In order to be able to compare directly with the results of the Orr-Sommerfeld analysis, we need to adopt the same length- and timescales, which necessitates a re-scaling of both time T and axial distance ξ with δ. Using the Leibnitz integral rule we transform the kinematic condition (6.37) into

$$\frac{\partial h}{\partial t} + U_0 \frac{\partial h}{\partial x} + \frac{\partial h}{\partial x} \int_0^h \frac{\partial U_0}{\partial h} \, \mathrm{dy} + \frac{\partial \mathrm{b}}{\partial \mathrm{x}} \int_0^{\mathrm{h}} \frac{\partial \mathrm{U_0}}{\partial \mathrm{b}} \, \mathrm{dy} = 0. \tag{6.71}$$

Note that $\partial U_0/\partial h$ and $\partial U_0/\partial b$ have been computed in evaluating the terms in (6.55). The re-scaled residual equation takes the form:

$$\begin{aligned} 0 \;=\; & A^h(h,b)\frac{\partial h}{\partial t} + A^b(h,b)\frac{\partial b}{\partial t} + C^h(h,b)\frac{\partial h}{\partial x} + C^b(h,b)\frac{\partial b}{\partial x} \\ & + \delta S(h,b)\left(\chi(1 - \tan\beta \frac{\partial h}{\partial x}) - b\right). \end{aligned} \tag{6.72}$$

Note that the coefficients A^k & C^k are linear in δ, so that (6.72) is independent of δ.

As is usual, we suppose a linear perturbation:

$$h = h_0 + h', \qquad b = b_0 + b', \tag{6.73}$$

and substitute (6.73) into (6.71) and (6.72), retaining only linear terms:

$$\frac{\partial h'}{\partial t} + \left(U_0 + \int_0^{h_0} \frac{\partial U_0}{\partial h}\ \mathrm{dy}\right)\frac{\partial h'}{\partial x} + \left(\int_0^{h_0} \frac{\partial U_0}{\partial b}\ \mathrm{dy}\right)\frac{\partial b'}{\partial x} = 0, \quad (6.74)$$

$$A^h\frac{\partial h'}{\partial t} + A^b\frac{\partial b'}{\partial t} + C^h\frac{\partial h'}{\partial x} + C^b\frac{\partial b'}{\partial x} - \delta S\chi\tan\beta\frac{\partial h'}{\partial x} - \delta S b' = 0, \quad (6.75)$$

Note that all algebraic functions above are evaluated at the steady $(h, b) = (h_0, b_0)$. We now assume a modal form for the linear perturbations, periodic in x, so that:

$$h' = \overline{h}\mathrm{e}^{\mathrm{i}\alpha(\mathrm{x}-\mathrm{ct})}, \quad \mathrm{b}' = \overline{\mathrm{b}}\mathrm{e}^{\mathrm{i}\alpha(\mathrm{x}-\mathrm{ct})}, \quad (6.76)$$

where $\overline{h}$ and $\overline{b}$ are constants. Substituting (6.76) into (6.74) and (6.75) leads to a dispersion relation that is quadratic in c:

$$\begin{vmatrix} \left(U_0 + \int_0^{h_0} \frac{\partial U_0}{\partial h}\ \mathrm{dy}\right) - c & \left(\int_0^{h_0} \frac{\partial U_0}{\partial b}\ \mathrm{dy}\right) \\ \mathrm{i}\alpha(\mathrm{C^h} - \mathrm{cA^h} - \mathrm{S}\chi\tan\beta) & \mathrm{i}\alpha(\mathrm{C^b} - \mathrm{cA^b}) - \mathrm{S} \end{vmatrix} = 0 \quad (6.77)$$

If the imaginary part of c is positive, the flow is linearly unstable. Although we can find c for any wave number α, for the values we have tested the sign of the imaginary part of c is determined by the long wavelength limit, and in any case we wish to benchmark the solution against the log-wavelength Orr-Sommerfeld solution. The long wavelength analysis ($\alpha \to 0$) is made by expanding c, $\overline{h}$ and $\overline{b}$ with respect to $\alpha \ll 1$:

$$c = c_0 + \alpha c_1 + ..., \quad \overline{h} = \overline{h}_0 + \alpha\overline{h}_1 + ..., \quad \overline{b} = \overline{b}_0 + \alpha\overline{b}_1 + ...$$

This gives at leading order $\overline{b}_0 = 0$ and:

$$c_0 = U_0 + \int_0^{h_0} \frac{\partial U_0}{\partial h}\ \mathrm{dy}, \quad (6.78)$$

$$= \frac{J_{H,m_H}(h_0)}{m_H} + \frac{\partial\tau_H}{\partial h}\int_0^{h_0} I_{H,m_H-1}(y)\ \mathrm{dy} - \mathrm{h}\frac{\partial \mathrm{f}}{\partial \mathrm{h}}\int_0^{\mathrm{h_0}} \mathrm{L_{H,m_H}(y)}\ \mathrm{dy}. \quad (6.79)$$

We note that c_0 is real. At first order we find that $c_1 = c_{1,R} + \mathrm{ic_{1,I}}$ is purely imaginary, determined by:

$$c_{1,I} = \frac{(C^h - c_0 A^h - \delta S\chi\tan\beta)}{\delta S}\int_0^{h_0} \frac{\partial U_0}{\partial b}\ \mathrm{dy}. \quad (6.80)$$

Note again that this quantity is independent of δ since the coefficients A^k & C^k are linear in δ.

6.4.2 Orr-Sommerfeld analysis

We consider two-dimensional linear perturbations to the two-layer base flow discussed at the start of §6.4.1 above. Perturbed solutions are assumed to have form: $\mathbf{u} = (U_0(y), 0) + \epsilon(\tilde{u}, \tilde{v})$, $p = P_0(x, y) + \epsilon\tilde{p}$, $h = h_0 + \epsilon\tilde{h}$ and we retain only terms linear in ϵ. The two-dimensional velocity field can be represented by means of a stream function, i.e. $(\tilde{u}, \tilde{v}) = (\Psi_y, -\Psi_x)$. We cross differentiate the linearised momentum equations to eliminate the pressure, and assume the following modal form for the linear perturbation:

$$\Psi = \psi(y)\mathrm{e}^{\mathrm{i}\alpha(\mathrm{x}-\mathrm{ct})}, \qquad \tilde{\mathrm{h}} = \bar{\mathrm{h}}\mathrm{e}^{\mathrm{i}\alpha(\mathrm{x}-\mathrm{ct})}.$$

In any layer in which the base flow is yielded we have the following linear stability problem:

$$\mathrm{i}\alpha c\Delta\psi = \mathcal{L}\psi. \tag{6.81}$$

The linear operator $\mathcal{L}$ has the following form in fluid k:

$$\begin{aligned}\mathcal{L}\psi \quad \equiv \quad & \mathrm{i}\alpha\mathrm{U}_0(\mathrm{D}^2 - \alpha^2)\psi - \mathrm{i}\alpha\mathrm{D}^2\mathrm{U}_0\psi + \frac{4\alpha^2}{\mathrm{Re_k}}\mathrm{D}[\eta_\mathrm{k}\mathrm{D}\psi] \\ & -\frac{1}{Re_k}(D^2 + \alpha^2)[\eta_{k,t}(D^2 + \alpha^2)\psi],\end{aligned}$$

where $D \equiv \frac{\mathrm{d}}{\mathrm{dy}}$ and $Re_k = Re(1 \pm At)$ in heavy and light fluids, respectively. Apart from the base velocity, the other functions appearing above are the effective viscosity $\eta_k(\dot{\gamma})$ and the tangent viscosity $\eta_{k,t}(\dot{\gamma})$; see (6.12) & (6.13). These are both evaluated using the strain rate of the base flow: $\dot{\gamma} = |DU_0|$.

Boundary and interface conditions

The boundary conditions for ψ may depend on the nature of the fluid and base flow. The simplest case is when both fluid layers are fully yielded (e.g. two power-law fluids). The boundary conditions on the walls are:

$$\psi = D\psi = 0, \qquad y = 0,\ 1. \tag{6.82}$$

The fluids are both yielded at the interface, which may itself deform. Interface evolution is governed by the following kinematic equation:

$$c\bar{h} = U_0\bar{h} + \psi, \qquad y = h_0, \tag{6.83}$$

which contributes directly to the eigenvalue problem. Coupling between the fluid layers is governed by the linearised conditions of continuity of velocity

and stress:

$$0 = \psi\big|_{h_0^+}^{h_0^-} \tag{6.84}$$

$$0 = (D\psi + \bar{h}DU_0)\big|_{h_0^+}^{h_0^-} \tag{6.85}$$

$$0 = [\eta_{k,t}(D^2+\alpha^2)\psi]\big|_{h_0^+}^{h_0^-} - \bar{h}\chi, \tag{6.86}$$

$$0 = \left(\mathrm{i}\alpha \mathrm{Re_k}[(\mathrm{c}-\mathrm{U_0})\mathrm{D}\psi + \psi \mathrm{DU_0}] - 4\alpha^2\eta_\mathrm{k}\mathrm{D}\psi + \mathrm{D}[\eta_{\mathrm{k,t}}(\mathrm{D}^2+\alpha^2)\psi]\right)\big|_{h_0^+}^{h_0^-} - \mathrm{i}\alpha\bar{\mathrm{h}}\chi\tan\beta. \tag{6.87}$$

Note that we neglect surface tension. Assuming that $\bar{h} \neq 0$, we may eliminate $\bar{h}$ from the above. However, doing this leads to c appearing quadratically in (6.87). Alternatively, setting $\bar{h} = 0$ allows us to study the shear modes directly.

If one or more of the fluids has a yield stress, the linear stability problem can only be posed in layers for which the fluid is yielded; see e.g. [52, 53]. If such a layer is bounded by an unyielded plug layer within the fluid layer then the unyielded plug layer is not accelerated by the flow. If the yield surface is at $y = y_y$ the boundary conditions are

$$\psi = D\psi = 0, \qquad y = y_y. \tag{6.88}$$

It may also happen that at least one fluid is unyielded at the interface. Neglecting borderline cases, this implies that the boundary of that layer cannot deform. If one of the fluids is unyielded at the interface (6.83)-(6.87) are replaced in that fluid layer by:

$$\psi = D\psi = 0, \qquad y = h_0. \tag{6.89}$$

In all cases where we have a layer bounded by unyielded fluid, the stability problem in that layer is completely decoupled from the behaviour of other fluid layers. As our main purpose in developing the Orr-Sommerfeld analysis is validation of the weighted residual approach, we do not investigate these more complicated scenarios.

Long-wave limit, $\alpha \longrightarrow 0$

We shall assume the two fluid layers are yielded everywhere and consider a perturbation with wavelength much larger than the channel width. We develop a regular perturbation expansion in powers of α for ψ, $\bar{h}$ and c:

$$(\psi, \bar{h}, c) = (\psi_0, \bar{h}_0, c_0) + \alpha(\psi_1, \bar{h}_1, c_1) + O(\alpha^2). \tag{6.90}$$

On inserting this expansion into (6.81) and into conditions (6.82)-(6.87), on separating powers of α we find:

Leading order:

$$\begin{aligned}
0 &= D^2(\eta_{k,t}D^2\psi_0), && (6.91)\\
\psi_0 &= D\psi_0 = 0, \quad y = 0,\ 1, && (6.92)\\
0 &= \psi_0|_L^H \quad y = h_0, && (6.93)\\
0 &= (D\psi_0 + \bar{h}_0 DU)|_L^H \quad y = h_0, && (6.94)\\
\eta_{H,t}D^2\psi_0 &= \eta_{L,t}D^2\psi_0 + \bar{h}_0\chi, \quad y = h_0, && (6.95)\\
D[\eta_{H,t}D^2\psi_0] &= D[\eta_{L,t}D^2\psi_0], \quad y = h_0, && (6.96)\\
c_0\bar{h}_0 &= U\bar{h}_0 + \psi_0, \quad y = h_0. && (6.97)
\end{aligned}$$

First order:

$$\begin{aligned}
0 &= D^2(\eta_{k,t}D^2\psi_1) + \mathrm{iRe_k[(c_0 - U)D^2\psi_0 + D^2U\psi_0]}, && (6.98)\\
\psi_1 &= D\psi_1 = 0, \quad y = 0,\ 1 && (6.99)\\
0 &= \psi_1|_L^H \quad y = h_0, && (6.100)\\
0 &= (D\psi_1 + \bar{h}_1 DU)|_L^H \quad y = h_0, && (6.101)\\
\eta_{H,t}D^2\psi_1 &= \eta_{L,t}D^2\psi_1 + \bar{h}_1\chi, \quad y = h_0, && (6.102)\\
\mathrm{i}\chi\tan\beta\bar{\mathrm{h}}_0 &= \left(\mathrm{iRe_H[(c_0 - U)D\psi_0 + \psi_0 DU] + D[\eta_{H,t}D^2\psi_1]}\right)\\
&\quad - \left(\mathrm{iRe_L[(c_0 - U)D\psi_0 + \psi_0 DU] + D[\eta_{L,t}D^2\psi_1]}\right), \quad y = h_0, && (6.103)\\
c_1\bar{h}_0 &= -c_0\bar{h}_1 + U\bar{h}_1 + \psi_1, \quad y = h_0, && (6.104)
\end{aligned}$$

Both leading and first order problems can be solved (formally at least) in terms of integral expressions involving the functions $I_{k,p}$ & $J_{k,p}$. The details of the solution are given in appendix D. Equation (6.97) gives the leading order eigenvalue:

$$\begin{aligned}
c_0 &= \frac{J_{H,m_H}(h_0)}{m_H} + A_p\int_0^{h_0} J_{H,m_H}(y)\ \mathrm{dy} + \mathrm{A_pB_H}\int_0^{\mathrm{h_0}} \mathrm{J_{H,m_H-1}(y)\ dy}\\
&\quad + \left[\frac{1}{2}\left(\chi - A_p\frac{\chi}{\chi - f}\tau_i\right) + \tau_{pi}\right]\int_0^{h_0} I_{H,m_H-1}(y)\ \mathrm{dy}, && (6.105)
\end{aligned}$$

where A_p and τ_{pi} are two real constants determined from two linear equations. We see that c_0 is always real, as is $(\psi_0/\bar{h}_0)$. The first order problem has a similar structure to the leading order problem and is also solved formally in appendix D. The main observation is that $c_1 = c_{1,R} + \mathrm{ic_{1,I}}$ is purely imaginary.

6.4.3 Comparisons with the Orr-Sommerfeld analysis

We have computed solutions of both the long wavelength Orr-Sommerfeld problem and the weighted residual stability equations. We have benchmarked our results against those of [107], who look at the linear stability analysis of a two-layer system (with upper layer being Newtonian fluid and lower layer being a Herschel-Bulkley fluid). The main assumption in their work is that the yield-stress layer is always yielded (i.e. low Bingham number). Figure 6.10a shows typical agreement obtained for a Newtonian-Newtonian case between weighted residual method, Orr-Sommerfeld analysis and Sahu *et al*'s results. Evidently the results are indiscernible, apart from a small numerical error. A number of authors have considered the linear stability of a two-layer power law fluid channel flow, using the Orr-Sommerfeld equation, e.g. [78, 94, 122]. The results of our long wavelength Orr-Sommerfeld analysis compare qualitatively well with these studies. Unfortunately however, no tabulated values are given in [78], who considers the long wavelength problem. We have tried to compare quantitatively with the tabulated values in [94, 122], who benchmark their numerical codes against results from the long wavelength analysis of [78]. However, the comparison is impossible to make from the parameters given in these papers as the authors have used a mix of dimensional and dimensionless parameters, as well as having different scaling than in [78].

With these benchmarks lacking, we have resolved the Orr-Sommerfeld problem directly in the long wavelength limit and made comparisons directly between Orr-Sommerfeld and weighted residual predictions. We have found that the prediction of the leading order c_0 is the same for both the Orr-Sommerfeld and the weighted residual approach for all model parameters that we have tested. The stability of the flow is governed by the sign of c_1/i (positive meaning unstable flow). Here also we have found excellent agreement between long wavelength Orr-Sommerfeld and weighted residual analyses. Examples are shown in Figs. 6.10b-d, for variations in n_H, B_H and χ.

6.4.4 Stability results

One form of analysis that allows for nonlinear evolution is to nonlinearly perturb both the kinematic condition (6.37) and depth-averaged momentum equation (6.55) about a uniform steady solution (h_0, b_0), but track the evolution of the instability by solving (6.37) and (6.55) numerically. This approach has been used in [1, 126], and a similar approach is adopted here.

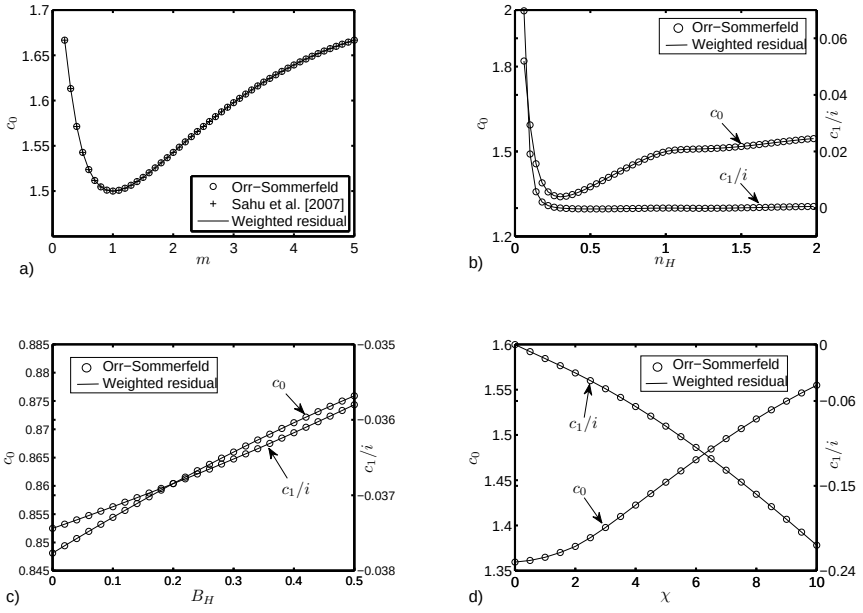

Figure 6.10: Comparison of the leading order growth rate c_0 and the imaginary part of the first order growth rate, c_1/i, in the long-wave limit: weighted residual and Orr-Sommerfeld analysis ($Re_H = Re_L = 1$). a) $B_H = 0$ with m varying ($B_L = 0$, $n_H = 1$, $n_L = 1$, $h_0 = 0.5$ and $\chi = 0$); b) $n_L = 1$ with n_H varying ($B_L = 0$, $B_H = 0$, $m = 1$, $h_0 = 0.5$ and $\chi = 0$); c) $m = 0.5$ with B_H varying ($B_L = 0$, $n_H = 1$, $n_L = 1$, $h_0 = 0.8$, $\chi = 10$ and $\beta = 60°$); d) $n_H = 0.5$, $n_L = 0.7$ with χ varying ($B_H = B_L = 0$, $m = 1$, $h_0 = 0.5$ and $\beta = 60°$).

As initial condition we assume

$$h(\xi,0) = \begin{cases} h_0, & \xi \notin [0,2], \\ h_0 + A^* \sin \pi\xi, & \xi \in [0,2], \end{cases} \tag{6.106}$$

typically for an amplitude $A^* = 0.05$. We integrate (6.37) and (6.55) until $T = 10$ and compare the amplitude of the perturbation with the initial amplitude to determine instability or otherwise.

An example of this is shown in Fig. 6.11 for iso-viscous Newtonian fluids at two different values of χ, at $h_0 = 0.8$. In both cases the initial waveform disperses axially as it propagates. For $\chi = 0$ (Fig. 6.11a) the amplitude decays, whereas for $\chi = 40$ (Fig. 6.11b) the amplitude grows. Larger χ promotes a backflow, which we have observed experimentally is generally destabilizing; see [126, 130]. A backflow implies an inflection point in the velocity profile, often associated with inviscid inertial instability. A precise explanation for our experimental observations is still lacking.

Figures 6.11c & d show the corresponding spatiotemporal diagrams of Figs. 6.11a & b respectively. In these the height of the interface perturbation is translated into a greyscale line, which evolves with time. This captures together both spatial and temporal aspects of the evolution. We see that the wave propagates at a speed that is approximately given by c_0 from the linear stability analysis (evaluated at h_0). The speed of propagation of disturbances is given by the inverse of the slopes in the spatiotemporal plot, and we have marked the speed corresponding to c_0 with the broken white line. Note that the propagation speed is typically different from the velocity at the unperturbed interface.

Results of the linear stability analysis for iso-viscous Newtonian fluids are shown in Fig. 6.12a as marginal stability curves for different h_0. These results agree with those in [126] (Fig. 20a), which have been computed using the (h, q)-formulation of the weighted residual method for Newtonian fluids, whereas Fig. 6.12a uses the (h, b)-formulation developed here. The spatiotemporal stability computation outlined earlier can be repeated successively over broad parameter ranges and compared with the linear stability results. This has been done in Fig. 6.12b and we see that spatiotemporally stable flows are found where the linear analysis predicts.

A large part of our motivation in studying these flows comes from displacement flows. As we have seen in §6.3, at long times a typical displacement consists of an advancing leading front potentially followed by trailing front(s). The advancing fronts maintain constant height and speed, and all other interface heights are progressively stretched as the displacement continues, eventually aligning with the channel. Therefore, there is a range

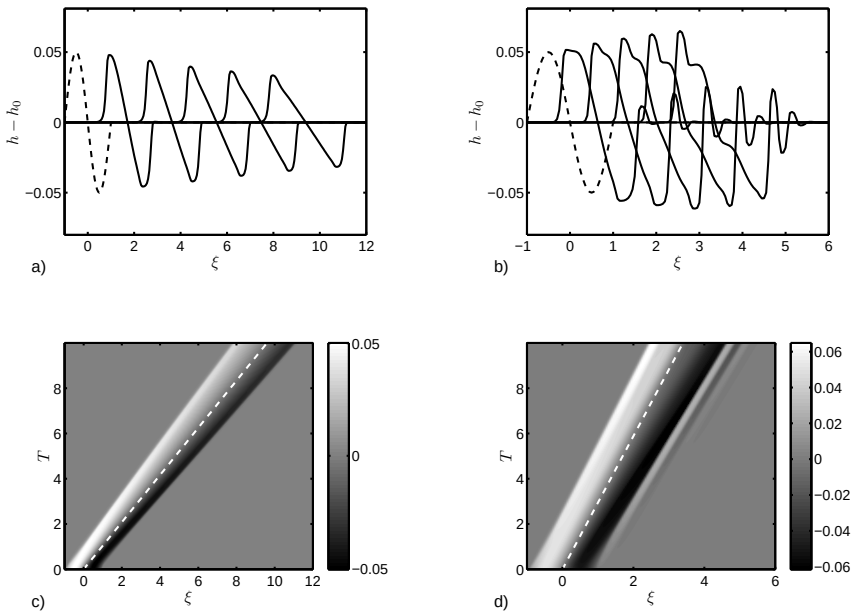

Figure 6.11: Evolution of the perturbation interface height, $h - h_0$, at times $T = 0, 2, 4, ..., 10$, and location, ξ for $h_0 = 0.8$, $B_H = B_L = 0$, $n_H = n_L = 1$, $m = 1$, $\delta Re = 10$ and a) $\chi = 0$ showing *stable* flow b) $\chi = 40$ showing *unstable* flow. Figures c & d show the corresponding spatiotemporal diagrams of Figs. a & b, respectively. The slope of the broken white line indicates $1/c_0$, as calculated from the linear stability analysis performed at h_0.

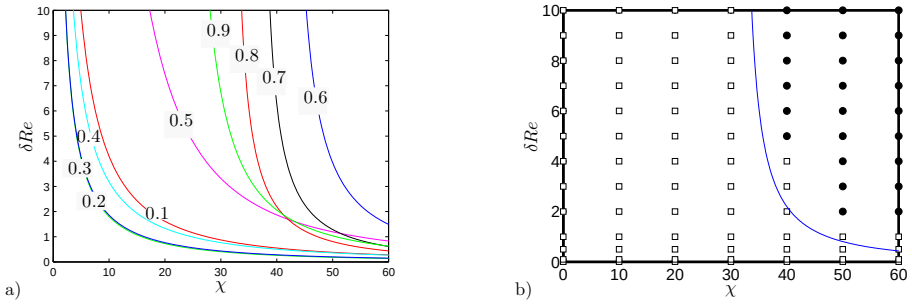

Figure 6.12: a) Marginal stability curves for the long-wave limit of the weighted residual model, for the indicated values of h_0. b) Stability diagram indicating stable flows (□) and unstable flows (•) resulting from our spatiotemporal computations at $h_0 = 0.8$. The superimposed line indicates the marginal stability curve for the long wave length limit. Other parameters are: $B_H = B_L = 0$, $n_H = n_L = 1$ and $m = 1$.

of h for which the stability analysis is likely to be increasingly relevant as the displacement progresses. The effect of inertia is quite subtle here. If we compare Figs. 6.5a & b, we see that the rounding of the front shape with increasing inertia (δRe) results in a wider range of h that are stretched along the channel and vulnerable to instability, even though the effect on the leading front velocity may be small.

Figure 6.13 shows the results of an inertial displacement flow of two isoviscous Newtonian fluids at $\delta Re = 10$, plotted as a spatiotemporal diagram. For this, we represent the interface height $h(\xi, T)$ at each T as a grey-scale vector, which is then plotted at successive T. In Fig. 6.13a ($\chi = 20$) there is no evidence of instability: the elongation of the interface takes place mostly for $h > 0.6$ for which Fig. 6.12a suggests stability. In contrast for $\chi = 60$, Fig. 6.12a suggests instability at all interface heights. In Fig. 6.13b we observe the evolution of streak-like wavy patterns during the displacement over a range of larger h, also reflecting those heights for which the interface is elongated.

It is worth noting that in the computation of Fig. 6.13 no artificial initial perturbation is introduced. In considering this as a parallel flow instability, the source of initial perturbation comes from a combination of: (a) the slope of the evolving interface; (b) numerical error. While (a) is clearly physical, (b) is spurious. Nevertheless, once instigated the propagation and growth of

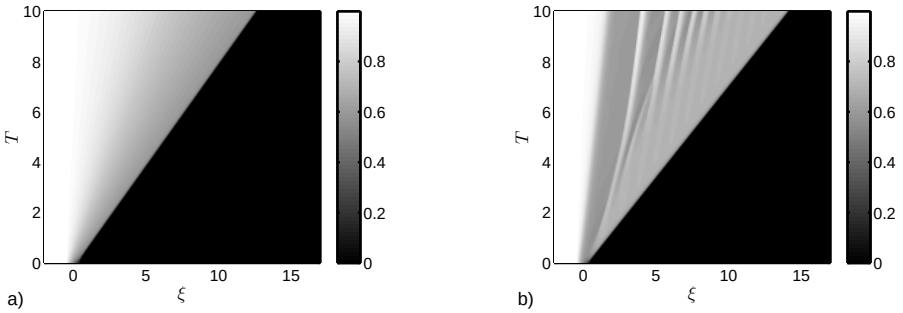

Figure 6.13: Spatiotemporal diagram of the interface height values, h (illustrated by contours of intensity) obtained from solving the displacement problem for the parameters used in Fig. 6.12 for $\delta Re = 10$ and a) $\chi = 20$ b) $\chi = 60$. The figure confirms that the stability analysis can indeed predict when the displacement flow goes unstable.

the perturbation waves to saturation amplitudes is physical. Allied to this, we have found that construction of plots such as Fig. 6.12b are not particularly sensitive to the perturbation amplitude A^*. We are simply triggering a linear instability, which is then propagated nonlinear via the numerical solution. We have seen in Fig. 6.11 that the wavespeeds are well represented by the celerity c_0, computed from the linear analysis. There is full agreement in c_0 computed from either the weighted residual or Orr-Sommerfeld approaches. We expect that the saturation amplitudes are controlled by the nonlinear aspects of the weighted residual model, which account for inertia in an averaged sense. Thus, the weighted residual computations have the potential to accurately represent instabilities of the underlying Navier-Stokes system. Having said this, as with all thin-film/lubrication methods, it is necessary to verify *a posteriori* that the model conditions are not violated. For example, unstable growth of a perturbation can lead to a solution with large interfacial gradients, which come to violate the model assumptions in reaching size δ^{-1}. Whether or not this happens depends partly on dispersion effects and the saturation amplitude of the perturbation.

Newtonian fluids with a viscosity ratio

In Fig. 6.14 we explore the effects of viscosity ratio on marginal stability of inertial Newtonian-Newtonian flows, at a fixed $h_0 = 0.5$. We observe that the viscosity contrast progressively destabilizes, reducing the value of δRe

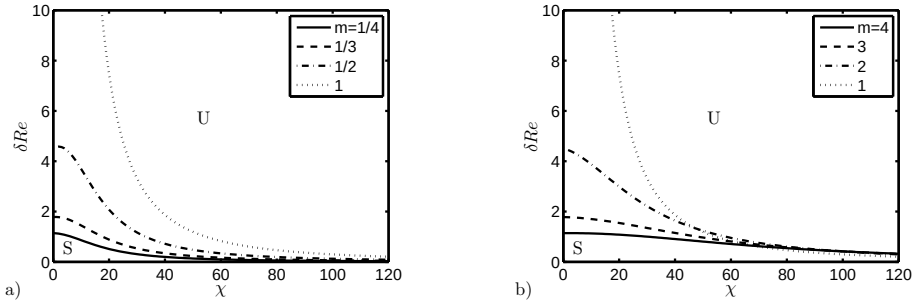

Figure 6.14: Marginal stability curves for the long-wave limit for $h_0 = 0.5$ for a) $m \leq 1$ and b) $m \geq 1$. Labels U and S represent unstable and stable flows respectively. The rest of parameters are $B_H = B_L = 0$ and $n_H = n_L = 1$.

required for instability at each χ. Effects are more evident at low χ. Fig. 6.15 contours in the $(\delta Re, m)$-plane the critical values of χ above which linear instability arises. We can observe that for a significant range of viscosity ratios the critical χ values are negative. Also observe in Fig. 6.15 that many contours become parallel at large δRe. This is linked to the asymptotic behaviour of the marginal stability curves as $\delta Re = \infty$. We have seen both here and in Fig. 6.12 that for fixed h_0 there can be a critical value, say χ_s, at which the marginal stability curves asymptote to $\delta Re = \infty$, i.e. for $\chi < \chi_s$ the flow is linearly stable for all δRe. This critical value of χ_s can be computed directly for Newtonian fluids, although algebraically complex (see equation (4.18) in [126] for $m = 1$).

Shear-thinning effects

We are also able to use the weighted residual stability analysis for non-Newtonian multi-layer flows. Figure 6.16 shows marginal stability curves for increasing degree of shear-thinning in either fluid H or L, while the other fluid is Newtonian. This figure is produced at $m = 1$ and for $h_0 = 0.5$, with marginal curves plotted in the $(\chi, \delta Re)$-plane. Recall that increasing χ induces backflow in the upper layer (fluid L), but that we also have a unit mean flow in the positive direction.

Two interesting features of our displacement flow experiments reported in [124, 129] are that in different situations an increase in the mean flow velocity can result in either stabilization or destabilization. These dual effects are illustrated in two sequences of experiments illustrated in Fig. 6 of [124],

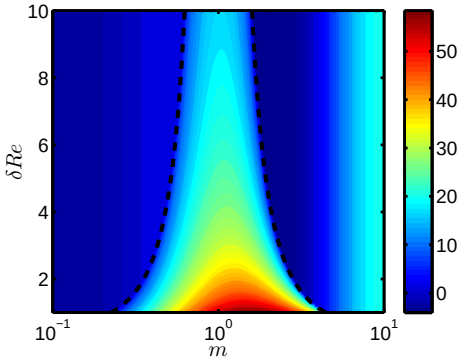

Figure 6.15: Contours of critical value of χ in $(\delta Re, m)$-plane, for $B_H = 0$, $B_L = 0$, $n_H = 1$, $n_L = 1$ and $h_0 = 0.5$. The bold dashed line corresponds to $\chi = 0$ plotted as a guide. The flow is linearly unstable at all χ larger than these values.

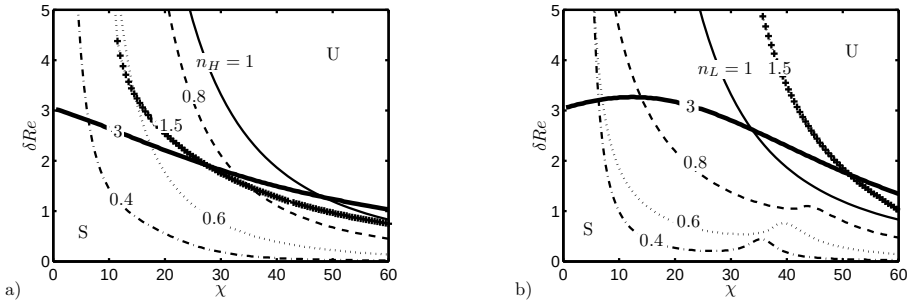

Figure 6.16: Marginal stability curves for the long-wave limit for $h_0 = 0.5$ for a) different n_H values with $n_L = 1$ and b) different n_L values with $n_H = 1$. Labels U and S represent unstable and stable flows respectively. The rest of parameters are $B_H = B_L = 0$ and $m = 1$.

which showed the results of water-xanthan displacement flows. Although a geometrically different situation is studied here, we can produce qualitatively similar effects with our weighted residual model. An example is shown in Fig. 6.17. Physically, as we increase $\hat{V}_0$ we vary both δRe and χ (increasing and decreasing respectively). If one of the fluids is shear-thinning, then we might also see a change in effective viscosity which (via the viscosity scales adopted) can further affect m, χ and Re. Here we assume only fluid H to be mildly shear-thinning ($n_H = 0.85$), freeze m and examine only the main effects on δRe and χ.

Figures 6.17a & b illustrate an approximately threefold increase in $\hat{V}_0$, at $m = 1$. For low $\hat{V}_0$ the value of χ is large enough to induce a backflow in the base flow, and we observe instability in Fig. 6.17a. As the imposed flow rate is increased the backflow is reduced and finally eliminated: the flow stabilizes. This phenomenon was first observed in [129] and is more thoroughly discussed in [124, 130]. The sequence in Figs. 6.17c & d at $m = 10$ shows the opposite effect, i.e. increasing $\hat{V}_0$ leads to interfacial instability due to the viscosity contrast and at sufficiently large δRe. Here the reduction in χ is stabilizing but competes against increasing δRe.

Bingham fluids

In dealing with Bingham fluids, we should note that although the weighted residual and Orr-Sommerfeld analyses agree in their predictions of both c_0 and c_1, we are restricted to base flows for which there is a single yielded layer. In the Orr-Sommerfeld context multiple yielded layers are dealt with successively, while assuming that the plugs remain rigid. For the weighted residual approach, the weight functions adapt to unyielded regions, so it may be that the underlying evolution model is still valid. Thus, the likely cause of any failure of this model is related to the stability analysis, which simply has not been developed for these situations. Examples of computed marginal stability boundaries are given in Fig. 6.18, plotted in the $(\chi, \delta Re)$-plane for Newtonian-Bingham multi-layer flows. In Fig. 6.18b we observe some strange profiles in the marginal stability curves at large χ. These are related to strong buoyancy forces inducing backflow in the base velocity profile. Fig. 6.19 shows a selection of base velocity profiles for $B_L = 0.5$, $h_0 = 0.5$ and $\chi = 40,\ 55$ and 70. As χ increases, first a stationary residual wall layer is developed (somewhere just above $\chi = 40$), followed by a progressively strong backflow. The backflow is associated with the non-monotone profiles in the marginal stability curve.

The parameters $\chi \leq 40$ and $B_L = 0.5$ lie in the range of validity of our

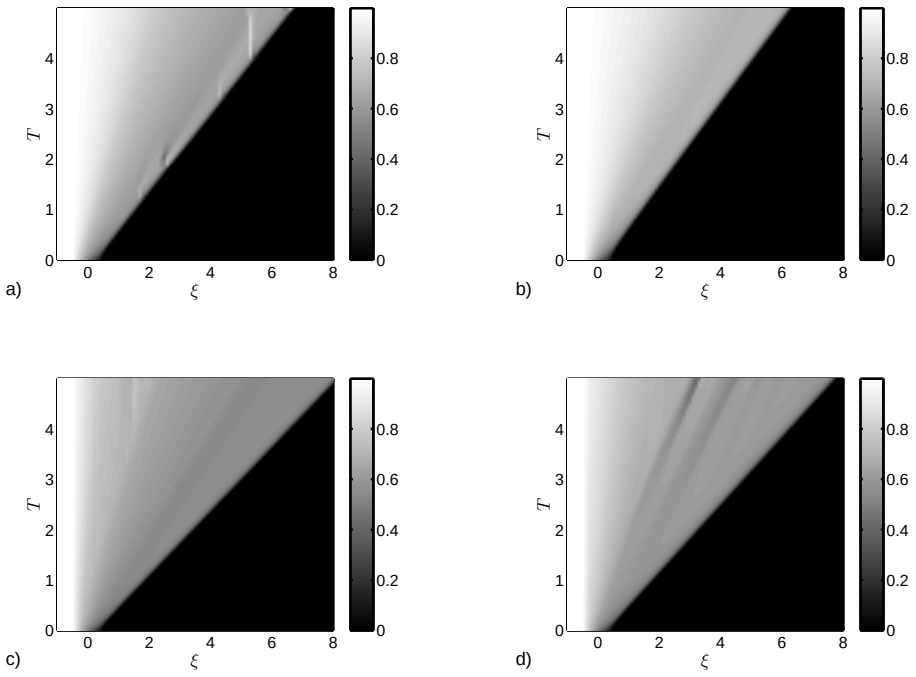

Figure 6.17: Spatiotemporal diagram of the displacement interface height, h, for $n_H = 0.85$, $n_L = 1$, $B_H = B_L = 0$ and a) $m = 1$, $\chi = 24$, $\delta Re = 5.6$ b) $m = 1$, $\chi = 15.5$, $\delta Re = 15.8$ c) $m = 10$, $\chi = 24$, $\delta Re = 5.6$ and d) $m = 10$, $\chi = 15.5$, $\delta Re = 15.8$. The imposed flow increases from figure 6.17a to 6.17b and from 6.17c to 6.17d.

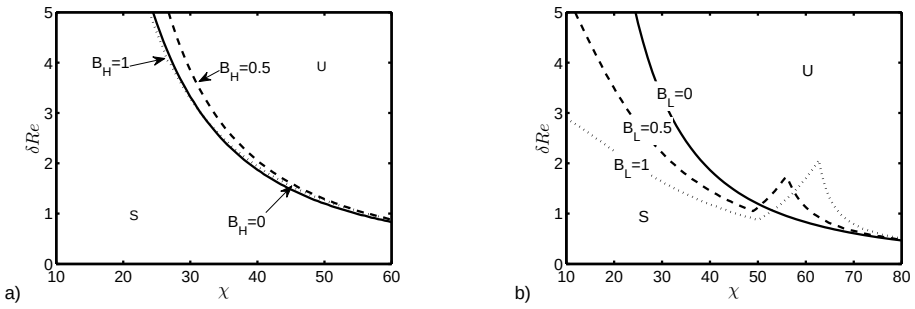

Figure 6.18: Marginal stability curves for the long-wave limit for $h_0 = 0.5$ for a) different B_H values with $B_L = 0$ and b) different B_L values with $B_H = 0$. Labels U and S represent unstable and stable flows respectively. The rest of parameters are $n_H = n_L = 1$ and $m = 1$.

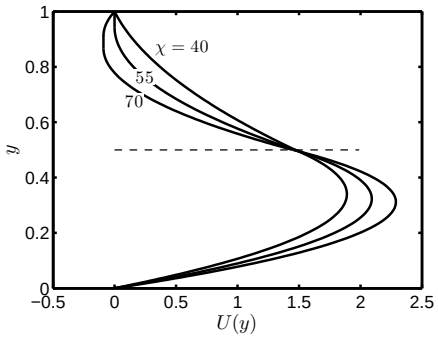

Figure 6.19: Base flow velocity profiles corresponding to Fig. 6.18b for $B_L = 0.5$ and $\chi = 40, 55$ and 70. The dashed line indicates the position of the interface, $h_0 = 0.5$.

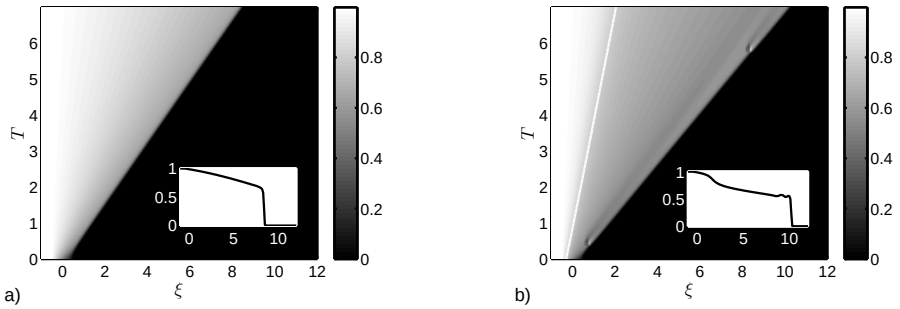

Figure 6.20: Spatiotemporal diagram of the interface height values, h (illustrated by contours of intensity) obtained from solving the displacement problem for the parameters used in Fig. 6.18b for $B_L = 0.5$, $\delta Re = 3$ and a) $\chi = 10$ b) $\chi = 40$. The insets in figures show the interface height, h, at $T = 7.5$. The white line added to Fig. 6.20b corresponds to $h = 0.8$. For the heights greater than this value the static layer is about to form due to the decrease in shear rate within light layer.

model and stability analysis. The results of two displacement computations are given in Fig. 6.20 for $\delta Re = 3$ and two values of χ. For small χ we observe a clean stable displacement. The inset of Fig. 6.20a shows the interface profile at $T = 7.5$. In Fig. 6.20b (at $\chi = 40$) we see slight instabilities close to the propagating front. The marginal stability curve in Fig. 6.18b indicates linear instability at $h_0 = 0.5$.

6.5 Discussion points

In this chapter we have developed a semi-analytical framework for applying the weighted residual method to two-layer channel flows of Herschel-Bulkley fluids, giving a first order accurate approximation to the interface thickness and volume fluxes in each layer. This has necessitated the construction of special functions to evaluate the various integral expressions that arise (appendices B and C). The base variables that it proves convenient to formulate the equations in terms of are the interface height h and a buoyancy parameter b. There is a one-to-one correspondence between b and the volumetric flux in the lower layer q.

We have developed a stability analysis for our weighted residual evolution equations and compared with the corresponding Orr-Sommerfeld results, in

the long wave limit. The celerity is predicted accurately by the weighted residual method for all parameters, as is the growth rate for Newtonian and non-Newtonian fluid layers. A restriction in the present stability analysis concerns yield stress fluids in the case where we have an unyielded plug. The Orr-Sommerfeld approach here considers only the yielded fluid layers, whereas the weighted residual averages over the entire layer. It is likely that this deficiency could be corrected but for simplicity and brevity we have postponed this.

We have used the weighted residual model to examine instabilities in displacement flows. As the displacement front progresses and the interface elongates between fronts moving at different speeds, we observe the growth of dispersive waves at the stretched interface over ranges of heights that the linear analysis predicts to be unstable. These waves move with a range of speeds given approximately by the celerity. The form of the observed instabilities computed numerically from our model are qualitatively similar to those we have observed experimentally, although of course quantitatively different due to the different geometries. This lends confidence to a further study of the onset and propagation of instabilities using this type of model.

As mentioned earlier, note that this channel flow configuration does not relate directly to the pipe flow experiments presented in chapter 4 for instance. However they can still be used to draw qualitative conclusions about the effect of different parameters. Upon simplifying the problem geometry from pipe to channel we have been able to investigate the effect of different parameters on displacement flow interface shape and/or its stability. The outcome findings and trends are likely to stay the same for pipe geometry at least in a qualitative manner.

Future directions in this work include the extension of the stability analysis to Bingham fluid flows with unyielded plug regions, closer examination of power law regimes with singular tangent viscosity and extension to core-annular geometries. In the latter case the type of analysis developed here may be effective in studying instabilities such as the inverse bamboo instabilities of [55, 56] and the pearl and mushroom instabilities of [37–39].

Chapter 7

Incomplete fluid-fluid displacement of yield stress fluids in inclined pipes

Chapters 3 and 4 presented experimental results of iso-viscous Newtonian displacement flows. In this chapter[6] we aim to study displacement flows when the displaced fluid is non-Newtonian and in particular when it has a yield stress. The focus is on density unstable configuration and on miscible fluids. For simplicity we take the displacing fluid to be Newtonian. We also concentrate on the industrially interesting case where the yield stress is significantly larger than a typical viscous stress in the displacing fluid, but where buoyancy forces may be significant.

There are many industrial processes in which it is necessary to remove a gelled material or soft solid from a duct. Examples include biomedical applications (mucus [73], biofilms [145]), cleaning of equipment and food processing [28], oil well cementing [89] and waxy crude oil pipeline restarts [144]. A wide range of material models are used to describe residual deposits in these situations. Some of these flows are turbulent, but equally often process limitations dictate that the flows be laminar, and it is the latter that we study here. Our main motivation comes from a number of problems relevant to the oil industry: mud removal, plug cementing, and waxy crude oil pipeline restarts.

The aim of the study presented in this chapter is to understand how the different observable flow regimes depend on the dimensionless parameters governing the flow. One way of looking at this chapter is by comparison to the Newtonian displacement flows (chapter 4) except that we have added a yield stress to the displaced fluid. A large number of parameters can influence the displacement of a yield-stress (visco-plastic) fluid along a pipe

[6] A version of this chapter has been submitted for publication: **K. Alba**, S.M. Taghavi, J.R. de Bruyn and I.A. Frigaard. *Incomplete fluid-fluid displacement of yield-stress fluids. Part 2: Highly inclined pipes.*

or duct, which makes comprehensive study impractical. This explains the decision to focus on specific regimes, which we make more precise in §7.1.

This chapter is also a sequel to [125], which used the same apparatus and similar fluids, but involved experiments at pipe inclinations that were close to the horizontal ($83^\circ < \beta < 90^\circ$). Here we study the effects of pipe inclination on the displacement of a yield-stress fluid (here Carbopol) by a Newtonian fluid of higher density. The pipe is inclined at an angle β to the vertical direction and the flows proceed downwards. The main observation made in [125] was that displacements fell into one of two main categories, referred to as centre-type displacements and slump-type displacements. Briefly, in centre-type displacements the displacing fluid advanced through the centre of the pipe, leaving an approximately uniform layer of Carbopol on the wall. The slump-type displacement involved the displacing fluid slumping underneath the lighter Carbopol. A more detailed description of these flows is given later in the chapter. The transition between these two flow regimes was found to be governed by the single dimensionless group Re/Fr, where Re is the Reynolds number based on the displacing fluid properties and Fr is the densimetric Froude number. This parameter reflects the balance between inertial stresses (promoted by buoyancy) and viscous stresses. In this study we investigate the effect on this picture of a wider range of pipe inclinations, such as commonly occur in oilfield cementing applications.

An outline of the chapter is as follows. In §7.1 we briefly review the experimental methodology and define the parameter space. The results follow in §7.2. We first give a primary classification of the observed flow regimes and investigate their location in our dimensionless parameter space. We then describe some of the interesting secondary flows that are found in the slump flow regime. Finally, we study flows in which there is no imposed velocity (i.e. exchange flows) and consider these flows in the context of previous studies of the stability of cement plugs (§7.2.4). The chapter concludes with a brief summary.

7.1 Experiments and parameters range

Our experimental study was performed in the same flow loop explained in appendix A. Briefly the 4-meter long pipe was mounted on a frame which could be tilted to any angle. Initially, the lower part of the pipe is filled with a less dense fluid (fluid 2) coloured with a small amount of ink. The upper part of the pipe, above the gate valve, is filled with the more dense fluid 1. In our experiments, the displacing fluid 1 was a Newtonian salt-water

solution and fluid 2 was a yield-stress fluid — a solution of Carbopol EZ-2 polymer (Noveon Inc). Carbopol is widely used as a thickener, stabilizer and suspending agent. The rheology of Carbopol is largely controlled by the concentration and pH of the solution. When initially mixed with water, Carbopol makes an acidic solution with no yield stress. A yield stress develops at intermediate pH when the solution is neutralized by addition of a base, which in our case was NaOH. The neutralized solution is fairly transparent and has the same density as water for low polymer concentrations. More details on making Carbopol solution and its rheology are given in appendix A. The only difference here with the Newtonian fluids experiments is that we added two first-surface mirrors above the pipe so that both top-view and side-view images of the flow could be recorded by each camera simultaneously. We have used the mirror data in viscoplastic displacement experiments only where asymmetry is a prevalent feature across the pipe. In fact more information than the facial view was required to understand the static layers across the pipe.

It was shown in chapter 4 that that the general qualitative and quantitative features of displacement flows are reproducible for repeated experiments on iso-viscous Newtonian displacements [3]. The same is true for the viscoplastic displacements studied here. Due to the chaotic nature of the flow in many cases, the fine details might not be exactly the same in two different experiments with the same governing parameters. Nonetheless, the general features and patterns remain the same for experiments performed under the same conditions.

As in [125], our intention was to investigate displacement flows for which some of the displaced yield-stress fluid could be left behind in the pipe. This corresponds to situations in which it might be considered "difficult" to displace the yield-stress fluid. This puts a number of constraints on our parameter space. First, we must assume that the viscous stresses $\hat{\tau}_v$ are small relative to the yield stress $\hat{\tau}_Y$, i.e.

$$\hat{\mu}\hat{V}_0/\hat{D} = \hat{\tau}_v \ll \hat{\tau}_Y, \tag{7.1}$$

where $\hat{\mu}$ is the viscosity of the Newtonian fluid, $\hat{V}_0$ is the mean velocity and $\hat{D}$ is the diameter of the pipe. We may reformulate this as

$$B_N \gg 1, \qquad B_N = \frac{\hat{\tau}_Y \hat{D}}{\hat{\mu}\hat{V}_0}. \tag{7.2}$$

Here B_N is a form of Bingham number, but with the viscous stress scale coming from the Newtonian fluid.

Secondly, since the flow close to the displacement front will be three-dimensional, we must consider inertial as well as viscous stresses. The inertial stress scale is $\hat{\tau}_t = \hat{\rho}\hat{V}_0^2$, where $\hat{\rho} = (\hat{\rho}_H + \hat{\rho}_L)/2$. If we were to consider flows for which $\hat{\tau}_t \sim \hat{\tau}_v$, meaning that $Re = \frac{\hat{\rho}\hat{V}_0\hat{D}}{\hat{\mu}}$ would be $\sim O(1)$, then Eq. (7.2) would imply that $\hat{\tau}_t \ll \hat{\tau}_Y$. It would then be unlikely that we would see much variation in our results as $\hat{V}_0$ was varied. We have therefore targeted our study on the range $Re > 1$, for which inertial effects are expected to be dominant close the displacement front. Since we also wanted to see how changes in flow rate might affect the type of displacement observed, we selected flow parameters such that

$$\hat{\rho}\hat{V}_0^2 = \hat{\tau}_t \lesssim \hat{\tau}_Y. \tag{7.3}$$

Note that if $\hat{\tau}_t > \hat{\tau}_Y$, then inertial stresses alone might be sufficient to yield and fully displace the yield-stress fluid; hence the inequality in Eq. (7.3, which is equivalent to $Re/B_N \lesssim 1$.

Thirdly, our study considers a range of pipe inclinations over which the buoyancy force will vary from being aligned with the flow to being transverse to the flow. The magnitude of the buoyant stresses are approximated by $\hat{\tau}_b = \Delta\hat{\rho}\hat{g}\hat{D}$, where $\Delta\hat{\rho}$ is the difference in density between the fluids. In order to observe significant buoyancy on yielding in this type of displacement flow, we require

$$\Delta\hat{\rho}\hat{g}\hat{D} = \hat{\tau}_b \sim \hat{\tau}_Y. \tag{7.4}$$

The three conditions given by Eqs. (7.2)-(7.4) define the parameter space of our experiments. Apart from the dimensionless groups introduced above, the density difference is characterized by the dimensionless Atwood number, $At = \frac{\hat{\rho}_H - \hat{\rho}_L}{\hat{\rho}_H + \hat{\rho}_L}$. The densimetric Froude number is defined as $Fr = \frac{\hat{V}_0}{\sqrt{At\hat{g}\hat{D}}}$. The quantity Fr^2 is the ratio of inertial and buoyancy forces. The parameter ranges covered by our experiments are given in Table 7.1.

Finally, the parameter that delineated the qualitatively different types of displacement flows observed in [125] is the ratio Re/Fr. This parameter is given by

$$\frac{Re}{Fr} = \frac{\hat{\rho}_H \left([\hat{\rho}_H - \hat{\rho}_L]\hat{g}\hat{D}^3\right)^{1/2}}{[\hat{\rho}_H + \hat{\rho}_L]^{1/2}\hat{\mu}}, \tag{7.5}$$

and is a natural parameter to represent a buoyancy-driven transition. The destabilizing buoyant stresses $[\hat{\rho}_H - \hat{\rho}_L]\hat{g}\hat{D}$ may be balanced locally by any combination of yield, viscous or inertial stresses. In balancing with inertia,

Parameter	Range
β	$0 - 85$ (deg)
$\hat{V}_0$	$0 - 120$ (mm/s)
$\hat{\tau}_Y$	$3.8 - 26$ (Pa)
At	0.001-0.016
B_N	650-∞
Re	0-2300
Fr	0.1-6
Re/Fr	260-1080

Table 7.1: Parameter ranges of viscoplastic experiments.

an appropriate velocity scale for buoyancy driven motion is $\hat{V}_t = [At\hat{g}\hat{D}]^{1/2}$. We see that for small At,

$$2\frac{Re}{Fr} \approx \frac{[\hat{\rho}_H - \hat{\rho}_L]\hat{g}\hat{D}}{[\hat{\mu}\hat{V}_t/\hat{D}]}. \tag{7.6}$$

An interpretation of this expression is as the relative strengths of buoyant stress, $(\hat{\rho}_H - \hat{\rho}_L)\hat{g}\hat{D}$, and viscous stress, $\hat{\mu}\hat{V}_t/\hat{D}$. Note, however, that since the velocity scale used in the viscous stress is $\hat{V}_t$, which is itself driven by buoyancy, this represents a self-reinforcement. If the viscous stresses induced by buoyancy-driven motion are unable to balance the buoyant stresses, then the balance must involve other stresses. in [125], it was observed that above some threshold in Re/Fr the displaced fluid yielded in a way that promoted stratification (i.e. slumping). This had the effect of reducing the local buoyant stresses.

7.2 Results

in [125], we presented the results of experiments on displacement flows in which the pipe was close to horizontal. As here, the focus in [125] was on the industrially interesting case that $\hat{\tau}_Y \gg \hat{\tau}_v$, but with significant buoyancy forces. Two distinct flow regimes were identified: centre-type displacements and slump-type displacements. In centre-type flows, static residual layers with a slowly-varying non-uniform thickness were found all around the pipe wall. In slump-type displacements, two propagating displacement fronts were generally observed: a fast front which propagated in a thin layer near the bottom of the pipe and a much slower front behind it which displaced

a thicker portion of the viscoplastic fluid. This second front sometimes stopped altogether. The thinness of the layer of displacing fluid flowing behind the first front amplifies the mean velocity in this layer, resulting in effective Reynolds numbers that can be as large as 1000-2000. This region of the flow is therefore highly inertial and the displacing fluid was often found to channel through the yield-stress fluid in an erratic fashion. The conditions under which the central and slump flow regimes were observed were determined by the value of Re/Fr [125].

In the present work, we study a full range of pipe inclinations. The range of Fr and Re spanned by our experiments is increased over that covered in [125] due to our wider range of $\hat{V}_0$, but we achieve similar maximum values of Re/Fr. Perhaps not surprisingly, the vast majority of our present results were also categorized as either central or slump-type flows. The slump-type displacements exhibited a rich variation of behaviour, which we explore in detail in §7.2.1. The central-type displacements were quite similar to those found previously, and we give a brief overview below in §7.2.2. A third type of displacement was also found, wherein the two fluids mixed fully in an apparently turbulent flow region. Only a limited number of experiments were performed in this regime; they are discussed in §7.2.3. Our results for exchange flows, in which the mean flow velocity $\hat{V}_0 = 0$ and the displacement is driven solely by gravity, are discussed in §7.2.4. We consider these exchange flows in the context of previous studies of the stability of cement plugs [49, 51, 54]. Finally, we discuss a more general dimensionless classification for the whole range of observed flows in §7.2.5.

Perhaps the most interesting result of the present work is that the appearance of the slump and centre flow types still appears to be dictated exclusively by the value of Re/Fr, despite the increased importance of buoyant forces at high inclinations. This is illustrated in Fig. 7.1a, in which data from [125] are also shown for comparison. The critical value of Re/Fr above which the flow changes from central to slump-type is in the range $600 < Re/Fr < 800$, in agreement with the results of [125], over all pipe inclinations. In fact the occurrence of these two regimes is primarily governed by approximately the same ratio of Reynolds number to densimetric Froude number, Re/Fr, as in near-horizontal case, meaning that the inclination angle does not directly contribute to the determining the flow regime. However, we do observe a range of exotic behaviour at higher inclinations within the slump regime that we discuss below in §7.2.1. In a single experiment with a very low Fr, a slump-type displacements was observed at a lower value of Re/Fr.

Figure 7.1b plots the observed flow types in terms of B_N and Re/B_N.

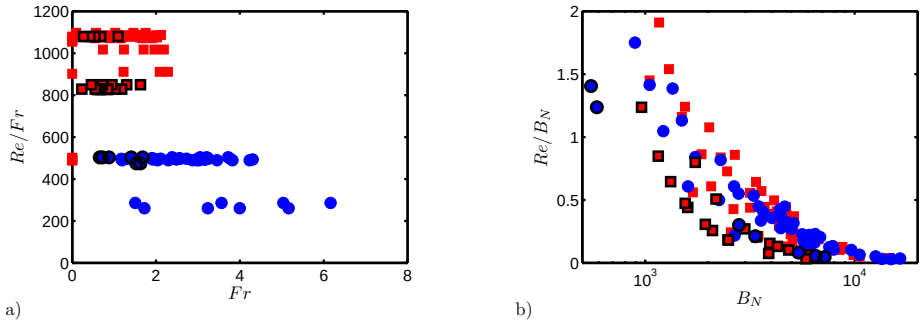

Figure 7.1: Primary classification of the observed flows into slump (squares) or central (circles) displacements. Experimental results for near-horizontal pipes [125] are indicated by black borders around the data symbols.

The first of these is the ratio of yield stress to viscous stress, as described by Eq. (7.2). The parameter Re/B_N captures the balance expressed in Eq. (7.3), i.e. the ratio of inertial stress to yield stress. This figure illustrates the extended range of parameters covered in the present work compared to that of [125], and also shows that these two parameters are not responsible for the determining the slump-centre transition, i.e. both flow types are observed over the full range of these parameters.

7.2.1 Slump regime

In this section we look at the slump-type displacements in detail. As in our previous study [125] it was found that the slump-type flows were associated with an initial displacing front moving under the viscoplastic fluid at relatively high speed (see Fig. 7.2a below). In all slump-type displacements, whether for nearly-horizontal or more inclined situations, we observed a breakage of the viscoplastic layer due to this fast-moving front. For nearly horizontal displacements the breakage is weaker than in the more inclined cases, and it happens at later times and further downstream since the streamwise component of buoyancy is smaller. In §7.2.1 we will describe what we refer to as "ripped" slump-type displacements and study the underlying mechanisms of gel layer breakage. In §7.2.1 some more exotic flows that were not observed in the nearly horizontal experiments will be presented and discussed.

Ripped-type displacement

Many of the slump regime displacements observed were qualitatively similar to those reported by Taghavi *et al.* [125] An example is shown in Fig. 7.2a. In this and similar figures, the displacing fluid is light in color, while the Carbopol appears dark. The left-hand end of the pipe is higher than the right-hand end, and the mean flow is to the right. The intensity scale, shown below the last image, is normalized so that intensity can be interpreted as a measure of concentration, averaged through the thickness of the pipe. In Fig. 7.2a, a thin layer of the displacing fluid can be seen to advance rapidly along the bottom of the pipe, under the Carbopol and ahead of the main front. A spatiotemporal diagram of the same flow is shown in Fig. 7.2b. Some loose pieces of Carbopol that have become detached from the main body and are being advected by the flow can be seen in the snapshots of Fig. 7.2a and in the form of black dots in the spatiotemporal diagram. The broken lines in Fig. 7.2b highlight the positions of the first and second fronts; their different slopes indicate that the two fronts move at different speeds.

The flow velocities measured with the UDV in the same experiment are shown in Fig. 7.2c. The fast front reaches the position of the UDV probe at $\hat{t} \approx 6$ (s). For $\hat{t} \gtrsim 6$ (s), a thin region of high velocity develops close to the bottom of the pipe, while there is a fairly thick static layer at the top. This asymmetry in the velocity profile is the most obvious difference between the slump and central displacements (as can be seen, for example, by comparing Fig. 7.2c with Fig. 7.10c below).

As noted above, in all the slump-type flows the viscoplastic layer is cut by the fast moving front of displacing fluid. The formation of a ripped displacement is shown in Fig. 7.3. Figure 7.3a shows a time sequence of images recorded by the upstream camera. The first front of the displacing fluid initially channels under the viscoplastic Carbopol. The thin lower layer then rises towards the top of the pipe in unsteady bursts. Towards the end of the sequence, the displacing fluid breaks the upper layer, isolating a large piece of Carbopol. Figure 7.3b tracks the progression of the displacement into the field of view of the downstream camera; the first frame of Fig. 7.3b follows the last frame of Fig. 7.3a in time. The unsteady bursts continue, fragmenting the Carbopol into a number of chunks. Some of the larger segments are advected downstream by the flow, but stationary residual deposits of Carbopol are also seen in the intermediate frames of Fig. 7.3b. In the last six images in this sequence, the remains of the large isolated segment of Carbopol that formed in Fig. 7.3a are pushed through the downstream part of the pipe by the slower second displacement front. The spatiotemporal plot

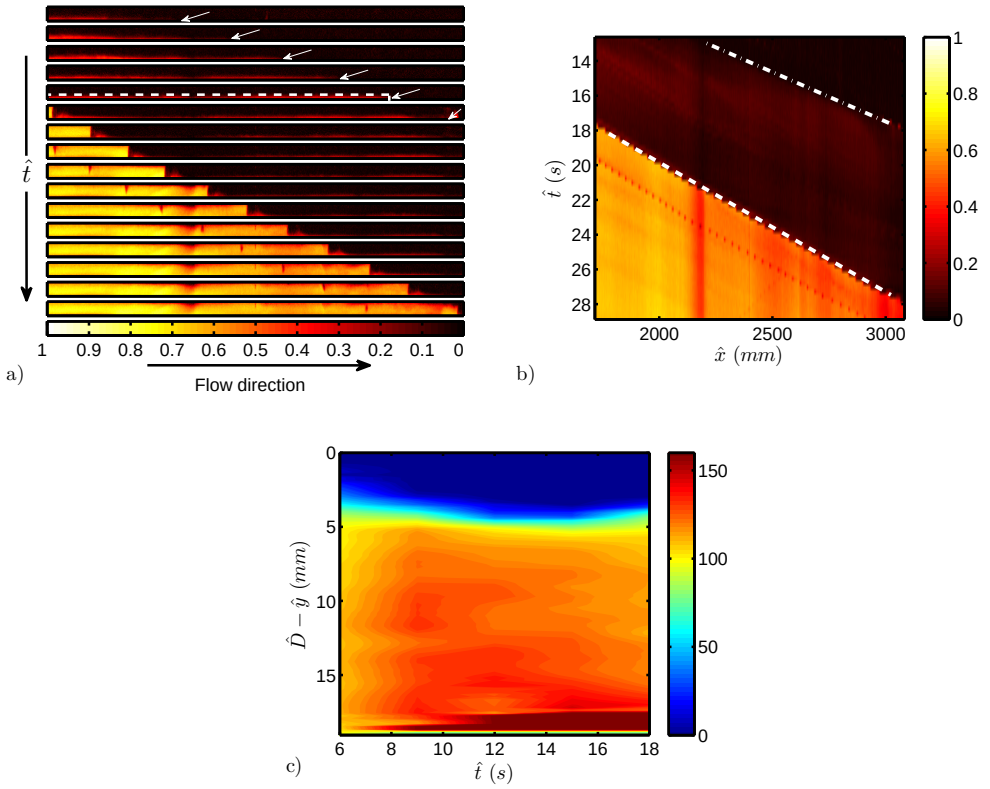

Figure 7.2: Slump-type displacement for $\beta = 45°$, $At = 0.01$, $\hat{\tau}_Y = 7.9$ (Pa), $\hat{V}_0 = 81.5$ (mm/s). a) Images of the displacement at $\hat{t} = 12$, 13, ..., 26, 27 (s) after opening the gate valve. The flow is from left to right. The field of view is 1367 (mm) by 19 (mm), taken 1716 (mm) below the gate valve. The white arrows indicate the position of the fast leading front. The white dashed lines in the fourth snapshot show the shape of the displacing layer qualitatively. The bottommost image is a colourbar showing the concentration C, with 0 referring to the displaced Carbopol and 1 the displacing fluid. b) Spatiotemporal image of the same displacement. $\hat{x}$ is the streamwise distance measured from the gate valve. The dash-dotted and dashed lines indicate the position of the fast slow displacement fronts, respectively. c) Plot of the velocity profile measured with the UDV for the same experiment. The UDV probe is located at $\hat{x} = 1560$ (mm).

corresponding to Fig. 7.3b is shown in Fig. 7.3c. The banded appearance in this diagram reflects the motion of several different pieces of Carbopol,

each moving downstream at a different speed. The flow velocities recorded by the UDV are shown in Fig. 7.3d and illustrate the unsteady nature of the flow. They also show periods of negative velocity close to the top of the pipe, indicating a back flow due to fluid being pushed upstream under the action of buoyancy. The detached pieces of Carbopol appear to decrease in size following the initial break-up. The decrease in size cannot be due to interfacial tension effects, as the two fluids are miscible (i.e. Carbopol is soluble in water). It could be due to viscosity gradients, adverse pressure gradients driven by axial buoyancy, or shear in the pipe, each of which could have a destabilizing effect.

A closer look at the unsteady bursting of the thin displacing layer referred to above is provided by Fig. 7.4 for a different set of experimental parameters. The time sequence shown in Fig. 7.4a captures the evolution of the advancing front to a burst that extends across the whole pipe. Fig. 7.4b shows the depth averaged concentration C corresponding to the images in Fig. 7.4a. $C = 0$ corresponds to 100% Carbopol, and $C = 1$ to 100% salt-water solution. The burst does not displace all of the Carbopol over its length, probably leaving residual Carbopol on the wall. It clearly extends across almost the full diameter of the pipe, however. The change in concentration due to the burst develops into a square-shaped pulse which grows in length as it propagates downstream, fed by the thin lower layer. The way in which the Carbopol layer breaks up is very similar to that described here for most of the slump-type displacements we observed for nearly-horizontal inclinations.

Once the initial ripping of the gel layer has occurred, it can break up in non-uniform manner, leading to unpredictable flow patterns. An example is shown in Fig. 7.5. Again the first front propagating rapidly below the Carbopol develops into an unsteady burst, as seen in the first few side-view images of Fig. 7.5a. In the example shown in Fig. 7.4, the bursting is intermittent and leaves large segments of Carbopol intact. In the example of Fig. 7.5, however, it develops into a larger region of very unsteady flow. Figures 7.5b shows the spatiotemporal plot corresponding to the side view images of Fig. 7.5a, and Fig. 7.5c shows the corresponding top view images. The images show that although the initial penetration of the displacing fluid into the Carbopol region is slump-like, there is little difference between top and side view once the gel layer becomes ripped: the distribution of residual Carbopol around the walls is fairly symmetric and appears more akin to that seen in central-type displacements. Both the snapshots and the spatiotemporal plot indicate that some pieces of Carbopol remain stationary, fixed to the pipe wall, while others are advected by the flow. The blue

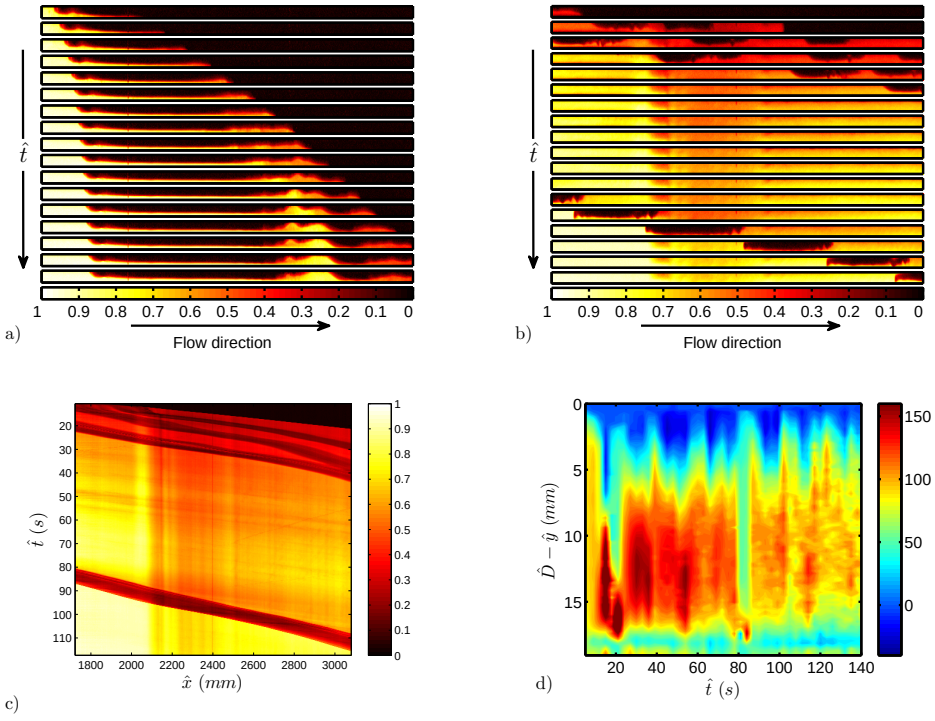

Figure 7.3: Ripped-type displacement for $\beta = 45°$, $At = 0.016$, $\hat{\tau}_Y = 16.4$ (Pa), $\hat{V}_0 = 61.3$ (mm/s). a) Images of the displacement at $\hat{t} = 2, 2.5, \ldots, 9.5, 10$ (s) after opening the gate valve. The flow is from left to right. The field of view is 1373 (mm) by 19 (mm), taken 102 (mm) below the gate valve. b) Images of the displacement at $\hat{t} = 10.75, 16.75, \ldots, 106.75, 112.75$ (s) after opening the gate valve. The field of view is 1357 (mm) by 19 (mm), taken 1723 (mm) below the gate valve. The last images at the bottom a and b are the concentration colourbar. c) Spatiotemporal image of the same displacement shown in b. d) Plot of the velocity profile measured with the UDV for the same experiment. The UDV probe is located at $\hat{x} = 1560$ (mm).

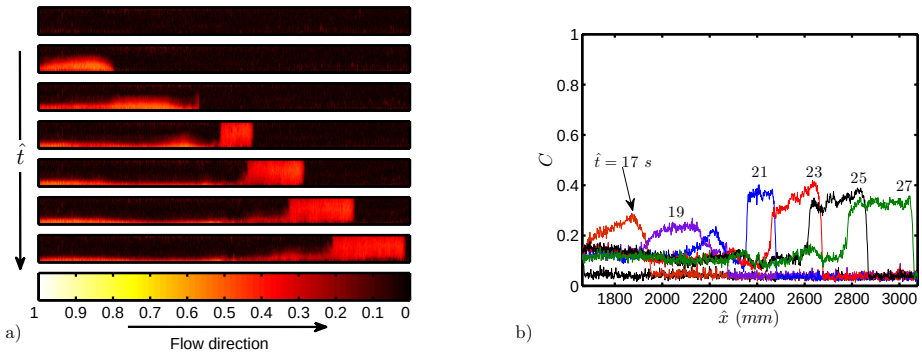

Figure 7.4: Formation of a ripped-type displacement for $\beta = 75°$, $At = 0.016$, $\hat{\tau}_Y = 4.3$ (Pa), $\hat{V}_0 = 48.1$ (mm/s). a) Images of the displacement at $\hat{t} = 15, 17, \ldots, 25, 27$ (s) after opening the gate valve. The field of view is 1411 (mm) by 19 (mm), taken 1663 (mm) below the gate valve. b) Evolution of the depth-averaged concentration with time and streamwise location for the same snapshots as in part a). At $\hat{t} \approx 21$ (s) the unstable leading front breaks off the gel layer, resulting in a jump in the concentration profile.

boxes in the last snapshot of Figs. 7.5a and c highlight stationary features, captured from different views. Careful inspection of these images shows that these portions of the gel layer are predominantly located at the sides of the pipe rather than its top, again emphasizing that the flow pattern is no longer purely slump-like. Although the displacing layer initially slumps beneath the viscoplastic layer, its motion becomes highly three-dimensional once the layer becomes unstable. This largely restores the up-down symmetry of the flow. The behaviour shown in Fig. 7.5 was not common, being observed in only a few of our experiments.

Detachment of Carbopol layers and corkscrews

An interesting and exotic flow pattern that was not observed in nearly-horizontal displacements is the formation of helical pieces of displaced Carbopol. We show an example of this in Fig. 7.6. Figures 7.6a and b show the image sequences and spatiotemporal diagram respectively, recorded with the downstream camera. The helical corkscrew structure is formed behind the leading displacement front. As it enters the images shown in the figure, the fluid immediately ahead of the helix is at least partially displaced. Our first thought on seeing these structures was that they might reflect an unstable mode developing from a Rayleigh-Taylor mechanism. However, we

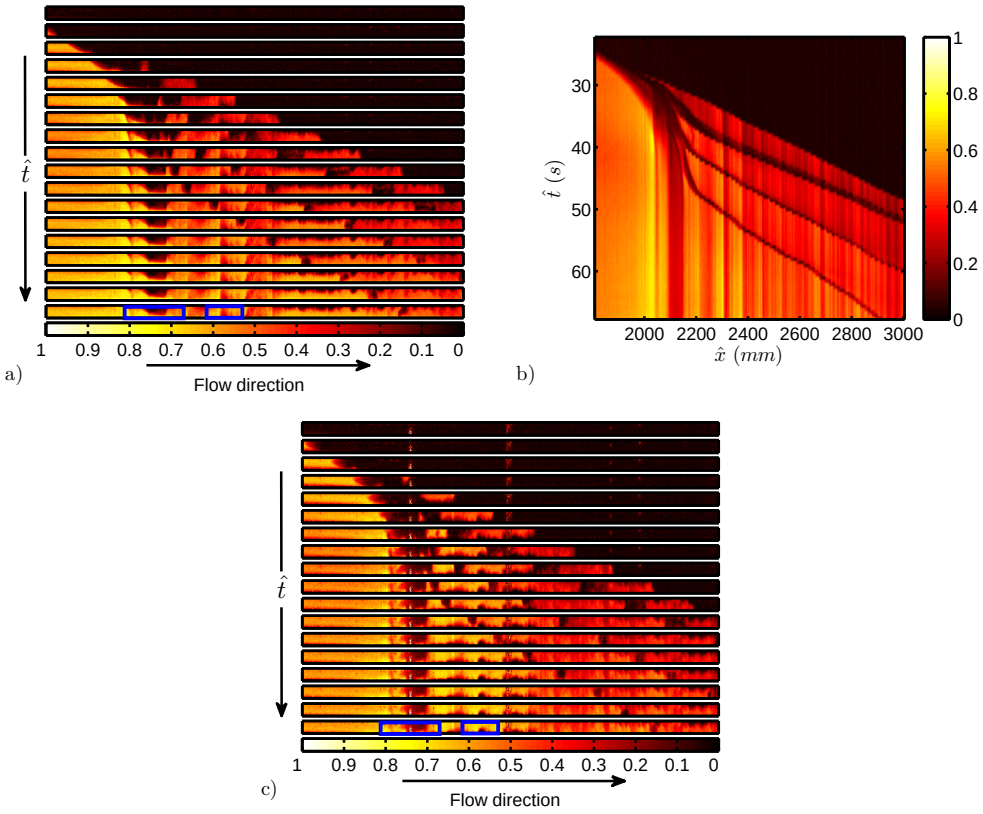

Figure 7.5: Ripped-type displacement for $\beta = 60°$, $At = 0.016$, $\hat{\tau}_Y = 14.9$ (Pa), $\hat{V}_0 = 26.8$ (mm/s). a) Images of the displacement at $\hat{t} = 22.5$, 25, ..., 62.5, 65 (s) after opening the gate valve. The field of view is 1195 (mm) by 19 (mm), taken 1809 (mm) below the gate valve. b) Spatiotemporal image of the same displacement. c) Top view images from the same experiment. The blue boxes in the last snapshots of a and c highlight static fragments of the Carbopol layer on the wall.

observed these helical structures over a broad range of pipe inclinations (up to $\beta = 60°$), and the initial stage of the displacement was always slump-like. We also considered the possibility that corkscrews were related to a helical mode of a core-annular shear instability [109], but this also proved incorrect.

The formation of the helices is instead associated with the removal of large pieces of Carbopol gel from the upper wall of the pipe, after the passage of the initial front and the breakup of the Carbopol into segments via the bursting behaviour described above. It appears that resistance to flow in

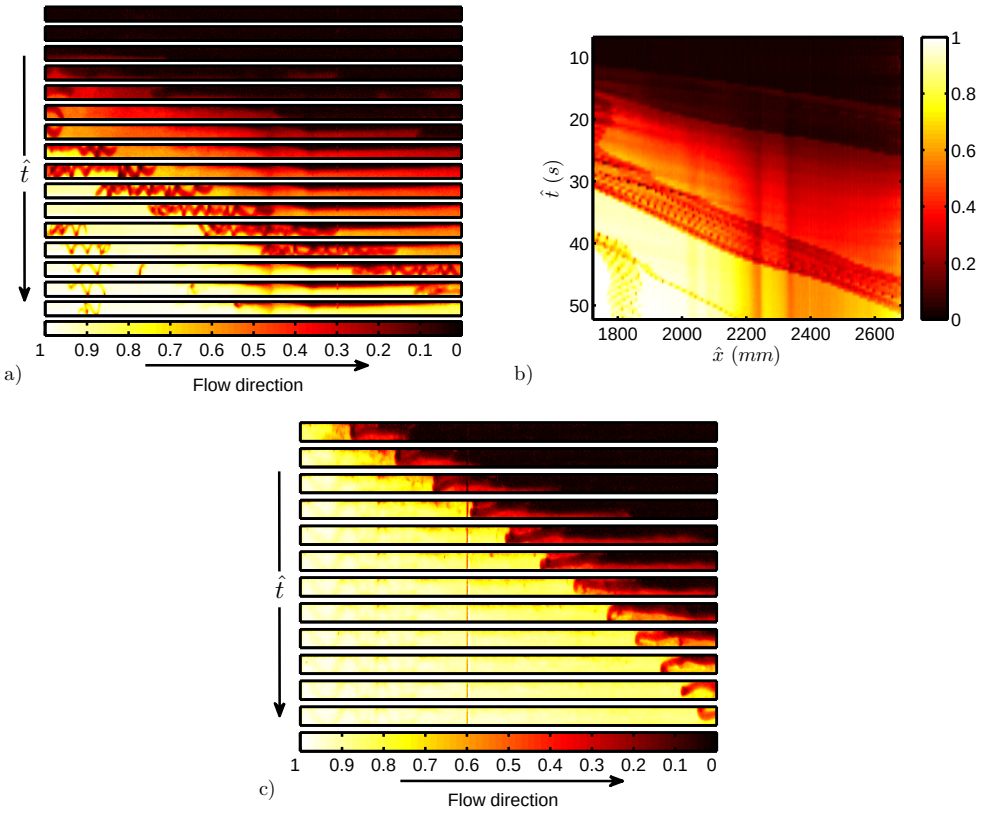

Figure 7.6: Corkscrew-type displacement for $\beta = 15°$, $At = 0.016$, $\hat{\tau}_Y = 19.7$ (Pa), $\hat{V}_0 = 61.3$ (mm/s). a) Images of the displacement at $\hat{t} = 7, 10, \ldots, 48, 52$ (s) after opening the gate valve. The field of view is 962 (mm) by 19 (mm), taken 1723 (mm) below the gate valve. b) Spatiotemporal image of the same displacement. c) Initial formation of the corkscrew structure. The field of view is 706 (mm) by 19 (mm), approximately 90 (mm) downstream of the gate valve. The images were recorded at $\hat{t} = 1, 2, \ldots, 11, 12$ (s) after the start of the experiment. The Newtonian displacing layer is pushed azimuthally around the dark viscoplastic layer, detaching it from the pipe wall.

the axial direction, due to partial blockage of the pipe by the gel, promotes azimuthal pressure gradients that push fluid around the wall, removing the Carbopol layer in the process. This process is less energetic than the initial unsteady bursting and so leaves the removed Carbopol intact. The penetrating film starts close to the upstream end of each segment and propagates

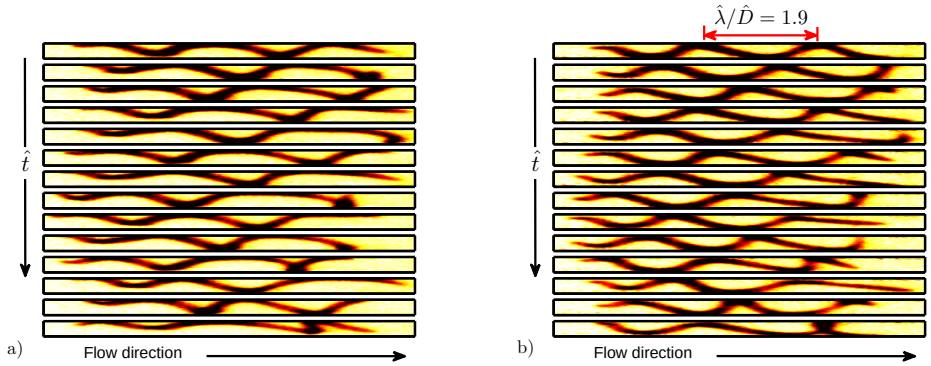

Figure 7.7: a) Front and b) top view images of the helical structure formed in the experiment shown in Fig. 7.6. The field of view is 115 (mm) by 19 (mm), approximately 1800 (mm) downstream of the gate valve. The images are taken at $\hat{t} = 44.5, 45, \ldots, 50.5, 51$ (s) after the start of the experiment. The contrast of these images has been enhanced to show the structure more clearly. The average wavelength of the helix is about 1.9 times the diameter of the pipe.

downstream as the layer is lifted from the wall. This process may involve an instability with an axial wavelength. As the layer is lifted from the wall into the main stream it is deformed axially into the helical form. The entire segment eventually lifts from the wall and propagates downstream. Figure 7.6c shows the early stages of the formation of a helix. An additional example is shown below in §7.2.4.

To better understand the behaviour of helical pieces of Carbopol within the surrounding displacing fluid, we focus on the motion of a single helix observed from both side and top views. Figures 7.7a and b show close-up images from the experiments. The helical shape does not appear to deform much over the period shown, which is approximately 6.5 (s), but it rotates about its axis and moves in three dimensions as it propagates. The wavelength $\hat{\lambda}$ of the helix is on the order of the pipe diameter; in this particular case we find $\hat{\lambda}/\hat{D} \approx 1.9$. The wavelength is probably determined by the formation mechanism discussed above, as the pipe diameter limits the lateral motion of the Carbopol layer as it is removed from the wall.

We also observed what we term "blockage-type" displacements, which appear to be closely related to the corkscrew-type displacements discussed above. Here the deformation of the viscoplastic layer itself helps displace the rest of its bulk in the pipe by forming a small plug which blocks the pipe.

Figure 7.8 shows results from an experiment showing such a blockage. The sequence of images in Fig. 7.8a shows that the initial displacement behaviour is characteristic of slumping. The viscoplastic layer becomes cut off by displacing liquid. One ripped segment of the dark gel layer then separates from the wall and becomes rolled up in such a way that it blocks the whole cross section of the pipe. Once formed, the blockage is pushed downstream by the flow and acts to remove the displaced fluid remaining inside the pipe. The moving blockage can be clearly seen in the spatiotemporal diagram, shown in Fig. 7.8b. The velocities measured with the UDV are plotted in Fig. 7.8c. Before the passage of the blockage, i.e. for $\hat{t} < 10$ (s), the velocity profile away from the wall of the pipe is quite flat. This plug flow profile is due to the yield stress of the fluid in the pipe. A similar plug flow region is seen at early times in Fig. 7.8d. Once the blockage of Carbopol gel passes the location of the UDV probe $\hat{t} \approx 15$ (s), the velocity profile evolves into a parabolic profile characteristic of Poiseuille flow. This indicates that the fluid behind the blockage has no yield stress, i.e. the passing blockage has pushed the yield-stress fluid out ahead of it. For $\hat{t}$ between 10 and 20 (s), the passage of the blockage of viscoplastic gel causes some oscillation in the UDV profiles. Figure 7.8d illustrates the change from plug flow to Poiseuille flow by showing velocity profiles across the pipe before and after the passage of the plug. The effect of the gel blockage can also be seen from the fact that the depth-averaged concentration C, calculated from the images in Fig. 7.8a increases from 0.45 before the its passage to 0.69 after.

A closer look at the way the blockage forms is given by Fig. 7.9. As with the corkscrews described above, the upstream end of the viscoplastic layer is removed from the wall and pushed towards the bottom of the pipe, making it roll up to the point that it blocks the pipe. The resulting plug and the Carbopol segment downstream are then pushed along the pipe by the displacing fluid. This motion can continue until the blockage exits the pipe, as in Fig. 7.8a, or until it becomes "unrolled" by the surrounding fluid, thus opening a passage for the displacing fluid. This latter behaviour can be seen in Fig. 7.3a.

7.2.2 Central regime

The central-type displacements observed in our experiments are similar to those described in [125]. We show just one example in Fig. 7.10. Figures 7.10a and b show time sequences of simultaneous side- and top-view images, respectively. Comparison of these images confirms that the displacing front travels approximately centrally through the pipe, leaving a (darker) residual

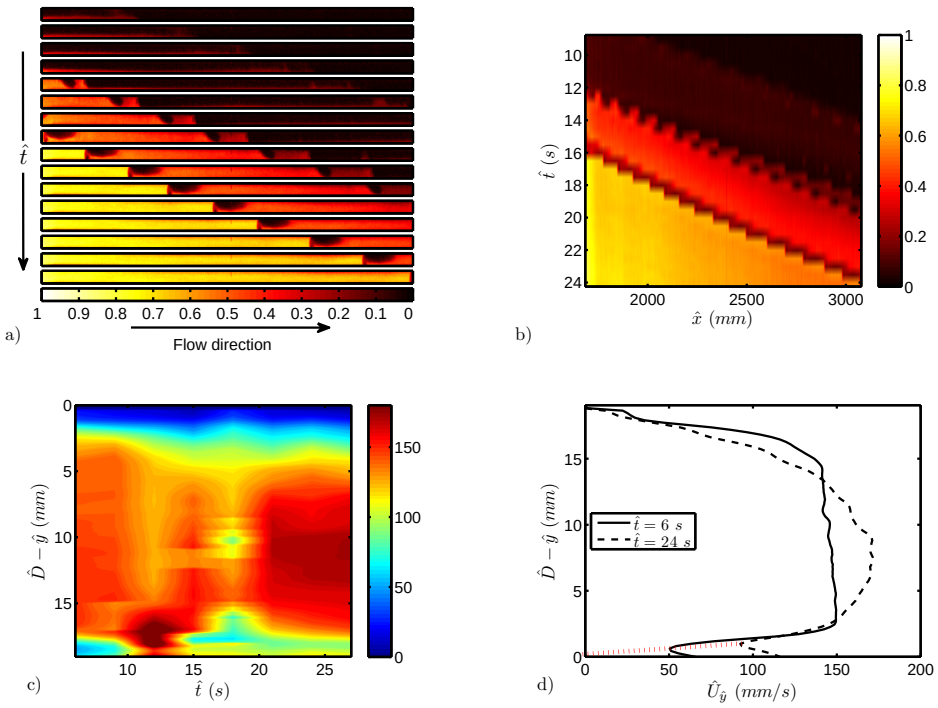

Figure 7.8: Blockage-type displacement for $\beta = 30°$, $At = 0.0143$, $\hat{\tau}_Y = 6.9$ (Pa), $\hat{V}_0 = 113.2$ (mm/s). a) Images of the displacement at $\hat{t} = 9$, 10, ..., 23, 24 (s) after opening the gate valve. The field of view is 1392 (mm) by 19 (mm), 1685 (mm) below the gate valve. b) Spatiotemporal image of the same displacement. c) The velocity profile measured with the UDV for the same experiment. The UDV probe is placed at $\hat{x} = 1560$ (mm). d) Profiles of the streamwise velocity obtained from the UDV at $\hat{t} = 6$ (s), showing a plug flow profile and 24 (s), when the profile is more closely parabolic. The dotted red line is an extension of the measured velocity profile intended as a guide to the eye; the UDV does not give 0 velocity at the lower wall due to refraction errors.

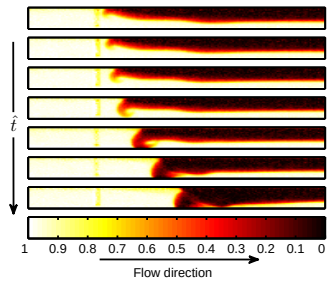

Figure 7.9: Slump-type displacement for the same parameters as used in Fig. 7.3 showing the formation of a blockage. The field of view is 192 (mm) by 19 (mm), 380 (mm) downstream of the gate valve. The images are taken at $\hat{t} = 63, 63.25, \ldots, 64.25, 64.5$ (s) after the start of the experiment. In this case the blockage did not persist for very long and instead unfolded back to a layer configuration.

layer of Carbopol all around the pipe. These residual layers are nonuniform with irregular, slow spatial variations in thickness, as was also the case in [125]. The images also show tendrils of the lighter-colored displacing fluid ahead of the main displacement front. These are due to initial mixing of the fluids that takes place when the gate valve is opened to start the experiment.

Figure 7.10c shows the flow velocities measured with the UDV, which was located 156 (cm) downstream from the gate valve. Before the displacing front reaches the position of the UDV probe, the velocity profile is plug-like, with a flat central region. After the front passes at $\hat{t} \approx 16$ (s) a static layer forms at the pipe wall and the velocity profile in the center of the pipe becomes much closer to parabolic. As the front motion is approximately steady, Fig. 7.10c can also be translated into a spatial map of the velocity distribution, (i.e. by multiplying the time axis by the mean front velocity). A similar transition from a fully mobile fluid to a situation with static residual layers during the steady passage of a displacement front was identified computationally by Allouche *et al.* [5] for plane channel displacements of two Bingham fluids, but to our knowledge this is the first time that such a transition has been visualized experimentally. It is interesting that the axial extent of the transition region inferred from Fig. 7.10c is very long. We observe the transition to take place over a period of roughly 10 (s), from $\hat{t} \approx 10$ (s) to $\hat{t} \approx 20$ (s). The mean speed in this experiment is $\hat{V}_0 = 73.3$ (mm/s), with the front velocity being significantly larger. This suggests a transition length of approximately 1 (m), equivalent to about $50\hat{D}$. This

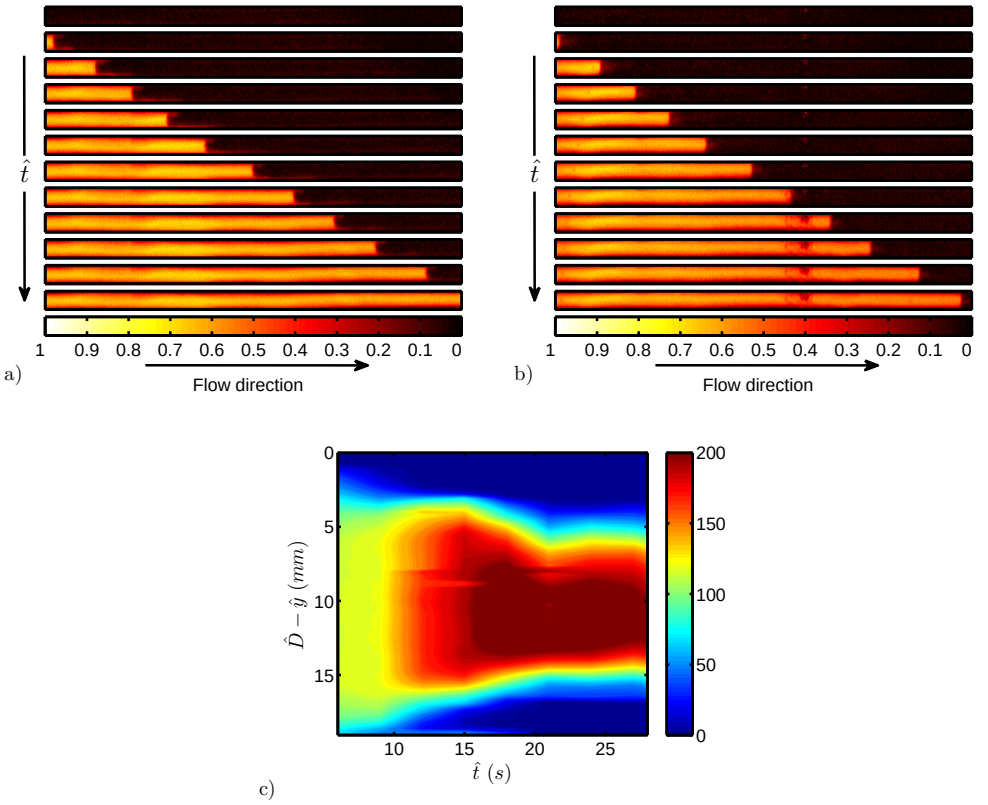

Figure 7.10: Central displacement for $\beta = 30°$, $At = 0.0035$, $\hat{\tau}_Y = 26.3$, $\hat{V}_0 = 73.3$ (mm/s). a) Side view images of the displacement at $\hat{t} = 20$, 20.5, ..., 25, 25.5 (s) after opening the gate valve. The field of view is 560 (mm) by 19 (mm), 2438 (mm) below the gate valve. b) Top view images of the displacement taken at the same times as in a. c) The velocity profile measured with the UDV for the same experiment. The UDV probe is 1560 (mm) downstream from the gate valve.

is significantly longer than anything observed in the computational studies [5, 149], in which the length of the transition region was typically a few channel widths. Although results for pipe and channel flows may not be directly comparable, this is nonetheless a large difference. It may be a result of the fact that $B_N \gg 1$ in our experiments; the large ratio of the yield stress of the displaced fluid to the viscous stress of the displacing fluid makes the former more resistant to being washed away by the latter. This resistance may result in a larger transition region. It may also be because our flows are

more inertial than those in the computations, perhaps causing the uneven residual wall layer to excite spatial frequencies behind the front.

7.2.3 Turbulent-mixed displacements

In some of our experiments at elevated flow rates, the flow of the displacing fluid becomes turbulent. Figures 7.11a-d show results for one such case; for this experiment $Re = 1890$. Strong transverse mixing makes the concentration profile uniform across the pipe, as is evident in the images of Fig. 7.11a. Instead of a sharp displacement front, we observe a discernible gradient in the mean concentration along the flow direction. Figure 7.11b shows the depth-averaged concentration as a function of axial position along the pipe and suggests that the concentration gradient broadens as the displacement progresses. Figure 7.11c shows the spatiotemporal diagram for the same experiment. There is no clear boundary between the displacing and displaced liquids, and again the extent of the mixing zone increases as time progresses. Sufficiently far ahead of the mixing front we would expect the Carbopol to be in laminar regime. Figure 7.11d shows the UDV data for the same experiment. At early times ($\hat{t} < 10$ s) the velocity profile at the UDV probe is plug-like and laminar, but it becomes spatially and temporally unsteady as the displacing fluid passes. The duration of the periods of high and low velocity visible in the core of the flow for $\hat{t} \gtrsim 15$ (s) imply lengths ranging 0.1 to 1 (m), indicating relatively long, streak-like structures characteristic of low Re turbulence. The slight up-down asymmetry of the streamwise velocity data shown in Fig. 7.11d may be due to UDV refraction errors close to the lower wall, or it may indicate that a slight slumping effect is still present despite the strong mixing across the pipe.

To characterize the spreading of the diffuse mixing region, we applied a similarity transform, $\hat{\xi} = (\hat{x} - \hat{V}_0\hat{t})/\sqrt{\hat{t}}$, to the mean concentration profiles plotted in Fig. 7.11b. The results are plotted in Fig. 7.12. The scaled concentration profiles collapse very well onto a single curve. The solid curve plotted in Fig. 7.12 is a fit to the data of the usual analytic solution to the one-dimensional linear diffusion equation, $C = 0.5\,\mathrm{erfc}\left((\hat{x} - \hat{V}_0\hat{t})/\left(2\sqrt{\hat{D}_M\hat{t}}\right)\right)$, with $\hat{D}_M = 2.5 \times 10^{-4}$ m^2/s. The reasonably good fit to the data coupled with the high value of the diffusion coefficient $\hat{D}_M$ strongly suggests that the observed axial spreading is due to turbulent diffusion. The value of $\hat{D}_M$ obtained here is approximately as order of magnitude lower than those obtained for iso-viscous Newtonian displacements in the same apparatus in [3], which suggests that the yield stress and high viscosity of the Carbopol

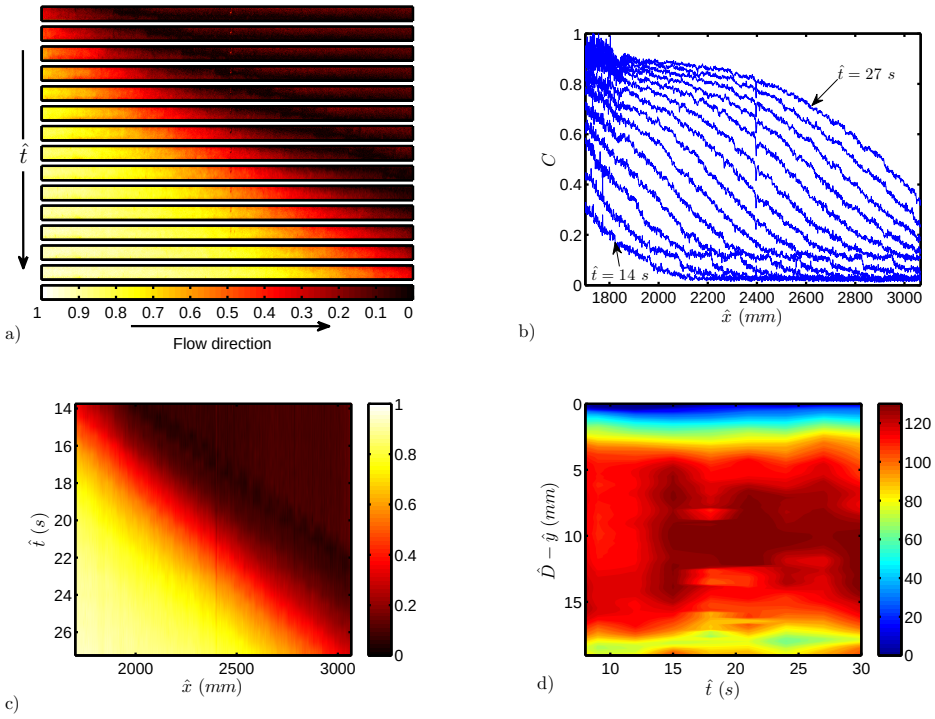

Figure 7.11: Displacement flow for $\beta = 0°$, $At = 0.016$, $\hat{\tau}_Y = 11.7$ (Pa), $\hat{V}_0 = 97.6$ (mm/s). a) Images of the displacement at $\hat{t} = 14$, 15, ..., 26, 27 (s) after opening the gate valve. The field of view is 1364 (mm) by 19 (mm), 1702 (mm) below the gate valve. b) Evolution of the depth-averaged concentration with time and streamwise position for the images in a. c) Spatiotemporal image of the same displacement. d) The velocity measured with the UDV for the same experiment. The UDV probe is located at $\hat{x} = 1560$ (mm).

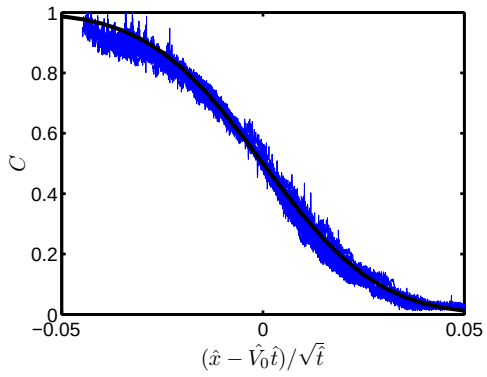

Figure 7.12: Collapse of the depth-averaged concentration profiles shown in Fig. 7.11b when plotted against $(\hat{x} - \hat{V}_0\hat{t})/\sqrt{\hat{t}}$. The collapse suggests that the spreading of the front is diffusive. The solid line is a fit to the form $C = 0.5\text{erfc}\left((\hat{x} - \hat{V}_0\hat{t})/\left(2\sqrt{\hat{D}_M\hat{t}}\right)\right)$ with the axial diffusion coefficient $\hat{D}_M = 2.5 \times 10^{-4}$ m^2/s.

limits dispersion along the pipe.

Our experiments were designed to be below the nominal transitional Reynolds number for pipe flow, $Re_{cr} \approx 2300$, and this type of flow occurred mostly for small values of β, i.e. for inclinations close to vertical, and high Atwood number ($At = 0.016$). It was observed for Reynolds numbers as low as $Re = 870$, suggesting that the onset of turbulence involves buoyancy as well as shear. The unevenness of residual deposits of Carbopol along the walls may also contribute to the unsteadiness of the flow. The majority of our experiments were done at lower Re, and we have insufficient data to determine the onset of this regime precisely. Although it would be interesting to study this regime in more detail, our apparatus and the UDV technique are not ideal for doing this.

In recent work we studied density unstable Newtonian-Newtonian displacement flows, using the same apparatus and over a similar range of pipe inclinations [3]. The images in Fig. 7.11a and the spatiotemporal plot in Fig. 7.11b are quite similar to those observed in [3]. In that work we also found fully diffusive turbulent displacements at Re much lower than expected, but with significant axial buoyancy contributions. It appears that once turbulence starts and the mixing becomes very efficient across the pipe, the rheology of the displaced fluid becomes immaterial.

7.2.4 Exchange flows

We also carried out a number of experiments with no imposed mean flow. In these experiments, the drain valve at the end of the flow loop remained closed throughout the experiment and only the gate valve is opened at $\hat{t} = 0$ (s). The balance between yield stress and buoyant forces determines whether an exchange flow occurs. In most of our experiments, and in particular in nearly-horizontal experiments in which the axial component of the buoyant force was weak, there was no motion after the gate valve was opened because of the yield stress of the Carbopol. Motion did occur in a significant number of experiments, however. In all cases the displacement flow was of the slump type, and we observed intact, ripped, and corkscrew behavior.

Figure 7.13 shows images from four exchange flows for $At = 0.016$ and different inclination angles. The field of view straddles the position of the gate valve, and the location of the valve is indicated on the images. Figure 7.13a shows snapshots from a close-to-horizontal exchange flow experiment in which the displacing layer has slumped beneath the gel layer, which remains intact. Figures 7.13b and c are from more steeply inclined experiments, $\beta = 45^\circ$ and 15° respectively. In almost all of the exchange flows observed, a relatively thin layer of displacing fluid initially slumps beneath the displaced layer, as in the slump flow displacements for $\hat{V}_0 > 0$ discussed above. This can be seen in Figs. 7.13a-c. In Fig. 7.13b the flow is of ripped type. As there is no imposed flow in this case, isolated segments of Carbopol are driven only by buoyancy and float upstream in the displacing fluid after they detach.

Figures 7.13c and d show an interesting example of a corkscrew-type exchange flow. As above, the displacing fluid again forms a thin layer along the bottom of the pipe, but then begins to push upwards azimuthally. Presumably the axial pressure gradient is insufficient to sustain the simple exchange configuration against the yield stress, and instead the displacing fluid is squeezed around the walls. Figure 7.13d shows that the azimuthal penetration of the clear fluid through the Carbopol becomes spatially uneven as it develops; this appears to be associated with the formation of the helical structure and its propagation upwards into the clear fluid.

These results are most interesting in the context of previous theoretical studies by Frigaard and coworkers on buoyancy-driven exchange flows with two yield-stress fluids [49, 51, 54]. The approach taken in [49, 54] was to study an intact slump type configuration, in which the interface remains stratified in the cross-section of the pipe, as it elongates, assuming a lubrication theory-type of scaling. For such configurations there is a balance

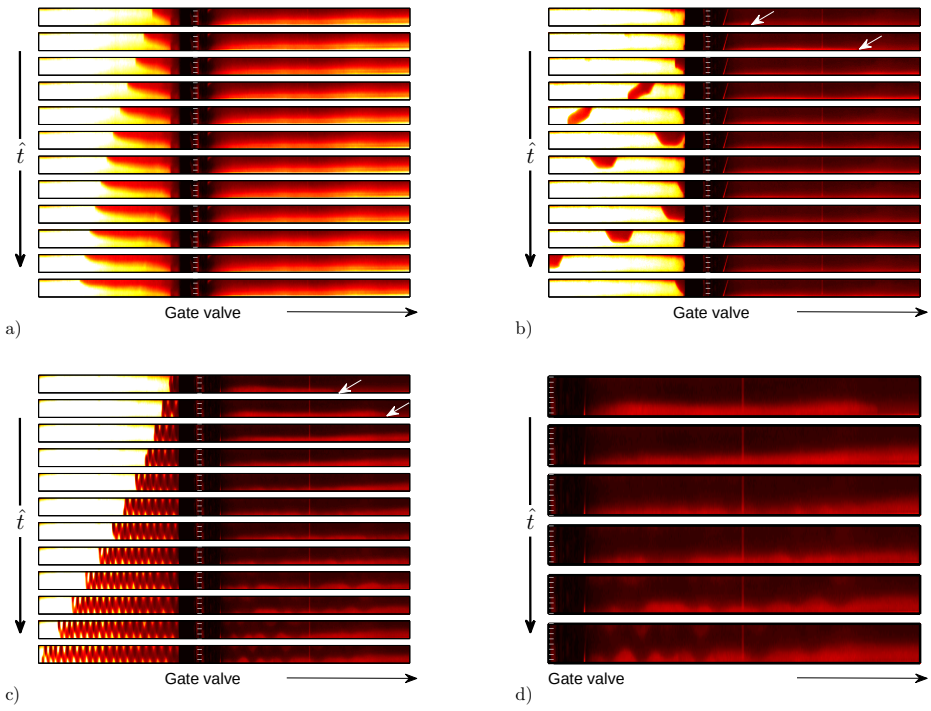

Figure 7.13: Snapshots of the exchange flow experiments carried out for $At = 0.016$ and a) $\beta = 75°$, $\hat{\tau}_Y = 4.3$ Pa at $\hat{t} = 40, 49, \ldots, 121, 130$ s; b) $\beta = 45°$, $\hat{\tau}_Y = 22.6$ Pa at $\hat{t} = 30, 32.5, \ldots, 52.5, 55$ s; and c) $\beta = 15°$, $\hat{\tau}_Y = 19.6$ Pa at $\hat{t} = 11, 13.5, \ldots, 36, 38.5$ (s). The field of view is 1370 (mm) by 19 (mm). The center of the gate valve in each image is indicated by a white dotted line; the valve body blocks the view of the fluids on either side of this line. The white arrows in b and c show the position of the fast displacing front. In a it has already passed through the field of view by the time of the first snapshot. The left end of the pipe is higher than the right; the black arrow at the bottom of each figure points downhill. d) Images from the same experiment as in c for $\hat{t} = 13.5, 18.5, \ldots, 33.5, 38.5$ (s) focused on the area below the gate valve to better show the formation of a corkscrew structure within the dark gel region. In all images the contrast has been enhanced to show the structures more clearly.

between axial buoyancy and yield stress, and for sufficiently high yield stress flow is not possible. A plane channel was considered in [49] and a pipe in [54]. For a pipe with a single yield-stress fluid the condition needed for a long thin slump flow to occur is

$$\frac{\hat{\tau}_Y}{\Delta\hat{\rho}\hat{g}\hat{D}\cos\beta} < 0.3043. \tag{7.7}$$

in [51] this approach was extended to configurations in which the interface is perpendicular to the axis of the pipe. For a horizontal pipe half filled with a yield-stress fluid and with both fluids initially stationary, motion will not be instigated if

$$\frac{\hat{\tau}_Y}{\Delta\hat{\rho}\hat{g}\hat{D}} > 0.25. \tag{7.8}$$

This estimate was combined with Eq. (7.7) to give an approximation for the yield stress required for a stationary flow at all inclinations β [51]. The expression in [51] is too complicated to repeat here, but the numerical results above are indicative of the value of $\hat{\tau}_Y/\Delta\hat{\rho}\hat{g}\hat{D}$ required to prevent motion. Reference [51] also reports a sequence of experiments that confirmed the bounds based on Eqs. (7.7) and (7.8), and indeed suggests that they are somewhat conservative. In contrast, for the exchange flow experiments reported here in which motion was observed, $\hat{\tau}_Y/\Delta\hat{\rho}\hat{g}\hat{D}$ is in the range 0.69-20.13, much larger than required to prevent flow according to the predictions of [51].

There are many possible reasons for this apparent discrepancy. First of all, the experiments in [51] differ from those reported here. In [51], experiments were performed in a sealed pipe initially filled with two fluids in a gravitationally stable configuration (i.e. light over heavy) that was turned rapidly and placed against an inclined plane in the unstable configuration. This process adds inertia to the system, but not specifically to the interfacial region. In contrast, opening the gate valve in our experiments undoubtedly shears and mobilizes the fluid locally.

Given this difference, the comparison with stability criteria based on static or slow flow configurations may not be valid. In the static configuration, dimensional analysis shows that $\hat{\tau}_Y/\Delta\hat{\rho}\hat{g}\hat{D}$ and β are the only important parameters [51]. In lubrication/thin-film flows an additional parameter relating viscosity and buoyancy comes into play. In terms of our parameters, this is roughly the combination $Re\cos\beta/Fr^2$. Where inertia is present, however, self-reinforcement of the inertia-buoyancy balance is critical. This is captured in the parameter Re/Fr. This effect is not included in the analysis of [49, 54].

It is nevertheless interesting to consider the propagation mechanism more closely. The only possible driving force is the buoyant stress, which has a magnitude of order $\Delta\hat{\rho}\hat{g}\hat{D}$. If $\hat{\tau}_Y$ is much larger than this, it is hard to see how the flow can progress. It is conceivable that significant extensional stresses are generated in the intact slump configurations, in which the layering is observed to be quite uneven. This may account for some flows for which $\hat{\tau}_Y/\Delta\hat{\rho}\hat{g}\hat{D} \sim 1$. It is interesting, however, that in Figs. 7.13b and c the yield-stress fluid only propagates upstream when it is separated from the wall, i.e. it is a solid body floating.

This suggests that the yield-stress fluid prevents exchange flows through continuity and contact with the wall. More specifically, in the absence of sufficient stresses, there is no deformation. If in addition the yield-stress fluid is in contact with the wall, then it simply does not flow. This in turn means that the net flux of the other fluid is zero. If, on the other hand, the yield-stress fluid is detached from the wall, it can move in an undeformed state and does not constrain the motion of the other fluid. As another example, a concentric core-annular system is analyzed in [54]. It is shown that if the yield-stress fluid is in a layer adjacent to the wall, a sufficiently high yield stress prevents motion, while if the yield stress is small or if the fluid on the wall is Newtonian and the yield-stress fluid is in the centre then motion cannot be stopped. All of this reinforces the idea that the flows of Carbopol observed above the gate valve are associated with detachment of the viscoplastic fluid from the wall.

Other possible explanations for the unexpected flows propagation invoke the effects of mixing or possible slip at the wall. The former does not appear substantial in our experiments and in any case would mitigate buoyancy effects. For the latter, we have no evidence of slip in any of our other experiments and see no reason for it to suddenly manifest here.

Whatever the explanation, these results are interesting from an industrial perspective. One motivation for the studies in [49, 51, 54] was the industrial process of plug cementing used to seal oil wells at abandonment, among other things. The placement of cement plugs is typically inertial: the cement and other fluids are pumped down the well through a narrow pipe. In this sense the practical conditions are closer to those in our experiments than to those of the experiments in [51]. The observed tendency for the yield-stress fluid to detach from the wall — either in segments or in a more complex pattern — raises concerns about the efficacy of the plug cementing process in cases where one of the fluids involved has no yield stress. Further study in this area would thus be beneficial.

7.2.5 Dimensionless flow classification

We have observed a rich range of phenomenology in slump-type displacement flows. On re-examination of the data from [125], we also found some of the same phenomena in their slump flow experiments, particularly later in some of their displacements. Although we have tried to classify each type of flow observed, some occur at different stages in the same experiment. Any such classification is therefore not exclusive. It therefore appears possible that there is a continuum of possible behaviour. We summarize the main trends observed.

First, as the pipe is inclined away from horizontal the effects of the axial buoyancy force start to become important. At low imposed flow rates we frequently observe detached pieces of the displaced fluid traveling upwards, driven against the imposed flow by buoyancy. Adopting terminology from [130], we classify experiments as "displacing instantaneously" if no displaced fluid is observed above the gate valve during an experiment. If the displacement is not instantaneous, there is back flow. This may be in the form of a sustained flow up the pipe or a transient flow that is eventually washed downstream, although this distinction may not be fundamentally relevant since the experiments are of finite duration.

Figure 7.14 shows the experimental data plotted in the Fr-$Re\cos\beta/Fr$ plane. The data points from experiments with back flow are labeled with an $\times$, while those which are instantaneous are unlabeled. The heavy line in Fig. 7.14 is the predicted boundary between instantaneous displacements and back flows, assuming two iso-viscous Newtonian fluids; see [130]. Flows below this line are theoretically predicted to displace instantaneously [130]. A similar figure is given in [3] for iso-viscous Newtonian fluid displacements. In that case, back flows were found only in the approximate range $0 \lesssim Fr \lesssim 3$ and $0 \lesssim Re\cos\beta/Fr \lesssim 800$. Figure 7.14 shows that when the displaced fluid has a yield stress, the maximum value of Fr for which back flows are found shrinks to 1.3, while the maximum value of $Re\cos\beta/Fr$ increases to 1100. The presence of the yield stress seems to change the region in which back flow occurs, but not by much. From the industrial point of view, it is beneficial to have instantaneous displacement of the displaced fluid.

The second main trend we have seen is a progression of mechanisms for the break up and removal of the yield-stress fluid layer. For slump-type displacements, the initial behaviour in all cases is very similar: a rapidly moving front flows along the lower side of the pipe. At lower Re/Fr the displaced yield-stress fluid remains largely intact. As Re/Fr increases, the focusing of the flow into a narrow layer increases the inertia [125] and we

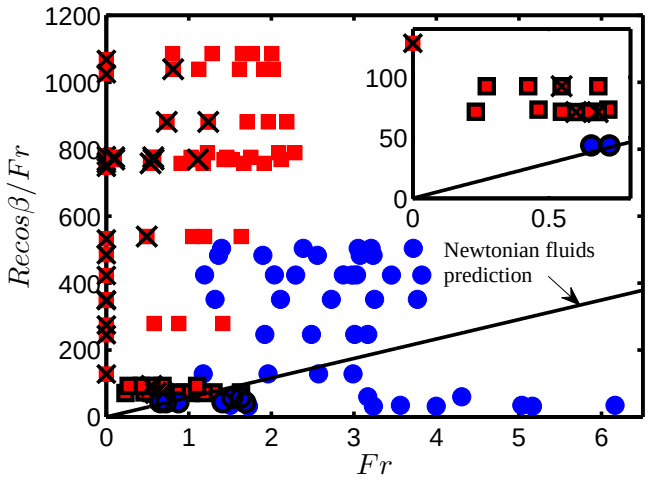

Figure 7.14: Presentation of our experimental results in the Fr–$Re\cos\beta/Fr$ plane. The line represents the prediction of the lubrication model of [130] for the stationary interface between two iso-viscous Newtonian fluids. Red squares indicate conditions for which slump-type displacements were observed. Blue circles indicate central-type displacements. Points marked $\times$ indicate displacement flows that are not instantaneous, i.e. that involved back flows. Experimental points for near-horizontal pipes from [125] are indicated by black borders around the symbols. The inset enlarges the region close to the origin to better display the non-instantaneous displacements observed for nearly-horizontal experiments.

begin to observe unsteady bursts that locally break the Carbopol layer. As the inclination angle β is decreased the axial component of the buoyancy force increases. The flows remain segregated but the unsteady bursts rip the Carbopol layer into pieces, some of which can move backwards against the flow. At large Re/Fr the degree of instability increases further, and structures such as corkscrews and blockages form in the Carbopol as it is removed from the pipe wall. At similar Re/Fr but larger Re we observe the onset of the turbulent mixed regime.

Figure 7.15 shows the experimental data points with their secondary classification indicated. All of the slump flows are of the "ripped" type, but within this class, corkscrew and plug structures are observed for $Re/Fr \gtrsim 950$. Turbulent/mixed flows appear in a similar range of Re/Fr. As a guide to the reader we have plotted a nominal transition curve for the onset of turbulence at $Re = 2300$ in Fig. 7.15a. Figure 7.15b presents the same data, but plotted with $Re\cos\beta/Fr$ on the y-axis. This quantity is a measure of the influence of the axial buoyancy force in promoting instability compared to viscous effects. We see that the unstable flow structures appear at pipe inclinations that are far from the horizontal, suggesting that they are associated with an increase in the effect of buoyancy.

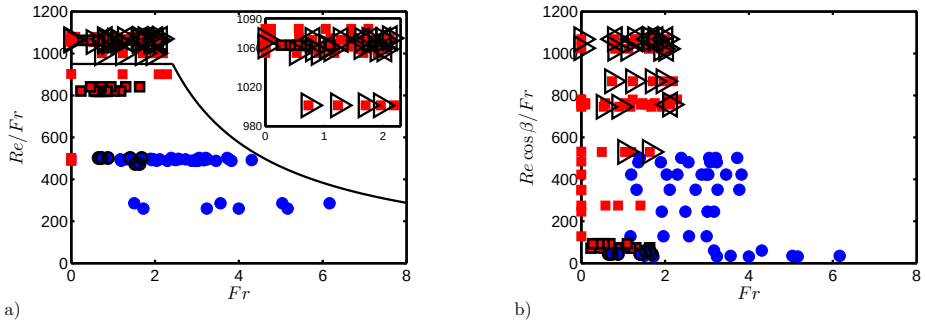

Figure 7.15: a) Experimental results plotted in the Fr–Re/Fr plane. The curve corresponds to $Re \approx 2300$. The horizontal line segment corresponds to $Re/Fr = 950$. The highly unsteady flow behaviour described in the text was observed above this line. $\triangleleft$: turbulent-mixed displacements; $\triangleright$: corkscrew and blockage-type displacements; red squares: slump-type displacement; blue circles: central-type displacement. Data from [125] for near-horizontal pipes are indicated by black borders around the symbols. The inset enlarges the region above $Re/Fr = 950$ and shows that there are some experiments in which none of the mixing, corkscrew and/or blockage type flows were observed. b) The same data plotted in the Fr–$Re\cos\beta/Fr$ plane. The figure shows that the highly unsteady flows (mixing, corkscrew and blockage-type) appear for $Re\cos\beta/Fr \gtrsim 500$.

7.3 Discussion points

We have presented experimental results in which a heavy Newtonian fluid displaces a lighter yield-stress fluid in the downwards direction. We have focused on the industrially interesting case where the yield stress is significantly larger than the viscous stress in the displacing fluid, but where buoyancy may be significant. We have described a number of distinct flow regimes and exotic behaviours that arise in the presence of a large yield stress of the displaced fluid.

As found previously for nearly horizontal pipes [125], the displacement flows were either slump or centre-type. The transition between the two flow regimes occurred in the range $600 < Re/Fr < 800$, as in [125]. This implies that the inclination angle does not directly determine the flow regime, although it did contribute to the range of secondary flow behaviour observed at higher inclinations.

In addition to the slump and centre-type displacement flows, we also observed a turbulent/mixed regime either when the flow rate was high (in which case the imposed flow is turbulent) or when the buoyancy parameter, $Re\cos\beta/Fr$, was large enough to cause instability and mixing. In all of the slump flows, the gel layer was broken up over time by a range of different mechanisms, including the formation of corkscrew structures and plugs which blocked the pipe.

Newtonian-viscoplastic fluid exchange flows were also studied over a range of inclination angles. The more dense Newtonian fluid was found always to slump beneath the gel layer, while the lighter viscoplastic layer showed a range of different behavior. The onset of exchange flow was characterized using the ratio between the yield stress of the displaced fluid to buoyant stress caused by the density difference.

Finally, the experimental data were characterized according to whether the displacement flows happen instantaneously or there exists a back flow. This is important for industrial applications, in which back flow is generally undesirable. The results were compared with those for iso-viscous Newtonian fluid displacements [3].

Chapter 8

Conclusions

In this chapter the main scientific conclusions and contributions of this thesis are summarized. This is followed by giving industrial recommendations based on the results. We conclude by looking into ways of improving the results and at future work that could undertaken to extend the results of this thesis.

8.1 Contributions to fluid dynamics understanding

In this section the key findings of the thesis are categorized into three groups namely, Newtonian iso-viscous displacement flows, yield stress fluid displacement flows and modeling/flow stability prediction.

8.1.1 Newtonian iso-viscous displacement flows

The majority of the results presented in this thesis focus on Newtonian iso-viscous displacement. This includes density stable and/or unstable experiments and both pipe/channel geometries. For pipe geometry the approach is wholly experimental and for 2D channel geometry the approach has been mostly numerical, but partly analytical.

It was found that the density difference (although very small) has a huge effect on the observed flow. When the configuration is density unstable the flow becomes quickly stratified and can potentially go unstable at inclinations away from horizontal. In this case the displacement efficiency is always less than 100% since the displaced layer has the tendency to flow back against the mean displacement flow. If there is no density difference, the two fluids are essentially the same and the flow pattern mimics that of a Poiseuille flow. By further changing the density difference to a stable configuration the flow again undergoes a major change and takes the form of a quasi-steady interface moving at a constant speed and washing the displaced fluid almost completely. Note that the displacement efficiency is very close to 1 in this case.

Although inertia plays an important rule in the case of density unstable flows, it barely seems to be important when the configuration is density stable. The governing force balance influencing the interface length appears to depends mostly on buoyancy and viscous forces. In density stable displacements the longitudinal extent of the interface (that we have called the stretch length) was measured for a wide range of parameters. It was found that the stretch length increases with mean flow speed and pipe inclination angle (β, measured from vertical) and increases with the common viscosity of the two fluids. While the former effects are somehow intuitive the latter is not intuitive at all. The stretch length also decreases when the density difference increases. Interestingly it is predicted that in the presence of the mean flow speed, the stretch length approaches the hydrostatic value only when the density difference is infinity.

Through use of a scaling argument, all the experimental data collapsed into a single curve giving the dimensionless value of the stretch length as a function of $\chi = 2Re\cos\beta/Fr^2$. The curve suggests the form $L = \tan\beta - 3680/\chi$. The formula is valid for all inclination angles except $\beta = 0°$, i.e. a strictly vertical pipe. In fact an almost zero value was found for the stretch length in this case, but due to a completely different flow pattern than that found at other inclination angles. A spike-like region was found at the displacing front which is typical of symmetric displacements [27, 81, 93, 109].

When the configuration is density unstable we have studied the isoviscous displacement flows in both pipe (experimentally) and 2D channel (numerically). For both methodologies the types of flow were first described qualitatively at different inclination angles, β, through snapshots of the experiment/simulation, spatiotemporal diagrams of the depth-averaged concentration and from the velocity distribution. From images of the flow we have extracted the speed of the displacing front $\hat{V}_f$, which is closely associated with the displacement efficiency. For those cases when instability is present and the fluids are well mixed (called diffusive flows), another important quantity that can be extracted from the data is the macroscopic diffusion coefficient $\hat{D}_M$. Both the front velocity and the macroscopic diffusion coefficient were measured over a wide range of parameters.

The most important contribution of the density unstable displacement study was defining different flow regimes in the dimensionless $Re\cos\beta/Fr$ and Fr plane. It was found that separate regimes for instantaneous and non-instantaneous, viscous/inertial and diffusive/non-diffusive displacement flows can identified in this plane. The related values of $Re\cos\beta/Fr$ and/or Fr were given along the boundaries of these different flow regimes. It was also found that due to the strong mixing at inclinations close to vertical

instantaneous displacements can still exist at values of χ higher than the predictions of the lubrication model ($\chi_c = 116.32$) from [130]. This is similar to the Boycott effect [61] discussed earlier in chapter 2. Once the regime classifications were made, appropriate predictions of the front velocity and macroscopic diffusion coefficients (where applicable) were given. In particular, it was found that when the flow is viscous the lubrication model (see [128]) can be an effective tool to predict $\hat{V}_f$, across all inclinations. In this case no bulk diffusion coefficient can be defined for the flow. On the other hand when the flow is fully diffusive, the front velocity is very close to the mean imposed velocity, $\hat{V}_f \approx \hat{V}_0$ in the case of pipe. The front velocity is approximately 1.5 times larger than the mean imposed velocity $\hat{V}_f \approx 1.5\hat{V}_0$ in the case of channel.

The key difference is that the mixing patterns are different in pipe and channel geometries. In particular, the slumping effect is less observed in the channel geometry than in the pipe. In fact the displacing layer tends to advance along the middle of the channel even if the density difference promotes a slump-type behavior. One reason for this is that 3D flows in a pipe, where the displacing layer is more dense, can tend to squeeze the displaced fluid layers azimuthally along the wall and towards upper side of the pipe. There is no such preference in a strictly 2D channel geometry and the displacing layer can thus travel in the middle of the channel.

It was found that for both channel and pipe geometries an imposed flow can increase the macroscopic diffusion coefficient (and thus the dispersion length), by comparison to an exchange flow. When the flows are inertial but not fully diffusive we have derived formulae to predict the front velocity, based on dimensionless analysis and curve fitting of the available data. The other essential difference found between channel and pipe displacement is that the former is much more unstable than the latter. In fact, viscous flows can not be found for $Re\cos\beta/Fr > 25$ [123] whereas in the pipe geometry we can still have viscous flows up to $Re\cos\beta/Fr = 270$ at least for some ranges of Fr, (see chapter 4).

Another important contribution of this work was in broadening our knowledge about the stabilizing/de-stabilizing effects of the mean flow on the well-studied exchange flows of [111–115]. Taghavi *et al.* [129] found that the mean flow has a stabilizing effect on buoyant lock exchange flows when the pipe is angled close to horizontal. In this thesis the effect of mean flow was investigated over all other inclination angles. Interestingly we have found that the imposed velocity can have quite different effects on the flow (both stabilizing and/or de-stabilizing) all controlled by the pa-

rameter $Re\cos\beta/Fr$. In particular we found that the stabilizing effect of the mean flow found in [129] is valid up to $Re\cos\beta/Fr \approx 270$. Above this limit the imposed flow was found to progressively destabilize the flow up to $Re\cos\beta/Fr \approx 500$. Above this limit the imposed flow has a neutral effect on the flow since the degree of mixing is already very high for exchange-dominated regimes and the nature of the system is diffusive. Further details in this regard can be found in chapter 4.

8.1.2 Yield stress fluids displacement

The displacement flow of yield stress fluids is also studied in the thesis. Although the analytical model developed in chapter 6 is for a general case of two Herschel-Bulkley fluids, the experimental results in chapter 7 are only for the case that the displaced layer has a yield stress. This has mostly an industrial motivation. We have used Carbopol solutions to mimic industrial shear-thinning yield stress fluids. The study has been focused at the regime where the yield stress is much larger than the characteristic viscous stress and the Reynolds numbers (although still laminar) are significant. The results are basically the continuation of the former study by Taghavi *et al.* [125] for viscoplastic displacement in nearly horizontal pipes.

The main finding of the current study is that the slump-type and center-type regimes first observed in nearly horizontal angles also persist at inclinations away from horizontal. Interestingly the transition between these regimes occurs at approximately the same value of Re/Fr obtained before $600 \lesssim Re/Fr \lesssim 800$. The results suggest that the inclination angle does not play a major rule in the leading order features of the flow (slump/center types). This is because of the dominance of the yield stresses over buoyant and viscous ones.

However, under the category of slump-type displacements, some new and exotic flows were observed as we move towards vertical pipe inclinations, due to the increasingly strong buoyancy force acting against the mean flow. These regimes are studied in detail through a phenomenological approach using the snapshots of the experiments, spatiotemporal diagram of the averaged concentration along the pipe and finally Ultrasound Doppler Velocimetry (UDV). The installment of first-surface mirrors around the pipes allowed us to not only obtain information from the facial view but also from the top view of our experiments. This in turn enabled us to better understand the 3D nature of different flow regimes.

Exchange flows of the same fluids were studied experimentally showing different patterns at different inclination angles. When there is yield stress

in the displaced layer it was found that the chance of displacing instantaneously is much higher. The main point is that the yield stress resists the buoyancy force pushing the fluid backwards against the mean flow. Instantaneous and non-instantaneous displacement flows are located on the plane of $Re\cos\beta/Fr$ and Fr and were compared to their iso-viscous Newtonian counterparts in chapter 4. Although the results and regime classifications developed are based on experiments with Carbopol, which has both shear-thinning and yield stress, we believe that the contribution of the shear-thinning viscosity contributes less than the yield stress towards the range of flows observed.

8.1.3 Modeling and stability of the displacement flows

During the 4-year course of this Ph.D. thesis 405 experiments were conducted in the flow loop built in complex fluids laboratory of the University of British Columbia. Despite the large number, only a narrow range of flow parameters were covered. For instance although almost all range of inclination angles were covered, the fluids used were limited to only iso-viscous Newtonian and (some) Herschel-Bulkley fluids. It is basically inevitable that one has to use a mathematical model in order to predict the important features of the displacement flows over a wider range of parameters.

In an attempt to mathematically model some of the displacement flows, in chapter 6 we developed an effective two-equation model following the weighted residual approach in [8]. This weighted residual model can be used for two generalized Newtonian fluids. Although the general formulation can be used for any weakly inertial two layer system such as co-extrusion and displacement flows, the focus of the study has been on the latter. The assumptions made are that the fluids are immiscible but with zero interfacial tension (equivalently miscible fluids with infinite Péclet number). Note that the interfacial tension effect can be easily added to the current formulation. The model equations are solved as an evolution problem using a shock capturing numerical scheme. The scheme in turn can solve for the displacement flow interface hight, h, and for a buoyancy parameter, b which can be directly related to the lower layer flow rate, q. Some key findings from the weighted residual model study are as follows.

It was found that inertia can change the shape of the interface by making the sharp and shock-like displacement front smoother. This can cause a slight increase in the displacement front velocity $\hat{V}_f$ or could decrease it, in the case where we have a strong back flow. Although the modifications of the interface shape and the increase or decrease in front velocity can be

minor, the more important effect can be on the stability of the interface and the whole flow. In fact when inertia increases, it smoothens the shock-like displacement interface. By this shape modification, a wider range of interface height values, h, become prone to instability and this is one mechanism through which the flow becomes unstable. The model developed is not necessarily reliable once an instability starts to grow (as some of the scaling arguments may become invalid), but it can be used to predict the onset of instability. The shape of the interface height and their corresponding front velocities were explored for a wide range of parameters. For instance it was found that for the case of Newtonian fluids when the displacing fluid is more viscous than the displaced fluid, the front velocity is lower, and therefore the displacement efficiency is higher. In the case of shear-thinning fluids, the mechanism is quite similar, meaning that a more shear-thinning displacing fluid can produce a less efficient displacement because its effective viscosity decreases in the presence of shear.

An important section of the weighted residual model study is devoted to a stability analysis of two-layer flows, which can be directly used for displacement flows. Note that the lubrication model developed in [128] can not be used to assess the stability of the flow since the inertial terms are neglected in that model. Assuming that the interface between the two fluids is stretched sufficiently over time to approach a locally constant value, a linear stability analysis of the weighted residual model was carried out in the long wavelength limit. In the pipe flow experiments it was observed that instabilities originated at the interface of the two fluids. Even in the cases where mixing is very high and the flow has a diffusive nature, we believe that there has initially been an unstable interface. This unstable interface grows in time and causes mixing of the fluids. Although in later stages these flows are far from a two-layer system, initially they have been similar. Linear stability analysis results are given over a wide range of parameters and rheological constants. The model results were also compared against the classical Orr-Sommerfeld equation predictions (in the long wave limit), showing complete agreement in the case of Newtonian and non-Newtonian fluids.

8.2 Industrial implications and recommendations

The underlying motivation in studying the displacement flows in this thesis comes from the process of well cementing. The objectives in this regard are to be able to predict the efficiency of the displacement of one fluid by another,

when traveling downwards within the well casing (= a pipe). In an ideal situation, one might hope for a perfect displacement, but in practice other constraints on the process mean that one cannot select all fluid properties and flow rates - hence the more modest objectives outlined. In this regard the following findings of the thesis are helpful.

- From the density stable experiments of this thesis, it was found that this configuration (light fluid displacing the heavy one) produces the most efficient displacement, as is intuitive. In fact the stable density configuration ensures that the displaced layer is washed steadily down the well with small amount of residual stuck to the pipe wall after the process. In the case of density stable iso-viscous Newtonian fluids we have obtained a curve-fit based formula $L = \tan\beta - 3680/\chi$ for predicting the longitudinal extent of the interface between the two fluids.

  From the industrial perspective, the stability of the interface is anticipated, but usual industrial recommendations (see e.g. in [89]) would suggest that a density difference of around 10% be used. Here we have seen stable displacements with significantly lower density differences, suggesting conservatism in the industrial practice. This could be investigated further.

  Specifically concerning primary cementing, a usual sequence of fluids might consist of: drilling mud, wash, spacer, lead slurry, main slurry, tail slurry, drilling mud. Physical plugs/darts often separate the cement slurries from the other fluids. The last interface (tail slurry:drilling mud) is typically density stable. Our results indicate that from the fluid displacement perspective, the second plug/dart may be largely unnecessary. This plug could perhaps be more effectively employed between the first drilling mud stage and the wash/spacer, which are density unstable.

- In the case of density unstable displacement flows we have identified three main flow regimes namely viscous, inertial non-diffusive and fully diffusive. In each regime we have been able to develop a simple predictive model for the dimensionless front velocity ($\hat{V}_f/\hat{V}_0$). The front velocity also gives a measure of the displacement efficiency (see [123]), which is simply $\hat{V}_0/\hat{V}_f$.

  Where possible, our recommendation to displace density unstable situations in the fully diffusive regime, for which the displacement efficiency is maximum. This regime is obtained for values of $Re\cos\beta/Fr$

larger than $-500 + 50Fr$, in the case of iso-viscous Newtonian fluids. Note that it is always useful to have an initial estimate of the flow regime assuming iso-viscous Newtonian fluids and build upon that.

- In the case of fully diffusive displacement flows a leading order model of the flow consists of a mixing region between the fluids that travels with speed $\hat{V}_0$ and which spreads dispersively in the axial direction. The extent of the mixed regions can be estimated obtained if the macroscopic diffusion coefficient is known.

  We have developed a simple predictive model of the diffusion coefficient, in the case of iso-viscous Newtonian fluids, based on the experimental data. The concentration evolution can be found from the system

  $$\frac{\partial C}{\partial \hat{t}} + \hat{V}_0 \frac{\partial C}{\partial \hat{x}} = \hat{D}_M \frac{\partial^2 C}{\partial \hat{x}^2}, \tag{8.1}$$

  where $\hat{D}_M$ is the macroscopic diffusion coefficient predicted from $\hat{D}_M = \hat{D}_{M,Exchange} + \hat{D}\hat{V}_0(c_0 + c_1(\beta)/\sqrt{Fr})$. The coefficients are explained in detail in chapter 4.

- As a rule of thumb, we have found that the macroscopic diffusion coefficient in a pipe for the case of fully diffusive flows was found to be of the order 10 times bigger than that of turbulent Taylor dispersion [134]. On the other hand, we must recognize that buoyancy is largely responsible for enhancing the mixing, which evolves in such a way as to spread density gradients axially along the pipe. Our experimental apparatus is limited in length (and hence transit time). In an oil well and/or over significantly longer times than possible in our experiments, we might expect that the dispersing mixture would eventually spread to such an extent that either the flow might re-laminarize or (if turbulent) would approach the turbulent Taylor dispersion coefficient from a single phase flow. Therefore, it might be prudent to consider Taylor dispersion as a lower limit for the axial spreading.

- An important aspect of the displacement flows is in determining whether there would be a back flow or not. In practice we would like to avoid back flow since it decreases the displacement efficiency by increasing the displacing front velocity. Taghavi *et al.* [130] found that the lubrication model can be a useful tool in predicting the onset of back flow for iso-viscous Newtonian fluids ($\chi_c = 2Re\cos\beta/Fr^2 \approx 116.32$).

This prediction was used mainly for nearly horizontal pipes. We further discovered that for higher inclination angles this criterion can still be used as a first guess. In fact all the experiments conducted with $\chi < \chi_c$ were found to be instantaneous displacement.

Even for $\chi > \chi_c$ some flows can still be instantaneous at inclination angles away from the horizontal, due to the strong mixing that dominates counter current motion and back flow. In the case of Newtonian fluids, back flows were found only in the approximate range $0 \lesssim Fr \lesssim 3$ and $0 \lesssim Re\cos\beta/Fr \lesssim 800$. When the displaced fluid has a yield stress, the maximum value of Fr for which back flows are found shrinks to 1.3, while the maximum value of $Re\cos\beta/Fr$ increases to 1100. The presence of the yield stress seems to change the region in which back flow occurs, but not by much. From the industrial point of view, it is beneficial to have instantaneous displacement of the displaced fluid (see chapters 4 and 7 for Newtonian and viscoplastic instantaneous displacements respectively). Our results suggest that the Newtonian iso-viscous predictions of an instantaneous displacement should prove conservative for other fluid types.

- In the case of displacing a yield stress fluid by a Newtonian fluid it was shown in [125] that two main regimes can appear depending on the ratio Re/Fr for nearly horizontal pipes. These regimes are called slump and center type displacements. The transition between the two regimes occurs at $600 \lesssim Re/Fr \lesssim 800$ when the yield stress is far larger than the characteristic viscous stress. In this thesis it was interestingly found that the same flow classification exists for inclinations away from horizontal. This suggests that yield stress effect can completely dominate the effect of buoyancy and viscosity.

  However as we decrease β some unstable and exotic flows form under the category of slump-type displacements that were not observed in the nearly horizontal situation. Among these are some flow structures that appear to help displace the yield stress fluid, e.g. the helical/corkscrew type displacements discussed in chapter 7. Although helpful to displacement, it is probably premature to make any recommendation based on these flows.

- When the displaced layer has a yield stress and in the limit of exchange flows (zero mean flow) it was also found that in some cases the gel layer moved upstream of the gate valve. This is associated with detachment of the viscoplastic fluid from the wall. These results are interesting in

the context of industrial process of plug cementing used to seal oil wells at abandonment. The placement of cement plugs is typically inertial: the cement and other fluids are pumped down the well through a narrow pipe. The observed tendency for the yield-stress fluid to detach from the wall, either in segments or in a more complex pattern, raises concerns about the efficacy of the plug cementing process in cases where one of the fluids involved has no yield stress. Further study in this area would thus be beneficial.

8.3 Limitations of the present study and future work

Although many aspects of displacement flows have been studied in this thesis (experimentally, numerically and analytically) there are certainly also limitations in what we have been able to study. These limitations are discussed here. We then consider possible future work in this area.

8.3.1 Main limitations of the current study

The main experimental limitations can be listed as the cost, the time that each experiment take, the length of the apparatus, the pipe diameter used and the working fluids. In more detail these are as follows.

- Throughout this thesis, only a single pipe diameter 19.05 (mm) was used. Two key dimensionless parameters that define different flow regimes are Re and Fr. Upon changing the mean flow rate, both Re and Fr increase linearly, obscuring an independent assessment of the effects of either parameter. If we were able to vary the pipe diameter $\hat{D}$, the Froude number decreases with $\hat{D}$ ($Fr = \hat{V}_0/\sqrt{At\hat{g}\hat{D}}$) whereas $Re = \hat{\rho}\hat{V}_0\hat{D}/\hat{\mu}$ increases with $\hat{D}$. This makes for an easier assessment of individual Re and Fr effects. Thus, in order to better understand the physical mechanisms behind different regimes observed i.e. viscous, inertial non-diffusive and fully diffusive flows, it would be advisable to run some experiments with pipes of differing diameter.

- Another experimental limitation was regarding the working fluids. In our series of experiments we did not degas our water-based solutions prior to each run. It is suggested to degas the solutions with vacuum pump in sealed tanks in order to reduce the effects associated with

dissolved air into the solutions. During the preparation of the solutions and mixing the powders, ink, salt, UDV particels etc., the air can be dissolved more into the liquid solution. The existence of gas bubbles in the liquid can then affect the characteristics of the fluid for instance its viscosity (although by not a lot) which in turn can affect the displacement flow results.

We have mostly used water as the base fluid, but it could be of interest to work with more viscous fluids and particularly with a significant viscosity ratio. Further, in dealing with non-Newtonian fluids, there are some limits to the number of suitable laboratory fluids available for use.

- When the flows are fully diffusive i.e. mixing is high, the main deriving mechanism of mixing is through dispersion due to the advective velocity field. In order to better observe these flows a longer pipe should be used (a 4 (m) long pipe was used in the current experiments). This will allow us to quantify the macroscopic diffusion coefficient and the long time mixing pattern with much higher accuracy. Note that an alternative to this might be using a pipe of smaller diameter but in that case our range of Re and Fr might become more limited.

- Although the Newtonian iso-viscous density stable experiments are run over a wide range of parameters with high accuracy, little attention has been paid to the velocity field (specially close to the fronts and along the interface). We believe that there is strong circulatory motion of inertial nature within these regions although the main flow is still controlled by buoyancy and viscosity only. A closer look at the velocity field either through Ultrasound Doppler Velocimetry (UDV) or Particle Image Velocimetry (PIV) could greatly enhance our knowledge about these flows. More broadly, our experimental studies have been limited in their analysis and scope to the examination of bulk flow characteristics (front velocity, axial dispersivity, etc). This leaves a lot of interesting detail largely unstudied.

- A very important phase in the displacement flows is the initial phase in which inertial forces are very strong after opening the gate valve. During this phase many instabilities might form and affect the long time pattern. The focus in the current study is on long time behavior where the flow is well developed. Although the short time effects are studied fairly well in the numerical simulation chapter (chapter 5), we have not paid much attention to these effects in the experiments.

- In the case of viscoplastic fluids, the transition between slump-type and center-type displacements ($600 \lesssim Re/Fr \lesssim 800$) is not well studied. It is recommended that some experiments are designed to cover this range and better see how the center-type displacements become slump type displacements within this range of Re/Fr. The amount of residual layer stuck to the pipe wall after pumping the displacing fluid has not been quantified properly. This can be done through translating the average concentration value to the volume of the displaced fluid left on the wall. The other analysis lacking in the viscoplastic displacement study is investigating the front velocity. There are inherent challenges in these experiments due to the instability of the flows and noise produced from the ripped pieces of Carbopol layer. However some useful information could certainly be extracted upon analysis of the front velocity and its short time behavior.

For the numerical simulations we have carried out, although the general qualitative features studied will remain the same after refining the mesh, a much finer mesh is needed to capture all the small scale effects in the flows, especially when the flow becomes unstable and mixing starts. The reasons why this has not been done in the framework of the thesis are first: we wanted a base set of results covering a wide parameter range and computed at the same mesh resolution used in the former Ph.D. thesis by S.M. Taghavi [123], on nearly horizontal displacements. Secondly, due to the intensive computational time cost of fine-resolution simulations, it was not feasible to run/analyse all simulations using both the regular mesh and the fine mesh. Upon comparison with very fine-mesh results, it was found that many important general features of the flow are not significantly affected by mesh refinement. These features are instantaneous/non-instantaneous classification, periodic front velocity characteristic, front detachment, spike-like tip, repetitive temporary back flow, viscous/inertial transitions, diffusive/non-diffusive classifications etc. However, it was found that the error in front velocity can be of order $5-12\%$ and the macroscopic diffusion coefficient can be affected too. We recommend choosing a much finer mesh size along with a much longer channel geometry to better assess the channel displacement flows.

From the mathematical modeling point of view the current weighted residual model also has some limitations. For instance the assumption that the streamwise velocities should be much larger than those in depthwise direction $u \gg v$ will not be valid at the very tip of the displacement front where shock-like gradients normally appear. The reasonable agreement obtained

from comparison of the front velocities and interface height profiles in the presence of inertia suggests that the frontal shock-like region does not affect the global features of the flow dramatically. Secondly, in our linear stability analysis of the equations we have assumed the long wavelength limit (also implicit in the derivation). We are not sure if short-wavelength perturbations might affect the flow stability in some situations. A more comprehensive study could be conducted considering the effect of short wavelength by comparing both Orr-Sommerfeld and weighted residual approaches.

8.3.2 Experimental perspectives

Considering the work in this thesis and the previous thesis on nearly horizontal displacement flows, [123], approximately 1000 displacement flow experiments have been run using this experimental apparatus. Although considerable, the reality is that when we consider the full range of industrial fluids and flows, a large number of dimensionless parameters govern the flow physics: 1000 experiments still leaves a lot of unanswered questions. To begin to redress the gaps in our knowledge, the following studies would be useful.

- Newtonian density stable displacements in the presence of a viscosity ratio. It would be very interesting to see how the viscosity ratio m can modify the stretch length predictive formula ($L = \tan\beta - 3680/\chi$) obtained previously for the iso-viscous case. The density stable displacements were found to be the least challenging to analyze and meanwhile the most robust experiments to run due to the simple form that the interface takes over time. More generally, the majority of our data to date concerns density unstable displacements and it would be of interest to extend the density stable data set in any direction.

- Newtonian density unstable displacements in the presence of viscosity ratio. In the industrial applications iso-viscous displacements do not occur and it is of interest to understand viscosity ratio effects on the front velocity, displacement efficiency and on the stabilizing/destabilizing effect of the mean flow, as well as the eventual transition to mixed regimes. In near-horizontal displacements, some viscosity ratio experiments have been performed, as described in [124], but for a wider range of pipe inclinations we still have no insights as to the effects.

- Shear-thinning displacement flows in density stable/unstable configurations. Whereas we have studied viscoplastic fluid displacements

in the extreme case of a very large yield stress, the majority of non-Newtonian fluids pumped in oil well cementing also have shear-thinning rheologies and are pumped down the casing at flow rates for which yield stress effects are not dominant. The effects of shear-thinning rheologies at different pipe inclinations are essentially unknown. A limited number of experiments were performed using Xanthan-water solutions in [124], but these were focused at near-horizontal pipe inclinations.

- Using Particle Image Velocimetry (PIV), Laser Induced Florescence (LIF) and 3D Ultrasound Doppler Velocimetry (UDV) to enhance the quality of the experimental data. In this thesis we have taken advantage of back-lit images of the flow field with high speed cameras and have also used 1D Ultrasound Doppler Velocimetry (UDV). The back-lit technique implies a form of averaging is carried out when we study the local concentrations of the mixed fluids, i.e. through the thickness of the pipe. Our image processing has also been largely focused at describing bulk properties of the displacement flows.

  It is clear that a lot of detailed data describing the flow physics could be measured and analysed from this style of experiment. In order to study the concentration field with a higher resolution, the use of LIF is advised. A similar study where this has been done is [113]. It is worth noting that in the course of the thesis we also ran some test experiments using a LASERGLOW 532 nm Diode-pumped solid-state (DPSS) laser of 300 mW power and by adding fluoroscein to the solutions. The preliminary results were satisfactory but could not be further analyzed due to the time constraints of the thesis study. We recommend to to improve the LIF technique and establish this as a main measurement technique, while also developing a PIV technique for high resolution velocity field data. Our displacement velocities are mostly modest.

  As mentioned before, in our experiments to date we have used a 1D UDV technique, with a single ultrasound probe. This gives only the streamwise velocity component. In order to get 3D velocity components, 2 more probes have to be added to the system. Note that the advantage of PIV over the UDV technique is that the former is able to get velocity field data in a sheet across the pipe (covering a wider streamwise and depthwise distance) whereas the UDV gives only local velocity measurements within a volume at a given streamwise position. In practice both techniques should be developed and targeted at flow

features where significant 3D effects are seen.

8.3.3 Numerical simulation perspectives

About 180 simulations were run using the code PELICANS. This study only covered iso-viscous Newtonian displacements. The code PELICANS is able to simulate the displacement of two generalized Newtonian fluids of Herschel-Bulkley type. As discussed earlier for any future study we suggest a much longer computational domain to capture the long time dynamics (or potentially a moving domain of limited length) and a finer mesh to capture small scale flow features associated with instability and mixing.

There are many potential studies that could usefully be carried, approximately covering a similar range of flows as proposed above for future experimental studies. For example: density stable displacements, Newtonian viscosity ratio displacements and shear-thinning fluid displacements (all with density unstable configurations) would all make sense. It would also be of interest to study displacement of yield stress fluids, to see if some of the complex and exotic flows we have observed experimentally could be found computationally.

In parallel with the suggestion to perform more detailed 3D experimental analyses of these flows, it would be of interest to develop 3D numerical simulations of pipe (and channel) flow displacements, to run on large parallel computational machines. Certainly, within the non-Newtonian fluid context these studies would be unique.

8.3.4 Mathematical modeling perspectives

Simplified mathematical models can be extremely useful in both process design and also in directing the experimental/numerical programs, as well as interpreting results. Ideally, such models should give reasonable predictions of bulk flow quantities (e.g. interface height, front velocity, bulk axial diffusivity, etc.) at a much lower computational/experimental cost. Some areas where further analytical work could be useful include the following.

- A simple mathematical model to estimate the stretch length in the case of density stable flows would be useful. The curious fact is that although our experimental data suggests that primarily the balance of viscous and buoyancy forces act to govern the stretch length, the lubrication model in [128] (which is based on this force balance) fails to predict a constant stretch length. Perhaps further velocity field

measurements from the experiments and/or numerical simulations can suggest alternative ways of modeling this flow.

- The weighted residual model that we have developed could be extended in a number of ways. Firstly, in the presence of a yield stress the linear stability analysis is only valid if the yield stress fluid layer is fully yielded. This restriction could be removed. Secondly, the same method could easily be developed for core-annular pipe (displacement) flows. These flows exhibit a number of interesting instabilities that have been studied recently, e.g. [39, 56]. Thirdly, if we wished to compare more directly against our numerical results from PELICANS it would be useful to extend the two-layer channel geometry formulation to a three-layer system, mimicking the tendency of the displacing fluid to advance along the channel centre. Note that the stability analysis carried in chapter 6 is only valid in linear limit (very small perturbation). It is not clear that non-linear analysis would add to our understanding. However, we have looked at non-linear perturbations numerically. Extending the weighted residual model from 2D to 3D can be quite challenging but will also be useful if carried out, specially when it comes to interpreting the two and/or three dimensional instability patterns.

- With respect to the results on unstable displacements that we have presented in the $(Fr, Re\cos\beta/Fr)$-plane, we have identified 3 domains: viscous, inertial and fully mixed. The weighted residual method is targeted at understanding the transition from a structured viscous flow to an inertial flow, at the inset of instability. We have however very little modeling work targeted at the inertial regime itself. Here we have largely relied on experimental correlations, motivated by dimensional analysis, fitted to our experimental results.

  Firstly, it would be interesting to try to develop a more predictive model of the inertial regime. A starting point could be Benjamin's classical study [15] of gravity currents, extended to include a mean flow and two (possibly counter-current) fluid streams. Hopefully this could result in predictions of the front velocities in the inertial non-diffusive regimes where the weak mean flow is mostly affected by the exchange component. Secondly, it would be interesting to see if this type of theory could be analysed to predict conditions for the transition to the fully mixed regime. Thirdly, it would be of value to understand how these theories are modified by weak viscous effects. If these (largely

inertial) flows are independent of fluid rheology, then from a practical perspective process design is greatly simplified.

Bibliography

[1] K. Alba, P. Laure, and R.E. Khayat, *Transient two-layer thin-film flow inside a channel.*, Phys. Rev. E **84** (2011), 026320.

[2] K. Alba, S.M. Taghavi, and I.A. Frigaard, *Miscible density-stable displacement flows in inclined tube*, Phys. Fluids **24** (2012), 123102.

[3] ———, *Miscible density-unstable displacement flows in inclined tubes*, accepted for publication, to appear in Phys. Fluids (2012).

[4] J.R.L. Allen, *Mixing at turbidity current heads, and its geological implications*, J. Sed.Res. **41** (1971).

[5] M. Allouche, I.A. Frigaard, and G. Sona, *Static wall layers in the displacement of two visco-plastic fluids in a plane channel*, J. Fluid Mech. **424** (2000), 243–277.

[6] M. Amaouche, A. Djema, and H.A. Abderrahmane, *Film flow for power-law fluids: Modeling and linear stability*, Eur. Phys. J. B **34** (2012), 70–84.

[7] M. Amaouche, A. Djema, and L. Bourdache, *A modified Shkadov's model for thin film flow of a power law fluid over an inclined surface*, C.R. Mecanique **337** (2009), 48–52.

[8] M. Amaouche, N. Mehidi, and N. Amatousse, *Linear stability of a two-layer film flow down an inclined channel: A second-order weighted residual approach*, Phys. Fluids **19** (2007), 084106.

[9] R. Aris, *On the dispersion of a solute in a fluid flowing through a tube*, Proc. Roy. Soc. **A235** (1956), 67–78.

[10] Baldwin L. Atesmen, K. and R. Haberstroh, *The dispersion of matter in turbulent pipe flows*, ASME J. Basic Engng **13** (1971), 461–477.

[11] R. Balasubramaniam, N. Rashidnia, T. Maxworthy, and J. Kuang, *Instability of miscible interfaces in a cylindrical tube*, Phys. Fluids **17** (2005), 052103.

[12] N.J. Balmforth and J.J. Liu, *Roll waves in mud*, J. Fluid Mech. **519** (2004), 33–54.

[13] G.K. Batchelor and J.M. Nitsche, *Instability of stationary unbounded stratified fluid*, J. Fluid Mech. **227** (1991), 357–391.

[14] P. Beghin, E.J. Hopfinger, and R.E. Britter, *Gravitational convection from instantaneous sources on inclined boundaries*, **107** (1981), 407–422.

[15] T.B. Benjamin, *Gravity currents and related phenomena*, J. Fluid Mech. **31** (1968), 209–248.

[16] V.K. Birman, B.A. Battandier, E. Meiburg, and P.F. Linden, *Lock-exchange flows in sloping channels*, J. Fluid Mech. **577** (2007), 53–77.

[17] K.B. Bischoff and O. Levenspiel, *Fluid dispersion-generalization and comparison of mathematical models-I generalization of models*, Chem. Eng. Sc. **17** (1962), 245–255.

[18] ———, *Fluid dispersiongeneralization and comparison of mathematical models-II comparison of models*, Chem. Eng. Sc. **17** (1962), 257–264.

[19] H. Brenner, *Dispersion resulting from flow through spatially periodic porous media*, Phil. Trans. Roy. Soc. **A297** (1980), 81–133.

[20] R.E. Britter and P.F. Linden, *The motion of the front of a gravity current travelling down an incline*, J. Fluid Mech. **99** (1980), 531–543.

[21] R.E. Britter and J.E. Simpson, *Experiments on the dynamics of a gravity current head*, J. Fluid Mech. **88** (1978), 223–240.

[22] B. Brunone and A. Berni, *Wall Shear Stress in Transient Turbulent Pipe Flow by Local Velocity Measurement*, J. Hydraul. Eng-ASCE **136** (2010), 716–726.

[23] M.I. Cantero, J.R. Lee, S. Balachandar, and M.H. Garcia, *On the front velocity of gravity currents*, J. Fluid. Mech. **586** (2007), 1.

[24] M.E. Charles and L.U. Lilleleht, *An experimental investigation of stability and interfacial waves in co-current flow of two liquids*, J. Fluid Mech. **22** (1965), 217–224.

[25] F. Charru and J. Fabre, *Long waves at the interface between two viscous fluids*, Phys. Fluids **6** (1994), 1223–1235.

[26] P.C. Chatwin and P.J. Sullivan, *The effect of aspect ratio on longitudinal diffusivity in rectangular channels*, J. Fluid Mech. **120** (1982), 347–358.

[27] C.-Y. Chen and E. Meiburg, *Miscible displacements in capillary tubes. part 2. numerical simulations*, J. Fluid Mech. **326** (1996), 57–90.

[28] G.K. Christian and P.J. Fryer, *The effect of pulsing cleaning chemicals on the cleaning of whey protein deposits*, Trans. IChemE C **84** (2006), 320–328.

[29] A.W. Cook and P.E. Dimotakis, *Transition stages of Rayleigh-Taylor instability between miscible fluids*, J. Fluid Mech. **443** (2001), 69–99.

[30] Canadian Broadcasting Corporation, *The BP oil spill, by the numbers*, Website; http://www.cbc.ca/news/world/story/2010/10/19/f-bp-oil-spill-numbers.html (2010).

[31] S.B. Dalziel, P.F. Linden, and D.L. Youngs, *Self-similarity and internal structure of turbulence induced by Rayleigh-Taylor instability*, J. Fluid Mech. **399** (1999), 1–48.

[32] S.B. Dalziel, M.D. Patterson, C.P. Caulfield, and I.A. Coomaraswamy, *Mixing efficiency in high-aspect-ratio Rayleigh-Taylor experiments*, Phys. Fluids **20** (2008), 065106–065114.

[33] M. Debacq, V. Fanguet, J.P. Hulin, D. Salin, and B. Perrin, *Self similar concentration profiles in buoyant mixing of miscible fluids in a vertical tube*, Phys. Fluids **13** (2001), 3097–3100.

[34] M. Debacq, J.P. Hulin, D. Salin, B. Perrin, and E.J. Hinch, *Buoyant mixing of miscible fluids of varying viscosities in vertical tube*, Phys. Fluids **15** (2003), 3846–3855.

[35] G. Dimonte and M. Schneider, *Density ratio dependence of Rayleigh-Taylor mixing for sustained and impulsive acceleration histories*, Phys. Fluids **12** (2000), 304.

[36] G. Dimonte, D.L. Youngs, A. Dimits, S. Weber, M. Marinak, S. Wunsch, C. Garasi, A. Robinson, M.J. Andrews, P. Ramaprabhu, et al., *A comparative study of the turbulent Rayleigh-Taylor instability using*

high-resolution three-dimensional numerical simulations: the alpha-group collaboration, Phys. Fluids **16** (2004), 1668.

[37] M. d'Olce, *Instabilités de cisaillement dans lécoulement concentrique de deux fluides miscibles*, Ph.D. thesis, These de l'Universite Pierre et Marie Curie, Orsay, France, 2008.

[38] M. d'Olce, J. Martin, N. Rakotomalala, and D. Salin, *Pearl and mushroom instability patterns in two miscible fluids core annular flows.*, Phys. Fluids **20** (2008), 024104.

[39] M. d'Olce, J. Martin, N. Rakotomalala, D. Salin, and L. Talon, *Convective/absolute instability in miscible core-annular flow. part 1. experiments.*, J. Fluid Mech. **618** (2009), 305–322.

[40] M.R. Doshi, P.M. Daiya, and W.N. Gill, *Three dimensional laminar dispersion in open and closed rectangular conduits*, Chem. Eng. Sc. **33** (1978), 795–804.

[41] PG Drazin, *Introduction to hydrodynamic stability*, Introduction to Hydrodynamic Stability, by PG Drazin, pp. 276. ISBN 0521804272. Cambridge, UK: Cambridge University Press, September 2002. **1** (2002).

[42] K. Ekambara and J.B. Joshi, *Axial mixing in pipe flows: turbulent and transition regions*, Chem. Eng. Sc. **58** (2003), 2715–2724.

[43] J.W. Elder, *The dispersion of marked fluid in turbulent shear flow*, J. Fluid Mech. **5** (1959), 544–560.

[44] M.E. Erdogan and P.C. Chatwin, *The effects of curvature and buoyancy on the laminar dispersion of solute in a horizontal tube*, J. Fluid Mech. **29** (1967), 6.

[45] J. Fernandez, P. Kurowski, P. Petitjeans, and E. Meiburg, *Density-driven unstable flows of miscible fluids in a Hele-Shaw cell*, J. Fluid Mech. **451** (2002), 239–260.

[46] H.J.S. Fernando, *Turbulent mixing in stratified fluids*, Ann. Rev. Fluid Mech. **23** (1991), 455–493.

[47] L.F. Flint and P. Eisenklam, *Longitudinal gas dispersion in transitional and turbulent flow through a straight tube*, Can. J. Chem. Eng. **47** (1969), 101–106.

[48] Carneiro de Araujo J. Freitas Rachid, F. and R. Baptista, *Predicting mixing volumes in serial transport in pipelines*, J. Fluids. Eng. **124** (2002), 528–534.

[49] I.A. Frigaard, *Stratified exchange flows of two Bingham fluids in an inclined slot*, J. non-Newt. Fluid Mech. **78** (1998), 61–87.

[50] ———, *Super-stable parallel flows of multiple visco-plastic fluids*, J. non-Newt. Fluid Mech. **100** (2001), 49–75.

[51] I.A. Frigaard and J.P. Crawshaw, *Preventing buoyancy-driven flows of two Bingham fluids in a closed pipe – fluid rheology design for oilfield plug cementing*, J. Eng. Math. **36** (1999), 327–348.

[52] I.A. Frigaard, S.D. Howison, and I.J. Sobey, *On the stability of poiseuille flow of a Bingham fluid.*, J. Fluid Mech. **263** (1994), 133–150.

[53] I.A. Frigaard and C. Nouar, *On three-dimensional linear stability of poiseuille flow of Bingham fluids.*, Phys. Fluids **15** (2003), 2843–2851.

[54] I.A. Frigaard and O. Scherzer, *The effects of yield stress variation on uniaxial exchange flows of two Bingham fluids in a pipe*, SIAM J. Appl. Math. **60** (2000), 1960–1976.

[55] C. Gabard, *Etude de la stabilité de films liquides sur les parois d'une conduite verticale lors de l'ecoulement de fluides miscibles non-Newtoniens*, Ph.D. thesis, These de l'Universite Pierre et Marie Curie, Orsay, France, 2001.

[56] C. Gabard and J.-P. Hulin, *Miscible displacements of non-Newtonian fluids in a vertical tube*, Eur. Phys. J. E **11** (2003), 231–241.

[57] R. Glowinski and P. Le Tallec, *Augmented Lagrangian and operator-splitting methods in nonlinear mechanics*, Phys. Fluids **19** (2007), 084106.

[58] N. Goyal, H. Pichler, and E. Meiburg, *Variable density, miscible displacements in a vertical Hele-Shaw cell: linear stability*, J. Fluid Mech. **584** (2007), 357372.

[59] I. Grants, C. Zhang, S. Eckert, and G. Gerbeth, *Experimental observation of swirl accumulation in a magnetically driven flow*, J. Fluid Mech. **616** (2008), 135–152.

[60] I.A. Gutowski, D. Lee, J.R. de Bruyn, and B.J. Frisken, *Scaling and mesostructure of carbopol dispersions*, Rheologica acta (2012), 1–10.

[61] E. Guyon and J.-P. Hulin, *Ce que disent les fluides*, Belin. Pour la science, 2006.

[62] Y. Hallez and J. Magnaudet, *Effects of channel geometry on buoyancy-driven mixing*, Phys. Fluids **20** (2008), 053306.

[63] ———, *A numerical investigation of horizontal viscous gravity currents*, J. Fluid. Mech. **630** (2009), 71–91.

[64] ———, *Turbulence-induced secondary motion in a buoyancy-driven flow in a circular pipe*, Phys. Fluids **21** (2009), 081704.

[65] V.G. Harris, J.A.H. Graham, and S. Corrsin, *Further experiments in nearly homogeneous turbulent shear flow*, J. Fluid Mech. **81** (1977), 657–687.

[66] T.I. Hesla, F.R. Pranckh, and L. Preziosi, *Squire's theorem for two stratified fluids*, Phys. Fluids **29** (1986), 2808–2811.

[67] C.E. Hickox, *Instability due to viscosity and density stratification in axisymmetric pipe flow*, Phys. Fluids **14** (1971), 251.

[68] A.P. Hooper, *Long-wave instability at the interface between two viscous fluids: Thin layer effects*, Phys. Fluids **28** (1985), 1613.

[69] A.P. Hooper and W.G.C. Boyd, *Shear-flow instability at the interface between two viscous fluids*, J. Fluid Mech. **128** (1983), 507–528.

[70] A.P. Hooper and R. Grimshaw, *Nonlinear instability at the interface between two viscous fluids*, Phys. Fluids **28** (1985), 37.

[71] S. Hormozi, K. Wielage-Burchard, and I.A. Frigaard, *Entry, start up and stability effects in visco-plastically lubricated pipe flows*, J. Fluid Mech. **673** (2011), 432–467.

[72] ———, *Multi-layer channel flows with yield stress fluids*, J. Non-Newt. Fluid Mech. **166** (2011), 262–278.

[73] P.D. Howell, S.L. Waters, and J.B. Grotberg, *The propagation of a liquid bolus along a liquid-lined flexible tube*, J. Fluid Mech. **406** (2000), 309–335.

[74] C.K. Huen, I.A. Frigaard, and D.M. Martinez, *Experimental studies of multi-layer flows using a visco-plastic lubricant*, J. non-Newt. Fluid Mech. **142** (2007), 150–161.

[75] C. Jiao and T. Maxworthy, *An experimental study of miscible displacement with gravity-override and viscosity-contrast in a Hele-Shaw cell*, Exp. Fluids **44** (2008), 781–794.

[76] D.D. Joseph, M. Renardy, and Y. Renardy, *Instability of the flow of two immiscible liquids with different viscosities in a pipe*, J. Fluid Mech. **141** (1984), 309–17.

[77] T.W. Kao and C. Park, *Experimental investigations of the stability of channel flows. part 2. two-layered co-current flow in a rectangular channel*, J. Fluid Mech. **52** (1972), 401–423.

[78] B. Khomami, *Interfacial stability and deformation of two stratified power law fluids in plane poiseuille flow Part I. Stability analysis* , J. non-Newt. Fluid Mech. **36** (1990), 289–303.

[79] J. Kuang, T. Maxworthy, and P. Petitjeans, *Miscible displacements between silicone oils in capillary tubes*, Eur. J. Mech.- B Fluids **22** (2008), 271–277.

[80] J. Kuang, P. Petitjeans, and T. Maxworthy, *Velocity fields and streamline patterns of miscible displacements in cylindrical tubes*, Exp. Fluids **37** (2004), 301–308.

[81] E. Lajeunesse, J. Martin, N. Rakotomalala, D. Salin, and Y. Yortsos, *Miscible displacement in a* H*ele* S*haw cell at high rates*, J. Fluid Mech. **398** (1999), 299–319.

[82] R.J. LeVeque, *Finite volume methods for hyperbolic problems*, vol. 31, Cambridge university press, 2002.

[83] R.J. Lowe, P.F. Linden, and J.W. Rottman, *A laboratory study of the velocity structure in an intrusive gravity current*, J. Fluid Mech. **456** (2002), 33–48.

[84] R.J. Lowe, J.W. Rottman, and P.F. Linden, *The non-boussinesq lock-exchange problem. part 1. theory and experiments*, J. Fluid Mech. **537** (2005), 101–124.

[85] N. Mehidi and N. Amatousse, *Modélisation dun écoulement coaxial en conduite circulaire de deux fluides visqueux*, C.R. Mecanique **337** (2009), 112–118.

[86] M. Mishra, A. De Wit, and K.C. Sahu, *Double diffusive effects on pressure-driven miscible displacement flows in a channel*, J. Fluid Mech. **1** (2012), 1–19.

[87] M. Moyers-Gonzalez, K. Alba, S.M. Taghavi, and I.A. Frigaard, *A semi-analytical closure approximation for pipe flows of two Herschel-Bulkley fluids with a stratified interface*, J. non-Newt. Fluid Mech. **193** (2013), 49–67.

[88] M.A. Moyers-Gonzalez, I.A. Frigaard, and C. Nouar, *Nonlinear stability of a visco-plastically lubricated viscous shear flow*, J. Fluid Mech. **506** (2004), 117–146.

[89] E.B. Nelson and D. Guillot, *Well cementing, 2nd edition*, Schlumberger Educational Services, 2006.

[90] M.K.A. Neophytou and R.E. Britter, *A simple model for the movement of fire smoke in a confined tunnel*, Pure and Applied Geophysics **162** (2005), 1941–1954.

[91] C. Nouar, A. Bottaro, and J.-P. Brancher, *Delaying transition to turbulence in channel flow: revisiting the stability of shear-thinning fluids*, J. Fluid Mech. **592** (2007), 177–194.

[92] R.J. Nunge and W.N. Gill, *Mechanisms affecting dispersion and miscible displacement*, Ind. Eng. Chem. **61** (1969), 33–49.

[93] P. Petitjeans and T. Maxworthy, *Miscible displacements in capillary tubes. part 1. experiments*, J. Fluid Mech. **326** (1996), 37–56.

[94] A. Pinarbasi and A. Liakopoulos, *Stability analysis of interafaces in two-layer, inelastic-fluid flows: Applications to coextrusion processes*, ASME, HTD **259** (1993), 113–125.

[95] L. Prandtl and O.G. Tietjens, *Applied hydro-and aeromechanics*, vol. 2, Dover publications, 1957.

[96] N. Rakotomalala, D. Salin, and P. Watzky, *Miscible displacement between two parallel plates:* BGK *lattice gas simulations*, J. Fluid Mech. **338** (1997), 277–297.

[97] N.S. Reejhsinghani, A.J. Barduhn, and W.N. Gill, *Laminar dispersion in capillaries: Part v. experiments on combined natural and forced convection in vertical tubes*, AIChE J. **14** (2004), 100–109.

[98] N.S. Reejhsinghani, W.N. Gill, and A.J. Barduhn, *Laminar dispersion in capillaries: Part iii. experiments in horizontal tubes including observations on natural convection effects*, AIChE J. **12** (1966), 916–921.

[99] Y. Renardy, *Instability at the interface between two shearing fluids in a channel*, Phys. Fluids **28** (1985), 3441–3443.

[100] O. Reynolds, *An experimental investigation of the circumstances which determine whether the motion of water shall be direct or sinuous, and of the law of resistance in parallel channels.*, Proc. Roy. Soc. **35** (1883), 84–99.

[101] A.N. Ross, P.F. Linden, and S.B. Dalziel, *A study of three-dimensional gravity currents on a uniform slope*, J. Fluid Mech. **453** (2002), 239–261.

[102] C. Ruyer-Quil, S. Chakrabortya, and B.S. Dandapata, *Wavy regime of a power-law film flow*, J. Fluid. Mech. **692** (2012), 220–256.

[103] C. Ruyer-Quil and P. Manneville, *Modeling film flows down an inclined planes*, Eur. Phys. J. B **6** (1998), 277292.

[104] ———, *Improved modeling of flows down inclined planes*, Eur. Phys. J. B **15** (2000), 357–369.

[105] F.L. Sabins, *Problems in cementing horizontal wells*, J. Petrol. Tech. **42** (1990), 398–400.

[106] K.C. Sahu, H. Ding, P. Valluri, and O.K. Matar, *Pressure-driven miscible two-fluid channel flow with density gradients*, Phys. Fluids **21** (2009), 043603.

[107] K.C. Sahu, P. Valluri, P.D.M Spelt, and O.K. Matar, *Linear instability of pressure-driven channel flow of a Newtonian and a Herschel-Bulkley fluid*, Phys. Fluids **19** (2007), 122101.

[108] G. Schramm, *Introduction to practical viscometry*, Haake Buchler. Int., Inc., 1981.

[109] J. Scoffoni, E. Lajeunesse, and G.M. Homsy, *Interface instabilities during displaceemnts of two miscible fluids in a vertical pipe*, Phys. Fluids **13** (2001), 553–556.

[110] T. Seon, *Du mélange turbulent aux courants de gravité en géométrie confinée*, Ph.D. thesis, Université Pierre et Marie Curie-Paris VI, 2006.

[111] T. Seon, J.-P. Hulin, D. Salin, B. Perrin, and E.J. Hinch, *Buoyant mixing of miscible fluids in tilted tubes*, Phys. Fluids **16** (2004), L103–L106.

[112] ———, *Buoyancy driven miscible front dynamics in tilted tubes*, Phys. Fluids **17** (2005), 031702.

[113] ———, *Laser-induced fluorescence measurements of buoyancy driven mixing in tilted tubes*, Phys. Fluids **18** (2006), 041701.

[114] T. Seon, J. Znaien, D. Salin, J.-P. Hulin, E.J. Hinch, and B. Perrin, *Front dynamics and macroscopic diffusion in buoyant mixing in a tilted tube*, Phys. Fluids **19** (2007), 125105.

[115] ———, *Transient buoyancy-driven front dynamics in nearly horizontal tubes*, Phys. Fluids **19** (2007), 123603.

[116] D.H. Sharp, *An overview of Rayleigh-Taylor instability*, Physica D: Nonlinear Phenomena **12** (1984), 3–18.

[117] J.O. Shin, S.B. Dalziel, and P.F. Linden, *Gravity currents produced by lock exchange*, J. Fluid Mech. **521** (2004), 1–34.

[118] V.Y. Shkadov, *Wave modes in the flow of thin layer of a viscous liquid under the action of gravity*, Izv. Akad. Nauk SSSR, Mekh. Zhidk. **Gaza 1** (1967), 43–51.

[119] J.E. Simpson and R.E. Britter, *The dynamics of the head of a gravity current advancing over a horizontal surface*, J. Fluid Mech. **94** (1979), 477–495.

[120] J.V. Smith and J.J. Perona, *Axial mixing of fluids in turbulent flow through concentric annuli*, Ind. Eng. Chem. **8** (1969), 621–625.

[121] R. Smith, *Easy-to-use formula for contaminant dispersion*, J. Fluid Mech. **215** (1990), 195–207.

[122] Y.Y. Su and B. Khomami, *Stability of multilayer power law and second-order fluids in plane poiseuille flow*, Chem. Eng. Comm. **109** (1991), 209–223.

[123] S.M. Taghavi, *From displacement to mixing in a slightly inclined duct.*, (2011).

[124] S.M. Taghavi, K. Alba, and I.A. Frigaard, *Buoyant miscible displacement flows at moderate viscosity ratios and low Atwood numbers in near-horizontal ducts*, Chem. Eng. Sc. **69** (2012), 404–418.

[125] S.M. Taghavi, K. Alba, M. Moyers-Gonzalez, and I.A. Frigaard, *Incomplete fluid-fluid displacement of yield stress fluids in near-horizontal pipes: experiments and theory*, J. non-Newt. Fluid Mech. **167-168** (2012), 59–74.

[126] S.M. Taghavi, K. Alba, T. Seon, K. Wielage-Burchard, D.M. Martinez, and I.A. Frigaard, *Miscible displacement flows in near-horizontal ducts at low Atwood number*, J. Fluid Mech. **696** (2012), 175–214.

[127] S.M. Taghavi and I.A. Frigaard, *Estimation of mixing volumes in buoyant miscible displacement flows along near-horizontal pipes*, Can. J. Chem. Eng. **91** (2013), 399–411.

[128] S.M. Taghavi, T. Seon, D.M. Martinez, and I.A. Frigaard, *Buoyancy-dominated displacement flows in near-horizontal channels: the viscous limit.*, J. Fluid Mech. **639** (2009), 1–35.

[129] ———, *Influence of an imposed flow on the stability of a gravity current in a near horizontal duct.*, Phys. Fluids **22** (2010), 031702.

[130] S.M. Taghavi, T. Seon, K. Wielage-Burchard, D.M. Martinez, and I.A. Frigaard, *Stationary residual layers in buoyant Newtonian displacement flows.*, Phys. Fluids **23** (2011), 044105.

[131] S. Tavoularis and S. Corrsin, *Experiments in nearly homogeneous turbulent shear flow with a uniform mean temperature gradient. part 1*, J. Fluid Mech. **104** (1981), 1–347.

[132] S. Tavoularis and U. Karnik, *Further experiments on the evolution of turbulent stresses and scales in uniformly sheared turbulence*, J. Fluid Mech. **204** (1989), 457–478.

[133] G. Taylor, *Conditions under which dispersion of a solute in a stream of solvent can be used to measure molecular diffusion*, Proc. Roy. Soc. **A225** (1954), 473–477.

[134] ———, *The dispersion of matter in turbulent flow through a pipe*, Proc. Roy. Soc. **A223** (1954), 446–468.

[135] G. I. Taylor, *Dispersion of soluble matter in a solvent flowing slowly through a tube*, Proc. Roy. Soc. **A219** (1953), 186–203.

[136] S.A. Thorpe, *A method of producing a shear flow in a stratified fluid*, J. Fluid Mech. **32** (1968), 693–704.

[137] ———, *Experiments on the instability of stratified shear flows: immiscible fluids*, J. Fluid Mech. **39** (1969), 25–48.

[138] ———, *Experiments on the instability of stratified shear flows: miscible fluids*, J. Fluid Mech. **46** (1971), 299–319.

[139] ———, *Experiments on instability and turbulence in a stratified shear flow*, J. Fluid Mech. **61** (1973), 731–751.

[140] L.J. Tichacek, C.H. Barkelew, and T. Baron, *Axial mixing in pipes*, AIChE J. **3** (1957), 439–442.

[141] G.A. Tickle, *A model of the motion and dilution of a heavy gas cloud released on a uniform slope in calm conditions*, J. Haz. Mat. **49** (1996), 29–47.

[142] B.S. Tilley, S.H. Davis, and S.G. Bankoff, *Linear stability theory of two-layer fluid flow in an inclined channel*, Phys. Fluids **6** (1994), 3906.

[143] ———, *Nonlinear long-wave stability of superposed fluids in an inclined channel*, J. Fluid Mech. **277** (1994), 55–83.

[144] G. Vinay, *Modélisation du redemarrage des écoulements de bruts parafiniques dans les conduites pétrolieres*, Ph.D. thesis, These de l'Ecole des Mines de Paris, Paris, France, 2005.

[145] O. Wanner, H.J. Eberl, E. Morgenroth, D. Noguera, C. Picioreanu, B.E. Rittmann, and M.C.M. Van Loosdrecht, *Mathematical modeling of biofilms.*, IWA Scientific and Technical Report Series,, vol. 18, IWA Publishing, ISBN 1843390876., 2006, pp. 1–199.

[146] D.T. Wasan and J. Dayan, *The dispersion of solute in turbulent pipe flow of non-Newtonian fluids*, Can. J. Chem. Eng. **48** (1970), 129–131.

[147] D.M. Webber, S.J. Jones, and D. Martin, *A model of the motion of a heavy gas cloud released on a uniform slope*, J. Haz. Mat. **33** (1993), 101–122.

[148] P. Wesseling, *Principles of computational fluid dynamics*, vol. 29, Springer, 2009.

[149] K. Wielage-Burchard and I.A. Frigaard, *Static wall layers in plane channel displacement flows*, J. non-Newt. Fluid Mech. **166** (2011), 245–261.

[150] _____, *Static wall layers in plane channel displacement flows*, J. Non-Newt. Fluid Mech. **166** (2011), 245–261.

[151] H.C. Yee, R.F. Warming, and A. Harten, *Implicit Total Variation Diminishing (TVD) Schemes for Steady-State Calculations*, J. Comput. Phys. **57** (1985), 327–360.

[152] S.G. Yiantsios and B.G. Higgins, *Linear stability of plane poiseuille flow of two superposed fluids*, Phys. Fluids **31** (1988), 3225–3238.

[153] C.-S. Yih, *Instability due to viscosity stratification*, J. Fluid Mech. **27** (1967), 337352.

[154] D.L. Youngs, *Modelling turbulent mixing by Rayleigh-Taylor instability*, Physica D: Nonlinear Phenomena **37** (1989), 270–287.

[155] J.Y. Zhang and I.A. Frigaard, *Dispersion effects in the miscible displacement of two fluids in a duct of large aspect ratio*, J. Fluid Mech. **549** (2006), 225–251.

[156] J. Znaien, F. Moisy, and J.-P. Hulin, *Flow structure and momentum transport for buoyancy driven mixing flows in long tubes at different tilt angles*, Phys. Fluids **23** (2011), 035105.

Appendix A

Research methodology

As stated earlier, in order to better understand the displacement flows we have taken three different approaches in this thesis, namely experimental, numerical and analytical. One of the most important parts of this study is through conducting dimensionally similar experiments in a small-scale laboratory apparatus. In the following section we will go over the details of the apparatus used and the experimental approach taken to obtain high-quality data. The experiments run have been analyzed in chapters 3, 4 and 7. The experimental techniques section will be followed by explaining the numerical technique used as a second approach to the problem. The numerical simulations were studied in detail in chapter 5. The data from the experimental and numerical approaches is analyzed and combined with the analysis of simpler mathematical models. The methodology of the modeling approach is explained later in chapter 6 where the model is developed from scratch.

A.1 Experimental technique

The apparatus used in the current study is based on the same principle as the one used by S.M. Taghavi [123] for nearly-horizontal experiments. However due to the higher inclination angles, several modifications were required. These include the way the fluids are transported to the pipe, how some of the valves involved in the flow loop are operated, and the imaging technique used. Three main criteria considered for design and modification were performance, safety and economic factors. Figure A.1 shows the schematic of the experimental setup used. As can be seen a 4 (m) long pipe is set-up on an aluminum frame which can be tilted at any angle using a ball-screw jack. In order to accurately tilt the whole system at an angle β, a digital angle meter was adopted from SmartTool company capable of measuring to 0.1° accuracy. Two fish tanks were used to reduce light refraction errors. Inside the fish tanks a 19.05 (mm) diameter, transparent acrylic pipe is placed which is the main section of the apparatus. The space between fish tank and pipe walls is simply filled with water that has approximately the same light

refraction index as that of acrylic. The gate valve is located 80 (cm) from the top end. Two high-speed digital cameras (with 4096 gray-scale levels, Basler Scout scA1600 and scA1400) were employed to capture the images of the flow field in each fish tank. The fish tanks were back-lit using Light Emitting Diode (LED) stripes. An Ultrasound Doppler Velocimeter (UDV) probe was placed at the end of the first fish tank where access to the bare pipe was easier. Two first-surface mirrors were also added to the system, angled such that the top view images can also be recorded. For pumping the fluids into the flow loop, two acrylic pressurized tanks were built (see details later in §A.1.1). Before discharging the fluids to the drain the flow rate is recorded using a rotameter and a magnetic flow meter.

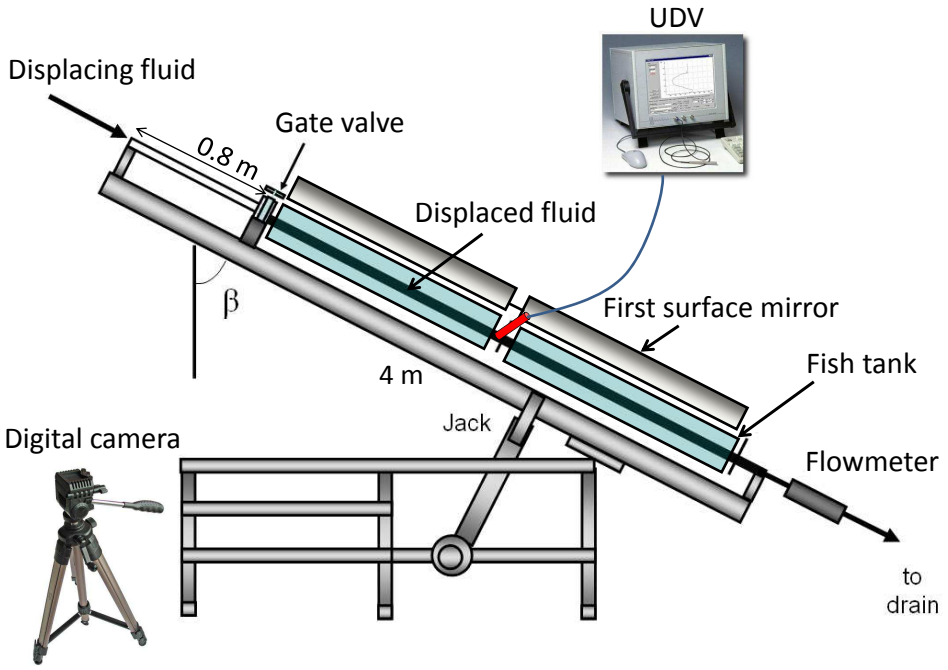

Figure A.1: Simplified schematic of the experimental apparatus used showing different parts and sections.

Figure A.2 shows an picture of the actual experimental setup used, with different parts marked on it for better understanding.

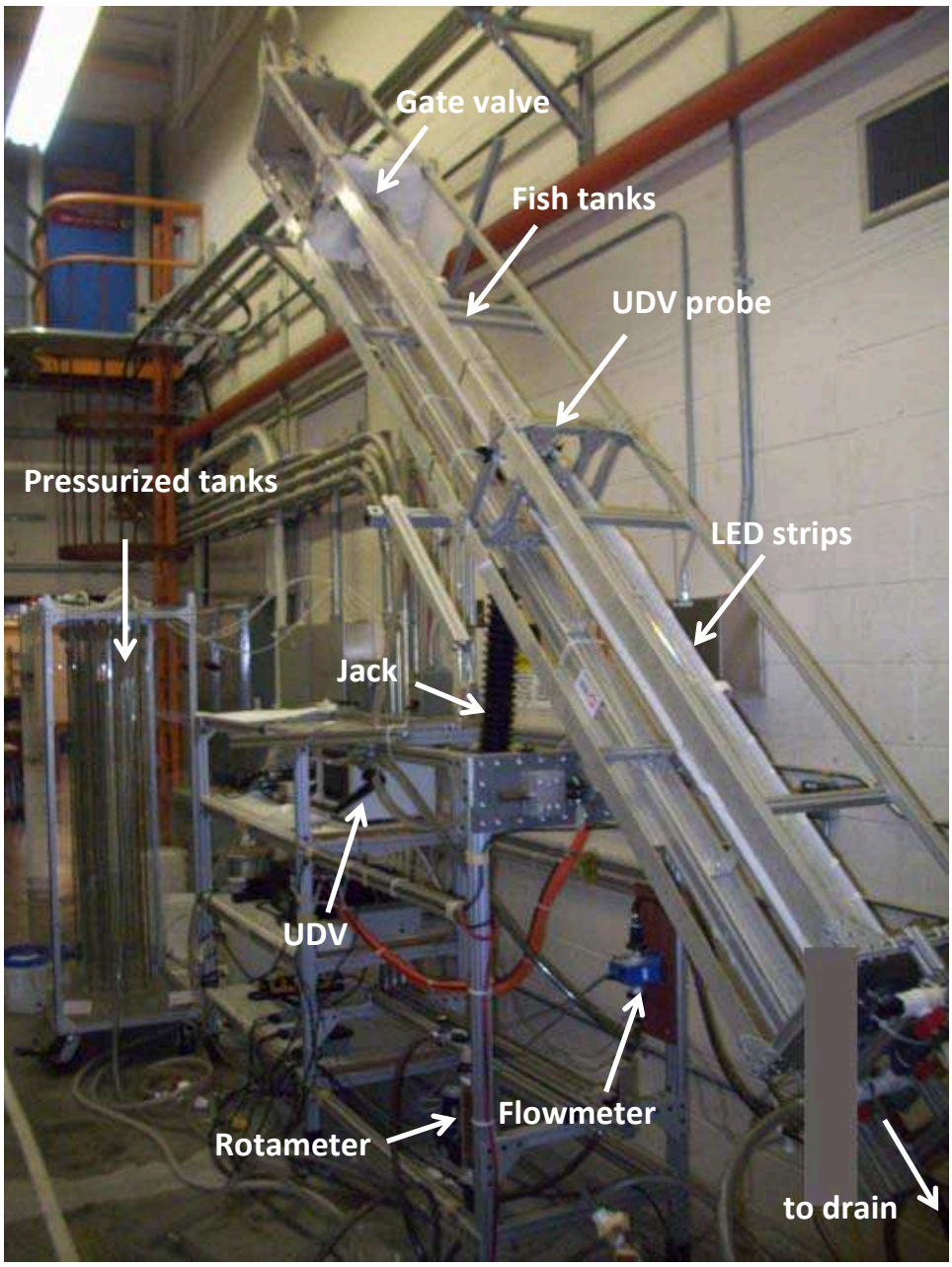

Figure A.2: The experimental setup used in the current project for running lab-scale experiments. The whole pipe system shown is tilted at an intermediate inclination angle. The length of the tilted pipe is 4 (m).

A.1.1 Fluid preparation and delivery

In this section we are going to explain how the solutions (either displacing or displaced fluids) were made and how they were transported into the flow loop. Most of the liquids used in the current thesis are water-based solutions.

For Newtonian fluids we simply used water and/or water-Glycerine solutions. In order to adjust the density difference and obtain the desired Atwood number, salt ($NaCl$) was added to the displacing liquid in the case of density unstable displacement, and to the displaced fluid in the case of density stable displacement. Within the range of salt concentrations added to the solutions the densities can change quite a bit while the viscosity of the solution remains largely unaffected; see [110]. To obtain higher viscosity (but still with a Newtonian fluid), glycerol solutions were prepared by diluting pure glycerol with water. We also added low concentrations of black non-waterproof ink to the displaced fluid in order to distinguish it from the displacing fluid. The low concentration of ink added did not significantly change either the density or viscosity of the fluid. The weight of the solutions and the amount of salt and ink to be added to them had to be measured carefully. For this we had to use three different scales with differing accuracies and maximum capacities. Figure A.3a shows the most accurate scale used in our experiments (Ohaus Corporation, Adventure Pro model) with accuracy of 0.001 (g) and maximum capacity of 51 (g). This scale was used for making small scale samples of solutions (usually with Carbopol powder) before deciding on the fluid to be used for the large scale experiment. In some cases the sodium hydroxide $NaOH$ needed for adding to the Carbopol solution was also measured with this scale. The second scale that was widely used for measuring the weight of the salt, ink and UDV particles in our experiments is shown in Fig. A.3b with readability of 0.1 (g) and capacity of 2400 (g) (from Acculab). The third scale used in the experimental study was for large scale solutions to be pumped into the flow loop and is shown in Fig. A.3c. The scale has readability of 1 (g) and the maximum capacity of 60 (kg) (from Sartorius).

Once the fluids, ink, salt etc. were weighted carefully they were mixed in a 40 L Polyvinyl Chloride (PVC) container using a mixer. The mixer and blade system used is shown in figure A.4. The mixer model used was EUROSTAR POWER made by IKA Werke company. For mixing the ink, salt, glycerine and UDV particles into the water-based solutions the mixer was set between $100 - 400$ (rpm) rotating for half an hour. In the case of yield stress fluid the procedure is a bit different and will be explained later in this section.

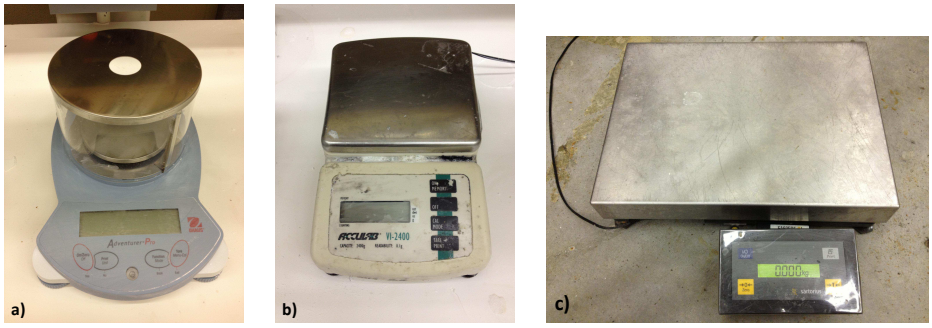

Figure A.3: The scales used in the experimental study a) 0.001 (g) readability and 51 (g) capacity b) 0.1 (g) readability and 2400 (g) capacity and c) 1 (g) readability and 60 (kg) capacity.

Figure A.4: The mixer-blade system used in the experimental study to prepare the displacing and displaced fluids solutions.

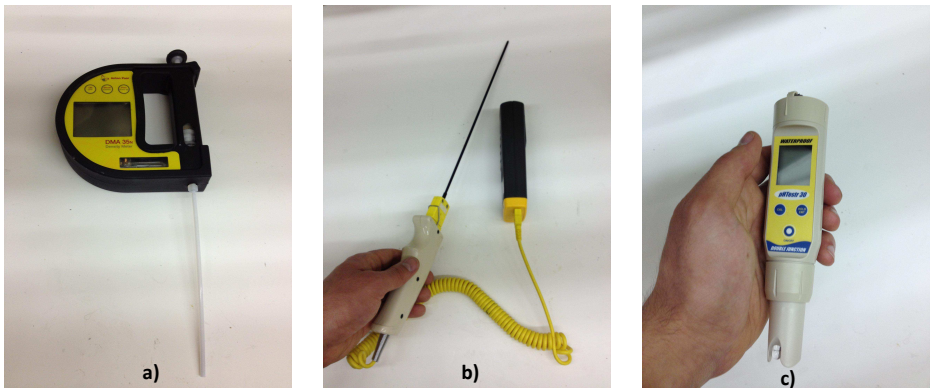

Figure A.5: a) The density meter b) thermometer and c) pH meter used in the experiments.

Once the solutions were mixed and just before transporting them into the acrylic pressurized tanks the density, temperature and pH of the fluids (in the case of viscoplastic fluids) were measured using digital density meter, thermometer and pH meter shown in figures A.5a-c respectively. The density meter used (Anton Paar, DMA 35N) had a resolution of 0.0001 (g/cm^3). The fluids densities were adjusted up to a point that the desired density difference (or Atwood number) was reached. The thermometer was an Omega mini thermocouple with resolution $\pm 0.1°C$. We recorded the temperature of the fluids in order to do the rheometry at the same condition later on, because the temperature can significantly affect the viscosity of the working fluids. The waterproof pH meter (pHTestr 30 model from Eutech instruments) can measure the pH range from 0 to 14 with an accuracy of ± 0.01 pH.

For our viscoplastic fluids, Carbopol EZ-2 polymer (Noveon Inc) was used. Carbopol is widely used as a thickener, suspending agent and stabilizer. It is utilized in a broad range of personal care products, pharmaceutical products and cleaners. Carbopol polymers are made of high molecular weight acrylic acid chains, usually cross-linked, and are available in the form of powder or liquid. The rheology of Carbopol is largely controlled by the concentration and pH of the solution. When we first mix Carbopol with water, it makes an acidic solution that has no yield stress. The yield stress is developed at intermediate pH upon neutralizing with a base agent, in our case $NaOH$. The neutralized solution is fairly transparent and has the same density as water (for low concentrations as is the case in this thesis).

In order to consistently make the Carbopol solutions, we followed the same procedure given below. According to the desired concentration and/or

yield stress, we first weighted Carbopol powder and then gradually added it to water while the blade was rotating and stirring the whole mixture. Carbopol molecules do not tend to accumulate in water thus making it easier to mix. Since the Carbopol concentration needed in our experiments was not too high, blade shape, its rotating speed and the mixing time was found to have negligible effect on rheometry. Note that in the case of Glycerine-water solutions the blade shape mixing speed and the mixing time did not have significant impact on the outcome viscosity either. The Carbopol-water solution is acidic (e.g. pH = 4 for a concentration 0.14 % (wt/wt)) and does not have any yield-stress. In order to make the gel we add Sodium-hydroxide, $NaOH$ to neutralize the acidic solution. For a given Carbopol solution, the neutralization takes place over a narrow range of $NaOH$ concentration. In other words, the weight-to-weight ratio of Carbopol to Sodium-hydroxide, at which the neutralisation occurs, is almost a constant and in our case was around 3.5. If too much and/or too little $NaOH$ is added to the Carbopol then the solution changes to liquid phase again. When neutralized, the gel has a pH of $6-8$ which is safe for human-related applications (e.g. hair gel). When adding $NaOH$ to Carbopol-water solution one should be very cautious about mixing and particularly the blade speed, to avoid entraining air bubbles into the gel-like solution. If the air bubbles become trapped within the solution, even with vacuum pumps it is very difficult to take them out because of the high viscosity of the yield-stress fluid.

We mixed Carbopol powder with water for 30 minutes at 400 (rpm). Then the Sodium-hydroxide was added with the mixer still rotating deep inside the solution. We then mixed the Sodium-hydroxide and Carbopol solution for 5 minutes at 500 (rpm). The ink was afterwards added and it was mixed for 5 minutes at 500 (rpm). Through a circulating loop we finally mixed the whole solution using a pump (which will be explained later) for $3-4$ minutes to ensure homogeneity of the gel everywhere in the bucket. Once the mixing was finished, the mixer was then turned off and samples were taken for rheometry purposes. The Carbopol solution is slightly thixotropic meaning that the rheological properties change with time. Therefore we had to carry out the rheometry on the same day the solutions were made right after each experiment. Once prepared the gel solution follows a Herschel-Bulkley rheological model:

$$\hat{\tau} = \hat{\tau}_Y + \hat{\kappa}\hat{\dot{\gamma}}^n. \tag{A.1}$$

This model includes the simpler Bingham, power law and Newtonian models and is defined by three parameters: a power law index n, a fluid consistency index $\hat{\kappa}$ and a yield stress $\hat{\tau}_Y$.

Once the solutions were made in the PVC buckets and the corresponding Atwood number and viscosities were satisfactory, they were sent into two acrylic tanks. These acrylic tanks (that will be explained in more detail) can be pressurized by compressed air and were used to drive the fluids to inside the flow loop. The pumps used to make this delivery from PVC buckets to acrylic tanks are shown in figure A.6. As shown in the picture we have used two pumps, one for the displacing liquid and the other for the displaced fluid. The pumps are of centrifugal type with constant rpm of 1725 and power of 0.5 (HP) (Moyno Inc.). Note that in the case of highly viscous fluids e.g. high concentration of Carbopol solutions the compressed air pressure was not enough to fill the pipe with the displaced liquid, thus the fluid was pumped directly into the loop from the PVC bucket.

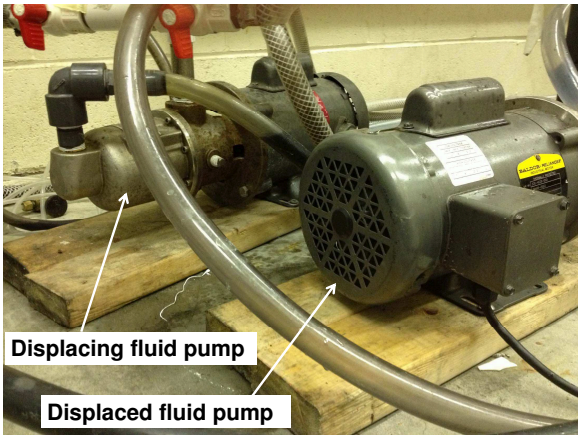

Figure A.6: The centrifugal pumps used in the experiments for transporting the fluids from buckets to acrylic pressurized tanks.

In the nearly horizontal flow experiments described in [123], the fluids were driven into the main pipe using gravity i.e. by raising the reservoir of fluids to an elevation higher than that of the pipe. In theory, the same method would still work for nearly vertical pipe, as flow at higher altitude with more potential energy will always flow down into beneath section. However, the top of the pipe, in a nearly vertical pipe experiment would be approximately 5 meters above ground, which means that the tank used to fill the upper fluid will have to be mounted higher up than that. As a result, this would be much less practical in terms of ease of assembling, accessibility for maintenance and safety. Hence, alternative methods have been explored.

A possible option is to simply pump fluid into the pipe using a regular fluid pump. Nevertheless, this is not the most suitable one as the pulsation in the pump will disturb the flow and thus affect the quality of the flow behavior observed. The method chosen is to use tanks pressurized by compressed air to send fluids up into the pipe. The advantage of this method is that it is possible to stably transport fluid and that all components of the tanks can be secured on the ground, allowing for ease of operation and maintenance.

The tanks, as shown schematically in figure A.7a and after being built in figure A.7b, are made from acrylic, which enable the operator to see what goes on inside the tanks, in case there is residual fluid or other contamination inside, thus minimizing errors incurred from them. Although acrylic is generally not the best material to be used under pressure due to its brittle property, the pressure used in running the experiments is below 15 (psi) ($\approx$ 103.4 (kPa)), a relatively low value compared to pressurized tanks in general. Preliminary calculation has confirmed that the acrylic under the design dimensions can withstand even higher pressure which is though not recommended. The tanks dimensions are 152.4 (cm) height, 19.05 (cm) inner diameter and 0.635 (cm) thickness which are chosen for the main part of the tanks as it is the most economical size that is at the same time feasible for operation and assembly. Engineering drawings were created using Unigraphics NX, for tank components. The flanges are joined to the main pipe section using weld-on acrylic glue which ensures that the glued part are at least as strong as the material, if not stronger. Just like in any engineering designs, safety is the number one priority. Long steel bolts, polycarbonate shields and pressure relief valves have been added to the system for additional safety factor. The pictures of the assembled tank system are shown in figure A.7b. There are 4 inlets to each tank, three of which are located on the lid and the last one on the bottom (figure A.7a). The three inlets/outlets at the top are for compressed air, bleed valve and pressure relief valve, while the one on the bottom is used for filling the tank and as outlet to the main pipe. As demonstrated in the figure, the bottom of the tank has been designed and machined into conical shape for easy drainage purposes, since some fluids used in the experiment are going to be gel-like. The completed tanks are secured on aluminum extrusion frame on wheels for easy transportation. Looking closely into figure A.7b one can see the sheets of polycarbonate surrounding three sides of the whole structure for enhanced safety. Once side is left uncovered to have access for mechanical/repair concerns. This side always faces the lab wall where there is no operator working. Note that the regulators for the pressurized tanks were set at 10 (psi) ($\approx$ 70 (kPa)) for most experiments and at slightly higher

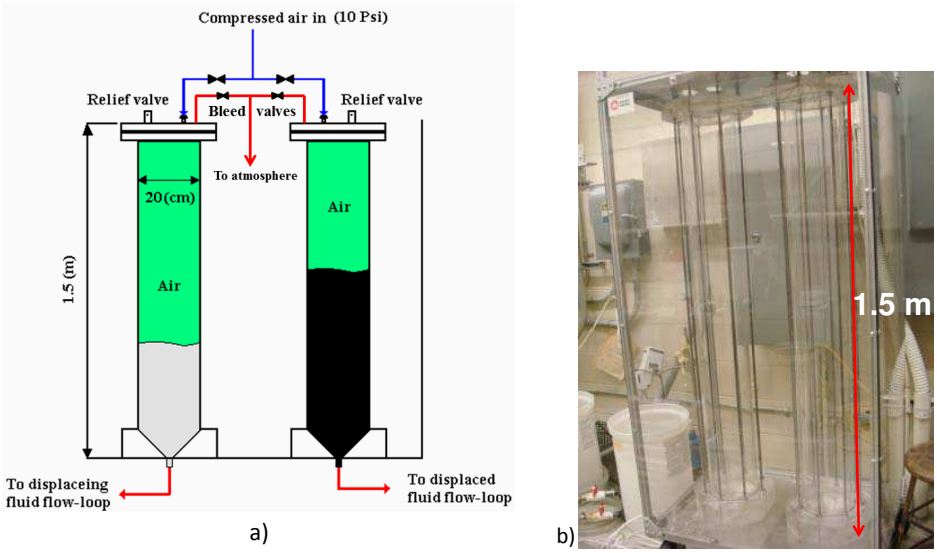

Figure A.7: a) Schematic of the acrylic pressurized tanks used for driving the fluids into the system. The tanks dimensions are 152.4 (cm) high × 19.05 (cm) inner diameter × 0.635 (cm) thickness. b) Actual picture of the acrylic pressurized tanks.

pressure for highly viscous cases.

A.1.2 Valves

There are several valves involved in controlling the fluid flow in our experimental setup. In the nearly horizontal experiments of [123], it was possible to manually operate all the valves as they were all in an accessible locations. Once the pipe is inclined at a higher angle, the gate valve and the valves for the upper fluid will not be within reachable distance of the operator. In this case operating the valves manually would be impossible to do and also dangerous. Instead of hand-operated PVC globe valves, solenoid valves were adopted in the current setup that can be activated using on/off switches from the ground. This in turn shortens the time taken for each experiment and enhances the quality of the experiment by operating the openning/closing steps quicker. Figure A.8 shows a section of the flow loop up the gate valve where three solenoid valves (from ASCO) are adopted. Each valve has a different task which becomes important in different stages of the experiment e.g. filling the pipe, washing the remaining fluids etc.

Also some valves were placed to let the air leave during the fill-up part of the experiments with the working fluids i.e. they acted as bleed valves.

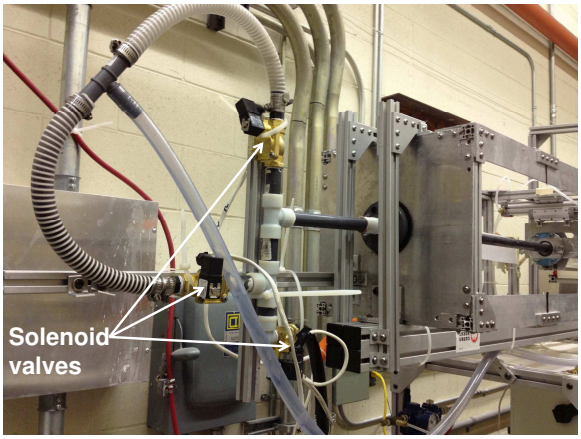

Figure A.8: The solenoid valves used in upper section of the flow loop. This area was not easy to access during the experiment due to the hight or structural constraints.

In addition to these valves, the most critical component of this set up is the gate valve that provides boundary between two fluids before they begin to mix. The gate valve was controlled using a simple manual push-pull handle during the nearly horizontal experiments of [123]. Several alternatives had been considered, including the use of electric and pneumatic gate valve. Commercially available valves as such are available only for larger pipe sizes and are quite costly. Although using pipe adapters would allow for the use of these valves for smaller diameter pipe like the one used in the experiment, the valve blades are so thick that they would largely disturb the flow during the opening and closing. In the end, it was decided that a customized valve would be constructed using the same principle as normal gate valve: a system that has a blade whose movement separates or allows two fluids to mix. The compressed air line that is made available for the pressurized tank makes it possible to also use a pneumatic system for this custom-made valve. The design is to use a pneumatic slider with stoppers on each end to accurately move the blade, with a hole across the pipe. The hole aligns with the pipe when the slider is at one end and the pipe is closed when it is at the other end. The slider is controlled using an A-B pneumatic solenoid valve, which is connected to a double pole double throw (DPDT) switch. Depending on the location of the switch, the valve is either open or

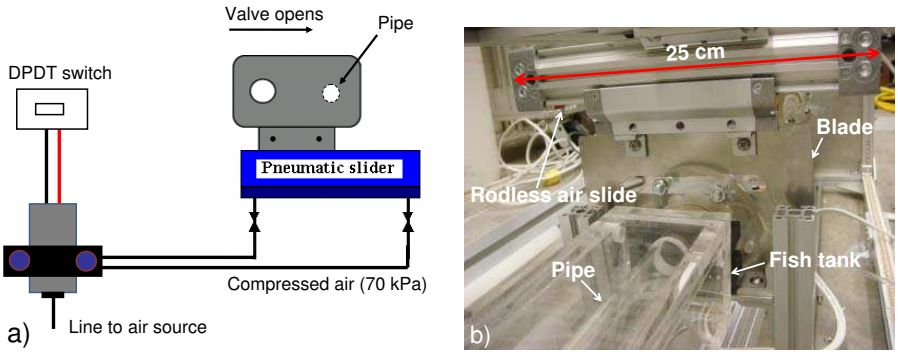

Figure A.9: a) The schematic of the pneumatic air slide used as gate valve. b) Picture taken from the actual gate valve in place.

closed; see figure A.9a for details. The compressed air pressure required at the gate valve was around 60 (psi) ($\approx$ 413 (kPa)) for most experiments.

The advantage of creating a customized gate valve, in addition to ease of operation, is that the blade can be designed to be as thin as possible (in this case approximately 1.6 (mm) thick) to minimize the flow disturbance during the experiment. Figure A.9b below shows the actual gate valve that has been installed into the setup.

A.1.3 Velocity measurements

As with the nearly horizontal experiments in [123], we have also used Ultrasound Doppler Velocimetry (UDV) to give a quantitative understanding of fluid velocity variations. Because the UDV probe needed to be as close as possible to the flow section, we mounted the UDV on a bare section of the pipe, in order to capture the velocity vectors through the central cross-sectional plane of the pipe. The probe was located at the end of the first fish tank (approximately 150 (cm) below the gate valve) where the flow is mostly fully developed. The velocity profile observed in that section of the pipe can be qualitatively representative velocity distributions elsewhere. The UDV used is DOP2000 (model 2125, Signal Processing SA) with 8 (MHz), 5 (mm) (TR0805LS) transducers with a duration of 0.5 (μs). This velocimetry technique does not require any transparent medium which is very suitable. Since the probe was mounted outside the pipe, our measurement technique was completely non-intrusive. The volume within which the measurement is carried out has a cylindrical shape and gives an axial resolution for our fluids and flows of around 0.375 (mm). The lateral resolution is equal to the

transducer diameter (5 mm) but varies slightly with depth due to divergence. The slightly diverging ultrasonic beam enters the fluids by first going through a 3.175 mm-thick plexiglass pipe wall. The UDV technique is based on sending the sound pulse and receiving its echo and allows measurement of the flow velocity projection on the ultrasound beam, in real time [59]. This projection therefore gives only the streamwise component of velocity. Thus it is important to know exactly the relative angle between the probe and the pipe axis. The instrument sends a series of 4-cycles of short bursts and records the echoes back scattered from the particles suspended in fluids. For the tracing particles, we have used polyamid seeding particles with a mean particle diameter of 50 (μm) and a volumetric concentration equal to 0.2 (g/l) in both fluids. Through the time elapsed between the pulse and the received echo, the distance of the particles from the transducers is computed; meanwhile the associated increased/decreased Doppler frequency shift gives the value of the velocity at each distance. Reflection effects at the lower wall of the pipe affect the velocity measurement locally and makes it hard to measure a zero velocity at the lower wall.

For a typical acquisition time of the velocity profiles, 120 (ms) per profile was set while no real time filtration of signals was applied during the recording process. However, when presenting the results we average the profiles over a few seconds (usually 3 (s)) to reduce the noise in the data. The probe was mounted at an angle in the range $60 - 80\,^{\circ}$ relative to the axis of the pipe considering the compromise between a good signal-to-noise ratio and small ultrasonic signal reflections [22]. It is also assumed that the density difference of the fluids used in our experiment is sufficiently small to neglect the differences in the speed of sound in the fluids.

A.1.4 Image Processing and Visualization Technique

In the nearly horizontal experiments described in [123], the pipe was backlit, with the cameras taking pictures from the received light, through the liquid medium. However, due to refraction errors, the data recorded at a particular depth of the pipe for instance, do not necessarily belong to that same depth in reality, although it must be mentioned that the principal measurement made in [123] was a computation of front velocity rather than concentration/interface height.

In order to reduce light refraction errors, for the experiments in this thesis a *fish tank* structure was added to the pipe section below the gate valve to obtain higher-quality images. The fish tank was filled with water, which has approximately the same refractive index as plexiglass. This in turn

minimizes the distortion in the image captured and leads to more accurate image processing. The fish tank enclosed pipe used in the experiments is illustrated in Fig. A.10.

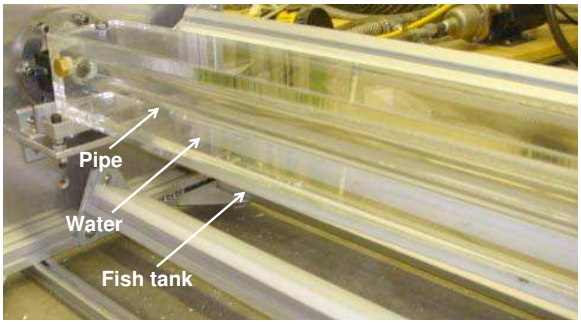

Figure A.10: The fish tank pipe system used in the experimental apparatus to reduce the light refraction error. The fluid filled in the space between the square box and the pipe is water.

We also improved the illumination system in this thesis, replacing the fluorescent light-box system in [123] by a series of Light-Emitting-Diode (LED) stripes behind a light diffuser. This technique results in much more homogeneous lighting both along and across the pipe. Figure A.11 shows how the lighting system was implemented. The figure shows the fish tank pipe setup, behind which the LED stripes and the diffusing layers are placed. The plastic light diffusers help disperse light beams in different directions thus giving homogeneous illumination rather than bright/dark spots. One should note that the distance between LED stripes and light diffuser must be adjusted to get the most homogeneous results.

A first-surface mirror set is also used in the apparatus to get images other than the frontal view. The term *first-surface* means that the reflecting coating is applied to the surface of the mirror rather than its back. The cost is higher than the usual mirrors since higher precision is required in the process of making these mirrors. The quality of the reflected image though is much higher in first-surface mirrors since the light beams do not break or change in angle within the thickness of the glass (ghosting effect). Note that we could equally add cameras into other views to capture those images too, though it is much more expensive and uses up more space than otherwise needed. An advantage of the mirror system is that images from different viewpoints are synchronized. For the current study, the mirror is placed such that it can show the top view (perpendicular to the frontal view) in

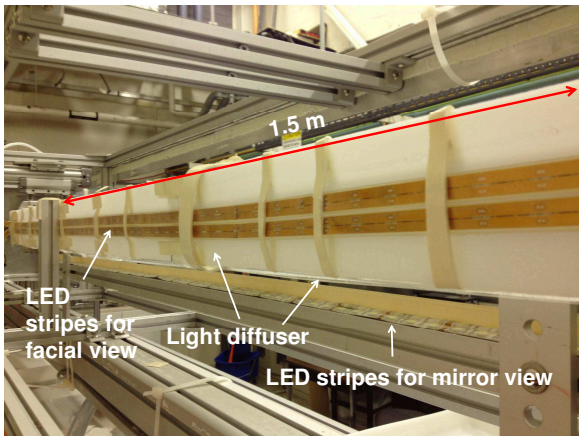

Figure A.11: The light-emitting-diode (LED) system used for illuminating the pipe from behind. The diffusive layers are also added to get homogeneous lighting within the field of view.

the same camera field of view. Figure A.12 shows the first-surface mirror system used for capturing the top view images. In this example the pipe is filled with black fluid and the reflection is apparent in the mirror. We have used this mirror data only in the viscoplastic fluid displacement experiments, where asymmetry is a more prevalent feature across the pipe. In fact more information than available from the frontal view was required to understand the static layers occurring across the pipe. Similar to the frontal view where LED strips and a light diffuser were required for camera images, for the top view images a similar system was adopted. Figure A.11 shows the LED stripes used for the mirror images and their corresponding diffusive layers as well.

Once the images are recorded, concentration values are calculated out of the light intensities in each pixel. The calibration was done based on correlating the concentration value of known fluids to the gray scale (0 being the displaced fluid and 1 the displacing fluid). On completion, the concentration of the fluids in mixing region can be inferred from the gray scale value. The second calibration is for the positioning of the images. The first step is to ensure that camera and the mirrors are able to capture all the views of the pipe. Changes can be made through repositioning of camera and mirrors. Once completed, the size of the captured image and that of the real object are matched, so that later on in the experiment the actual

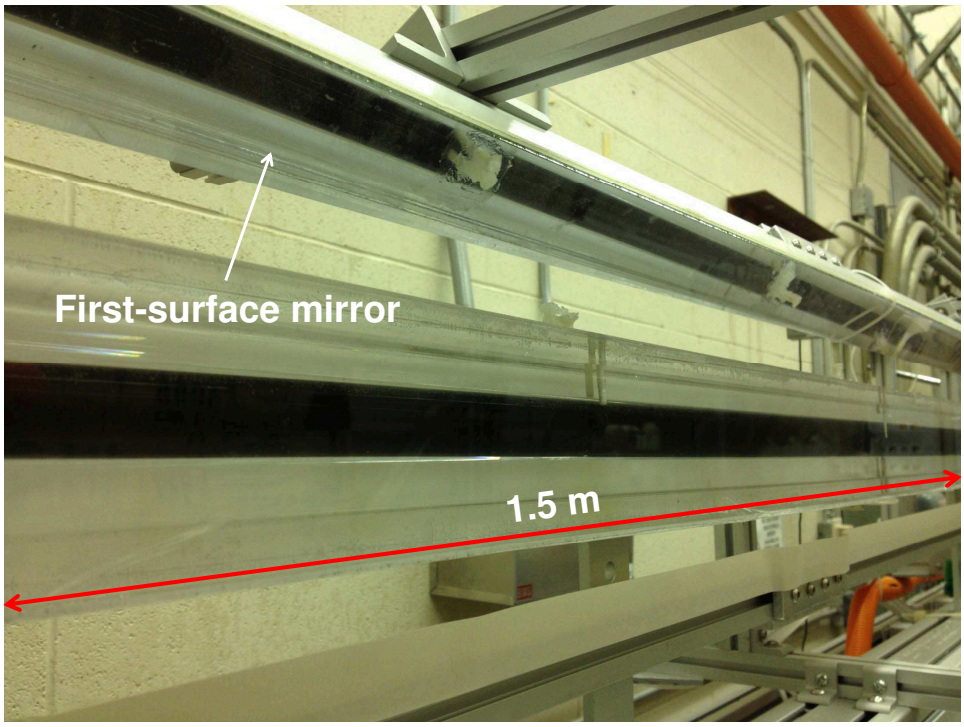

Figure A.12: The first-surface mirror used in the experimental apparatus to obtain images from top view (perpendicular to frontal view).

size of fluids volumes, especially at the interface, can be calculated. The calibration process is one of the most important steps in the project because errors that occur here will be greatly magnified when results from the experiments are analyzed in the later stages. As we have 4096 gray-scale levels in our cameras the minimum error in measured concentration value would be approximately 0.02 %. As will be seen in experimental results later (chapters 3, 4 and 7 for instance) the concentration values will be used to obtain two other major quantities namely the displacing front velocity and the macroscopic diffusion coefficient of the displacement flow. It is shown that the measurement errors for these quantities are approximately 3 % in our study.

The light calibration procedure is basically similar to that used in [123] for nearly horizontal experiments, except that it was repeated with the new lighting system (fish tanks, LED lighting etc.). The idea is basically to convert the light intensity absorbed by the cameras to a concentration value varying from 0 to 1. The amount of ink present is determined by assuming an exponential dependency of the light intensity on concentration: $I(C) = \Psi \exp^{\alpha C}$, where I and C are light intensity and fluid concentration respectively and Ψ and α are physical constants, (see [123] for more details). In our case the maximum concentration of ink that could be added was found to be 300 mg/l as shown in Fig. A.13. Above this concentration we begin to deviate from the exponential law and thus can not use the pure black and light fluids intensity to find the constants Ψ and α. In other words for values above 300 mg/l of ink, the pixels with displaced fluids in their view would start to become saturated and thus mixed fluids might still appear as pure displaced fluid.

Once the light calibration is performed, images from the actual flow field of an experiment can be taken with the light intensities translated into concentration values. Figure A.14 shows an example of a density unstable experiment carried out for iso-viscous Newtonian water-based solutions, for $\hat{\nu} = 1$ (mm^2/s), $\beta = 30°$, $At = 0.0035$ and $\hat{V}_0 = 70$ (mm/s). Note that $\hat{\nu}$ is the kinematic viscosity defined as the ratio of the common viscosity of the fluids to the average density. As can be seen from the figure, the concentration values very between 0 and 1 corresponding to the black displaced and the white displacing fluids respectively. We will discuss the results in more depth in the following chapters. The figure only shows an example of how the image processing is done for a typical experiment.

If we now take the average concentration of the images shown in Fig. A.14 across the pipe diameter, we will have a concentration value C that is only a function of streamwise distance $\hat{x}$ and time $\hat{t}$. As later on will be seen, very

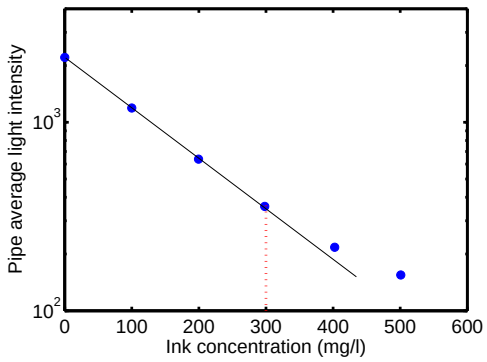

Figure A.13: Average light intensity within the second fish tank varying as a function of ink added for a domain of size 19×1500 (mm^2) located almost 1600 (mm) down the gate valve. After ink concentration of 300 (mg/l) we see deviation from the exponential dependency of the light intensity on concentration.

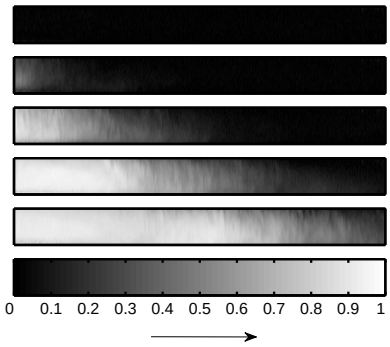

Figure A.14: Sample snapshots of a density unstable displacement at $\beta = 30\,^\circ$, $\hat{\nu} = 1$ (mm^2/s), $At = 0.0035$ and mean velocity $\hat{V}_0 = 70$ (mm/s). Dark fluid is less dense than the light fluid. The images are taken at $\hat{t} = 14, 19.5, .., 36$ (s). The field of view is 1330×19 (mm^2), taken 1740 (mm) below the gate valve. The last image at the bottom of the figure shows the grayscale for the concentration values. The arrow indicates the flow direction. The left end of the pipe is higher than the right (the fluid flows downhill).

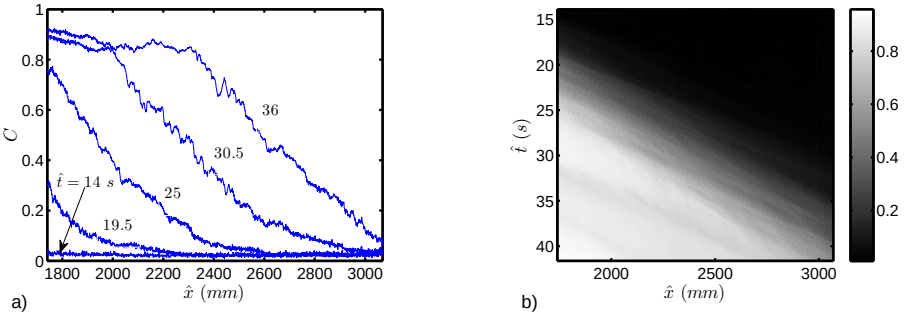

Figure A.15: a) Evolution profiles of the averaged concentration across the pipe with time $\hat{t} = 14, 19.5, .., 36$ (s) and streamwise location for the same experiment as shown in figure A.14. b) The spatiotemporal diagram of the same experiment in the plane of $\hat{x}$ and $\hat{t}$.

useful information can be extracted from this depth-averaged concentration field, for instance the velocity of the displacing front, displacement efficiency etc. Figure A.15a shows the concentration evolution profiles of the same images shown in Fig. A.14. If we record the averaged concentration values across the pipe at each time and streamwise location we can then plot the spatiotemporal diagram of the averaged concentration field. Figure A.15b shows the spatiotemporal diagram of averaged concentration field for the same experiment as in Figs. A.14 and A.15a. Note that the data plotted in figures such as Figs. A.15a and b is interchangeable. As later on will be seen, the concentration evolution and the spatiotemporal diagrams will be used very often to investigate the quality of mixing, displacement efficiency and more dynamical characteristics of the flow.

A.1.5 Fluid rheology

Our rheological measurements were performed using a Bohlin Gemini (HR Nano) digital controlled shear stress, shear rate rheometer. The rheometer was used to measure the viscosity of the water-Glycerine solutions and also Carbopol gels. For Newtonian solutions we used a simple controlled strain rate ramp over the range $0.001 - 100$ 1/s. In order to ensure that the viscoplastic gels will be yielded in our tests, a controlled-shear rate method is used usually in the range of $0.001 - 10$ 1/s of shear rate with logarithmic progression in time to have enough data points at low shear rates where yielding occurs. Each rheometry measurement took about 200 seconds to

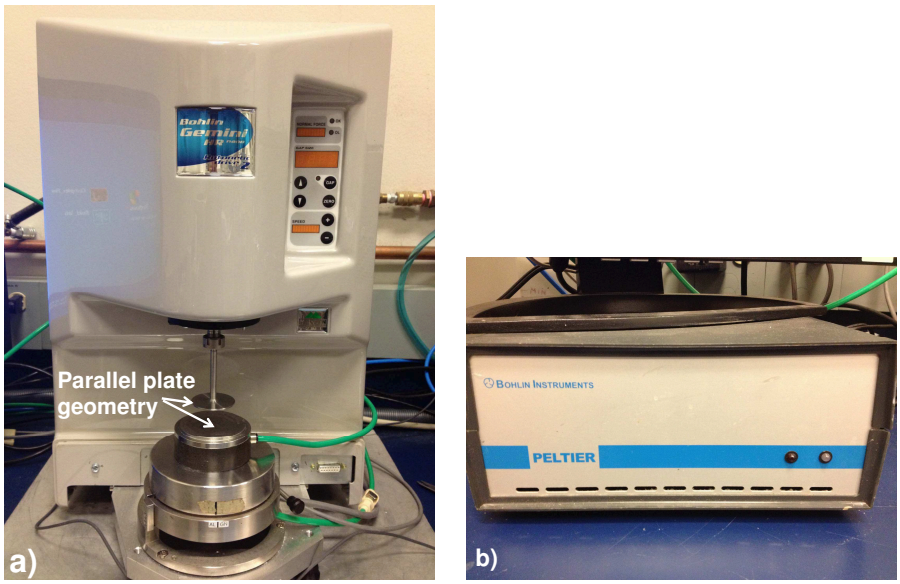

Figure A.16: a) The rheometer used for measuring the viscosity of the fluids b) The thermal unit attached to the rheometer for adjusting the temperature of the samples.

ensure the steady variations of shear rate within samples. We also note that samples did not evaporate during the course of rheometry. A smooth parallel plate geometry of 40 (mm) diameter and 1 (mm) gap, was used for rheometry. Fluid samples were first placed on the bottom plate. The top plate was then lowered by the rheometer to the desired gap height of 1 (mm) by squeezing the extra paste out from between the plates. The excess fluid at the plate edges was carefully trimmed with cotton sticks. Identical procedures were followed in all the tests. Temperature was also controlled by a Peltier heater/cooler (Bohlin instruments) based on water circulation under the rheometer's plate and according to the temperature of the fluids recorded before experiments. For yield stress measurements, we also had to add a tiny layer of sand paper (with 400 grit roughness) to both plates to be able to read the yield stress value and avoid slip. Figures A.16a,b show the rheometer used for measuring the viscosity of the fluids and the thermal unit attached to it for adjusting the temperature of the samples respectively.

We measured the flow curve using a controlled shear rate incremented logarithmically. Parallel plates 40 (mm) in diameter with a 1 (mm) gap

were used for the measurements. 400 grit sandpaper was glued to the plates to prevent wall slip. The sample temperature was controlled at the desired temperature using a Peltier device. We took the yield stress $\hat{\tau}_Y$ to be the stress at a shear rate of 0.1 s^{-1}. The uncertainty in $\hat{\tau}_Y$ is estimated to be in the range 2-5%. Afterwards, we subtracted the yield stress value from the remaining shear stress data and then we found the best fit to a power law curve using log-log plot of the effective viscosity versus strain rate. The standard deviation in determining the yield stress value of the Carbopol solution in this way is estimated to be in the range $2-5$ %. The errors in the consistency ($\hat{\kappa}$) and the power law index (n) were below 12 % and 5 % respectively. In fact, our displacement flow experiments revealed that the results were not particularly dependent on the value of the yield stress, since the yield stress was always much larger the viscous stresses in the displacing fluid, as discussed in chapter 7. Figure A.17 shows the dependency of the shear stress on shear rate for a typical Carbopol solution used in this study. Note that the very low shear-rate data shown in the figure are not reliable from the quantitative point of view since a much longer time than the approximate time of 1 s per data point should be spent to reach a steady state measurement. The longer measurement time could in turn result in evaporation of the solution during the rheometry. Note that the related errors to the steady-state measurement time also fall in the same range of $2-5$ %. More details on the rheology and structure of Carbopol solution can be found in [60].

A.1.6 Experimental results validation

We first calibrated our apparatus against exchange flow results of Seon *et al.* [112, 115] for $At = 0.01$ at $\beta = 60\,^\circ$ and $\beta = 70\,^\circ$. The errors in measured front velocity were always below 3% for the cases studied and the experiments had a high degree of repeatability. The dimensionless macroscopic diffusion coefficients were also compared against the results of Seon *et al.* [114] for different Atwood numbers and the error was found to be less than 2%. Another natural comparison was with the displacement flow results in nearly-horizontal pipes in [123]. The error in measured front velocity values were also in the same range reported for exchange flows. More comparisons with literature, on displacing front velocities and other relevant quantities will be given in the following chapters when appropriate.

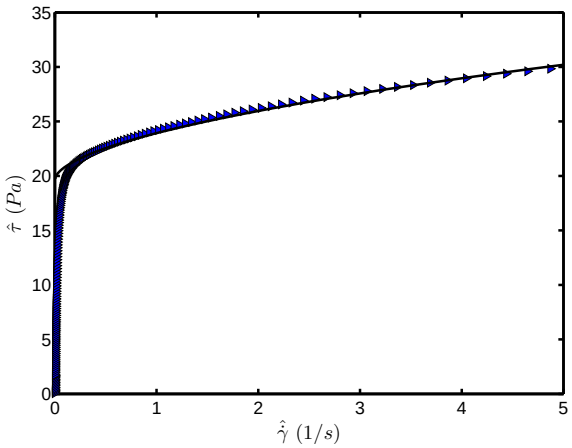

Figure A.17: Example flow curve for a viscoplastic solution with Carbopol=0.14% (wt/wt) and $NaOH$=0.04% (wt/wt) solution. The solid line shows the Herschel-Bulkley model curve fit $\hat{\tau} = \hat{\tau}_Y + \hat{\kappa}\hat{\dot{\gamma}}^n$ with parameters $\hat{\tau}_Y = 19.7$ (Pa), $\hat{\kappa} = 4.3$ (Pa.s^n) and $n = 0.56$.

A.2 Numerical technique

Besides the experimental approach, we have carried out a number of numerical simulations of 2D displacements in an inclined plane channel. The geometry and notation are represented in figure A.18. The computations are fully inertial, solving the full 2D Navier-Stokes equations with change of fluid modelled via a scalar concentration, c. The system of equations solved and the numerical technique is explained in detail in [123] related to the nearly horizontal simulations. However we briefly outline these again for completeness. The code, meshes, time stepping etc. are all kept the same for the more inclined simulations presented in the current thesis. When the degree of mixing is higher a finer resolution is adopted to ensure that we capture all important effects. The system for two Newtonian fluids of equal viscosity is given below as this is the only regime we have studied numerically in the current thesis:

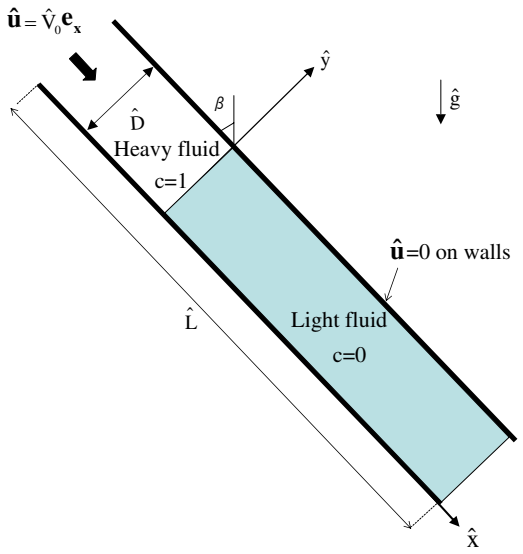

Figure A.18: Schematic view of the numerical domain used.

$$[1+\phi At]\,[\mathbf{u}_t + \mathbf{u}\cdot\nabla\mathbf{u}] = -\nabla p + \frac{1}{Re}\nabla^2\mathbf{u} + \frac{\phi}{Fr^2}\mathbf{e}_g, \tag{A.2}$$

$$\nabla\cdot\mathbf{u} = 0, \tag{A.3}$$

$$c_t + \mathbf{u}\cdot\nabla c = \frac{1}{Pe}\nabla^2 c. \tag{A.4}$$

Here $\mathbf{e}_g = (\cos\beta, -\sin\beta)$ and the function $\phi(c) = 2c - 1$ interpolates linearly between -1 and 1 for $c \in [0,1]$. The 4 dimensionless parameters appearing in (A.2) are the angle of inclination from vertical, β, the Atwood number, At, the Reynolds number, Re, and the (densimetric) Froude number, Fr. These are defined as follows:

$$At \equiv \frac{\hat\rho_1 - \hat\rho_2}{\hat\rho_1 + \hat\rho_2}, \quad Re \equiv \frac{\hat V_0 \hat D}{\hat\nu}, \quad Fr \equiv \frac{\hat V_0}{\sqrt{At\hat g \hat D}}. \tag{A.5}$$

Here $\hat\nu$ is defined using the mean density $\hat\rho = (\hat\rho_1 + \hat\rho_2)/2$ and the common viscosity $\hat\mu$ of the fluids. In (A.4) appears a 5th dimensionless group, the Péclet number, Pe, defined by:

$$Pe \equiv \frac{\hat V_0 \hat D}{\hat D_m}, \tag{A.6}$$

with $\hat{D}_m$ the molecular diffusivity (generally assumed constant for simplicity in our work). In our computations, the effect of molecular diffusion is neglected, due to the large Péclet number that corresponds to our experimental flows, where we have a well defined interface.

Equations (A.2)-(A.4) are discretised using a mixed finite element, finite volume method. The Navier-Stokes equations are solved using Galerkin finite element method. The divergence-free condition is enforced by an augmented Lagrangian technique [57]. A fixed time step is used for the Navier-Stokes equations, advancing from time step N to $N + 1$. The convective velocity is approximated at time step N while the linear spatial derivatives of the velocity are approximated implicitly at time step $N+1$. The pressure is approximated at time step $N + 1$ (semi-implicit method regarding the nonlinear terms).

A structured rectangular mesh is considered, with linear elements (Q1) for the velocity and constant elements (P0) for the pressure discretisation. The concentration equation (A.4) uses a finite volume method. The concentration is approximated at the center of each regular mesh cell. The advective terms are dealt with via a MUSCL scheme (Monotone Upstream-centered Schemes for Conservation Laws). These are essentially slope-limiter methods for reducing oscillations close to discontinuities; see e.g. [148] and [82] for more description. On each (Navier-Stokes) time step a splitting method is used to advance the concentration equation over a number of smaller sub-timesteps. This time advance is explicit and a CFL (Courant-Friedrichs-Lewy) condition is implemented for the sub-timesteps to ensure numerical stability.

The numerical algorithm is implemented in C++ as an application of PELICANS. PELICANS is an object oriented platform developed at IRSN (the French Nuclear Safety Research Institute), to provide a general framework of software components for the implementation of partial differential equation solvers. PELICANS is distributed under the CeCILL license agreement (http:// www.cecill.info/ licences/ Licence_CeCILL_V2-en.html). PELICANS can be downloaded from https:// gforge.irsn.fr/ gf/ project/ pelicans/. Although the equations could have been implemented in a commercial CFD (Computational Fluid Dynamics) code, these codes are often over-stabilised and give little access to the detailed implementation.

As boundary conditions for our simulations, we impose no-slip and zero flux of c at the solid walls. A plane Poiseuille flow is imposed at the inflow, along with $c = 0$. Outflow conditions are imposed at the channel exit. The initial interface starts within the channel, with $c = 1$ upstream and $c = 0$ downstream. The initial velocity is $\mathbf{u} = 0$. Usually a range of dimensional

parameters is selected that is similar in scope to those of our pipe flow experiments.

Typically we choose the channel thickness equal to the pipe diameter in our experiments ($\hat{D} = 19.05$ mm). The channel length is typically $\hat{L} = 100 \times \hat{D}$ with gate vale positioned $\hat{L}/4$ above the midst of the channel. This is because of having an imposed flow where most of the information would be obtained downstream of the channel rather than upstream. However, some important features of the flow for instance displacing instantaneously/non-instantaneously are revealed from the information obtained in the upper $\hat{L}/4$ length of the computational domain (above the gate valve). For the meshes in most of the computations we used 28 cells across the channel, refined slightly towards the walls, and 400 cells along the length of the channel. However, we have conducted a number of simulations with (e.g. up to twice as much or even higher) finer mesh resolution, but producing only a little difference in the measured front velocities, within the limits of our desired accuracy. We acknowledge that the meshes used are relatively coarse, but note that the principal information being extracted from the simulations is bulk information, e.g. spatiotemporal plots, front speeds, having a back flow etc. These features appear to be less sensitive to refinement than local features, (as checked with much finer meshes than 28×400 in the chapter 5). It would of course be advisable to choose a finer mesh if e.g. flow instabilities and mixing were to be directly studied.

Note that there is numerical diffusion present in solution of (A.2)-(A.4). For the mesh sizes used however, it was found that for Péclet number values larger than about 10^5 there was no noticeable difference in results, with or without the diffusive terms. In other words the numerical diffusion is dominant. In our experiments the range of Péclet used is easily above than 10^5. the fact that in most of our simulations (specially the more inclined cases) substantial mixing is observed reveals that the primary cause is dispersion via secondary flows and instability.

After running each simulation, snapshots of the concentration filed can be extracted along with the concentration evolution profiles and the spatiotemporal diagrams of c ca be constructed. In other words we can mimic all the information obtainable from the experiments (as seen in figures A.14 and A.15) in our simulations. The advantage in simulations over the experiments is that we can have the full time-varying velocity field at each location within the domain whereas we only know the streamwise velocity components at a fixed position along the pipe. Figure A.19 shows computational concentration field evolution obtained for a typical simulation with parameters $\beta = 20\,^\circ$, $At = 0.001$, $\hat{\nu} = 1$ (mm^2/s), $\hat{V}_0 = 21$ (mm/s), (equally

$Re = 400$). In figure A.19a the sequence of images at different instants of times are shown. Figure A.19b shows the corresponding velocity field to each graph in part a over the whole domain. Similar to the experimental analysis, once the snapshots of the concentration are recorded we can find the quantitative value of the depth-averaged concentration at each time, $\hat{t}$, and the streamwise location, $\hat{x}$. Figure A.19c in turn shows the evolution of the depth-averaged concentration values for the same instants shown in parts a-b. Equally we can plot these concentration values at all times and locations in a spatiotemporal diagram, an example of which is shown in Fig. A.19d. In chapter 5 we discuss the analysis of the computational results in more details.

A.2.1 Code benchmarking

Numerous validations and benchmarking tests for the code PELICANS in the displacement flow and similar setups have been mentioned in [123], showing good quantitative comparisons. These include comparisons with computational work of Sahu *et al.* [106] for displacement flows and Hallez & Magnaudet [62] for exchange flows in 2D channels. Apart from these comparisons, the same code has been used extensively in [71] for miscible core-annular Newtonian flows of differing viscosities in which pearl and mushroom shaped instabilities develop. The results have been benchmarked against the recent experiments of [37, 38].

To summarize, our code has produced similar results compared to the existing computational and experimental studies in the literature. It is worth noting that the flows at hand are complex, such that only few precise analytical solutions to them exist. It is also acknowledged that there are numerically more sophisticated codes in current usage, e.g. [16, 62, 63] that may have higher resolution and be capable of capturing a broader range of modes of instabilities. If inertial and unstable regimes were to be studied in detail, the usage of such codes would be advisable. Here however, our principal aim is to extract bulk flow features such as spatiotemporal plots, front speeds, having back flow etc. over a range of parameters for which our code is adequate. Our particular code is also being extended to non-Newtonian multi-fluid flows, which is the eventual aim of the study of these flows [71, 72, 150].

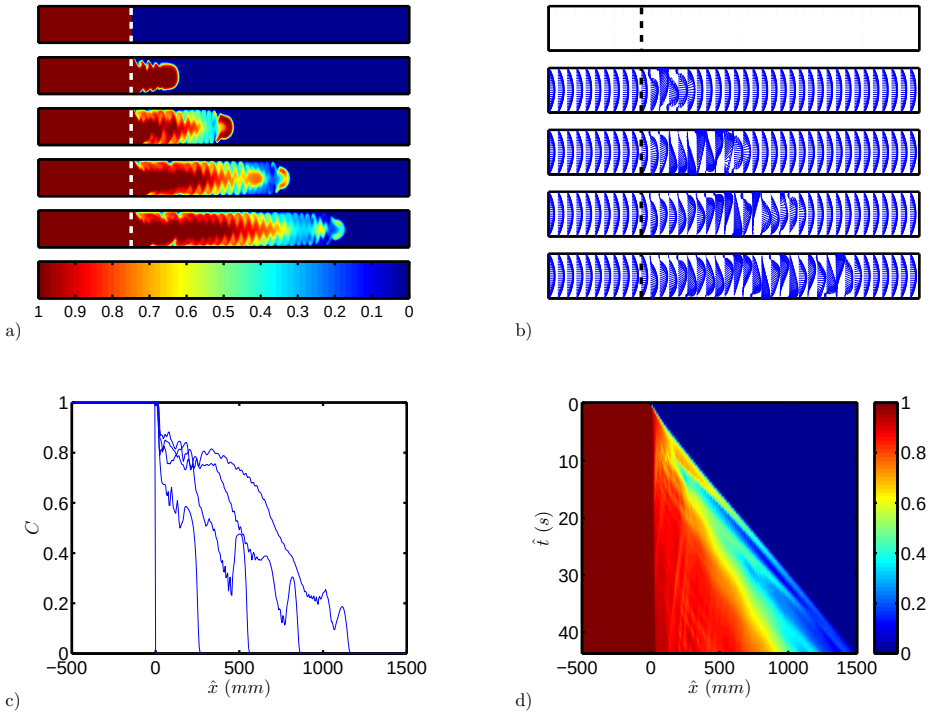

Figure A.19: a) Snapshots of the numerical simulation at times $\hat{t} = [0, 8.5, ..., 34]$ (s) run for $\beta = 20°$, $At = 0.001$, $\hat{\nu} = 1$ (mm^2/s) and $\hat{V}_0 = 21$ (mm/s). The last image at the bottom of the figure is the colourbar of the concentration values. The size of the domain shown is 19×2000 (mm^2). b) Vectors of velocity field with time for the same simulations shown in part a. The dashed lines in parts a and b show the position of the gate valve. c) Evolution of the depth-averaged concentration field, C, with time and streamwise location for the same simulation as in parts a and b. d) Spatiotemporal diagram of the depth-averaged concentration field obtained for the same simulation as parts a-c.

Appendix B

Weight functions and residual equation

Here we give various details related to algebraic calculation of the weight functions and the terms in the residual equation in chapter 6. Many of the expressions derived require the expressions in appendix C to evaluate them. Apart from the general expressions, we give below the solution for 2 Newtonian fluids, which can be used as a test case to check implementation of the more general formulae.

B.1 Newtonian fluids

For 2 Newtonian fluids, both effective and tangent viscosities are constant and equal, $\kappa_H = 1$, $\kappa_L = m$. After some algebra, f is given in terms of (h, b) by:

$$f = \frac{[(1-h)^4 + mh(1-h)^2(4-h)]b + 12m(1-h+mh)}{(1-h)^4 + 2mh(1-h)(2-h+h^2) + m^2h^4}. \quad \text{(B.1)}$$

The velocity in the two layers is given in terms of (h, b) by:

$$U_0(y) = -\frac{y(1-h)^2}{2(1-h+hm)}b + \frac{1-y+h(m-1)(h-y)}{2(1-h+hm)}fy, \quad y \in [0,h], \quad \text{(B.2)}$$

$$U_0(y) = -\frac{(1-y)[(1-h)(y-h)+mh(1+y-2h)]}{2m(1-h+hm)}b + \frac{(1-y)[(1-h)(y-h)+mh(1+y-h)]}{2m(1-h+hm)}f, \quad y \in [h,1]. \quad \text{(B.3)}$$

The flux in the lower layer can be calculated directly and is given in terms of (h, b) by:

$$q = \frac{1}{3}\left[\frac{b[h^3(1-h)^3(1-h+mh)] + 3mh^2[(1-h)(3+h)+mh^2]}{(1-h)^4 + 2mh(1-h)(2-h+h^2) + m^2h^4}\right]. \quad \text{(B.4)}$$

We can see that there is a 1-to-1 correspondence between using b as the second variable, or using q, as is done in e.g. [8].

We can see that the weight functions are quadratic in y. After some algebra the parameter a and the functions $g_H(y)$ and $g_L(y)$ are given by:

$$a = \frac{(1-h)^4 + mh(1-h)^2(4-h)}{(1-h)^4 + 2mh(1-h)(2-h+h^2) + m^2h^4}, \tag{B.5}$$

$$\begin{aligned} g_H(y) &= -\frac{y^2}{2}\left[\frac{(1-h)^4 + mh(1-h)^2(4-h)}{(1-h)^4 + 2mh(1-h)(2-h+h^2) + m^2h^4}\right] \\ &\quad + y\left[\frac{h(1-h)^4 + mh^2(1-h)^2(2-h)}{(1-h)^4 + 2mh(1-h)(2-h+h^2) + m^2h^4}\right], \end{aligned} \tag{B.6}$$

$$\begin{aligned} g_L(y) &= \frac{(1-y)^2}{2}\left[\frac{h^2[mh^2 + (1-h)(3+h)]}{(1-h)^4 + 2mh(1-h)(2-h+h^2) + m^2h^4}\right] \\ &\quad - (1-y)\left[\frac{h^2(1-h)[1+h^2(m-1)]}{(1-h)^4 + 2mh(1-h)(2-h+h^2) + m^2h^4}\right]. \end{aligned} \tag{B.7}$$

The terms in the residual equation (6.55) can then be evaluated straightforwardly using a symbolic algebra code, but are too long to list.

B.2 General specification of the weight functions

For more general fluids, we have seen that the weight functions are given by:

$$g_H(y) = ah[I_{H,m_H-1}(y) - L_{H,m_H}(y)] + \tau_{w,i} I_{H,m_H-1}(y), \tag{B.8}$$

$$g_L(y) = (1-a)(1-h)[L_{L,m_L}(y) - I_{L,m_L-1}(y)] - \tau_{w,i} I_{L,m_L-1}(y) \tag{B.9}$$

where $\tau_{w,i}$ and a are unknown constants. Imposing (6.46), gives one linear equation relating $\tau_{w,i}$ and a:

$$\tau_{w,i} = \frac{ah[L_{H,m_H-1}(h) - I_{H,m_H}(h)] + (1-a)(1-h)[L_{L,m_L}(h) - I_{L,m_L-1}(h)]}{[I_{H,m_H-1}(h) + I_{L,m_L-1}(h)]}. \tag{B.10}$$

We determine a by satisfying (6.51). This is a linear equation for a, with solution:

$$a = \frac{A_w}{B_w} \tag{B.11}$$

$$
\begin{aligned}
A_w &= (1-h)\left(\left[\int_h^1 I_{L,m_L-1}\ \mathrm{dy} - \int_{\mathrm{h}}^1 \mathrm{L_{L,m_L}}\ \mathrm{dy}\right][I_{L,m_L-1}(h) + I_{H,m_H-1}(h)]\right. \\
&\qquad \left. + \left[\int_h^1 I_{L,m_L-1}\ \mathrm{dy} - \int_0^{\mathrm{h}} \mathrm{I_{H,m_H-1}}\ \mathrm{dy}\right][L_{L,m_L}(h) - I_{L,m_L-1}(h)]\right) \\
B_w &= \left[h\left(\int_0^h I_{H,m_H-1}\ \mathrm{dy} - \int_0^{\mathrm{h}} \mathrm{L_{H,m_H}}\ \mathrm{dy}\right) + (1-h)\left(\int_h^1 I_{L,m_L-1}\ \mathrm{dy} - \int_{\mathrm{h}}^1 \mathrm{L_{L,m_L}}\ \mathrm{dy}\right)\right] \\
&\quad \times[I_{L,m_L-1}(h) + I_{H,m_H-1}(h)] + \left[\int_0^h I_{H,m_H-1}\ \mathrm{dy} - \int_{\mathrm{h}}^1 \mathrm{I_{L,m_L-1}}\ \mathrm{dy}\right] \\
&\quad \times[h(L_{H,m_H}(h) - I_{H,m_H-1}(h)) - (1-h)(L_{L,m_L}(h) - I_{L,m_L-1}(h))]
\end{aligned}
$$

We use the expressions given in appendix C to evaluate the various integrals of the functions $I_{k,p}$, $J_{k,p}$ and $L_{k,p}$.

B.3 Calculating the terms in the residual equation (6.55)

To calculate the terms in (6.55) we first evaluate the partial derivatives of (f, τ_i) with respect to (h, b). As discussed in §6.1.2 the velocity closure, including (f, τ_i), can be computed robustly to any given tolerance. Therefore, it is straightforward to compute these derivatives numerically. This enables us to compute partial derivatives of the wall shear stresses $\tau_H = \tau_i + fh$ and $\tau_L = \tau_i + (1-h)(b-f)$. Within the heavy fluid layer, we construct:

$$\frac{\partial \tau_H}{\partial h} = \frac{\partial \tau_i}{\partial h} + h\frac{\partial f}{\partial h} + f, \tag{B.12}$$

$$\frac{\partial \tau_H}{\partial b} = \frac{\partial \tau_i}{\partial b} + h\frac{\partial f}{\partial b}, \tag{B.13}$$

and within the light fluid layer:

$$\frac{\partial \tau_L}{\partial h} = \frac{\partial \tau_i}{\partial h} - (1-h)\frac{\partial f}{\partial h} - b + f, \tag{B.14}$$

$$\frac{\partial \tau_L}{\partial b} = \frac{\partial \tau_i}{\partial b} + (1-h)\left(1 - \frac{\partial f}{\partial b}\right). \tag{B.15}$$

Let us consider the first terms in (6.54), within the heavy fluid layer:

$$\int_0^h \frac{\partial U_0}{\partial T} g_H\ \mathrm{dy} = \int_0^h \left[\frac{\partial U_0}{\partial h} h_T + \frac{\partial U_0}{\partial b} b_T\right] g_H\ \mathrm{dy} = \mathrm{A_{H,h} h_T + A_{H,b} b_T}, \tag{B.16}$$

$$\int_h^1 \frac{\partial U_0}{\partial T} g_L\ \mathrm{dy} = \int_h^1 \left[\frac{\partial U_0}{\partial h} h_T + \frac{\partial U_0}{\partial b} b_T\right] g_L\ \mathrm{dy} = \mathrm{A_{L,h} h_T + A_{L,b} b_T}, \tag{B.17}$$

where we have denoted the different contributions to the acceleration terms as follows:

$$A_{H,h} = \int_0^h \frac{\partial U_0}{\partial h}(y) g_H(y)\ \mathrm{dy}, \qquad A_{H,b} = \int_0^h \frac{\partial U_0}{\partial b}(y) g_H(y)\ \mathrm{dy},$$
$$A_{L,h} = \int_h^1 \frac{\partial U_0}{\partial h}(y) g_L(y)\ \mathrm{dy}, \qquad A_{L,b} = \int_h^1 \frac{\partial U_0}{\partial b}(y) g_L(y)\ \mathrm{dy}.$$

The weight functions are expressed as linear functions of the functions $I_{k,p}$ and $J_{k,p}$; see (6.65) & (6.67). Now we develop similar expressions for the partial derivatives of U_0 in each layer. Within the heavy fluid layer, using (6.28)

$$\begin{aligned}\frac{\partial U_0}{\partial h} &= \frac{1}{m_H}\frac{\partial}{\partial h} J_{H,m_H}(y) = m_H \int_0^y \frac{(|\tau_{H,xy}| - B_H)_+^{m_H-1}}{\kappa_H^{m_H}} \frac{\partial}{\partial h}\tau_{H,xy}\ \mathrm{d\tilde{y}} \\ &= m_H \int_0^y \frac{(|\tau_{H,xy}| - B_H)_+^{m_H-1}}{\kappa_H^{m_H}} \left[\frac{\partial \tau_H}{\partial h} + (\tau_{H,xy} - \tau_H)\left(\frac{\frac{\partial \tau_i}{\partial h} - \frac{\partial \tau_H}{\partial h}}{\tau_i - \tau_H} - \frac{1}{h}\right)\right]\ \mathrm{d\tilde{y}}\end{aligned}$$

This last expression can be evaluated in terms of the functions $I_{H,m_H-1}(y)$ and $L_{H,m_H}(y)$. We then treat the partial derivative with respect to b analogously and those in the light fluid layer. This leads to the following expressions:

$$\frac{\partial U_0}{\partial h} = \frac{\partial \tau_H}{\partial h} I_{H,m_H-1}(y) - h\frac{\partial f}{\partial h} L_{H,m_H}(y), \tag{B.18}$$
$$\frac{\partial U_0}{\partial b} = \frac{\partial \tau_H}{\partial b} I_{H,m_H-1}(y) - h\frac{\partial f}{\partial b} L_{H,m_H}(y), \tag{B.19}$$
$$\frac{\partial U_0}{\partial h} = -\frac{\partial \tau_L}{\partial h} I_{L,m_L-1}(y) - (1-h)\frac{\partial f}{\partial h} L_{L,m_L}(y), \tag{B.20}$$
$$\frac{\partial U_0}{\partial b} = -\frac{\partial \tau_L}{\partial b} I_{L,m_L-1}(y) - (1-h)\left[\frac{\partial f}{\partial b} - 1\right] L_{L,m_L}(y), \tag{B.21}$$

We recall that the weight functions are also linear combinations of the functions I_{k,m_k-1} and L_{k,m_k}; see (B.8)-(B.9). It follows that each of the terms contributing to the linear acceleration in (6.54) can be expressed as integrals of quadratic products of the functions I_{k,m_k-1} and L_{k,m_k}. Having evaluated these terms (explained below) we proceed to construct the terms $A^h(h,b)$ and $A^b(h,b)$ in (6.54):

$$A^h(h,b) = \delta Re\,[1+At]\,A_{H,h} + \delta Re\,[1-At]\,A_{L,h} \tag{B.22}$$
$$A^b(h,b) = \delta Re\,[1+At]\,A_{H,b} + \delta Re\,[1-At]\,A_{L,b} \tag{B.23}$$

For the terms leading to $C^h(h,b)$ and $C^b(h,b)$ we follow a similar path, but the algebraic complexity increases. Basically we have an expression that involves linear, quadratic and cubic products of the functions $I_{k,p}$, $J_{k,p}$ and $L_{k,p}$, each of which can be evaluated algebraically. These expressions are then integrated across the respective fluid layers.

$$C^h(h,b) = \delta Re\,[1+At]\,C_{H,h} + \delta Re\,[1-At]\,C_{L,h} \tag{B.24}$$
$$C^b(h,b) = \delta Re\,[1+At]\,C_{H,b} + \delta Re\,[1-At]\,C_{L,b} \tag{B.25}$$

We now deal with the specific terms in heavy and light fluid layers.

B.4 Terms in the residual equation: acceleration terms

We have seen that the weight functions and each partial derivative of U_0 can be expressed as a linear combination of I_{k,m_k-1} and L_{k,m_k}, i.e.

$$g_k(y) = g_{c1}I_{k,m_k-1}(y)+g_{c2}L_{k,m_k}(y), \quad \frac{\partial U_0}{\partial h}(y) = u_{c1}I_{k,m_k-1}(y)+u_{c2}L_{k,m_k}(y),$$

where the constants are specified above (and we have a similar expression for the b-derivatives). In general therefore, we have:

$$A_{k,h} = \int [u_{c1}I_{k,m_k-1}(y) + u_{c2}L_{k,m_k}(y)][g_{c1}I_{k,m_k-1}(y) + g_{c2}L_{k,m_k}(y)]\ \mathrm{dy}, \tag{B.26}$$

where the integral is over $[0,h]$ or $[h,1]$, for heavy and light fluid layers respectively. Expressions for the integrals of the quadratic products above are given in appendix C.

B.5 Terms in the residual equation: convective terms

We start with the heavy layer and the terms contributing to $C^{(h)}(h,b)$, which are:

$$\int_0^h \frac{\partial U_0}{\partial h}\left[U_0 g_H - \int_0^h \frac{\partial U_0}{\partial y} g_H\ \mathrm{d\tilde{y}} + \int_0^{\mathrm{y}} \frac{\partial \mathrm{U_0}}{\partial \mathrm{y}} \mathrm{g_H}\ \mathrm{d\tilde{y}}\right]\ \mathrm{dy} = \mathrm{C_{H,h,1}} + \mathrm{C_{H,h,2}} + \mathrm{C_{H,h,3}}.$$

For the first term: $C_{H,h,1}$ we recall that $U_0(y)$ is given in terms of $J_{H,m_H}(y)$ and therefore,

$$C_{H,h,1} = n_H \int_0^h J_{H,m_H}[u_{c1}I_{H,m_H-1}(y) + u_{c2}L_{H,m_H}(y)][g_{c1}I_{H,m_H-1}(y) + g_{c2}L_{H,m_H}(y)]\ \mathrm{dy}. \tag{B.27}$$

For the next two terms, we first to evaluate the integral expression:

$$\begin{aligned}\int_0^y \frac{\partial U_0}{\partial y} g_H \ \mathrm{d}\tilde{\mathrm{y}} &= h g_{c1} \frac{I_{H,2m_H}(y) - \mathrm{sgn}(\tau_\mathrm{H})(|\tau_\mathrm{H}| - \mathrm{B_H})_+^{\mathrm{m_H}} \mathrm{J_{H,m_H}(y)}}{m_H \kappa_H^{m_H}(\tau_i - \tau_H)} \\ &\quad + h g_{c2} \frac{L_{H,2m_H+1}(y) + \frac{(|\tau_H| - B_H)_+^{m_H+1} J_{H,m_H}(y) - J_{H,2m_H+1}(y)}{(m_H+1)(\tau_i - \tau_H)}}{m_H \kappa_H^{m_H}(\tau_i - \tau_H)}.\end{aligned} \tag{B.28}$$

When arranged as above, the singularities as $\tau_i \to \tau_H$ are removed on expanding the individual terms about τ_H. Since we have

$$\frac{\partial U_0}{\partial h} = u_{c1} I_{H,m_H-1}(y) + u_{c2} L_{H,m_H}(y),$$

we see that $C_{H,h,2}$ is evaluated as integrals of quadratic products of the special functions. Equally, $C_{H,h,3}$ is the quadratic product of integrals of the special functions. To evaluate $C^{(b)}(h,b)$. the approach and expressions are identical, except that the constants u_{c1} and u_{c2} are different.

Turning to the light layer, we have that:

$$\int_h^1 \frac{\partial U_0}{\partial h} \left[U_0 g_L + \int_h^1 \frac{\partial U_0}{\partial y} g_L \ \mathrm{d}\tilde{\mathrm{y}} - \int_\mathrm{y}^1 \frac{\partial \mathrm{U_0}}{\partial \mathrm{y}} \mathrm{g_L} \ \mathrm{d}\tilde{\mathrm{y}} \right] \ \mathrm{dy} = \mathrm{C_{L,h,1}} + \mathrm{C_{L,h,2}} + \mathrm{C_{L,h,3}}.$$

with an analogous expression for the contributions to $C^{(b)}(h,b)$. In the light fluid layer the velocity is $-n_L J_{L,m_L}(y)$ and therefore:

$$C_{L,h,1} = -n_L \int_h^1 J_{L,m_L} [u_{c1} I_{L,m_L-1}(y) + u_{c2} L_{L,m_L}(y)][g_{c1} I_{L,m_L-1}(y) + g_{c2} L_{L,m_L}(y)] \ \mathrm{dy}. \tag{B.29}$$

For the next two terms, we evaluate the integral expression:

$$\begin{aligned}\int_y^1 \frac{\partial U_0}{\partial y} g_L \ \mathrm{d}\tilde{\mathrm{y}} &= (1-h) g_{c1} \frac{I_{L,2m_L}(y) - \mathrm{sgn}(\tau_\mathrm{L})(|\tau_\mathrm{L}| - \mathrm{B_L})_+^{\mathrm{m_L}} \mathrm{J_{L,m_L}(y)}}{m_L \kappa_L^{m_L}(\tau_i - \tau_L)} \\ &\quad + (1-h) g_{c2} \frac{L_{L,2m_L+1}(y) + \frac{(|\tau_L| - B_L)_+^{m_L+1} J_{L,m_L}(y) - J_{L,2m_L+1}(y)}{(m_L+1)(\tau_i - \tau_L)}}{m_L \kappa_L^{m_L}(\tau_i - \tau_L)}.\end{aligned}$$

and then combine with

$$\frac{\partial U_0}{\partial h} = u_{c1} I_{L,m_L-1}(y) + u_{c2} L_{L,m_L}(y).$$

Therefore, $C_{L,h,2}$ is evaluated as integrals of quadratic products of the special functions and $C_{L,h,3}$ is the quadratic product of integrals of the special functions. To evaluate $C^{(b)}(h,b)$. the approach and expressions are identical, except that the constants u_{c1} and u_{c2} are different.

B.5.1 Buoyancy term and flux function

The buoyancy term $S(h, b)$ is simply:

$$\int_h^1 g_L(y)\ \mathrm{dy} \quad = \quad g_{c1} \int_h^1 I_{L,m_L-1}(y)\ \mathrm{dy} + \mathrm{g_{c2}} \int_{\mathrm{h}}^1 \mathrm{L_{L,m_L}(y)}\ \mathrm{dy}. \quad \text{(B.30)}$$

The flux function is simply:

$$q = \int_0^h \frac{J_{H,m_H}(y)}{m_H}\ \mathrm{dy}. \quad \text{(B.31)}$$

Expressions for the integrals of the special functions are given in appendix C.

Appendix C

The functions $I_{k,p}$ and $J_{k,p}$

Here we give those expressions that are useful in evaluating the functions $I_{k,p}$ and $J_{k,p}$, as well as the various integrals that contribute to the weight functions and residual terms, all related to the contents in chapter 6. In each case we give expressions that are valid for $\tau_i \neq \tau_H$ (or $\tau_i \neq \tau_L$). To resolve the limiting behaviour as $\tau_i \to \tau_H$ (or $\tau_i \to \tau_L$) is not particularly difficult, but involves a series expansion about the wall shear stress, which removes any singular behaviour. This detail is omitted for brevity. We start with the heavy fluid layer.

C.1 Heavy fluid layer

We start with the heavy fluid layer.

C.1.1 $I_{H,p}$ and $J_{H,p}$

$$I_{H,p}(y) = \frac{hm_H[\mathrm{sgn}(\tau_{\mathrm{H},\xi\mathrm{y}}(\mathrm{y}))(|\tau_{\mathrm{H},\xi\mathrm{y}}|(\mathrm{y}) - \mathrm{B_H})_+^{\mathrm{p}+1} - \mathrm{sgn}(\tau_{\mathrm{H}})(|\tau_{\mathrm{H}}| - \mathrm{B_H})_+^{\mathrm{p}+1}]}{(p+1)\kappa_H^{m_H}(\tau_i - \tau_H)} \quad \text{(C.1)}$$

$$J_{H,p}(y) = \frac{hm_H[(|\tau_{H,\xi y}|(y) - B_H)_+^{p+1} - (|\tau_H| - B_H)_+^{p+1}]}{(p+1)\kappa_H^{m_H}(\tau_i - \tau_H)} \quad \text{(C.2)}$$

The function $L_{H,p}$ is evaluated as a linear combination of the above.

C.1.2 Integrals of $I_{H,p}$ and $J_{H,p}$

$$\int_0^h I_{H,p}(y)\ \mathrm{dy} = \frac{hJ_{H,p+1}(h)}{(p+1)(\tau_i - \tau_H)} - \frac{h^2 m_H \mathrm{sgn}(\tau_{\mathrm{H}})(|\tau_{\mathrm{H}}| - \mathrm{B_H})_+^{\mathrm{p}+1}}{(p+1)\kappa_H^{m_H}(\tau_i - \tau_H)} \quad \text{(C.3)}$$

$$\int_0^h J_{H,p}(y)\ \mathrm{dy} = \frac{hI_{H,p+1}(h)}{(p+1)(\tau_i - \tau_H)} - \frac{h^2 m_H(|\tau_H| - B_H)_+^{p+1}}{(p+1)\kappa_H^{m_H}(\tau_i - \tau_H)} \quad \text{(C.4)}$$

The integral of $L_{H,p}$ is evaluated as a linear combination of the above.

C.1.3 Integrals of quadratic products of $I_{H,p}$ and $J_{H,p}$

$$\begin{aligned}
\int_0^h I_{H,p}(y)I_{H,q}(y)\,\mathrm{dy} &= \frac{h^2 m_H I_{H,p+q+2}(h)}{(p+1)(q+1)\kappa_H^{m_H}(\tau_i-\tau_H)^2} + \frac{h^3 m_H^2(|\tau_H|-B_H)_+^{p+q+2}}{(p+1)(q+1)\kappa_H^{2m_H}(\tau_i-\tau_H)^2} \\
&\quad -\frac{h^2 m_H \mathrm{sgn}(\tau_\mathrm{H})(|\tau_\mathrm{H}|-\mathrm{B_H})_+^{\mathrm{p+1}}\mathrm{J_{H,q+1}(h)}}{(p+1)(q+1)\kappa_H^{m_H}(\tau_i-\tau_H)^2}, \\
&\quad -\frac{h^2 m_H \mathrm{sgn}(\tau_\mathrm{H})(|\tau_\mathrm{H}|-\mathrm{B_H})_+^{\mathrm{q+1}}\mathrm{J_{H,p+1}(h)}}{(p+1)(q+1)\kappa_H^{m_H}(\tau_i-\tau_H)^2}, \qquad \text{(C.5)} \\
\int_0^h I_{H,p}(y)J_{H,q}(y)\,\mathrm{dy} &= \frac{h^2 m_H[J_{H,p+q+2}(h)-(|\tau_H|-B_H)_+^{p+1}J_{H,q+1}(h)]}{(p+1)(q+1)\kappa_H^{m_H}(\tau_i-\tau_H)^2} \\
&\quad -\frac{h^2 m_H \mathrm{sgn}(\tau_\mathrm{H})(|\tau_\mathrm{H}|-\mathrm{B_H})_+^{\mathrm{q+1}}\mathrm{I_{H,p+1}(h)}}{(p+1)(q+1)\kappa_H^{m_H}(\tau_i-\tau_H)^2} \\
&\quad +\frac{h^3 m_H^2 \mathrm{sgn}(\tau_\mathrm{H})(|\tau_\mathrm{H}|-\mathrm{B_H})_+^{\mathrm{p+q+2}}}{(p+1)(q+1)\kappa_H^{2m_H}(\tau_i-\tau_H)^2}, \qquad \text{(C.6)} \\
\int_0^h J_{H,p}(y)J_{H,q}(y)\,\mathrm{dy} &= \frac{h^2 m_H I_{H,p+q+2}(h)}{(p+1)(q+1)\kappa_H^{m_H}(\tau_i-\tau_H)^2} + \frac{h^3 m_H^2(|\tau_H|-B_H)_+^{p+q+2}}{(p+1)(q+1)\kappa_H^{2m_H}(\tau_i-\tau_H)^2} \\
&\quad -\frac{h^2 m_H[(|\tau_H|-B_H)_+^{p+1}I_{H,q+1}(h)+(|\tau_H|-B_H)_+^{q+1}I_{H,p+1}(h)]}{(p+1)(q+1)\kappa_H^{m_H}(\tau_i-\tau_H)^2}. \qquad \text{(C.7)}
\end{aligned}$$

C.1.4 Integrals of selected cubic products of $I_{H,p}$ and $J_{H,p}$

$$\begin{aligned}
\int_0^h J_{H,p}J_{H,q}J_{H,r}\,\mathrm{dy} &= \frac{h^3 m_H^2}{(p+1)(q+1)(r+1)\kappa_H^{2m_H}(\tau_i-\tau_H)^3} I_{H,p+q+r+3}(h) \\
&\quad -\frac{h^3 m_H^2(|\tau_H|-B_H)_+^{p+1}}{(p+1)(q+1)(r+1)\kappa_H^{2m_H}(\tau_i-\tau_H)^3} I_{H,q+r+2}(h) \\
&\quad -\frac{h^3 m_H^2(|\tau_H|-B_H)_+^{q+1}}{(p+1)(q+1)(r+1)\kappa_H^{2m_H}(\tau_i-\tau_H)^3} I_{H,p+r+2}(h) \\
&\quad -\frac{h^3 m_H^2(|\tau_H|-B_H)_+^{r+1}}{(p+1)(q+1)(r+1)\kappa_H^{2m_H}(\tau_i-\tau_H)^3} I_{H,p+q+2}(h) \\
&\quad +\frac{h^3 m_H^2(|\tau_H|-B_H)_+^{p+q+2}}{(p+1)(q+1)(r+1)\kappa_H^{2m_H}(\tau_i-\tau_H)^3} I_{H,r+1}(h) \\
&\quad +\frac{h^3 m_H^2(|\tau_H|-B_H)_+^{p+r+2}}{(p+1)(q+1)(r+1)\kappa_H^{2m_H}(\tau_i-\tau_H)^3} I_{H,q+1}(h)
\end{aligned}$$

$$
\begin{aligned}
&+\frac{h^3 m_H^2 (|\tau_H| - B_H)_+^{q+r+2}}{(p+1)(q+1)(r+1)\kappa_H^{2m_H}(\tau_i-\tau_H)^3} I_{H,p+1}(h) \\
&-\frac{h^4 m_H^3 (|\tau_H| - B_H)_+^{p+q+r+3}}{(p+1)(q+1)(r+1)\kappa_H^{3m_H}(\tau_i-\tau_H)^3},,
\end{aligned}
$$

$$
\begin{aligned}
\int_0^h J_{H,p}J_{H,q}I_{H,r}\ \mathrm{dy} \;=\;& \frac{h^3 m_H^2}{(p+1)(q+1)(r+1)\kappa_H^{2m_H}(\tau_i-\tau_H)^3} J_{H,p+q+r+3}(h) \\
&-\frac{h^3 m_H^2 (|\tau_H| - B_H)_+^{p+1}}{(p+1)(q+1)(r+1)\kappa_H^{2m_H}(\tau_i-\tau_H)^3} J_{H,q+r+2}(h) \\
&-\frac{h^3 m_H^2 (|\tau_H| - B_H)_+^{q+1}}{(p+1)(q+1)(r+1)\kappa_H^{2m_H}(\tau_i-\tau_H)^3} J_{H,p+r+2}(h) \\
&-\frac{h^3 m_H^2 \mathrm{sgn}(\tau_\mathrm{H})(|\tau_\mathrm{H}| - \mathrm{B_H})_+^{\mathrm{r}+1}}{(p+1)(q+1)(r+1)\kappa_H^{2m_H}(\tau_i-\tau_H)^3} I_{H,p+q+2}(h) \\
&+\frac{h^3 m_H^2 (|\tau_H| - B_H)_+^{p+q+2}}{(p+1)(q+1)(r+1)\kappa_H^{2m_H}(\tau_i-\tau_H)^3} J_{H,r+1}(h) \\
&+\frac{h^3 m_H^2 \mathrm{sgn}(\tau_\mathrm{H})(|\tau_\mathrm{H}| - \mathrm{B_H})_+^{\mathrm{p+r+2}}}{(p+1)(q+1)(r+1)\kappa_H^{2m_H}(\tau_i-\tau_H)^3} I_{H,q+1}(h) \\
&+\frac{h^3 m_H^2 \mathrm{sgn}(\tau_\mathrm{H})(|\tau_\mathrm{H}| - \mathrm{B_H})_+^{\mathrm{q+r+2}}}{(p+1)(q+1)(r+1)\kappa_H^{2m_H}(\tau_i-\tau_H)^3} I_{H,p+1}(h) \\
&-\frac{h^4 m_H^3 \mathrm{sgn}(\tau_\mathrm{H})(|\tau_\mathrm{H}| - \mathrm{B_H})_+^{\mathrm{p+q+r+3}}}{(p+1)(q+1)(r+1)\kappa_H^{3m_H}(\tau_i-\tau_H)^3},
\end{aligned}
$$

$$
\begin{aligned}
\int_0^h J_{H,p}I_{H,q}I_{H,r}\ \mathrm{dy} \;=\;& \frac{h^3 m_H^2}{(p+1)(q+1)(r+1)\kappa_H^{2m_H}(\tau_i-\tau_H)^3} I_{H,p+q+r+3}(h) \\
&-\frac{h^3 m_H^2 (|\tau_H| - B_H)_+^{p+1}}{(p+1)(q+1)(r+1)\kappa_H^{2m_H}(\tau_i-\tau_H)^3} I_{H,q+r+2}(h) \\
&-\frac{h^3 m_H^2 \mathrm{sgn}(\tau_\mathrm{H})(|\tau_\mathrm{H}| - \mathrm{B_H})_+^{\mathrm{q}+1}}{(p+1)(q+1)(r+1)\kappa_H^{2m_H}(\tau_i-\tau_H)^3} J_{H,p+r+2}(h) \\
&-\frac{h^3 m_H^2 \mathrm{sgn}(\tau_\mathrm{H})(|\tau_\mathrm{H}| - \mathrm{B_H})_+^{\mathrm{r}+1}}{(p+1)(q+1)(r+1)\kappa_H^{2m_H}(\tau_i-\tau_H)^3} J_{H,p+q+2}(h) \\
&+\frac{h^3 m_H^2 \mathrm{sgn}(\tau_\mathrm{H})(|\tau_\mathrm{H}| - \mathrm{B_H})_+^{\mathrm{p+q+2}}}{(p+1)(q+1)(r+1)\kappa_H^{2m_H}(\tau_i-\tau_H)^3} J_{H,r+1}(h)
\end{aligned}
$$

$$+\frac{h^3 m_H^2 \mathrm{sgn}(\tau_\mathrm{H})(|\tau_\mathrm{H}| - \mathrm{B_H})_+^{\mathrm{p+r+2}}}{(p+1)(q+1)(r+1)\kappa_H^{2m_H}(\tau_i - \tau_H)^3} J_{H,q+1}(h)$$
$$+\frac{h^3 m_H^2 (|\tau_H| - B_H)_+^{q+r+2}}{(p+1)(q+1)(r+1)\kappa_H^{2m_H}(\tau_i - \tau_H)^3} I_{H,p+1}(h)$$
$$-\frac{h^4 m_H^3 (|\tau_H| - B_H)_+^{p+q+r+3}}{(p+1)(q+1)(r+1)\kappa_H^{3m_H}(\tau_i - \tau_H)^3}.$$

C.2 Light fluid layer

For the light fluid layer the expressions are similar.

C.2.1 $I_{L,p}$ and $J_{L,p}$

$$I_{L,p}(y) = \frac{(1-h)m_L[\mathrm{sgn}(\tau_{\mathrm{L},\xi\mathrm{y}}(\mathrm{y}))(|\tau_{\mathrm{L},\xi\mathrm{y}}|(\mathrm{y}) - \mathrm{B_L})_+^{\mathrm{p+1}} - \mathrm{sgn}(\tau_\mathrm{L})(|\tau_\mathrm{L}| - \mathrm{B_L})_+^{\mathrm{p+1}}]}{(p+1)\kappa_L^{m_L}(\tau_i - \tau_L)} \quad \text{(C.8)}$$

$$J_{L,p}(y) = \frac{(1-h)m_L[(|\tau_{L,\xi y}|(y) - B_L)_+^{p+1} - (|\tau_L| - B_L)_+^{p+1}]}{(p+1)\kappa_L^{m_L}(\tau_i - \tau_L)} \quad \text{(C.9)}$$

The function $L_{L,p}$ is evaluated as a linear combination of the above.

C.2.2 Integrals of $I_{L,p}$ and $J_{L,p}$

$$\int_h^1 I_{L,p}(y)\ \mathrm{dy} = \frac{(1-h)J_{L,p+1}(h)}{(p+1)(\tau_i - \tau_L)} - \frac{(1-h)^2 m_L \mathrm{sgn}(\tau_\mathrm{L})(|\tau_\mathrm{L}| - \mathrm{B_L})_+^{\mathrm{p+1}}}{(p+1)\kappa_L^{m_L}(\tau_i - \tau_L)} \quad \text{(C.10)}$$

$$\int_h^1 J_{L,p}(y)\ \mathrm{dy} = \frac{(1-h)I_{L,p+1}(h)}{(p+1)(\tau_i - \tau_L)} - \frac{(1-h)^2 m_L (|\tau_L| - B_L)_+^{p+1}}{(p+1)\kappa_L^{m_L}(\tau_i - \tau_L)} \quad \text{(C.11)}$$

The integral of $L_{L,p}$ is evaluated as a linear combination of the above.

C.2.3 Integrals of quadratic products of $I_{L,p}$ and $J_{L,p}$

$$\int_h^1 I_{L,p}(y) I_{L,q}(y)\ \mathrm{dy} = \frac{(1-h)^2 m_L I_{L,p+q+2}(h)}{(p+1)(q+1)\kappa_L^{m_L}(\tau_i - \tau_L)^2} + \frac{(1-h)^3 m_L^2 (|\tau_L| - B_L)_+^{p+q+2}}{(p+1)(q+1)\kappa_L^{2m_L}(\tau_i - \tau_L)^2}$$

$$
\begin{aligned}
& -\frac{(1-h)^2 m_L \mathrm{sgn}(\tau_L)(|\tau_L|-B_L)_+^{p+1} J_{L,q+1}(h)}{(p+1)(q+1)\kappa_L^{m_L}(\tau_i-\tau_L)^2}, \\
& -\frac{(1-h)^2 m_L \mathrm{sgn}(\tau_L)(|\tau_L|-B_L)_+^{q+1} J_{L,p+1}(h)}{(p+1)(q+1)\kappa_L^{m_L}(\tau_i-\tau_L)^2},
\end{aligned} \tag{C.12}
$$

$$
\begin{aligned}
\int_h^1 I_{L,p}(y) J_{L,q}(y)\,\mathrm{dy} &= \frac{(1-h)^2 m_L [J_{L,p+q+2}(h) - (|\tau_L|-B_L)_+^{p+1} J_{L,q+1}(h)]}{(p+1)(q+1)\kappa_L^{m_L}(\tau_i-\tau_L)^2} \\
& -\frac{(1-h)^2 m_L \mathrm{sgn}(\tau_L)(|\tau_L|-B_L)_+^{q+1} I_{L,p+1}(h)}{(p+1)(q+1)\kappa_L^{m_L}(\tau_i-\tau_L)^2} \\
& +\frac{(1-h)^3 m_L^2 \mathrm{sgn}(\tau_L)(|\tau_L|-B_L)_+^{p+q+2}}{(p+1)(q+1)\kappa_L^{2m_L}(\tau_i-\tau_L)^2},
\end{aligned} \tag{C.13}
$$

$$
\begin{aligned}
\int_h^1 J_{L,p}(y) J_{L,q}(y)\,\mathrm{dy} &= \frac{(1-h)^2 m_L I_{L,p+q+2}(h)}{(p+1)(q+1)\kappa_L^{m_L}(\tau_i-\tau_L)^2} + \frac{(1-h)^3 m_L^2 (|\tau_L|-B_L)_+^{p+q+2}}{(p+1)(q+1)\kappa_L^{2m_L}(\tau_i-\tau_L)^2} \\
& -\frac{(1-h)^2 m_L [(|\tau_L|-B_L)_+^{p+1} I_{L,q+1}(h) + (|\tau_L|-B_L)_+^{q+1} I_{L,p+1}(h)]}{(p+1)(q+1)\kappa_L^{m_L}(\tau_i-\tau_L)^2}.
\end{aligned} \tag{C.14}
$$

C.2.4 Integrals of selected cubic products of $I_{L,p}$ and $J_{L,p}$

$$
\begin{aligned}
\int_h^1 J_{L,p} J_{L,q} J_{L,r}\,\mathrm{dy} &= \frac{(1-h)^3 m_L^2}{(p+1)(q+1)(r+1)\kappa_L^{2m_L}(\tau_i-\tau_L)^3} I_{L,p+q+r+3}(h) \\
& -\frac{(1-h)^3 m_L^2 (|\tau_L|-B_L)_+^{p+1}}{(p+1)(q+1)(r+1)\kappa_L^{2m_L}(\tau_i-\tau_L)^3} I_{L,q+r+2}(h) \\
& -\frac{(1-h)^3 m_L^2 (|\tau_L|-B_L)_+^{q+1}}{(p+1)(q+1)(r+1)\kappa_L^{2m_L}(\tau_i-\tau_L)^3} I_{L,p+r+2}(h) \\
& -\frac{(1-h)^3 m_L^2 (|\tau_L|-B_L)_+^{r+1}}{(p+1)(q+1)(r+1)\kappa_L^{2m_L}(\tau_i-\tau_L)^3} I_{L,p+q+2}(h) \\
& +\frac{(1-h)^3 m_L^2 (|\tau_L|-B_L)_+^{p+q+2}}{(p+1)(q+1)(r+1)\kappa_L^{2m_L}(\tau_i-\tau_L)^3} I_{L,r+1}(h) \\
& +\frac{(1-h)^3 m_L^2 (|\tau_L|-B_L)_+^{p+r+2}}{(p+1)(q+1)(r+1)\kappa_L^{2m_L}(\tau_i-\tau_L)^3} I_{L,q+1}(h) \\
& +\frac{(1-h)^3 m_L^2 (|\tau_L|-B_L)_+^{q+r+2}}{(p+1)(q+1)(r+1)\kappa_L^{2m_L}(\tau_i-\tau_L)^3} I_{L,p+1}(h) \\
& -\frac{(1-h)^3 m_L^3 (|\tau_L|-B_L)_+^{p+q+r+3}}{(p+1)(q+1)(r+1)\kappa_L^{3m_L}(\tau_i-\tau_L)^3},
\end{aligned}
$$

$$
\int_h^1 J_{L,p} J_{L,q} I_{L,r}\,\mathrm{dy} = \frac{(1-h)^3 m_L^2}{(p+1)(q+1)(r+1)\kappa_L^{2m_L}(\tau_i-\tau_L)^3} J_{L,p+q+r+3}(h)
$$

$$
\begin{aligned}
&-\frac{(1-h)^3 m_L^2 (|\tau_L|-B_L)_+^{p+1}}{(p+1)(q+1)(r+1)\kappa_L^{2m_L}(\tau_i-\tau_L)^3} J_{L,q+r+2}(h)\\
&-\frac{(1-h)^3 m_L^2 (|\tau_L|-B_L)_+^{q+1}}{(p+1)(q+1)(r+1)\kappa_L^{2m_L}(\tau_i-\tau_L)^3} J_{L,p+r+2}(h)\\
&-\frac{(1-h)^3 m_L^2 \mathrm{sgn}(\tau_\mathrm{L})(|\tau_\mathrm{L}|-\mathrm{B_L})_+^{\mathrm{r}+1}}{(p+1)(q+1)(r+1)\kappa_L^{2m_L}(\tau_i-\tau_L)^3} I_{L,p+q+2}(h)\\
&+\frac{(1-h)^3 m_L^2 (|\tau_L|-B_L)_+^{p+q+2}}{(p+1)(q+1)(r+1)\kappa_L^{2m_L}(\tau_i-\tau_L)^3} J_{L,r+1}(h)\\
&+\frac{(1-h)^3 m_L^2 \mathrm{sgn}(\tau_\mathrm{L})(|\tau_\mathrm{L}|-\mathrm{B_L})_+^{\mathrm{p+r}+2}}{(p+1)(q+1)(r+1)\kappa_L^{2m_L}(\tau_i-\tau_L)^3} I_{L,q+1}(h)\\
&+\frac{(1-h)^3 m_L^2 \mathrm{sgn}(\tau_\mathrm{L})(|\tau_\mathrm{L}|-\mathrm{B_L})_+^{\mathrm{q}+\mathrm{r}+2}}{(p+1)(q+1)(r+1)\kappa_L^{2m_L}(\tau_i-\tau_L)^3} I_{L,p+1}(h)\\
&-\frac{(1-h)^3 m_L^3 \mathrm{sgn}(\tau_\mathrm{L})(|\tau_\mathrm{L}|-\mathrm{B_L})_+^{\mathrm{p}+\mathrm{q}+\mathrm{r}+3}}{(p+1)(q+1)(r+1)\kappa_L^{3m_L}(\tau_i-\tau_L)^3},
\end{aligned}
$$

$$
\begin{aligned}
\int_h^1 J_{L,p} I_{L,q} I_{L,r}\ \mathrm{d}y \quad = \quad & \frac{(1-h)^3 m_L^2}{(p+1)(q+1)(r+1)\kappa_L^{2m_L}(\tau_i-\tau_L)^3} I_{L,p+q+r+3}(h)\\
&-\frac{(1-h)^3 m_L^2 (|\tau_L|-B_L)_+^{p+1}}{(p+1)(q+1)(r+1)\kappa_L^{2m_L}(\tau_i-\tau_L)^3} I_{L,q+r+2}(h)\\
&-\frac{(1-h)^3 m_L^2 \mathrm{sgn}(\tau_\mathrm{L})(|\tau_\mathrm{L}|-\mathrm{B_L})_+^{\mathrm{q}+1}}{(p+1)(q+1)(r+1)\kappa_L^{2m_L}(\tau_i-\tau_L)^3} J_{L,p+r+2}(h)\\
&-\frac{(1-h)^3 m_L^2 \mathrm{sgn}(\tau_\mathrm{L})(|\tau_\mathrm{L}|-\mathrm{B_L})_+^{\mathrm{r}+1}}{(p+1)(q+1)(r+1)\kappa_L^{2m_L}(\tau_i-\tau_L)^3} J_{L,p+q+2}(h)\\
&+\frac{(1-h)^3 m_L^2 \mathrm{sgn}(\tau_\mathrm{L})(|\tau_\mathrm{L}|-\mathrm{B_L})_+^{\mathrm{p}+\mathrm{q}+2}}{(p+1)(q+1)(r+1)\kappa_L^{2m_L}(\tau_i-\tau_L)^3} J_{L,r+1}(h)\\
&+\frac{(1-h)^3 m_L^2 \mathrm{sgn}(\tau_\mathrm{L})(|\tau_\mathrm{L}|-\mathrm{B_L})_+^{\mathrm{p}+\mathrm{r}+2}}{(p+1)(q+1)(r+1)\kappa_L^{2m_L}(\tau_i-\tau_L)^3} J_{L,q+1}(h)\\
&+\frac{(1-h)^3 m_L^2 (|\tau_L|-B_L)_+^{q+r+2}}{(p+1)(q+1)(r+1)\kappa_L^{2m_L}(\tau_i-\tau_L)^3} I_{L,p+1}(h)\\
&-\frac{(1-h)^3 m_L^3 (|\tau_L|-B_L)_+^{p+q+r+3}}{(p+1)(q+1)(r+1)\kappa_L^{3m_L}(\tau_i-\tau_L)^3}.
\end{aligned}
$$

Appendix D

Long-wave limit of the Orr-Sommerfeld problem

Here we outline the steps needed in semi-analytical solution of the long-wave limit of the Orr-Sommerfeld problem, $\alpha \longrightarrow 0$ discussed in §6.4.2 of chapter 6.

D.1 Solution of the leading order problem

We assume that $\bar{h}_0 \neq 0$ and divide through by $\bar{h}_0$, as we can see that only $(\psi_0/\bar{h}_0)$ is determined by the system (6.91)-(6.96). There is a similarity between the leading order problem and the earlier derivation of the weight functions, in §6.2.3. Since $\eta_{k,t} \sim \dot{\gamma}^{n_k-1}$, it seems that $D^2(\psi_0/\bar{h}_0)$ must mimic the behaviour of the strain rate, in each layer. This prompts definition of $\eta_{k,t}D^2(\psi_0/\bar{h}_0)$ as a linear function of the shear stress of the base flow in each layer. We find that (6.91) and (6.95)-(6.96) are satisfied by:

$$\eta_{H,t}D^2\left(\frac{\psi_0}{\bar{h}_0}\right) = A_p\tau_{H,\xi y}(y) + \tau_{pi} + \frac{1}{2}\left(\chi - A_p\frac{\chi}{\chi - f}\tau_i\right), \tag{D.1}$$

$$\eta_{L,t}D^2\left(\frac{\psi_0}{\bar{h}_0}\right) = -\frac{f}{\chi - f}A_p\tau_{L,\xi y}(y) + \tau_{pi} - \frac{1}{2}\left(\chi - A_p\frac{\chi}{\chi - f}\tau_i\right) \tag{D.2}$$

where A_p and τ_{pi} are arbitrary constants to be determined. The other parameters are defined via the base flow. These expressions may be rearranged and integrated, via the functions $I_{k,p}(y)$ and $J_{k,p}(y)$, defined earlier. The perturbed axial velocity is given by:

$$D\left(\frac{\psi_0}{\bar{h}_0}\right) = A_pJ_{H,m_H}(y) + A_pB_HJ_{H,m_H-1}(y) + \left[\frac{1}{2}\left(\chi - A_p\frac{\chi}{\chi - f}\tau_i\right) + \tau_{pi}\right]I_{H,m_H-1}(y), \qquad y \in [0, h_0), \tag{D.3}$$

$$D\left(\frac{\psi_0}{\bar{h}_0}\right) = \frac{f}{\chi - f}A_pJ_{L,m_L}(y) + \frac{f}{\chi - f}A_pB_LJ_{L,m_L-1}(y) + \left[\frac{1}{2}\left(\chi - A_p\frac{\chi}{\chi - f}\tau_i\right) - \tau_{pi}\right]I_{L,m_L-1}(y), \qquad y \in (h_0, 1]. \tag{D.4}$$

Note that we have also satisfied (6.92) in deriving the above.

We now determine the constants A_p and τ_{pi}. Using (6.94) we have:

$$\begin{aligned} DU|_{h_0^+}^{h_0^-} &= \frac{f}{\chi-f}A_pJ_{L,m_L}(h_0)+\frac{f}{\chi-f}A_pB_LJ_{L,m_L-1}(h_0)-A_pJ_{H,m_H}(h_0) \\ &\quad -A_pB_HJ_{H,m_H-1}(h_0)+\left[\frac{1}{2}\left(\chi-A_p\frac{\chi}{\chi-f}\tau_i\right)-\tau_{pi}\right]I_{L,m_L-1}(h_0)- \\ &\quad \left[\frac{1}{2}\left(\chi-A_p\frac{\chi}{\chi-f}\tau_i\right)+\tau_{pi}\right]I_{H,m_H-1}(h_0). \end{aligned} \tag{D.5}$$

A second equation for A_p and τ_{pi} is obtained by integrating (D.3) and (D.4) across their respective layers and applying the continuity condition (6.93):

$$\begin{aligned} 0 &= A_p\int_0^{h_0}J_{H,m_H}(y)\ \mathrm{dy}+\mathrm{A_pB_H}\int_0^{\mathrm{h_0}}\mathrm{J_{H,m_H-1}(y)\ dy}+\frac{\mathrm{A_pf}}{\chi-\mathrm{f}}\int_{\mathrm{h_0}}^1\mathrm{J_{L,m_L}(y)\ dy}+ \\ &\quad \frac{A_pB_Lf}{\chi-f}\int_{h_0}^1J_{L,m_L-1}(y)\ \mathrm{dy}+\left[\frac{1}{2}\left(\chi-\mathrm{A_p}\frac{\chi}{\chi-\mathrm{f}}\tau_\mathrm{i}\right)+\tau_\mathrm{pi}\right]\int_0^{\mathrm{h_0}}\mathrm{I_{H,m_H-1}(y)\ dy} \\ &\quad +\left[\frac{1}{2}\left(\chi-A_p\frac{\chi}{\chi-f}\tau_i\right)-\tau_{pi}\right]\int_{h_0}^1I_{L,m_L-1}(y)\ \mathrm{dy}. \end{aligned} \tag{D.6}$$

Algebraic expressions for the integrals above are given in appendix C. Having solved the two linear equations for A_p and τ_{pi}, equation (6.97) gives the leading order eigenvalue:

$$\begin{aligned} c_0 &= \frac{J_{H,m_H}(h_0)}{m_H}+A_p\int_0^{h_0}J_{H,m_H}(y)\ \mathrm{dy}+\mathrm{A_pB_H}\int_0^{\mathrm{h_0}}\mathrm{J_{H,m_H-1}(y)\ dy} \\ &\quad +\left[\frac{1}{2}\left(\chi-A_p\frac{\chi}{\chi-f}\tau_i\right)+\tau_{pi}\right]\int_0^{h_0}I_{H,m_H-1}(y)\ \mathrm{dy} \end{aligned} \tag{D.7}$$

We see that c_0 is always real, as is $(\psi_0/\bar{h}_0)$.

D.2 Solution of the first order problem

The first order problem has a similar structure to the leading order problem. Using linearity and superposition, we can see that

$$\frac{\psi_1}{\bar{h}_0}=\frac{\bar{h}_1}{\bar{h}_0}\frac{\psi_0}{\bar{h}_0}+\mathrm{i}\phi,$$

where $\phi(y)$ is real and satisfies the following problem:

$$D^2(\eta_{k,t}D^2\phi)+Re_k[(c_0-U)D^2(\psi_0/\bar{h}_0)+(\psi_0/\bar{h}_0)D^2U]=0 \tag{D.8}$$

with boundary and interface conditions:

$$\begin{aligned}
\phi &= D\phi = 0, \quad y = 0,\ 1 && \text{(D.9)}\\
0 &= \phi|_L^H \quad y = h_0, && \text{(D.10)}\\
0 &= D\phi|_L^H \quad y = h_0, && \text{(D.11)}\\
\eta_{H,t} D^2\phi &= \eta_{L,t} D^2\phi, \quad y = h_0, && \text{(D.12)}\\
\chi \tan\beta &= \left(Re_H[(c_0 - U)D(\psi_0/\bar{h}_0) + (\psi_0/\bar{h}_0)DU] + D[\eta_{H,t} D^2\phi]\right) && \text{(D.13)}\\
&\quad - \left(Re_L[(c_0 - U)D(\psi_0/\bar{h}_0) + (\psi_0/\bar{h}_0)DU] + D[\eta_{L,t} D^2\phi]\right), \quad y = h_0,
\end{aligned}$$

The stability of the system is found from

$$c_1 = \mathrm{i}\phi(\mathrm{y} = \mathrm{h}_0).$$

Let $\mathcal{F}_k(y)$ be defined by:

$$\mathcal{F}_H(y) = -Re_H[(c_0 + U)(\psi_0/\bar{h}_0) - 2\int_0^y UD(\psi_0/\bar{h}_0)\ \mathrm{ds}],$$

$$\mathcal{F}_L(y) = -Re_L[(c_0 + U)(\psi_0/\bar{h}_0) - 2\int_1^y UD(\psi_0/\bar{h}_0)\ \mathrm{ds}],$$

so that $[\eta_{k,t} D^2\phi - \mathcal{F}_k(y)]$ is linear in each layer. We find that:

$$\begin{aligned}
\eta_{H,t} D^2\phi &= \mathcal{F}_H(y) + A_H \tau_{H,\xi y} + D_H, && \text{(D.14)}\\
\eta_{L,t} D^2\phi &= \mathcal{F}_L(y) - \left(\frac{f}{\chi - f} A_H + \frac{\chi}{\chi - f}\tan\beta\right)\tau_{L,\xi y} + D_H + \mathcal{F}_H(h_0) - \mathcal{F}_L(h_0)\\
&\quad + \frac{\chi\tau_i}{\chi - f}(A_H + \tan\beta), && \text{(D.15)}
\end{aligned}$$

for constants A_H and D_H. These expressions already satisfy (D.12) & (D.13). The constants A_H and D_H are determined by integrating twice with respect to y, away from each wall, using (D.9), and then applying (D.9) & (D.10). The relevant expressions are as follows.

$$D\phi(h_0^-) = \int_0^{h_0} \frac{\mathcal{F}_H}{\eta_{H,t}}\ \mathrm{dy} + \mathrm{A_H J_{H,m_H}(h_0) + A_H B_H J_{H,m_H-1}(h_0) + D_H I_{H,m_H-1}(h_0)}, \quad \text{(D.16)}$$

$$\begin{aligned}
D\phi(h_0^+) &= -\int_{h_0}^1 \frac{\mathcal{F}_L}{\eta_{L,t}}\ \mathrm{dy} + \left(\frac{\mathrm{f}}{\chi - \mathrm{f}}\mathrm{A_H} + \frac{\chi}{\chi - \mathrm{f}}\tan\beta\right)[\mathrm{J_{L,m_L}(h_0) + B_L J_{L,m_L-1}(h_0)}]\\
&\quad - \left[D_H + \mathcal{F}_H(h_0) - \mathcal{F}_L(h_0) + \frac{\chi\tau_i}{\chi - f}(A_H + \tan\beta)\right] I_{L,m_L-1}(h_0). && \text{(D.17)}
\end{aligned}$$

$$\begin{aligned}
\phi(h_0^-) &= \int_0^{h_0} (h_0 - y)\frac{\mathcal{F}_H}{\eta_{H,t}}\ \mathrm{dy} + \mathrm{A_H}\int_0^{\mathrm{h_0}} \mathrm{J_{H,m_H}(y)\ ds} + \mathrm{A_H B_H}\int_0^{\mathrm{h_0}} \mathrm{J_{H,m_H-1}(y)\ ds} +\\
&\quad D_H \int_0^{h_0} I_{H,m_H-1}(y)\ \mathrm{ds} && \text{(D.18)}
\end{aligned}$$

$$\begin{aligned}\phi(h_0^+) \quad = \quad & \int_{h_0}^{1}(y-h_0)\frac{\mathcal{F}_L}{\eta_{L,t}}\ \mathrm{dy} - \left(\frac{\mathrm{f}}{\chi-\mathrm{f}}\mathrm{A_H}+\frac{\chi}{\chi-\mathrm{f}}\tan\beta\right)\int_{\mathrm{h_0}}^{1}\mathrm{J_{L,m_L}(y)\ dy} \\ & -\left(\frac{f}{\chi-f}A_H+\frac{\chi}{\chi-f}\tan\beta\right)B_L\int_{h_0}^{1}J_{L,m_L-1}(y)\ \mathrm{dy}+ \\ & +\left[D_H+\mathcal{F}_H(h_0)-\mathcal{F}_L(h_0)+\frac{\chi\tau_i}{\chi-f}(A_H+\tan\beta)\right]\int_{h_0}^{1}I_{L,m_L-1}(y)\ \mathrm{dy}. \qquad \text{(D.19)}\end{aligned}$$